



**University of
Nottingham**
UK | CHINA | MALAYSIA

Experimental Studies of Ammonia Co-Fuelled Combustion for Future Internal Combustion Engines

Thesis submitted to the University of Nottingham for the degree of
Doctor of Philosophy, January 2024.

William Bowling

14239336

Supervised by

**Professor Alasdair Cairns
Professor Antonino La Rocca
Dr Abdelrahman Hegab**

Abstract

The demand for rapid global decarbonisation has driven the emergence of zero-carbon alternative fuels for internal combustion engines (ICE). In order for the hard-to-abate industries such as shipping and heavy duty to meet the stringent targets, a diverse range of alternative fuels must be employed. Ammonia, being a more effective carrier of hydrogen than liquid hydrogen on a volumetric basis, with established production and transportation infrastructure, is poised to hold a significant fraction of the future fuel share. Overcoming the challenges such as high toxicity, low burning velocity, and high ignition energy is crucial in enabling the uptake of the fuel. A key opportunity to improve the combustion characteristics of ammonia is to co-fuel with hydrogen, a high energy fuel able to be produced from ammonia. Increasing interest in ammonia as a fuel has resulted in a new wave of literature focused on the fundamentals of ammonia and ammonia-hydrogen combustion as well as limited applied engine studies. The focus of this research was to enhance understanding of utilising combustion promoters, particularly hydrogen, to enable ammonia as a fuel for ICEs. The conducted studies aimed to advance knowledge regarding the trade-offs associated with optimising combustion, performance, efficiency, and pollutant emissions in the context of ammonia co-fuelling.

The first study consisted of the design and build of a novel optical con-

stant volume combustion chamber and test-rig control circuit that enabled fundamental investigation into ammonia-hydrogen combustions within an engine-like environment. The chamber was successfully designed, hydrostatically tested, and validated to British Standards. Flame imaging and analysis techniques were derived to enable insights into flame structures. Subsequent benchmarking testing with methane-air flames revealed a good correlation with previous literature values. Alongside this, ammonia-hydrogen-air combustion testing provided further detail around buoyancy impacts and the development of cellularity within mixtures at pressure with between 20-30% mixtures showing clear influence from hydrogen. The test data produced from these studies will be used in future comparisons of advanced ignition systems such as turbulent jet ignition.

The second study was a retrofit of a fully-instrumented modern diesel compression ignition (CI) engine to operate with gaseous ammonia co-fuelling with diesel and/or hydrogen. The upgrade was completed iteratively, with the first iteration providing key learning that was carried forward. The first iteration achieved low ammonia substitution ratios, 18% (energy basis), due to limitations from cylinder-to-cylinder fuelling imbalance, ammonia liquid within the line and engine control. Upgrading the original fuelling system and engine control unit provided a finer level of control of injection of all fuels. A substitution ratio of 90% (energy basis) ammonia was achieved at full load, 600 rpm. At lower loads, significantly higher diesel quantities were required to maintain effective combustion, indicating limitations for future transient engine operation, approaching stoichiometric air-fuel ratios was an influential factor in enabling high ammonia substitution ratios. Throughout testing high levels of ammonia slip (10,000 ppm) were observed indicating the clear need for advanced exhaust after-treatment and/or in-cylinder mitigation strategies in future work.

Acknowledgements

First and foremost, I would like to thank my supervisor, Professor Alasdair Cairns, Head of the Powertrain Research Center at the University of Nottingham. His continued support and guidance have been invaluable, instilling in me the confidence to persevere.

Thanks to Dr. Abdelrahmen Hegab, whose engine expertise, training, and friendship made the hours of coding, problem-solving, and engine testing all the more bearable. I am also grateful to Sikai Geng, Ajith Ambalakatte, and the entire research group for their time and collaborative efforts.

I extend my appreciation to the technical support staff whose expertise and support were indispensable to the success of this work. Especially to Nigel Sykes whose wealth of knowledge and willingness to listen to my frustrations significantly aided in navigating challenges.

I want to express my gratitude to Jacob Prosser and Chris Ryder for their contributions in making this journey enjoyable.

A special acknowledgment to my girlfriend, Ruth Atkinson, whose unwavering belief in me has been a constant source of inspiration and encouragement. Last but not least, heartfelt thanks to my family for their enduring support and countless phone calls throughout this research endeavor.

Thank you all for your contributions, support and encouragement.

Contents

Abstract	i
Acknowledgements	iii
List of Tables	ix
List of Figures	x
Abbreviations	xxiii
Chapter 1 Introduction	1
1.1 Decarbonising shipping	2
1.2 Alternative fuels	4
1.3 Summary	11
Chapter 2 Literature Review	13
2.1 Background	16
2.2 Combustion and burning velocity fundamentals	22
2.3 Optical research on flame speed measurements	34
2.4 Laminar burning velocity investigations	41
2.5 Ammonia in engines	50
2.6 Summary	58
Chapter 3 Design of a Novel Optically Accessible Constant Volume Combustion Chamber	60
3.1 Design functionality and requirements	61
3.2 Material selection and compatibility	64
3.3 Design calculations	66
3.4 Optical window design	73
3.5 Bolt loading calculations	76

3.6	Thermal expansion	78
3.7	Simulation	79
3.8	Instrumentation and control overview	85
3.9	System schematics	95
3.10	Data acquisition and processing	98
3.11	Conclusion	101
Chapter 4	Analytical Techniques	103
4.1	Imaging setup	104
4.2	Image processing	107
4.3	Side combustion view	112
4.4	Unstretched laminar burning velocity	113
4.5	Uncertainty	117
Chapter 5	Constant Volume Combustion Chamber Re-	
	sults	120
5.1	Key experimental parameters	121
5.2	Methane benchmarking study	124
5.3	Ammonia testing	138
5.4	Ammonia/hydrogen testing	145
5.5	Side combustion imaging results	155
5.6	Discussion	159
Chapter 6	Experimental Engines	170
6.1	Background	171
6.2	Engine test facilities	171
6.3	Diesel fuelling system	173
6.4	Instrumentation	176
6.5	Data acquisition and processing	177
6.6	Emissions analysis and smoke meter	187
6.7	Engine control unit (ECU) development	189

6.8	Ammonia upgrade	191
6.9	Hydrogen upgrade	198
Chapter 7	Dual Fuel Results	202
7.1	First iteration: Ammonia fumigation	202
7.2	Second iteration: Ammonia port-fuel injection	216
7.3	Discussion	227
Chapter 8	Conclusions & Recommendations for Future	
	Work	234
8.1	Novel optical constant volume combustion chamber	235
8.2	Diesel engine retrofit for ammonia	236
8.3	Overall implications and future work	238
	Bibliography	242
	Appendices	268
Appendix A	Combustion Chamber Technical Drawings	269
Appendix B	Finite Element Analysis Report	278
Appendix C	Combustion Chamber Assembly Manual	295
Appendix D	Combustion Chamber Mixture Properties	298

List of Tables

1.1	Comparison of different fuels used for marine and heavy-duty engines, adapted from [27], [78], [127],[160], and [168].	5
2.1	Table showing the health effects of ammonia exposure, adapted from [31, 35]	18
2.2	Summary of relevant research studies relating to methane-air laminar burning velocity investigations.	42
2.3	Summary of relevant research studies relating to ammonia-air laminar burning velocity investigations.	47
2.4	Summary of relevant research studies relating to ammonia-air laminar burning velocity investigations.	50
3.1	Requirements for the Constant Volume Combustion Chamber	62
3.2	List of parts used in the constant volume combustion chamber assembly with associated part numbers and materials. . .	64
3.3	Comparison of the thermal and mechanical properties of fused silica and sapphire [72].	65
3.4	Latent heat of vaporisation of the three fuels considered in this study, taken from NIST [113].	68
3.5	Minimum values for the 0.2% (Rp0.2) and 1.0% (Rp1.0) proof strength of stainless steel 316 (1.4401) at elevated temperatures in the solution annealed condition (100 – 300°C) from BS EN 10272:2016 [15]	71

3.6	Minimum values for the tensile strength of austenitic steels at elevated temperatures in the solution annealed condition from BS EN 10272:2016 [15]	71
3.7	O-ring selection and dimensions from BS EN 4518 [14].	76
3.8	Combustion chamber material thermal expansion coefficients	78
3.9	Material properties	79
3.10	Mesh properties	80
3.11	Finite element analysis results per component.	82
3.12	Vacuum purge cycling contaminant concentration per iteration.	86
3.13	Gas pressure regulator settings	97
3.14	National Instruments DAQ modules	98
5.1	Experimental conditions used in this study.	122
5.2	Measured unstretched laminar burning velocity and corresponding Markstein Length at 0.1 MPa methane-air flames.	133
5.3	Measured unstretched laminar burning velocity and corresponding Markstein Length at 0.3 MPa methane-air flames.	133
5.4	Measured unstretched laminar burning velocity and corresponding Markstein Length at 0.5 MPa methane-air flames.	133
5.5	Measured unstretched laminar burning velocity at 0.3 MPa - ammonia-air flames.	142
5.6	Measured unstretched laminar burning velocity at 0.5 MPa - ammonia-air flames.	142
5.7	Measured unstretched laminar burning velocity at 0.1 MPa with varying ammonia/hydrogen SRs.	152
5.8	Measured unstretched laminar burning velocity at 0.3 MPa with varying ammonia/hydrogen SRs.	152

5.9	Measured unstretched laminar burning velocity at 0.5 MPa with varying ammonia/hydrogen SRs.	152
5.10	Experimental conditions of the side imaging testing	155
6.1	Main specifications of the test engine used in the present work.	173
6.2	National Instruments DAQ modules.	178
6.3	Summary of emissions analysers used in conjunction with the Volvo test rig including measuring principles, range and model.	188
6.4	Hydrogen flow meter sizing information and minimum flow rate with 1% error.	200
D.1	Properties of methane-air mixtures employed in this study. .	299
D.2	Properties of ammonia-air mixtures employed in this study. .	299
D.3	Properties of ammonia-hydrogen-air mixtures employed in this study.	300

List of Figures

1.1	Three decarbonisation scenarios with targets compared to business as usual GHG emissions taken from [20].	3
1.2	Comparison of the volumetric and gravimetric energy density of various alternative fuels.	5
2.1	Laminar flame structure with temperature and heat release rate profiles based on experimental results of Friedman and Burke [38].	23
2.2	Historical measured laminar burning velocity for methane-air flames at atmospheric conditions adapted from Egolfopoulos et al. [33], Hinton [62] and Law [90].	26
2.3	Depiction of a cellular hydrogen-air flame using schlieren imaging [84].	29
2.4	Progression of a stoichiometric ammonia-air flame influenced heavily by buoyancy [21].	30
2.5	Typical combustion chamber setup with schlieren imaging system taken from [96].	37
2.6	Dual field lens schlieren system from Floryan et al. [37].	39
2.7	Schematic of a PIV-based imaging setup from Bradley et al.[10].	40
2.8	Comparison of the measured burning velocity of CH ₄ -air flames at 0.1 MPa and between 298 - 300 K. References in Table 2.2.	43

2.9	Comparison of the measured burning velocity of CH ₄ -air flames at 0.3 MPa and between 298 - 300 K. References in Table 2.2.	44
2.10	Comparison of the measured burning velocity of CH ₄ -air flames at 0.5 MPa and between 298 - 300 K. References in Table 2.2.	44
2.11	Comparison of the measured burning velocity of CH ₄ -air flames across various pressures, 298 - 300 K. References can be found in Table 2.2.	45
2.12	Comparison of the measured burning velocity of NH ₃ -air flames at 0.1 MPa, 298 - 300 K. References in Table 2.3.	48
2.13	Burning velocity measurements of NH ₃ -H ₂ -air flames with varying substitution ratios at 0.1 MPa, 298 - 300 K. References in Table 2.4.	49
3.1	Render of the combustion chamber.	63
3.2	Cross-section of the combustion chamber.	63
3.3	Transmission data for UV and IR grade fused silica for a 5mm thick sample without Fresnel reflections [25].	66
3.4	Plot of the approximate maximum post-combustion pressure for various fuel mixtures at 298K.	69
3.5	Representative cross-section used for stress calculations.	73
3.6	Representative diagram of a clamped pressure vessel window.	75
3.7	Cross-section showing the window sealing.	76
3.8	Boundary constraints, fixtures and loading constraints added to simplified main body assembly.	81
3.9	Von Mises stress plots; (a) side view, (b) top-down section view.	83

3.10	Exaggerated deformation plots (a)front view (b)side section view.	84
3.11	Side-on cross-section of the combustion chamber showing the location of key instrumentation and heaters.	91
3.12	Comparison of two combustions with the pressure transducer protected from the thermal shock and uncovered.	93
3.13	Comparison of different thermal shock protections used on the piezoelectric pressure transducer.	93
3.14	Combustion chamber intake and exhaust schematics.	95
3.15	Screenshot of LabView dashboard.	99
4.1	Image of the constant volume combustion chamber optical setup with the high speed camera.	104
4.2	High-speed camera setup with blackout frame.	106
4.3	Pixel calibration and spark center check, calibration code output.	107
4.4	Image processing steps: 1.Raw TIFF image taken directly from high speed camera with no processing. 2.Image is brightened for ease of processing to find edge. 3.Image is binarised for edge detection and regionprops function. 4.Flame boundary is identified to calculate wrinkle factor, radius and flame speed. 5.Processed image is output with flame edge identified for checking.	109
4.5	(a)Ammonia-air flame at 0.5 MPa, $\phi = 1.0$, (b)Ammonia-hydrogen-air flame at 0.5 MPa, $\phi = 1.0$, SR = 0.5.	110
4.6	Ammonia-hydrogen-air(50:50) flame at 0.5 MPa, $\phi = 1.0$, with identification of flame centroid, flame outline (blue), and mean radius (red).	111
4.7	Side on configuration view of a combustion event.	113

4.8	Ellipsoidal buoyancy calculation using the bounding box (green). Mean radius (red) from standard assumptions shown along with flame boundary (blue).	116
4.9	Pressure rise plot with flame radius progression for;(a)Ammonia- air flame at 0.5 MPa, $\phi = 1.0$ (b)Ammonia-hydrogen-air flame at 0.5 MPa, $\phi = 1.0$, SR = 0.5.	118
5.1	High speed images of spherically propagating methane pre- mixed flame at an initial pressure of 0.1MPa with varying equivalence ratios.	125
5.2	Flame contours of methane air flames at 0.1 MPa at different equivalence ratios.	126
5.3	Plots for the 0.1 MPa methane-air test condition for the av- erage of each equivalence ratio for; (a)shape ratio, (b)wrinkle factor against radius.	126
5.4	High speed images of spherically propagating methane pre- mixed flame at an initial pressure of 0.3MPa with varying equivalence ratios.	127
5.5	Flame contours of methane air flames at 0.3 MPa at different equivalence ratios.	128
5.6	Plots for the 0.3 MPa methane-air test condition for the av- erage of each equivalence ratio for; (a)shape ratio, (b)wrinkle factor against radius.	128
5.7	High speed images of spherically propagating methane pre- mixed flame at an initial pressure of 0.5 MPa with varying equivalence ratios.	129
5.8	Flame contours of methane air flames at 0.5 MPa at different equivalence ratios.	130

5.9	Plots for the 0.5 MPa methane-air test condition for the average of each equivalence ratio for; (a)shape ratio, (b)wrinkle factor against radius.	130
5.10	High speed images of spherically propagating methane premixed flame at an equivalence ratio of 1.0 across different pressures.	131
5.11	Flame contours of methane-air flames at various pressures at an equivalence ratio of 1.0	131
5.12	Plots presenting (a) flame luminosity at a radius of 20 mm for each of the methane air test conditions, and (b)flame centroid deviation rate against laminar burning velocity (LBV) for each pressure condition for methane-air flames.	132
5.13	Maximum pressure vs equivalence ratio for premixed methane-air combustion	134
5.14	Laminar burning velocity vs equivalence ratio for premixed methane-air combustion at 0.1 MPa initial pressure compared to literature.	135
5.15	Laminar burning velocity vs equivalence ratio for premixed methane-air combustion at 0.3 MPa initial pressure compared to literature.	136
5.16	Laminar burning velocity vs equivalence ratio for premixed methane-air combustion at 0.5 MPa initial pressure compared to literature.	136
5.17	Laminar burning velocity vs initial pressure for premixed methane combustion at 1.0 equivalence ratio compared to literature values.	137
5.18	High speed images of spherically propagating ammonia premixed flame at an initial pressure of 0.3MPa with varying equivalence ratios.	139

5.19	High speed images of spherically propagating ammonia pre-mixed flame at an initial pressure of 0.5MPa with varying equivalence ratios.	139
5.20	Flame contours of ammonia-air flames at 0.5 MPa at varying equivalence ratios.	140
5.21	Flame contours of ammonia-air flames at various pressures at an equivalence ratio of 1.0.	140
5.22	Plots for the 0.3 MPa ammonia-air test condition for the average of each equivalence ratio for; (a)shape ratio, (b)wrinkle factor against radius.	141
5.23	Plots for the 0.5 MPa ammonia-air test condition for the average of each equivalence ratio for; (a)shape ratio, (b)wrinkle factor against radius.	141
5.24	Plots presenting (a) flame centroid deviation rate against LBV for each pressure condition for ammonia-air flames, and (b)flame luminosity at a radius of 20 mm for each of the ammonia air test conditions.	142
5.25	Laminar burning velocity vs equivalence ratio for premixed ammonia-air combustion at 0.5 MPa initial pressure compared to literature. Three techniques compared to account for buoyancy as described in Section 4.4.1.	143
5.26	Plot presenting the buoyancy adjusted laminar burning velocity against equivalence ratio for the 0.3 and 0.5 MPa pressure conditions.	144
5.27	Plots presenting the (a)Max pressure vs equivalence ratio for premixed ammonia combustion at 0.1 MPa - 0.5 MPa initial pressure and (b)the laminar burning velocity results against literature for ammonia-air flames at varying pressures. . . .	144

5.28	High speed images of spherically propagating ammonia-hydrogen-air premixed flame at an initial pressure of 0.1 MPa with varying SRs at an equivalence ratio of 1.0.	146
5.29	Flame contours of ammonia-air flames at 0.1 MPa at varying SRs.	146
5.30	Plots for the 0.1 MPa ammonia-hydrogen-air test condition for the average of each SR for; (a)shape ratio, (b)wrinkle factor against radius.	147
5.31	High speed images of spherically propagating ammonia-hydrogen-air premixed flame at an initial pressure of 0.3MPa with varying SRs at an equivalence ratio of 1.0.	147
5.32	Flame contours of ammonia-air flames at 0.3 MPa at varying SRs.	148
5.33	Plots for the 0.3 MPa ammonia-hydrogen-air test condition for the average of each SR for; (a)shape ratio, (b)wrinkle factor against radius.	148
5.34	High speed images of spherically propagating ammonia-hydrogen-air premixed flame at an initial pressure of 0.5MPa with varying SRs at an equivalence ratio of 1.0.	149
5.35	Flame contours of ammonia-air flames at 0.5 MPa at varying SRs.	149
5.36	Plots for the 0.5 MPa ammonia-hydrogen-air test condition for the average of each SR for; (a)shape ratio, (b)wrinkle factor against radius.	150
5.37	Plot of flame centroid deviation rate against LBV for each pressure condition for ammonia-hydrogen-air flames.	151

5.38	(a)Plot of flame luminosity vs hydrogen SR of an ammonia-air premixed flame at an initial pressures of 0.1, 0.3, and 0.5 MPa at an equivalence ratio of 1.0. (b)Max pressure vs SR for premixed ammonia-hydrogen-air combustion at 0.1 MPa - 0.5MPa initial pressure.	151
5.39	Laminar burning velocity vs SR for premixed ammonia-hydrogen-air combustion at 0.1 MPa initial pressure	153
5.40	Laminar burning velocity vs SR for premixed ammonia-hydrogen-air combustion at 0.3 MPa initial pressure	154
5.41	Laminar burning velocity vs equivalence ratio for premixed ammonia-hydrogen-air combustion at 0.5 MPa initial pressure	154
5.42	High speed images of spherically propagating methane premixed flame at an initial pressure of 0.1MPa with varying equivalence ratios, side-on view.	156
5.43	Plot of flame radius and apparent flame speed in horizontal and vertical direction against time for methane-air flames at 0.1 MPa, equivalence ratio $\phi = 1.0$	157
5.44	Plot of the variation in radius between the horizontal and vertical radii for different equivalence ratios.	157
5.45	Plot of the apparent flame speed against the flame radius for various equivalence ratios considering both the horizontal flame Sn_x and vertical (wall influenced) flame Sn_y	158
5.46	Plot of side combustion laminar burning velocities with literature data and previous data.	159
5.47	Plot of flame centroid deviation rate against LBV for each pressure condition for all flames measured.	168
6.1	Volvo engine test rig.	171
6.2	Volvo Engine Diesel Fuelling System	175

6.3	Main LabVIEW dashboard used during engine operation. . .	179
6.4	Diesel injector current clamp comparison for two injection modes.	190
6.5	First iteration of the ammonia fuelling design.	194
6.6	First iteration ammonia port fuel injection rail highlighted in red. Ammonia feed from the left side and venting from the right.	196
6.7	Image of Icing on Cylinder 1 and 2 injection pipes.	196
6.8	New integrated NH_3 and H_2 rail.	198
6.9	CAD schematic of new rail incorporating ammonia and hydrogen Clean Air Power injectors.	198
6.10	Hydrogen fuel delivery system.	201
7.1	Plot of the $IMEP_n$ for each cylinder against injection duration in CAD for the fixed point testing - all cylinder injection active.	204
7.2	Plot of the change in $IMEP_n$ for each cylinder against injection duration for the fixed point testing - all cylinder injection active.	204
7.3	Diesel mass flow rate and cylinder one approximate ammonia SR against injection duration - all cylinder injection active. .	205
7.4	Plot for the fixed point ammonia engine testing - all cylinder injection active, of in-cylinder pressure for 500 cycles against crank angle for baseline - no ammonia injection	206
7.5	Plot for the fixed point ammonia engine testing - all cylinder injection active, cylinder 1 in-cylinder pressure for 500 cycles against crank angle for 36 CAD ammonia injection.	206
7.6	Plot of CoV of $IMEP_n$ against ammonia injection duration for each cylinder - all cylinder injection active.	207

7.7	Rate of heat release against crank angle degree in cylinder 1 for various ammonia injection durations - all cylinder injection active.	208
7.8	Plot of the IMEP _n for each cylinder against injection duration in CAD for the fixed point testing - cylinder 3 & 4 injection active.	209
7.9	Plot of the change in IMEP _n for each cylinder against injection duration for the fixed point testing - cylinder 3 & 4 injection active.	209
7.10	Plot of CoV of IMEP _n against ammonia injection duration for each cylinder - cylinder 3 & 4 injection active.	210
7.11	Diesel mass flow rate and average cylinder approximate ammonia SR against injection duration - cylinder 3 & 4 injection active.	211
7.12	Rate of heat release in cylinder 3 against crank angle degree for various ammonia injection durations - cylinder 3 & 4 injection active.	212
7.13	Plot of the IMEP _n for each cylinder against injection duration in CAD for the fixed point testing - cylinder 6 injection active.	213
7.14	Plot of the change in IMEP _n for each cylinder against injection duration for the fixed point testing - cylinder 6 injection active.	213
7.15	Plot of CoV of IMEP _n against ammonia injection duration for each cylinder - cylinder 6 injection active.	214
7.16	Diesel mass flow rate and cylinder approximate ammonia SR against injection duration - cylinder 6 injection active.	215

7.17	Rate of heat release in cylinder 6 against crank angle degree for various ammonia injection durations - cylinder 6 injection active.	215
7.18	Plot of maximum SR (energy basis) achieved at 600 rpm and measured lambda across various engine rated loads - unthrottled (100% throttle) and throttled (10% throttle). . .	217
7.19	Plot of ammonia slip and NO_x emissions at 600 rpm across various engine rated loads - unthrottled (100% throttle) and throttled (10% throttle).	218
7.20	Plot of in-cylinder pressure at 600 rpm across various engine rated loads - unthrottled (100% throttle).	218
7.21	Plot of in-cylinder pressure at 600 rpm across various engine rated loads - throttled (10% throttle).	219
7.22	Plot of IMEP _n variation from the mean for each cylinder with varying SR and load - unthrottled (100% throttle). . .	220
7.23	Plot of net heat release at 600 rpm across various engine rated loads - unthrottled (100% throttle).	221
7.24	Plot of cumulative heat release at 600 rpm across various engine rated loads - unthrottled (100% throttle).	222
7.25	Plot of net heat release at 600 rpm across various engine rated loads - throttled (10% throttle).	223
7.26	Plot of cumulative heat release at 600 rpm across various engine rated loads - throttled (10% throttle).	223
7.27	Plot of maximum SR (energy basis) achieved at 9 bar BMEP and measured lambda across various engine speeds.	225
7.28	Plot of ammonia and diesel mass flow rates achieved at 9 bar BMEP at various engine speeds.	225
7.29	Plot of in-cylinder pressure against crank angle at 9 bar BMEP for various engine speeds.	226

7.30 Plot of net heat release against crank angle at 9 bar BMEP for various engine speeds.	227
---	-----

Abbreviations

BMEP Brake mean effective pressure.

CAD Crank angle degree.

CFR Cooperative fuel research-engine.

CI Compression ignition.

CoV Coefficient of variance.

CVCC Constant volume combustion chamber.

DAQ Data acquisition.

ECU Engine control unit.

EGR Exhaust gas re-circulation.

FEA Finite element analysis.

GHG Greenhouse gas.

HFO Heavy fuel oil.

HVO Hydrogenated vegetable oils.

ICE Internal combustion engine.

IMEP Indicated mean effective pressure.

IMO International Maritime Organisation.

LNG Liquefied natural gas.

MGO Marine gas oil.

Mtoe Million tonnes of oil equivalent.

NBR Nitrile rubber.

OEM Original equipment manufacturer.

PIV Particle image velocimetry.
PTFE Polytetrafluoroethylene.
SAF Sustainable aviation fuel.
SCR Selective catalytic reduction.
SI Spark ignition.
SR Substitution ratio.
TDC Top dead center.
TJI Turbulent jet ignition.

Chapter 1

Introduction

The Intergovernmental Panel on Climate Change states with high confidence that human activity, principally through greenhouse gas (GHG) emissions have unequivocally caused global warming [77]. In 2015, the Paris Agreement, a legally binding international treaty on climate change, was signed by 196 countries with the overarching goal to “limit the increase in the global average temperature to well below 2°C above pre-industrial levels” and pursue efforts “to limit the temperature increase to 1.5°C above pre-industrial levels.” [154]. All of the modelled pathways that limit the global rise in temperature to within 2°C involve rapid, deep, and in most cases immediate reduction in GHGs across all sectors this decade. Amongst these sectors it is recognised that the following are considered difficult to decarbonise; aviation, steel, and shipping. 80% of global trade by volume is transported by shipping, and although considered one of the most efficient ways of transporting material, it represents 3% of global emissions, with 99% of the final energy demand being met using fossil fuels [78, 153].

1.1 Decarbonising shipping

The shipping industry is a global industry that relies on large, long-life assets operating with thin margins, and a massive dependence on fossil fuels. Taking into consideration the average age of the existing global fleet as well as the technical lifetime of large vessels (25-30 years), vessels deployed in the next decade will characterise the global fleets' carbon emissions in 2050. The global challenge presents itself in many ways, including fuel production and storage, fuelling infrastructure, ship design, and fuel characteristics, with a key factor being flexibility and speed of technological maturity.

1.1.1 Policy and regulation

In 2011 the International Maritime Organisation (IMO) adopted the first set of international mandatory measures to improve the energy efficiency of ships [73], these measures were applied to all ships of at least 400 gross tons. The measures were intended to save fuel and reduce GHG emissions by optimising the speed and course of the vessel, amongst other things. Since then, the IMO has continued to strengthen regulatory measures with the adoption of the Initial IMO GHG Strategy [75] with the most recent targeting net zero GHG emissions by or around 2050 [74].

The updated strategy is an ambitious decarbonisation goal, as shown in Figure 1.1. The primary method is to switch to low or zero-carbon fuel alternatives, it is understood that a variety of energy sources must be utilised in order to achieve this. The criteria for the selection of these fuels must meet the rigorous requirements of shipping, which necessitates a sustained,

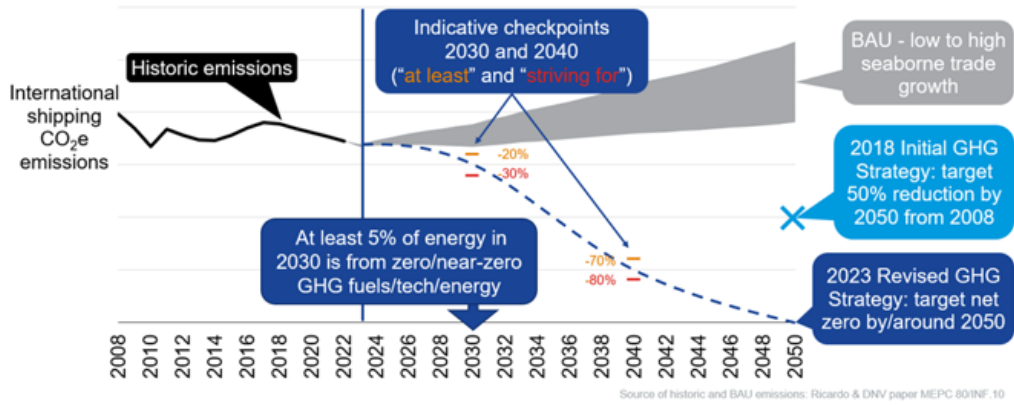


Figure 1.1: Three decarbonisation scenarios with targets compared to business as usual GHG emissions taken from [20].

high level of power for extended periods. Currently the sources being considered include, methanol, green ammonia, synthetic and bio-based fuels. Each of the fuel options has varying benefits and challenges with considerations needing to be made in terms of; combustion properties, energy density (volumetric and gravimetric), availability, cost, technical maturity, and environmental impact. One of the key drivers in shipping is economical, with the cost of fuel being the main determinant of decision making. This can vary greatly depending on length of voyage, geographical location, and the policy and regulations in place. These fuels must be financially viable for ship owners, but developments around logistical, infrastructural, and safety aspects will need to occur. Adding to these considerations is the introduction of the EU Emissions Trading System from 2024 which will significantly alter the costs of fuels, especially considering that the emissions are recorded on a well-to-wake basis, this means that the entire fuel life-cycle emissions will be considered.

1.2 Alternative fuels

Fuels and power sources that function as partial or complete substitutes for conventional fossil oil sources are referred to as alternative fuels. There is a large variety of these fuels, however when considering marine and heavy duty applications the following are highlighted as key contenders;

- Advanced Biofuels - these fuels are synthesized from advanced feedstocks such as algae and waste products that do not compete for food/feed land use. Examples include hydro-treated vegetable oil (HVO) and bio-methanol.
- E-Fuels - these fuels are hydrogen based fuels, synthesised using hydrogen produced using renewably powered electrolysis. Production of e-fuels is not yet technologically mature, although it is expected to reach maturity in the 2030s [20].
- Blue Fuels - these fuels are hydrogen based fuels, synthesised using hydrogen derived from fossil fuels with a degree of carbon capture technologies.

Examples of e-fuels and blue fuels consist of fuels such as ammonia, hydrogen, methanol, and liquefied natural gas (LNG). The defining factor that categorises the fuel into either e-fuel or a blue fuel is the production method [141]. Electrification is not considered for heavy duty and marine applications due to the power and energy density demand required of these sustained high power modes of operation. The battery size required, along with the demands on recharging times are not achievable with current or future battery solutions [163]. Common implementation barriers currently applicable to most carbon-neutral fuels include; increased capital

investment, limited fuel availability, lack of global bunkering infrastructure, additional training of crew, high cost of fuel, and additional demand for storage space on board [20]. Table 1.1 presents key characteristics of alternative fuels that have been identified as options for both the heavy duty and marine sectors.

Fuel Type	MGO	LNG	Methanol	Ammonia	H_2 Liquid	H_2 Gas
LHV [MJ/kg]	42.7	50	19.9	18.6	120	120
Volumetric Energy Density [GJ/m ³]	36.6	23.4	15.8	12.7	8.5	7.5
Storage Pressure [bar]	1	1	1	8.6 or 1	1	700
Storage Temperature [°C]	120	-162	20	20 or -34	-253	20
Auto-ignition Temperature [°C]	257	537	464	651	571	571
Stoichiometric air-fuel ratio by mass	14.6	17.2	6.44	6.05	34.3	34.3
Flammability Limits [%]	0.6 - 7.5	5 - 15	6.7 - 36	16 - 25	4 - 75	4 - 75

Table 1.1: Comparison of different fuels used for marine and heavy-duty engines, adapted from [27], [78], [127],[160], and [168].

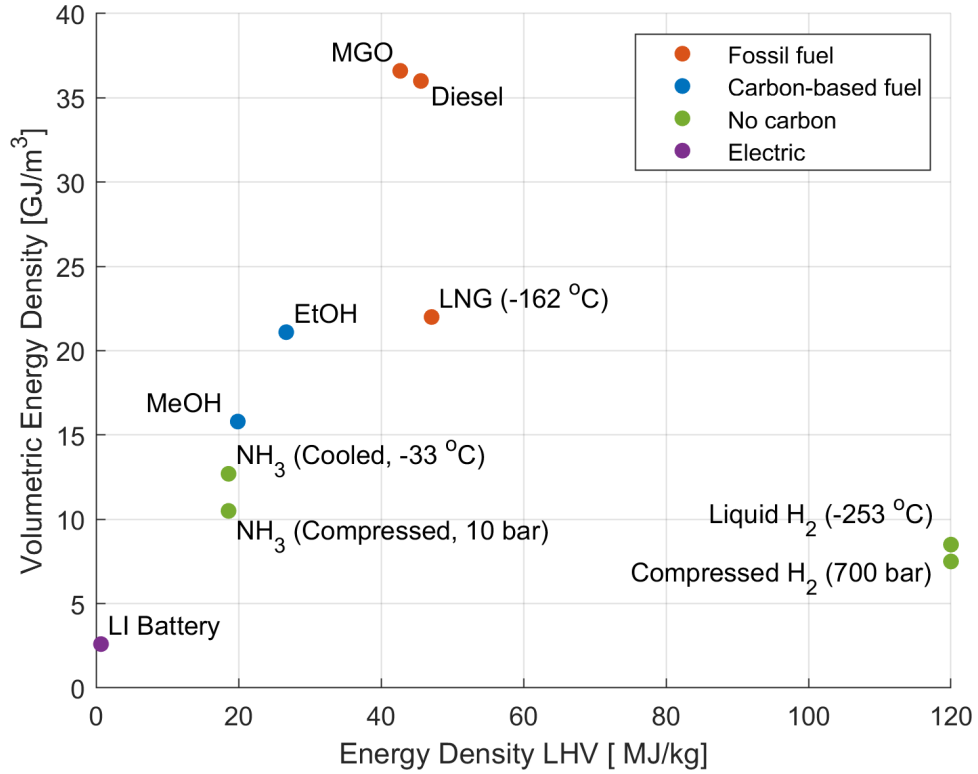


Figure 1.2: Comparison of the volumetric and gravimetric energy density of various alternative fuels.

Figure 1.2 presents a wider range of fuels, showcasing a comparison between their volumetric and gravimetric energy densities. Ultimately the choice of fuel is application dependent, however maximizing the potential of each fuel's properties is essential for optimal performance.

1.2.1 Biofuels

Drop-in biofuels are defined as “liquid bio-hydrocarbons that are functionally equivalent to petroleum fuels and are fully compatible with existing petroleum infrastructure” [71]. In the short term, it is expected that these will be the fuels of choice for decarbonisation of many industries, with advanced biofuels offering a level of fast decarbonisation without substantial engine modification. Biofuels are fuels that are derived from various types of biomass which are processed to form methanol, they can either be blended with fossil fuels or used as standalone fuels. These fuels are considered to be the most 'technologically ready' of the current fuel options, with fuels such as HVO, already being used in heavy duty transportation. The challenge with these fuels is based around scalability, sustainability and demand from other industries such as aviation. In 2023, current global production of biofuels is at 11 Million tonnes of oil equivalent (Mtoe) per annum, with an expectation of new projects coming on stream to increase this to 23 Mtoe by 2026. DNV's white paper forecasts production could reach up to between 500 - 1300 Mtoe per annum by 2050, shipping would need 20-50% of this share alongside energy efficiency measures if it was to decarbonise with biofuels primarily [29].

Shipping represents 3% of the global energy demand, it is therefore unlikely that shipping will be able to obtain such a high proportion of the supply. The aviation industry are already moving to utilise biofuel to aid in

decarbonisation, targeting fast uptake of sustainable aviation fuel (SAF). SAF is a biofuel produced from a number of feed-stocks including waste oils and fats, green and municipal waste, and non-food crops. It can also be produced synthetically via a carbon capture process. SAFs are expected to provide aviation with the ability to reduce the carbon emissions of the industry by up to 65%. From 2025, at least 2% of jet fuel content for journeys from EU airports must come from SAF with that figure rising to 20% in 2035 and 70% by 2050 [36]. In order to achieve this, a massive increase in production will be required resulting in a huge demand for sustainable biomass.

1.2.2 Hydrogen

Hydrogen is a molecule that is currently being put forward as a route to decarbonisation for many areas including steel production, domestic heating, and as a renewable energy storage [67]. There are currently numerous paths proposed for its production, distribution, and consumption across many different sectors resulting in a high degree of complexity when considering costs, emissions, and scalability. Hydrogen can be used to fuel both internal combustion engines (ICEs) and fuel cells in the context of shipping and heavy duty, however there are a number of challenges that the fuel must overcome in order to become a viable zero-carbon alternative fuel. This includes challenges with a high diffusivity, low volumetric energy density, and a high flammability range [156].

In production, the majority of hydrogen is produced using “brown/grey” methods; these processes such as coal gassification and steam methane reformation are very carbon intensive processes and intrinsically linked to fossil fuels. “Green” hydrogen can be produced from sustainable methods

via electrolysis powered by renewable electricity such as solar and wind [30]. High costs to scale the production and transportation of the fuel will add significant cost to green hydrogen, this however will decrease significantly as the price of renewables decreases [70].

The low volumetric energy density presents serious challenges when it comes to fuel containment especially if considering gaseous storage similar to that seen in hydrogen fuel cell passenger vehicles. When it comes to power generation, there are significant successes in the use of hydrogen fuel-cells for off-grid power generation with gaseous storage. Companies such as GeoPura have commercialised and successfully operated hydrogen fuel cell generators for a number of projects, with a target of producing over 3,600 250kW power units by 2033 [42].

There are a number of hydrogen fuelled ships currently in use globally, however the application has not been scaled for larger vessels as pressurised storage would require enormous volumes for long-range shipping with high energy demands [155]. One option proposed is cryogenic liquid hydrogen storage, in this state the gravimetric energy density is high enough that hydrogen becomes a viable fuel candidate for the aviation industry, although there are still challenges around the auxiliary equipment required for on-board storage [106]. In their review of liquid hydrogen for shipping, Ustolin et al [155], summarised a number of challenges that needed to be overcome to enable the technology including regulation, auxiliary equipment, and capital cost. Liquid hydrogen storage for transporting hydrogen has been demonstrated at full scale by the Susio Frontier produced by Kawasaki Heavy Industries [82].

1.2.3 Methanol

Methanol is a key competitor in the future of heavy duty fuelled engines, it presents a solution with very little engine modification and significant carbon emissions reduction when produced using sustainable sources. It exists in a liquid state at ambient conditions lending itself to current fuelling infrastructure and is able to be handled with relative ease. The viability of using methanol as a maritime fuel has been investigated through a number of research and projects, including Effship, Spireth, and Greenpilot [163]. As a result of its molecular oxygen, methanol is able to achieve more efficient combustion in engines, with lower NO_x production due to reduced in-cylinder combustion temperature. Replacing heavy fuel oil (HFO) with methanol could cut emissions of SO_x by 99%, particulate matter by 95%, NO_x by 60%, and CO_2 by 25% during ship operations [105].

Current production of methanol is very mature with factories in many countries across the world producing large quantities from fossil fuel sources [78]. Proven green production technology does exist and a variety of feedstocks can be used however scaling production is a significant investment. Initial production has been suggested to make use of biomass or highly concentrated CO_2 sources (over 100 ktons per annum), however in the longer term in order to reach net zero carbon, the CO_2 must be captured from other sources involving direct air capture [159].

Methanol has a lower energy content per volume in comparison to HFO, an equivalent methanol fuelled ship would require 2.5 times the size of HFO tanks. The engine technology for methanol has already been proven with up to 40 two-stroke methanol burning marine engines currently in operation from MAN-ES [104].

1.2.4 Ammonia

Ammonia's advantage as a future fuel is the lack of carbon in its chemical composition, as a result it will not produce any carbon dioxide when combusting. Like methanol, ammonia is also a very widely produced chemical, mainly for use in the agricultural sector as a chemical feed-stock. This indicates that not only are production methods very mature, there are also operating procedures and standards already in place for handling ammonia. Current ammonia production is via the use of natural gas, producing large quantities of GHG emissions however there are proven routes to producing green ammonia via electrolysis powered by renewables [78]. In terms of chemical properties ammonia is relatively simple to store due to being liquefied at $-33\text{ }^{\circ}\text{C}$ or at 10 bar, as a result its cost per volume of stored energy is three times less expensive than hydrogen [150]. It also has a lower energy density, with an equivalent ammonia fuelled ship requiring 2.9 times the storage size of HFO tanks.

Ammonia faces some challenges with regards to its combustion characteristics, it is slow burning with a relatively high ignition energy, this can be addressed using combustion promoters or running engines at slower speeds such as within two strokes. Incomplete combustion of ammonia could lead to increased NO_x emissions as well as unburned ammonia emissions [163]. Ammonia is toxic, with exposure to high concentrations causing serious health issues such as lung damage and potentially death [59].

1.3 Summary

Although the future energy landscape in 2050 is uncertain, it is understood that in order to achieve decarbonisation targets prime movers will utilise a diverse range of fuels and alternative power solutions. For marine and heavy duty, ammonia will hold a significant fraction of the fuel share [78]. The size of the fraction will be dependent on a number of factors including, availability, cost, ease of use, and emissions. Due to ammonia's undesirable characteristics when it comes to laminar burning velocity, ignition delay and challenges with fuelling circuits, further research is required in order to enable it as a future fuel. One of the key mitigation's to improve the combustion characteristics is blending ammonia with hydrogen, a method used in literature.

The intention of this study was to investigate utilising combustion promoters to enable the operation of ammonia fuelled heavy-duty ICEs during low load operation, during which the combustion is the most unstable. The investigation consisted of two experimental studies; a constant volume combustion chamber study that enabled a fundamental look at the combustion phenomena of ammonia and hydrogen mixtures occurring in a quiescent environment with engine-like geometries, and an engine study which focused on how the introduction of ammonia fuelling will impact engine parameters and general operation in a more applied sense. Bringing together the results of the two studies will enable a more in-depth understanding of ammonia combustion in the context of heavy-duty engines, with the fundamental analysis providing and insight into single combustion events that will be carried across into the analysis of the engine data.

1.3.1 Aims and objectives

To investigate the use of combustion promoters, such as hydrogen, to facilitate the utilisation of ammonia as a fuel for heavy-duty and marine engines, and to promote the retrofit opportunities for dual-fuel diesel-ammonia compression ignition engines by furthering understanding of the trade-offs between optimising combustion, performance, efficiency, and pollutant emissions.

1. **To develop a bespoke optical combustion chamber:** Design and construct a bespoke optical combustion chamber capable of investigating apparent flame speeds in a quiescent environment, incorporating engine-like geometries. Obtain baseline results using a spark ignition system and varied fuels to establish a future platform for studying and optimising “real world” combustion systems. (Chapters 3, 4, and 5)
2. **To assess the influence of hydrogen substitution on ammonia combustion (dual-fuel):** Investigate the influence of hydrogen substitution on an ammonia combustion event within a quiescent environment, utilising the developed optical combustion chamber to analyze the combustion characteristics. (Chapter 5)
3. **To retrofit a 6-cylinder diesel engine for ammonia dual-fuel operation:** Demonstrate the ability to retrofit a standard heavy-duty diesel CI to operate ammonia as the primary fuel with diesel as a co-fired pilot fuel. Evaluate the trade off of engine performance, efficiency, and pollutant emissions across various substitution ratios. (Chapters 6 and 7)

Chapter 2

Literature Review

A critical review of the literature addressing ammonia's potential as a fuel for heavy duty combustion engines is provided in the section that follows. Beginning with a background on ammonia as a molecule, the section discusses current and future production and application globally. The fundamentals of combustion and burning velocity are then explored, covering flame structures and laminar burning velocity, discussing the impacts of flame stretch, cellularity, and buoyancy on flame propagation.

Optical research methodologies for flame speed measurement are then discussed including further detail around constant volume combustion chambers and imaging techniques used in literature. Following this, a review of fundamental combustion studies revolving specifically around methane, ammonia, and hydrogen laminar burning velocity measurements is undertaken to enable future comparisons to be drawn with the current research. Finally a historical trajectory of ammonia as a fuel is outlined, discussing research in both spark ignition (SI), compression ignition (CI), and dual-fuelled engines.

Contents

2.1	Background	16
2.1.1	Ammonia as a molecule	16
2.1.2	Production and use of ammonia	17
2.2	Combustion and burning velocity fundamentals	22
2.2.1	Flame structures	22
2.2.2	Laminar burning velocity	24
2.2.3	Influence of flame stretch	26
2.2.4	Flame cellularity	28
2.2.5	Flame buoyancy	29
2.2.6	Chemical kinetic modelling	31
2.2.7	Flame propagation and engine performance	32
2.3	Optical research on flame speed measurements	34
2.3.1	Constant volume combustion chambers	35
2.3.2	Optical imaging techniques	37
2.4	Laminar burning velocity investigations	41
2.4.1	Methane studies	41
2.4.2	Ammonia studies	46
2.4.3	Ammonia-hydrogen studies	47
2.5	Ammonia in engines	50
2.5.1	History of ammonia as a fuel	51
2.5.2	Ammonia fuel combustion characteristics	51
2.5.3	Compression ignition engines	53
2.5.4	Spark ignition engines	54
2.5.5	Dual fuel engines	55

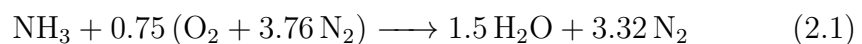
2.6	Summary	58
-----	-------------------	----

2.1 Background

Ammonia is an essential global commodity, known as one of the seven basic chemicals used to synthesise all other molecules in the chemical industry [79]. Its production and subsequent use in the manufacture of fertilisers has been credited as key in the expansion of the global population over the past century, and is seen to be one of the most important technological advances in the 20th century [142]. The following section will provide a background to the molecule and its chemical characteristics as well as detail around its production and use globally.

2.1.1 Ammonia as a molecule

Ammonia is a compound made up of nitrogen and hydrogen, it has the formula NH_3 . At room temperature and pressure it exists as a colourless, toxic gas. It can be compressed or cooled to liquefy at around 10 atm or -33°C enabling bulk storage at relatively high energy densities. Ammonia contains 17.8 wt% hydrogen and is able to store 30% more energy by volume than liquid hydrogen (liquid hydrogen at -253°C has approximately 70 kg of H_2/m^3 whereas liquid ammonia at 25°C and 1.0 MPa has 106 kg of H_2/m^3 [28]). This is the predominant reasoning for ammonia being recognised as a potential green energy store [102]. As ammonia does not contain any carbon atoms, complete combustion in air does not produce any CO_2 . Its stoichiometric oxidation in air can be seen below;



Ensuring ammonia is handled and contained with the correct measures in place to limit the likelihood and effect of exposure to humans and the environment is key to its usage. Ammonia is highly toxic and can be lethal to humans at 2,500 ppm when exposed for a duration of 30 minutes, however it is also perceptible and safe at 25 ppm [59]. Further health effects are shown in Table 2.1. In the event of a spillage in water approximately 70% will dissolve into the water forming a balance of mostly ammonium and ammonia depending on pH and water temperature. The remaining 30% will evaporate. The dissolved ammonia presents a serious threat to aquatic life, killing most in close proximity. A significant amount of time will be required for the area to recover to its natural state due to the enormous nitrogen imbalance [160].

Despite its high toxicity, ammonia can be transported safely as proven by the excellent safety record in the fertiliser industry [34]. As a result of this usage, there is already a well-established transportation network for ammonia, with over 20 million tonnes transported via shipping annually [32]. The experience and significant infrastructure that is already in place for ammonia reduces the cost of uptake in comparison to fuels such as hydrogen where the infrastructure is less mature.

2.1.2 Production and use of ammonia

The process of manufacturing ammonia was invented by F. Haber and C. Bosch in the early 1900s and was later modified to become an industrial process to make fertilizers. Currently the estimated global production of ammonia is approximately 150 million metric tonnes, with projections to increase by nearly 40% by 2050 [69]. The Haber-Bosch process converts hydrogen and nitrogen into ammonia by using a catalyst alongside high

Effect	NH_3 concentration in air (by volume)
20 - 50	Perceptible odour
25	8 hour LTEL – long-term exposure limit
35	15 min STEL – short-term exposure limit
50	Irritation to eyes, nose and throat (2 hours' exposure)
100	Rapid eye and respiratory tract irritation
250	Tolerable by most people (30–60 minutes' exposure)
700	Immediately irritating to eyes and throat
>1500	Pulmonary oedema, coughing, laryngospasm
2500 - 4500	Fatal (30 minutes' exposure)
5000 - 10000	Rapidly fatal due to airway obstruction, may also cause skin damage

Table 2.1: Table showing the health effects of ammonia exposure, adapted from [31, 35]

pressures (200 - 400 atm) and temperatures (400 - 650 °C). The process consists of multiple reactors; a reformer/gasifier to convert the feed stock fuel into syngas (a mixture of H_2 and CO), shift reactors to convert the CO into hydrogen, CO_2 removal, a methanation stage to convert leftover CO to methane, a compression stage of the H_2/N_2 gas mixture to synthesis pressures, and then ammonia synthesis in the Haber-Bosch reactor [8]. Over 70% of ammonia is produced via steam methane reformation with the majority of the remainder produced via coal gassification. These processes are very energy intensive and emit 450 Mt CO_2 annually [69]. The Haber-Bosch process is one of the largest global energy consumers and GHG emitters making up for 1% of the energy demand and 1.2% of global anthropogenic CO_2 emissions [143]. Current optimised plants using methane-fed Haber-Bosch processes emit 1.5 - 1.6 tonnes CO_2 per ton of ammonia. The most efficient plants operate at around 10 MWh per metric ton of ammonia. With ammonia having an energy content of 5.2 MWh per ton based on its lower heating value, the best efficiency is just over 50% [43].

When developing the initial process, the optimisation focus was weighted

towards feed-stock reduction. It has been shown that with the use of new technologies, the CO₂ emissions can be substantially reduced as well as the efficiencies increased. Smith et al. [143] highlights the following recommendations for improvements;

- Decouple hydrogen production from steam methane reformation.
- Replace steam turbine compressors with electrical compressors.
- Alternative ammonia separation techniques to decrease operating pressures.

Hydrogen production accounts for more than 90% of the energy demand and 90% of the associated emissions, decoupling the production and utilising proven technologies such as water electrolysis will drastically reduce the environmental impact of ammonia production [150]. However the demand for green hydrogen is not exclusively from ammonia production, other sectors such as aviation and the steel industry are looking to green hydrogen to aid in decarbonisation [70]. Alongside this there are still societal, technical, and economic barriers that face the proliferation of green hydrogen technologies. These include, high demands for critical materials for production and challenges for storage, lack of clear policies and regulation in many countries, and a high cost of investment for early adopters [1].

In an assessment of current and emerging production technologies for ammonia, MacFarlane et al. [101], suggested ammonia developments will occur in three stages or “generations”. Generation one and two capitalise on current decarbonisation trends for hydrogen production, firstly utilising carbon sequestration on the hydrogen production to reduce the net carbon impact of the ammonia production, and secondly fuelling the production with green hydrogen produced from renewable sources. Both methods are

proven with a key obstacle to deployment being high capital cost and complexity.

Generation one is based on the use of blue hydrogen, hydrogen produced using carbon capture, utilisation and storage. This is a method that has been present in many hydrogen road maps globally and is often described as having low or zero GHG emissions, this however is not currently correct. Not all of the carbon dioxide emissions are able to be captured from the process, with industry targeting 90% capture rate from the steam methane reformation process only and commercially operating plants achieving mean capture rates of 76% [138]. The combustion of natural gas used to provide the high pressure and temperatures for the steam methane reformation process are not considered in these facilities. When considering the best case scenario that the temperatures and pressures are achieved using renewable means, Howarth et al. concluded the CO_2eq would be reduced by 53% when considering the commonly excluded fugitive methane emissions [65]. Some of the figures used in the paper were contested by Romano et al, due to the breadth of the assumption using the fugitive emissions from all of the methane production in the US however highlighting the presence of those emissions is still valid [129]. The main benefit of utilising carbon capture, utilisation and storage for hydrogen production is for speed of uptake as the infrastructure is already available, unlike green hydrogen production that will require a larger capital investment to ramp up to meet the demand.

Green hydrogen usage also has its challenges, especially when powered using wind or solar as the intermittency can cause challenges matching to the Haber-Bosch process which relies on steady state operation for maximum efficiency. When comparing future advancements in technologies for ammonia production, Smith et al. projected electrically driven processes will improve and overtake the industry best available technique vs methane-fed

ammonia [143]. Electrifying the processes enable a more agile production system that is able to match the intermittency of renewables. Pfromm showed that using currently available industrial scale technology in 2017, the energy demand increase between methane-fed and electrical based ammonia production is around 14% [121].

Analyses of the energy consumption of both the methane-fed processes and the electrical processes of ammonia production shows the competitiveness of the green ammonia solution, especially when considering the emissions associated with the current methane-fed process. The main key performance index of both processes is related to cost, due to the significantly cheaper cost of natural gas currently this process is a lot cheaper. In green ammonia production 85% of the cost is the electricity input. In order for electrolysis to be cost competitive against steam methane reformation with carbon capture, the price of the supplied electricity needs to be between 1.2 to 4.0 GBP pence/kWh (assuming gas prices are between 2.3 to 7.7 GBP pence/MMBtu) [70]. The International Energy Association has projected that the cost of producing hydrogen from renewable electricity could fall by 30% by 2030, as a result of declining costs of renewables and scaling up of hydrogen production [70]. Regions rich in wind and solar energy are already close to a tipping point for affordable production of zero carbon ammonia [150].

The third generation proposed produces ammonia via the electro-reduction of N_2 . This method completely removes the Haber-Bosch process from ammonia production and instead drives the reaction using electrochemical reduction in which the hydrogen is source from water. Macfarlane suggests a higher resilience to intermittency, lower sensitivity to N_2 supply purity and greater energy efficiencies however this is not a proven technology and has a long time to reach maturity [101].

2.2 Combustion and burning velocity fundamentals

The processes of an ICE can be understood when simplifying the system down into its key energy flows. Starting as chemical energy in the fuel, the combustion process, a fast-exothermic gas-phase reaction is used to react the fuel with oxygen and convert said chemical energy into the thermodynamic heat and kinetic energy. The thermodynamic heat is shown by a pressure increase in the cylinder that in turn is translated to kinetic energy via the linear motion of the piston. This linear motion is then translated into rotational motion via the crankshaft and then utilised from the output shaft. The initial conversion of chemical energy via the combustion reaction is one of the key processes that dictate engine power, efficiency, and emissions [60].

2.2.1 Flame structures

A flame is a region within which the combustion reaction takes place, it is defined as the luminous part of the burning gases caused by highly exothermic, rapid oxidation. One section of the flame is the flame front, this is where the unburnt mixture is heated and converted into products. The flame front consists of two regions, the preheat zone and the reaction zone, as shown in Figure 2.1. The preheat zone occurs between the cold boundary and the location of the ignition temperature. In this region, the temperature of the unburnt gas is raised mainly by heat conduction and some convection from the reaction zone, because of this temperature increase the unburnt gas expands and is accelerated. Once the unburned mixture

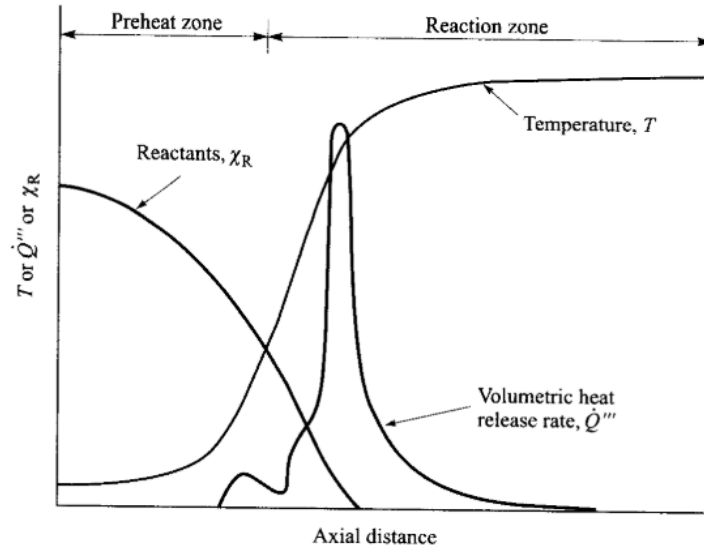


Figure 2.1: Laminar flame structure with temperature and heat release rate profiles based on experimental results of Friedman and Burke [38].

reaches the ignition temperature, it begins the exothermic chemical reaction that continues to release heat that continues to increase the temperature until its equilibrium value is reached. The distance between the ignition temperature and the hot boundary at the equilibrium temperature is the reaction zone.

Flames are defined by how the fuel and the oxidiser are mixed, and can generally be separated into two categories, premixed and non-premixed/diffusion flames. In a premixed flame, the fuel and the oxidiser are mixed at the molecular level prior to any combustion occurring. A practical example of this is the flame inside of a SI engine. In a non-premixed or diffusion flame, the fuel and oxidiser are initially separated and the flame only occurs where the two meet and ignite. Flames are further defined based on the flow characteristics of the event, either laminar or turbulent. In a non-turbulent environment, the flame propagation is laminar, and the flame has a smooth surface and relatively thin reaction zone. The speed at which the flame moves relative to the unburned mixture is the laminar burning velocity. Laminar burning velocity (S_L) is defined as the velocity at which

unburned gases move through the combustion wave in the direction normal to the wave surface [45]. This velocity is a property of the unburned mixture and is dependent on the mixture composition, fuel properties, and mixture temperature and pressure. It is considered to be a metric of the global rate of chemical reaction of a premixed mixture without additional complexities of bulk air flow and turbulence.

When turbulence is present, the flame speed is dictated by a combination of the laminar transport processes in conjunction with the turbulent convection phenomena. The flame front will no longer be smooth, and the reaction zone will be thicker. The flame speed will be significantly increased depending on the intensity of turbulence [88]. Unlike laminar burning velocity, this flame speed is not a unique property of the combustion mixture, but a sum of the burning and expansion velocities. It is affected by many different factors including the flow field, geometry, wrinkling of the flame front, pressure effects on the flame thickness, and the history of the flame. Modern ICEs utilise specifically designed port geometries that generate bulk air “tumble” and/or axial “swirl” motions, which in turn result in increased turbulence intensity in order to speed up fuel air mixing and flame development. Only with the augmentation of the laminar processes can the mixing, burning, and flame propagation rates be fast enough to complete the engine combustion process in the time available [60].

2.2.2 Laminar burning velocity

Laminar burning velocity is a fundamental property of a fuel-air mixture at a specified temperature and pressure, it describes the propagation speed of a planar one-dimensional premixed flame relative to the fresh gas mixture.

It can be defined by the following equation;

$$S_u = S_n - S_g \quad (2.2)$$

where S_u is the unstretched laminar burning velocity, S_n is the stretched laminar flame speed, and S_g is the unburnt gas velocity immediately adjacent to the flame front. It is assumed that the flame is one-dimensional, and that the unburned gas is entering the flame normal to the flame sheet. During this occurrence the flame is heating the products and therefore the density of the products will be less than that of the reactants. Continuity requires the burned gas velocity to be higher than the unburned gas velocity. The unburnt gas velocity is dependent on the density of the burned and unburned mixtures as shown in equation 2.3. This equation relates the velocities, v , of the burned, b , and unburned gases, u , where A is the flame area and ρ is the density.

$$\rho_u S_u A = \rho_u v_u A = \rho_b v_b A \quad (2.3)$$

Laminar burning velocity is a physio-chemical parameter dependent on various factors including the chemical composition of the mixture as well as the physical properties such as temperature and pressure. It is typically measured experimentally and utilised in computational models to optimise combustion processes. Practical measurement is complex with no agreement on a standardised method of testing. The choice of method depends the precision, reliability, and simplicity of experimental setup. As a result of the numerous techniques that have been used over the years to determine laminar burning velocity, there are large discrepancies in the results. Figure 2.2 shows a spread of maximum burning velocity results of methane air mixtures at atmospheric conditions plotted against year of study. Bradley

et al. concluded that the influence of flame stretch on burning velocity was the key factor in discrepancies between flame speed measurements [13]. A better understanding of this influence has lead to a convergence of results in recent years [62].

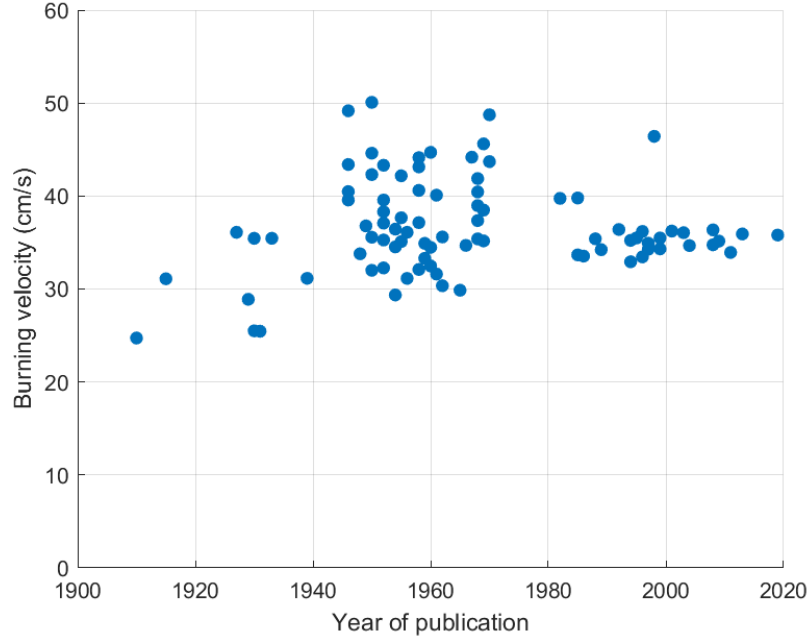


Figure 2.2: Historical measured laminar burning velocity for methane-air flames at atmospheric conditions adapted from Egolfopoulos et al. [33], Hinton [62] and Law [90].

2.2.3 Influence of flame stretch

Real flame sheets are subject to transverse velocity components and curvature that stretch the surface of the flame and influence the measured flame speed. Equation 2.3 requires the components of velocity of the flame to remain straight and parallel, as this is not the case of the real flame in the measuring techniques it needs to be accounted for. The stretch rate, ϵ , is defined by the following equation;

$$\epsilon = \frac{1}{A} \frac{dA}{dt} = \frac{2}{r} \frac{dr}{dt} \quad (2.4)$$

Where A is the flame area, t is time and r is the flame radius. There are multiple stretch extrapolation correlations that have been used in the literature to extrapolate the flame speed to calculate the unstretched laminar burning velocity, the main relationships are defined by Wu et al. [166]. A major cause of uncertainty in the laminar burning velocity calculation can be attributed to the variation in procedures and relationships used across literature. A commonly used relationship especially for spherically expanding flames is the linear stretch based relationship proposed by Wu and Law [165], it is based on the assumption that the Le , Lewis number, is close to unity and the flame is weakly stretched. The Lewis number is a dimensionless number that characterises the ratio of thermal diffusivity and mass diffusivity. In this relationship the change in flame speed due to stretch is defined as;

$$S_s - S_n = L_b \epsilon \quad (2.5)$$

where S_s is the unstretched flame speed, S_n is the stretched flame speed, L_b is the Markstein Length a property of the gas mixture that defines the effect of stretch on flame speed, and ϵ the stretch rate. The unstretched flame speed is calculated by finding the intercept value of S_n by linearly extrapolating the stretched flame speed to an infinite flame radius (or a stretch rate of zero). The unstretched laminar burning velocity, S_L , is then obtained using the ratio of burned, ρ_b , to unburned, ρ_u , densities of the mixtures as shown in 2.6.

$$S_L = S_s \frac{\rho_u}{\rho_b} \quad (2.6)$$

Kelley and Law [83] found when the Lewis Number Le is far from unity, the relationship between S_n and ϵ may not be linear. They proposed the following non-linear correlation for extracting flame speed and Markstein numbers. This method relies on weak flame stretch however allows for

arbitrary Le numbers and hence is more general than the linear model.

$$\left(\frac{S_n}{S_s}\right)^2 \ln\left(\frac{S_n}{S_s}\right)^2 = -2\frac{L_b\epsilon}{S_s} \quad (2.7)$$

Equation 2.7 shows a linear relationship between $\ln(S_n)$ and ϵ/S_n^2 , with an intercept on the $\ln(S_n)$ axis equal to $\ln(S_s)$, and a gradient equal to $-S_s L_B$. The improved accuracy with this method has been demonstrated in [23, 83]. Chen concludes that there is a strong dependence on the accuracy of various correlations against the Lewis number of each mixture [23]. It was noted that for mixtures with the Lewis numbers close to unity, the non-linear correlation is sufficient whilst the non-linear correlation suits a wider range of Lewis numbers. Okafor et al. found however when investigating methane-ammonia-air flames that the linear correlation may not always be suitable, especially as the ammonia mixture in the fuel and equivalence ratio increased. This was attributed to non-linearity as a result of an increase in flame thickness [116].

2.2.4 Flame cellularity

Due to the flame speed dependence on flame area, the occurrence of cellularity prevents accurate measurement of flame speed. Cellularity is a flame phenomenon that occurs due to a number of factors based on the environmental conditions and the flame composition, it is caused by flame instability. In early flame development, the flame front is stabilised by the high stretch rate and thermodiffusive effects combat hydrodynamic or Darrieus-Landau instability [11]. The instability is caused by the density variation due to the thermal expansion of the products of the combustion. This initial stabilisation is related to the Markstein length, a higher

Markstein length leads to greater stabilisation.

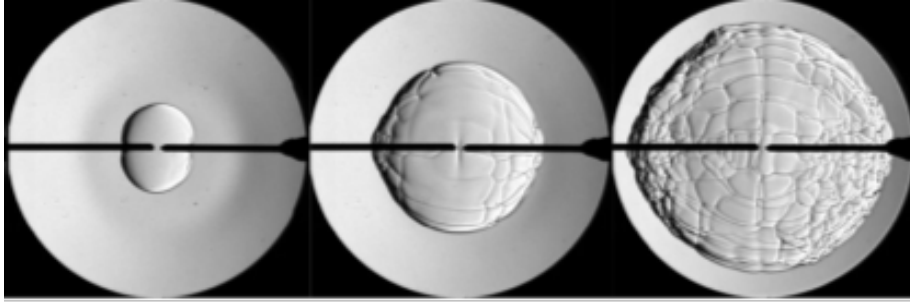


Figure 2.3: Depiction of a cellular hydrogen-air flame using schlieren imaging [84].

As the flame radius increases, the stretch rate decreases and instabilities can begin to form. The instabilities form cracks on the surface of the flame, next cross-cracks form between these and develop until the flame surface becomes completely cellular, shown in Figure 2.3. The cellularity is associated with an increase in the flame speed - sometimes referred to as self-acceleration - and rate of pressure-rise, this is due to the dramatic increase in flame area resulting in a larger surface for the reaction to occur.

The main parameters influencing flame stability and therefore flame cellularity are the initial pressure, initial temperature, and the equivalence ratio [6, 84]. Fuel type also influences this, with hydrogen air mixtures showing both early onset cellularity in comparison with hydrocarbons and at lower pressures and temperatures [167].

2.2.5 Flame buoyancy

The influence of buoyancy effects all flames to some degree, however for the majority of flames the burning speed is sufficiently high enough that the deformation velocities induced by the buoyancy are insignificant and do not affect flame shape in a meaningful way. Ronney et al. concluded that the effect of buoyancy will lead to uncertainty for flames with speeds

of less than 15 cm/s however the strength of buoyancy is mixture and temperature dependent so this value could change in different conditions [130]. For some papers the solution to addressing the influence of buoyancy was to only consider regions in which the buoyancy effect was weak, this is reasonable for high speed flames however when analysing low speed flames it can lead to narrow ranges of available data [21].

Both Kanoshima et al [81], and Hayakawa et al [57] identified the quasi-steady region between the spark influenced region and the buoyancy influence region defined by the region in which the flame shape ratio and the flame propagation ratio change smoothly. This reduced uncertainty by removing the buoyancy affected regions from the flame speed calculations, enabling wider ranges of data. This lead to a reduction in the number of flame images able to be considered and reduces accuracy, only measuring from $r = 10\text{mm}$ to 14mm . Pfahl et al. considered the horizontal development of the flame and took that as the radius, although generalising the flame this completely removes any vertical velocity component and therefore provides a reasonable representation of the expanding flame without buoyancy considered [120].

Chen et al [21], developed a different technique, attempting to dissect the velocities into their components of buoyancy affected velocity and true

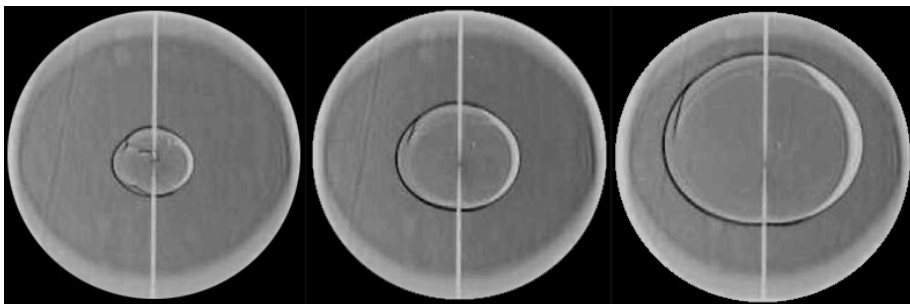


Figure 2.4: Progression of a stoichiometric ammonia-air flame influenced heavily by buoyancy [21].

flame velocity, redefining the outwardly expanding spherical flame as an outwardly expanding quasi-ellipsoid flame. This enabled the definition of a new method which can negate the influence of buoyancy by understanding the constituent velocities at various points. By assuming an ellipsoidal approximation of the flame, the vertical and horizontal flame speeds can then be understood as combinations of buoyancy induced and flame induced velocities.

2.2.6 Chemical kinetic modelling

Understanding the underlying chemical pathways that occur during the combustion of a fuel is key to the understanding of combustion events. The chemical reaction rates determine the rate of the combustion as well as the production of the pollutants/concentration of various products. In addition to this, ignition and flame extinction are also intrinsically linked to the reaction chemistry [152].

Laminar burning velocity experiments are a key tool used to validate chemical kinetic models, these models are becoming increasingly more complex as the demands for more fuel molecules and conditions grow. Small fuel molecules such as methane can be modelled using full mechanisms due to the size, however larger molecules and mixes of molecules dramatically increase the complexity, therefore requiring simplified mechanisms. In order to simplify the mechanisms, the full mechanism is analysed and the less significant reactions in the mechanism are systematically removed. Sensitivity analysis is then performed to ensure the mechanism is still accurate to the scenario [62]. The accuracy of the result is dictated by the complexity and accuracy of the mechanism, as a result these models require tuning of specific reactions inside the mechanism using sensitivity analysis

and comparisons to experimental data to improve the simulations. The mechanisms developed are able to improve the efficiency and the cost of design of combustion devices as they are coupled with computational fluid dynamics to model combustion scenarios.

2.2.7 Flame propagation and engine performance

The combustion phenomena observed are different between conventional spark-ignition (SI) engines and compression ignition (CI) engines. In a SI engine, the fuel and air are already mixed either in the engine's intake ports or within the cylinders. The mixture is compressed and then combusted following an electrical discharge that initiates the sequence. From the point of ignition, a flame front propagates outwards until it is quenched at the combustion chamber wall. From Heywood [60], the flame can be described as a premixed unsteady turbulent flame propagating through a gaseous mixture. Steady or unsteady differentiates whether the flame structure and motion change with time and turbulent or laminar describe the gas flow through the reaction zone. Considering a combustion event inside a SI engine, when the combustible mixture is ignited at the centre, a laminar flame kernel is initiated which ideally develops into a turbulent spherical flame. In reality, the bulk air motions within the cylinder can persist, rapidly distorting and convecting the flame, in extreme cases leading to premature truncation at the cylinder walls. As described previously, the turbulent effects can be described as time-varying curvature and flow straining which result in the stretching of the flame front. As the flame develops the reaction zone thickness increases and the propagation speed increases until the flame reaches the outer walls where heat transfer occurs and eventually quenching. In a diesel CI engine, the combustion process is described as an unsteady tur-

bulent diffusion flame. In a diffusion flame, the fuel and air are initially separate, the fuel flows to the inside of the flame and the air flows to the flame from the outside. This is caused by the injection of liquid fuel into the combustion chamber. In some modern diesel engines, a multiple direct fuel injection strategy is employed, resulting in a degree of fuel premixing in the piston bowl which can improve the soot-NO_x trade off. In an engine cylinder, the burned mass of charge, $m_{b(t)}$, is given by

$$m_{b(t)} = (\overline{S_x}, \overline{S_y}, \overline{S_z})_{(t)} \rho_{b(t)} S f_t \quad (2.8)$$

where $\overline{S_x}, \overline{S_y}, \overline{S_z}$ are the average flame speeds in the x,y and z directions, determined experimentally by optical methods. $S f$ is a shape-specific function, and ρ_b is the density of burned mass. When the fuel burns the chemical energy is released into the working fluid of the cylinder, given by,

$$m_b LHV - (m C_v dT) - \Sigma h_i dm_i - dQ_{ht} = p dV \quad (2.9)$$

where m_b is the mass of burned fuel, LHV is the latent heat of vaporisation forming the term that represents the energy released from burning the fuel. m is the mass of the charge, C_v is the specific heat capacity, and dT is the change in temperature, forming the term deriving the energy required to heat the charge. $\Sigma h_i dm_i$ represents the sum of energy that has left/entered the chamber as a result of crevices, blowby and other engine phenomena that make the chamber an open system. h_i and m_i are the enthalpy and mass of the components joining/leaving the system. dQ_{ht} is the heat transfer to the cylinder walls. $p dV$ is the work done on the piston during the combustion.

The rate of burning of the air-fuel mixture affects the chemical energy change of the fluid which in turn directly affects the indicated work and power output of the engine.

2.3 Optical research on flame speed measurements

Large amounts of information can be obtained using pressure transducers, thermocouples, and flow meters in a running engine, however without optical access, the information around the combustion characteristics such as flame shape is implied. Visualisation of the in-cylinder mixing, and the subsequent combustion process has been vital in the development of modern ICEs [60]. The usage of various materials and engine chamber designs to provide the optical access limits the outputs to qualitative, but the measurements offer a non-intrusive way to see combustion within the engine cylinder. The ability to observe the surface of the flame can provide insight into the onset of instabilities, from initial flame cracking to developed cellular structure [51]. With the wide use of computer simulations to model engine environments, this information not only furthers understanding of engine operation but is also used to validate and develop confidence in the use of these computational methods. As discussed in Section 2.2.2, laminar burning velocity can be determined via several experimental approaches that utilise different flame configurations such as spherically expanding flames, counter-flow/stagnation flames, burner flat flames, and Bunsen flames. These methods can be defined into two groups, stationary flame measurements and non-stationary flame measurements. In the critical review by Andrews and Bradley [3], it is highlighted that the

wide range of measurement techniques has lead to a wide scatter in measurements to some extent dependent on experimental method. Following the descriptions in said review, Duynslaegher and Hinton continue updated reviews of the breadth of experimental techniques [31, 62].

For non-stationary flames, the spherically propagating expanding flame configuration is most commonly used, utilising constant volume combustion chambers. This method, commonly used across literature, was commented on by Rallis and Garforth as “the most versatile and accurate” of the propagating flame methods [125]. There are a number of advantages to this method, including the ability to have precise control over the initial pressures and temperatures as well as being able to cope with high absolute pressures during combustion.

2.3.1 Constant volume combustion chambers

Typically constant volume combustion chambers (CVCCs), also known as combustion bombs, have a spherical or cylindrical internal chambers. The fuel air mixture is contained within the chamber and ignited usually with a centrally located spark, resulting in a spherical flame propagating through the unburned mixture. Due to the constant volume, the combustion leads to an increase in pressure in the system. There are two methods demonstrated by literature that are used to measure the flame speed; imaging of the flame front propagation within conditions of constant pressure or measurement of the pressure rise combined with a constant volume combustion model. These methods are usually completed in isolation as highlighted by Hinton et al, and have various advantages and disadvantages [61].

The pressure method, first introduced by Lewis and von Elbe [93], consists

of utilising high frequency pressure measurements to record the increase in the chamber pressure during combustion and then relate this pressure rise to a combustion model to calculate the mass fraction burned and derive the laminar burning velocity from that. The original model proposed was a linear assumption between mass fraction and pressure rise. Metghalchi and Keck introduced a two-zone numerical model in which the chamber is divided into a burned and unburned gas zone separated by a thin flame front [109]. This model however does not take into account the re-compression of the burned gas mixture that leads to a temperature gradient within the zone as identified by Hopkinson [64]. Modern pressure rise methods utilise more complex multi-zone analysis to take the temperature gradients into account. These methods have the advantage of generating data across different pressures and temperatures, therefore obtaining data for engine like conditions [134]. There are some challenges around uncertainty when identifying flame cellularity, if cellularity occurs, the assumptions of a smooth flame front are no longer valid and the models do not work [61].

Flame front imaging is a more commonly found approach in literature, there are multiple benefits to the method including the ability to understand the influence of ignition as well as understand the flame stretch in a way not possible using the pressure technique. In this approach, various imaging techniques have been demonstrated in literature to record the flame propagation directly during the constant pressure region of the combustion, the main imaging techniques seen in literature are the following;

- Direct or natural light imaging
- Chemiluminescent (wavelength-focused) imaging
- Schlieren imaging

- Laser based imaging

In the paper by Hinton et al, it is proven that with appropriate processing of data, consistent values of laminar burning velocity can be obtained using both flame front imaging and pressure rise data measurement [61].

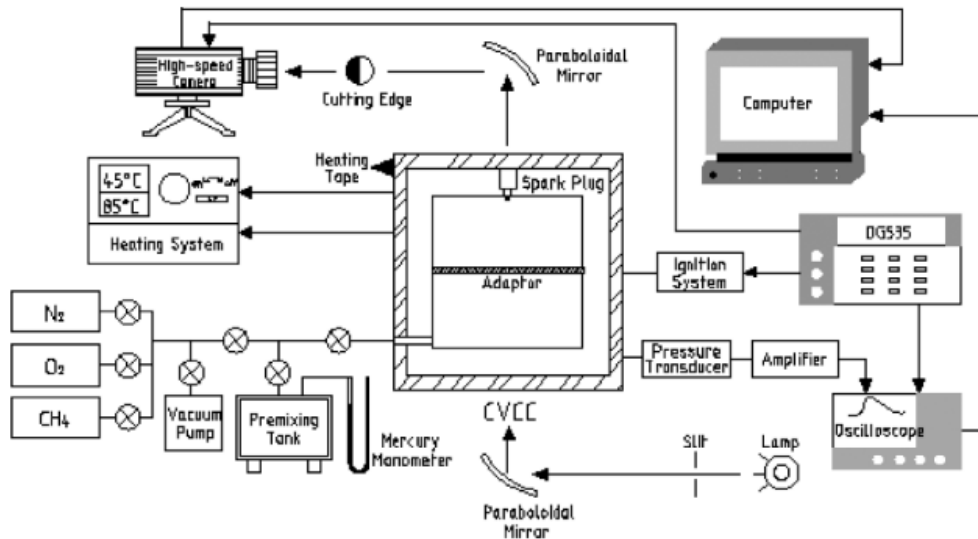


Figure 2.5: Typical combustion chamber setup with schlieren imaging system taken from [96].

2.3.2 Optical imaging techniques

Throughout literature there are a number of techniques used in the field of optical combustion research, the following section discusses the more commonly used methods; natural light or direct imaging, schlieren imaging, laser based methods and chemiluminescent imaging. These techniques offer a range of information about the flame front. A typical schlieren imaging setup can be seen in Figure 2.5.

Direct flame chemiluminescence imaging is the simplest method of capturing the flame, it utilises a high speed camera to capture the flames natural luminescence to identify the flame front. The natural luminescence for a

hydrocarbon flame is as a result of the electromagnetic radiation emitted during the formation of various species in the flame front. Formaldehyde (CH_2O^*), CH^* , C_2^* , and hydroxyl OH^* radicals, are largely responsible for the emission of visible and ultraviolet chemiluminescence [52]. This method relies on the combustion event to produce enough luminosity for the aperture to capture, which is suitable for hydrocarbon flames but becomes a challenge with fuels such as hydrogen [103]. These imaging techniques must be used with caution owing to their line of sight nature, leading to issues when dealing with three dimensional flames where the flame image can become blurred. It also does not give details on flame wrinkling or thickness [136].

One challenge with many flame imaging techniques is agreement within literature on the identification of the position of the flame edge. With direct flame imaging, the technique is limited to the only option available which makes the assumption that the brightest point - highest chemiluminescent release, is the location of the edge. Chemiluminescence is dependent on a number of mixture properties including fuel type, equivalence ratio, and pressure [114].

Shadowgraph imagery uses a collimated light source directed through the working section facing the camera, the light is refracted due to density changes that affect the refractive index of the working environment. Its response to the second spatial derivative of the refractive index makes it well suited for experiments with large density gradients such as fuel spray analysis, however the method does not produce a focused optical image of the object [103].

Schlieren imaging utilises a similar principle that large changes in temperature, composition, and therefore density, in a flame will give rise to rapid

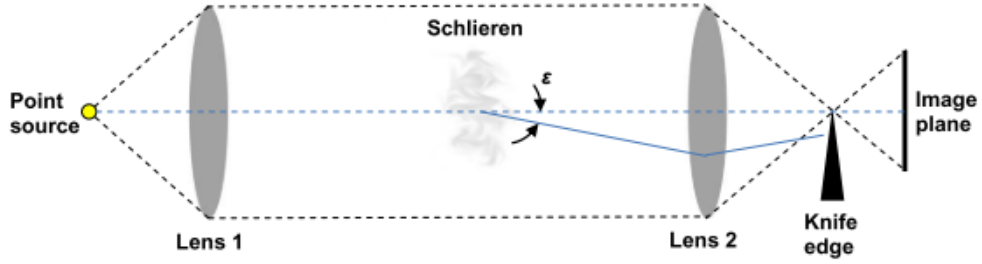


Figure 2.6: Dual field lens schlieren system from Floryan et al. [37].

variations in the refractive index of a volume [118]. If collimated light is directed through a medium, the variations in the refractive index of the volume will introduce distortions. Due to the collimated light having an infinite depth of field, any density gradient between the collimated lenses and the focal point will be present in the final image [37]. The light is then focused to a point where part of the light is cut using a sharp edge or graded filter. This results in images that respond to the first derivative of refractive index and therefore are very sensitive to changes [103]. As the density is directly related to the temperature, this method enables the temperature gradient of the flame to be captured, providing an accurate representation of the flame front position [125]. A diagram presenting the concept of this technique is shown in Figure 2.6.

Another system that has been used for flame image analysis in the past is particle image velocimetry (PIV), shown in Figure 2.7. This method utilises flow seeding and a laser sheet to illuminate a cross section of a volume, a high speed camera is focused on the sheet and the particles are tracked between each frame enabling instantaneous velocity vector maps to be created at that given time [5, 157]. Within flame measurement, the technique measures the flame speeds and gas velocities just ahead of the flame front, the differences in these values gives a burning velocity that can provide a mass rate of burning in addition to flame curvature and strain rate contributions to the flame stretch rate [10]. It is not as common due

to the experimental difficulties and necessary post-processing of many data points.

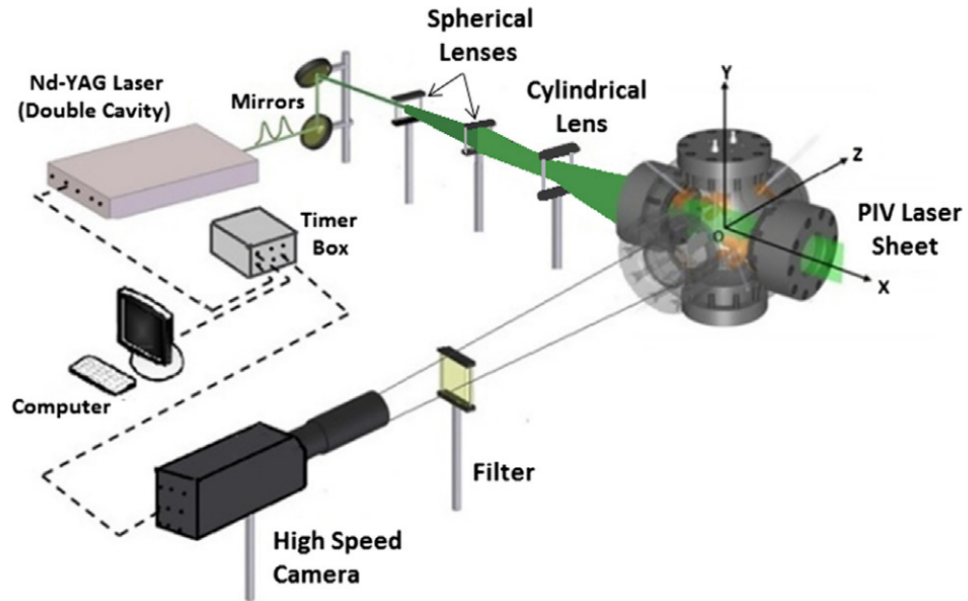


Figure 2.7: Schematic of a PIV-based imaging setup from Bradley et al.[10].

Direct, schlieren and PIV based techniques provide an understanding of the overall characterisation of the combustion reaction, in some instances an understanding of the specific reactions and species is also desirable [175]. In these cases, laser-based techniques such as planar laser induced fluorescence imaging, chemiluminescent imaging techniques are used. Planar laser induced fluorescence (PLIF) uses a laser sheet to excite radicals that are then captured by an intensified charge couple device (ICCD) camera. Depending on the wavelength of the laser, different radicals can be excited which enables the visualisation of reaction zones and as a result characterisation of the flame structure [11, 44, 103].

Chemiluminescent imaging relates the chemiluminescence of certain species directly to the start of a flames heat release both temporally and spatially [114]. This relation can be drawn due to chemiluminescence only occurring during an exothermic reaction. In order to capitalise on this, certain filters

such as narrow band pass interference filters are used to isolate specific wavelengths associated with different radicals. In some instances this can be weak and therefore require an image intensifier in order to capture the luminescence [107]. An intensifier has the ability to make the camera more sensitive to different reactive species depending on wavelength, for example OH* radicals [87].

2.4 Laminar burning velocity investigations

As discussed in Section 2.2.2, laminar burning velocity is a key fundamental physio-chemical property of a combustion mixture. In order to form a reasonable basis of understanding of the measurement a literature review was completed on the various fuels used with the combustion chamber experiment. This enables comparisons to be drawn to assess the performance of the novel combustion chamber in optical flame analysis as well as the impact of the novel design.

2.4.1 Methane studies

Methane is one of the most studied fuels in literature, this is attributed to it being the main component in natural gas which has been a staple fuel for many years. Its properties have been measured at a wide range of temperatures, pressures, and mixtures. Early studies utilised a pressure derived method as seen in Hinton et al. [61], with no observation of the flame. As a result the effect of any distortion to the flame and the impact of cellularity was not considered when calculating the burning rate. Cellularity can enhance the burning rate and skew results if not observed. In addition to this, the pressure measurement relies on the rate of mass

burning rather than the rate of propagation of the flame into the mixture [51]. Another defining factor that leads to clear variation in results is the consideration of the influence of flame stretch, early studies related flame stretch and burning velocity with a linear correlation however the modern determination considers a non-linear correlation as defined by Kelley and Law [83].

Table 2.2: Summary of relevant research studies relating to methane-air laminar burning velocity investigations.

Study	Year	Equivalence Ratio ϕ	Temp. [K]	Pressure [MPa]	Ref.
Hassan et al.	1998	0.6 - 1.4	300	0.5 - 4.0	[55]
Gu et al.	2000	0.8 - 1.2	300 - 400	0.1 - 1.0	[51]
Rozenchan et al.	2002	0.5 - 1.5	298	0.1 - 2	[132]
Tahtouh et al.	2009	0.5 - 1.3	298	0.1	[146]
Varea et al.	2012	0.6 - 1.3	298	0.1	[157]
Goswami et al.	2013	0.8 - 1.4	298	0.1 - 0.5	[46]
Reyes et al.	2017	0.7 - 1.2	300 - 650	0.05 - 1.6	[128]
Pizzuti et al.	2017	0.3 - 1.4	298	0.1	[123]
Okafor et al.	2018	0.8 - 1.3	298	0.1	[116]
Bradley et al.	2019	0.7 - 1.3	300	0.1	[10]
Okafor et al.	2019	0.8 - 1.3	298	0.1 - 0.5	[117]
Varghese et al.	2019	0.7 - 1.3	300 - 650	0.1 - 0.5	[158]
Laverda et al.	2021	0.7 - 1.4	298 - 338	0.1	[89]

Figure 2.8 presents a range of literature data for the laminar burning velocity of methane-air mixtures at 0.1 MPa across various equivalence ratios. The literature correlation is a culmination of all the literature data points. This test condition, with a temperature between 298K - 300K, is one of the most commonly used benchmarking points in literature. There is a wide range of data spanning back to the early 1900s as shown by Figure 2.2. For the literature values used to compare against in this thesis, more recent findings were used as shown in Table 2.2. The most common method used in these studies has previously been described in Section 2.3.1 as flame front imaging of an outwardly propagating spherical flame utilising different imaging techniques such as schlieren imaging and PIV. There are some

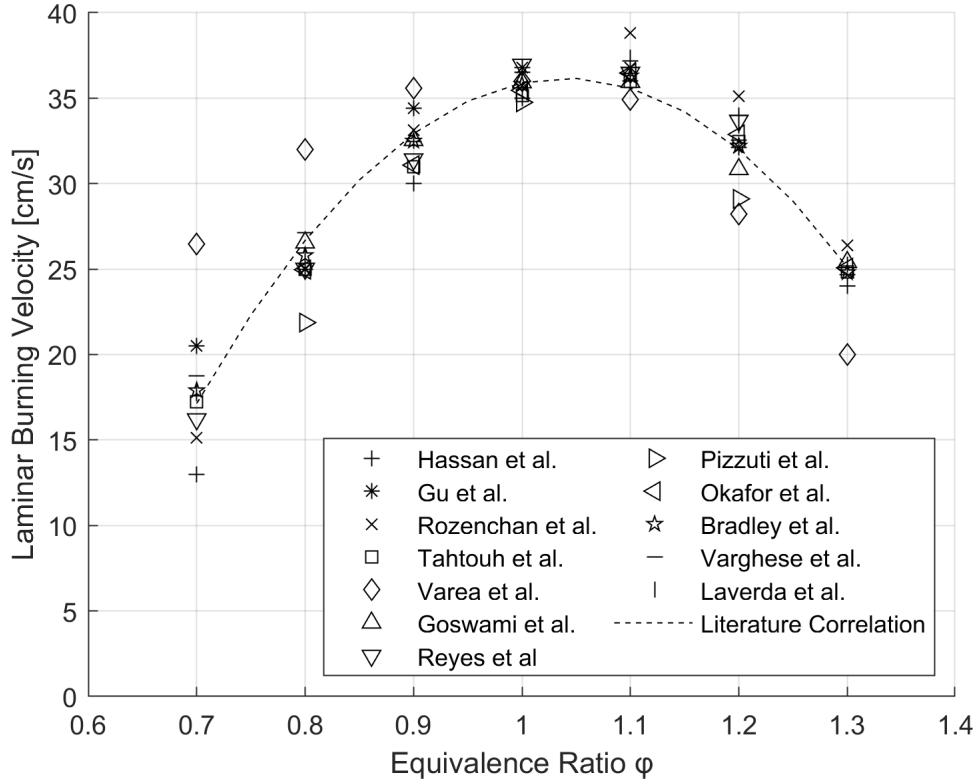


Figure 2.8: Comparison of the measured burning velocity of CH_4 -air flames at 0.1 MPa and between 298 - 300 K. References in Table 2.2.

variations in technique by Goswami et al. [46] who utilised the heat flux method and Varchese et al. [158] who used the diverging channel method. The majority of the literature data shows a very strong correlation across the equivalence ratios, with a flat peak observed between $\phi = 1.0 - 1.1$. At the fringes of the testing around 0.7 and 1.3 equivalence ratios the correlation weakens slightly. At both conditions the methane-air flames are less stable and more susceptible to influences such as temperature, pressure, and geometries. Additionally, the consideration of the flame stretch correlation will impact higher equivalence ratio flames as highlighted by Kelley and Law [83].

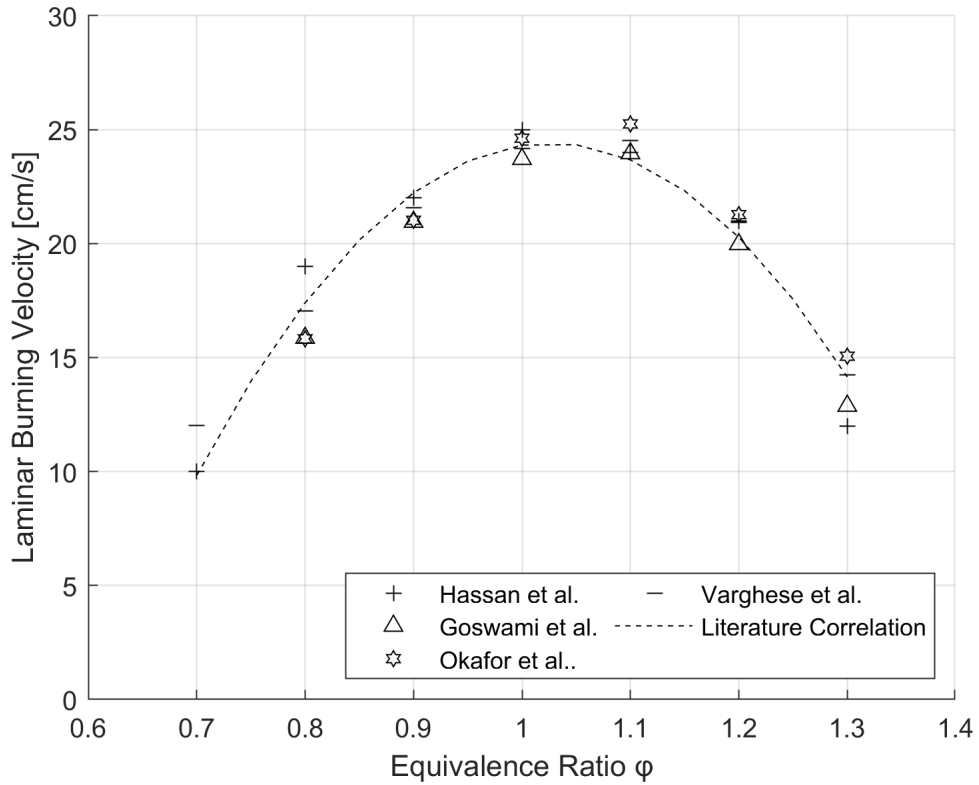


Figure 2.9: Comparison of the measured burning velocity of CH_4 -air flames at 0.3 MPa and between 298 - 300 K. References in Table 2.2.

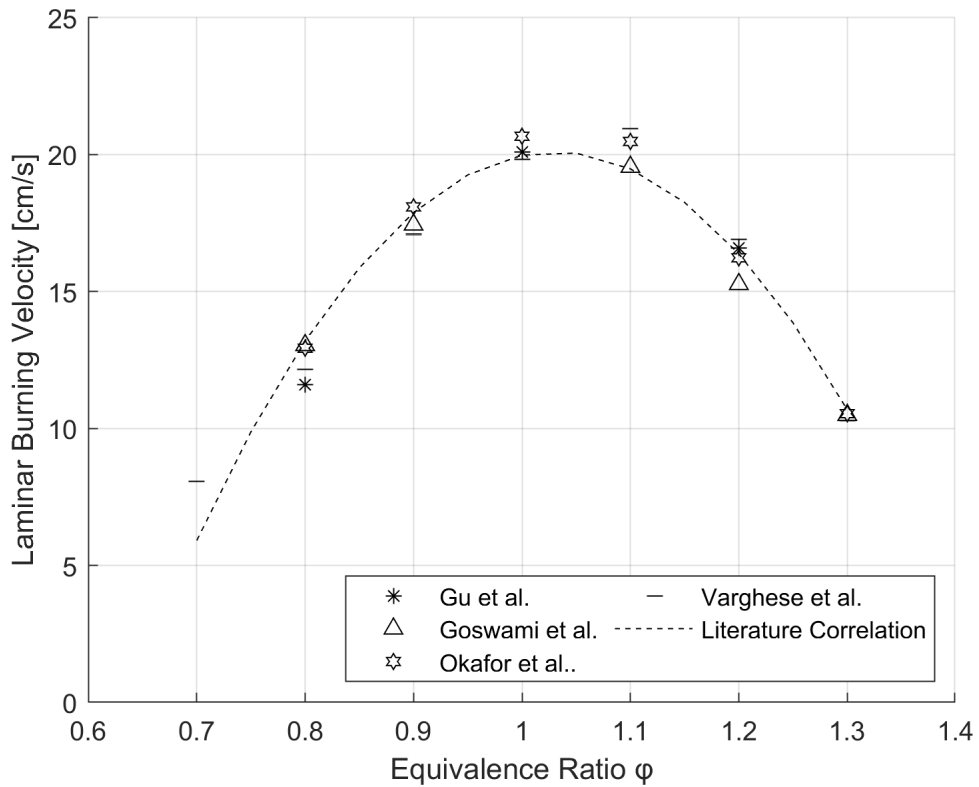


Figure 2.10: Comparison of the measured burning velocity of CH_4 -air flames at 0.5 MPa and between 298 - 300 K. References in Table 2.2.

At higher pressures, equivalence ratio sweeps in literature become less common with the focus switching to the relationship of pressure and laminar burning velocity with a stoichiometric mixture. The literature for initial pressures of 0.3 MPa and 0.5 MPa are shown in Figures 2.9 and 2.10. Once again, the plotted literature correlation is a culmination of all the literature data points. Hassan et al. [55], investigated the properties of methane-air flames at elevated pressure of 0.5 - 4.0 atm across varying equivalence ratios using a spherical combustion chamber. Although predating the introduction of the non-linear stretch correlation, the results at high pressures had a high correlation with more recent studies at pressure from Okafor et al. [116], Varghese et al [158] and Gu et al [51]. The laminar burning velocity decreased as the temperature increased.

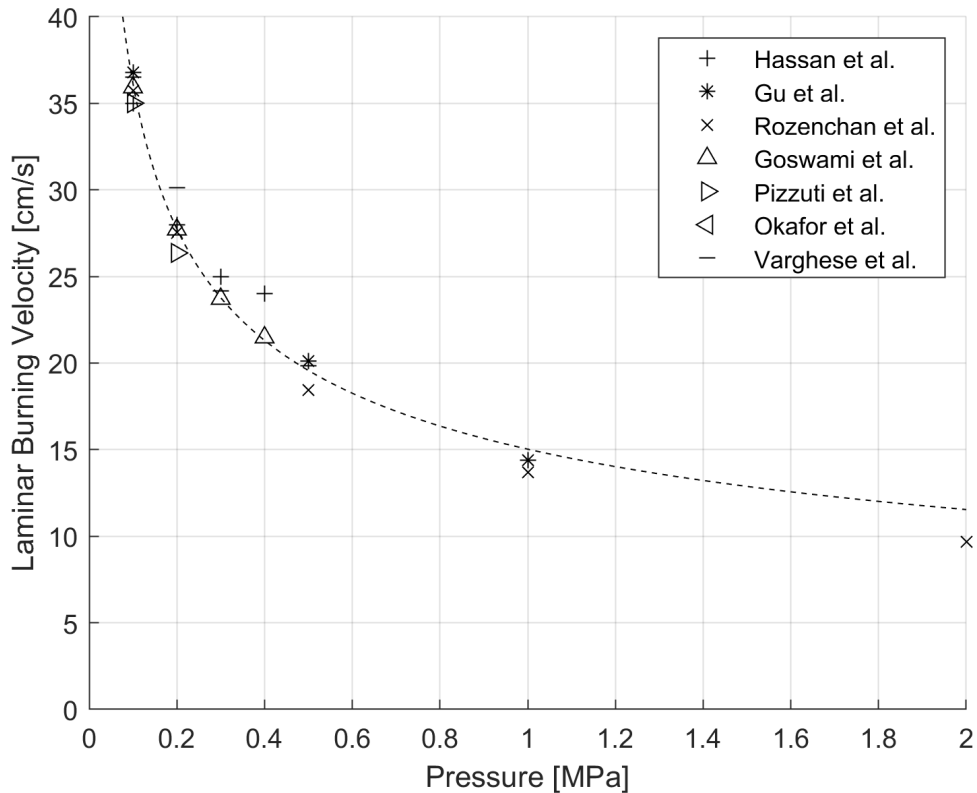


Figure 2.11: Comparison of the measured burning velocity of CH_4 -air flames across various pressures, 298 - 300 K. References can be found in Table 2.2.

Figure 2.11 depicts the correlation of laminar burning velocity and pressure

taken from literature values. Rozenchan et al. [132] identified the need for higher pressure experimental data to validate kinetic models for ICE applications and studied pressures up to 20 atm.

2.4.2 Ammonia studies

Experimental research investigating the combustion properties of ammonia-air mixtures has increased in recent years as a result of the increased interests in its use as a fuel. Most of the experiments were carried out at room temperature and pressure as shown in Table 2.3. The general results of these studies concluded the laminar burning velocity of a stoichiometric ammonia-air mixture at room temperature and pressure was approximately 7 cm/s, a fifth of the equivalent methane-air velocity.

Early investigations, such as those performed by Phfal [120], Takizawa [147] and Zakaznov [171], do not consider the burning velocity stretch correlation in their calculation of laminar burning velocity. As discussed in Section 2.2.3, this will result in a change of flame speed due to the thermo-diffusive effects and will lead to inaccurate flame speed measurements. More recently Hayakawa et al. [58, 56, 57] experimentally and numerically investigated ammonia-air laminar flames at both atmospheric and elevated pressures up to 0.5 MPa, across a range of equivalence ratios. They found the laminar burning velocity reaches its peak value at an equivalence ratio of 1.1 for all initial pressures considered as well as a decreasing trend of burning velocity with increased initial pressure, similar to hydrocarbon fuels.

There are limited studies addressing the impact of temperature on ammonia-air flames, the first being performed by Cohen [24], investigating temperatures from 323 K to 423 K. More recently, Lhuillier et al. [95] investigated

Table 2.3: Summary of relevant research studies relating to ammonia-air laminar burning velocity investigations.

Study	Year	Equivalence Ratio ϕ	Temp. [K]	Pressure [MPa]	Ref.
Takizawa et al.	2007	0.8 - 1.3	298	0.1	[147]
Hayakawa et al.	2015	0.8 - 1.2	298	0.1 - 0.5	[57]
Okafor et al.	2018	0.8 - 1.3	298	0.1	[116]
Bradley et al.	2019	0.7 - 1.3	300	0.1	[10]
Okafor et al.	2019	0.8 - 1.3	298	0.1 - 0.5	[117]
Varghese et al.	2019	0.7 - 1.3	350 - 650	0.1 - 0.5	[158]
Mei et al.	2019	0.9 - 1.1	298	0.1	[108]
Han et al.	2020	0.85 - 1.25	298	0.1	[53]
Lhuillier et al.	2020	0.8 - 1.4	298	0.1	[95]
Wang et al.	2021	0.7 - 1.4	298	0.1	[162]
Laverda et al.	2021	0.7 - 1.4	298 - 338	0.1	[89]

ammonia-air and ammonia-hydrogen-air mixtures from 298 K to 473 K, proposing a correlation that conflicted with the values proposed by Cohen. Han et al. [54] measured the flame propagation of ammonia using the heat flux method, taking results from 298 K to 448 K, finding a close agreement to the proposed correlation from Lhuillier et al. Continuing the work of Hayakawa, Kanoshima et al. [81], investigated the influence of temperature up to 500 K and also found agreement to Lhuillier’s correlation.

Figure 2.12 presents the range of data measured at 0.1 MPa and 298 K for ammonia air flames across a range of equivalence ratios. The literature correlation is a culmination of all the literature data points. Further detail and references are included in Table 2.3.

2.4.3 Ammonia-hydrogen studies

One method commonly used to overcome the challenges associated with pure ammonia combustion is blending other fuels to enhance the combustion characteristics. There have been a number of studies focused on the

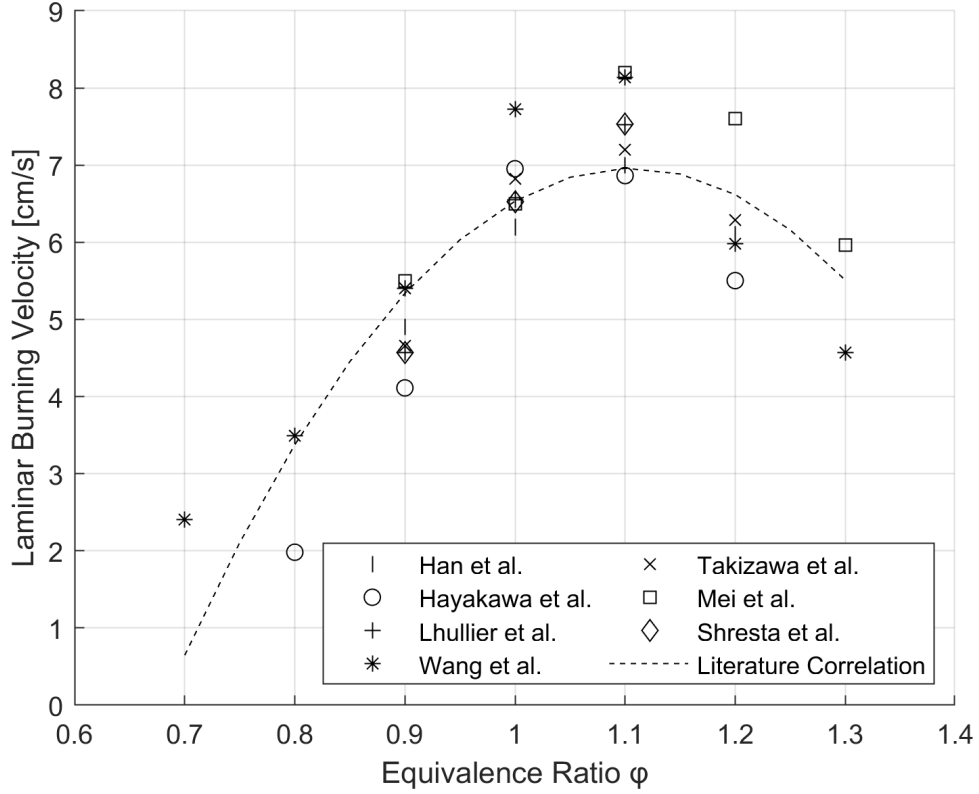


Figure 2.12: Comparison of the measured burning velocity of NH_3 -air flames at 0.1 MPa, 298 - 300 K. References in Table 2.3.

laminar burning velocity enhancement of ammonia using hydrogen as the combustion promoter, these are summarised in Table 2.4.

Across the majority of literature, as well as within this report, the substitution ration is defined as the hydrogen concentration within the fuel. Equation 2.10 shows the definition of the hydrogen substitution ration, where $[X]$ is the mole fraction of the relevant fuel.

$$X_{H_2} = \frac{[H_2]}{[H_2] + [NH_3]} \quad (2.10)$$

The studies show that the introduction of hydrogen will increase the flame speed exponentially, despite equivalence ratio and initial conditions [169]. Lee et al. [91] investigated ammonia-hydrogen flames at 298 K and 0.1 MPa across a range of substitution ratios from 0.1 - 0.5 both experimentally and computationally, observing substantial effects of flame stretch

on the burning velocities as well as a reduction in NO_x formation in fuel rich conditions. Ichikawa et al. [68] expanded the parameters, investigating mixtures from 0 - 1.0 hydrogen substitution ratio at pressures up to 0.5 MPa, finding that similarly to other fuels an increase in pressure reduces the burning velocity. Lhuillier et al. [95] investigated the impact of increased temperature on ammonia-hydrogen flames with substitution ratios ranging from 0 to 0.6 and temperatures from 298 to 473 K, finding an increasing burning velocity with temperature increase. The results of the literature studies varying substitution ratio at a pressure of 0.1 MPa and room temperature are shown in 2.13. The literature correlation is a culmination of all the literature data points.

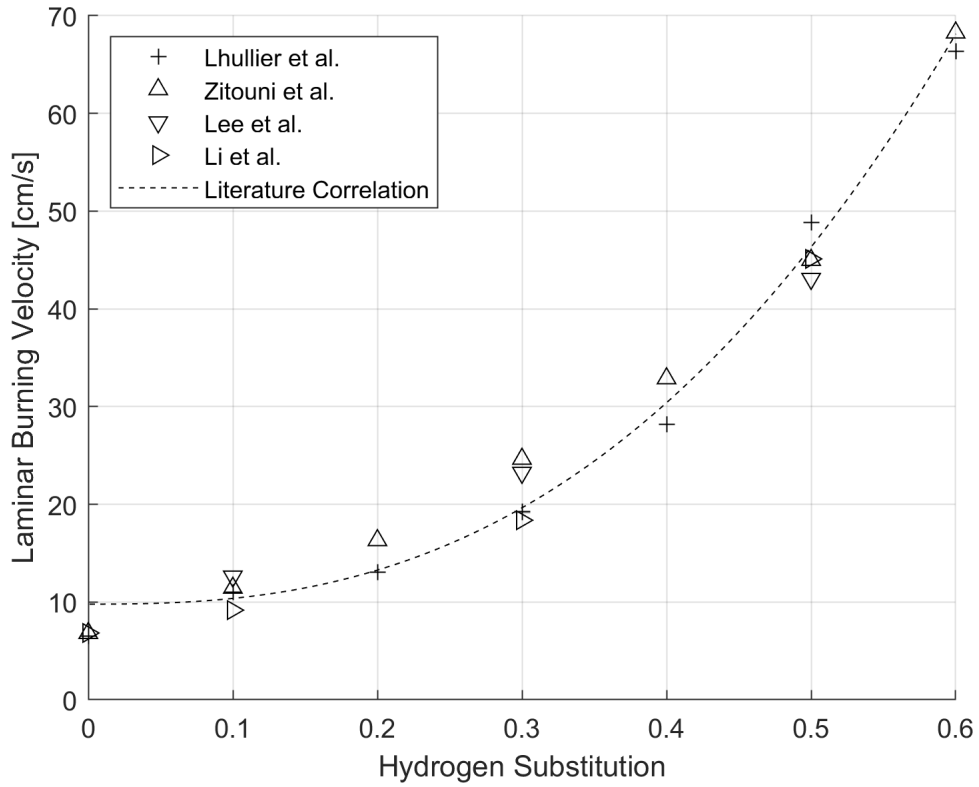


Figure 2.13: Burning velocity measurements of $\text{NH}_3\text{-H}_2\text{-air}$ flames with varying substitution ratios at 0.1 MPa, 298 - 300 K. References in Table 2.4.

Table 2.4: Summary of relevant research studies relating to ammonia-air laminar burning velocity investigations.

Study	Year	Substitution Ratio SR	Temp. [K]	Pressure [MPa]	Ref.
Lee et al.	2010	0.1 - 0.5	298	0.1	[92]
Ichikawa et al.	2015	0 - 1	298	0.1 - 0.5	[68]
Li et al.	2017	0 - 0.9	298	0.1	[97]
Lhullier et al.	2020	0 - 0.60	298	0.1	[95]
Gotama et al.	2021	0.4	298	0.1 - 0.5	[47]
Shresta et al.	2021	0 - 0.3	473	0.3, 0.7	[139]
Wang et al.	2021	0 - 0.2	298	0.1	[162]
Zitouni et al.	2023	0 - 0.8	298	0.1	[176]
Yasiry et al.	2023	0 - 0.4	298	0.1	[169]

2.5 Ammonia in engines

Research in engines is moving away from the previous focus on energy efficiency and into a focus on carbon neutrality. Assessing potential options for an alternative fuel for power-generation and heavy duty engines involves considering a wide range of factors, including operational flexibility, ease of storage, cost of production, diversity of supply sources, emissions, and safety [168]. Whilst hydrocarbon fuels are able to store more energy at higher densities and lower volumes, the absence of chemical-bound carbon in ammonia positions it as a compelling alternative fuel. Noteworthy alternatives, such as batteries and fuel cells hold promise particularly for passenger vehicle applications. However the viability of the fuel solution is dependent on the energy demands of the transport mode. For scenarios characterised by sustained high energy demands such as shipping and off-grid power generation, ammonia is a strong contender [149].

2.5.1 History of ammonia as a fuel

The exploration of ammonia as a fuel in engines dates back to World War II, when the war efforts demand for fossil-based fuels resulted in shortages for public transport. Ammonia was used as an alternative fuel in eight buses in Belgium. This trial, employing a combination of coal gas and anhydrous ammonia, spanned a year during which tens of thousands of miles were covered [86]. Two decades later, the US army conducted a series of investigations into the feasibility of ammonia as a fuel for ICEs [119, 145]. Despite technically proving ammonia as a fuel, replacing the less expensive fossil fuels with ammonia was not economically viable. At the time, it was quoted that ammonia was ten times more expensive than hydrocarbon fuels for the same energy output. More recently, there have been demonstrations of ammonia used as a fuel in various ICEs;

- Compression ignition (CI) [49, 126, 170].
- Spark ignition (SI) [94, 112, 133, 164].
- Dual-fuelled [48, 50, 94, 115].

2.5.2 Ammonia fuel combustion characteristics

Due to having a lower energy content in comparison to its fossil fuel equivalents as shown in Table 1.1, it is even more important for an ammonia engine to operate at high efficiencies with minimal power losses. Higher efficiencies will minimise the additional space the ammonia fuel storage takes. The stoichiometric air-fuel ratio of ammonia is 6.046, compared to 14.3 for diesel. This means that when combined with air, the stoichiometric energy content of an ammonia-air mixture is 2.64 MJ/kg which is comparable to

a diesel air mixture of 2.77 MJ/kg [126]. This indicates the potential for ammonia to fuel a combustion system with very similar outputs to a diesel system. Ammonia has a high auto-ignition temperature (651°C) resulting in a high resistance to ignition in an engine environment. In an analysis of a dual-fuelled ammonia-diesel engine, Reiter and Kong found that the ignition delay would increase as higher proportions of ammonia were added [126].

In early testing of ammonia SI engines, Mozafari-Varnusfadrani [112] suggested the high latent heat of vaporisation of ammonia reduced the temperature during the compression stroke and caused mixture non-uniformity as a result of the cooled intake. Concluding it was counter-productive to the task of improving the combustability of ammonia. In more recent reports, induction of the liquid phase ammonia provides an increase in volumetric efficiency and encourages close to isothermal compression [94]. When taking this into account Zamfirescu and Dincer proposed a system effectiveness of 46% with the cooling power representing 7.2% from the engine power [172].

A key consideration in engine testing, especially for alternative fuels is emissions analysis. In multiple studies [95, 126, 164, 170], significant amounts of ammonia slip have been reported. Slip occurs when unburnt fuel leaks past the pistons in an engine, in the case of ammonia this will result in a toxic gas being released via the exhaust system, a potentially dangerous scenario. Zacharakis-Jutz recognised that the level of slip reduced at high loads, however it still remained at a toxic concentration of approximately 1000 ppm [170]. This was very similar to quoted values produced from Reiter and Kong of emissions ranging between 1000 – 3000 ppm [126]. Both studies have proposed to include an appropriate exhaust after treatment to convert the exhaust ammonia and any remaining NO_x simultaneously.

In an investigation of nitrogen based emissions from an ammonia fuelled SI engine, it was found that the temperature in the exhaust is sufficient to support selective catalytic reduction of the excess ammonia/ NO_x emissions [164].

Ammonia has a high octane rating which enables extremely high compression ratios resulting in potentially very high engine-cycle efficiencies [99]. Duynslaegher assessed the effect of compression ratio, spark timing, and equivalence ratio on multiple engine performance measures including the quantity of unburned ammonia in the exhaust [31]. For conventional fuels an acceptable value was 3%, in the study the percentages for ammonia ranged between 8 - 10% which is significantly higher. It was hypothesised that the presence of some of this unburnt ammonia was a similar effect described by Smith et al. called ‘bulk quenching’ that is used to describe the high percentage of unburned hydrocarbon emissions in emissions from lean operating fossil fuelled ICEs [144]. The mechanism occurs due to the fuel having a low flame speed, the combustion expansion is too fast in comparison to the flame propagation. This results in a dilution of the flame front that in turn does not preheat the fresh combustion mixture enough to allow complete flame propagation. The ‘bulk quenching’ is influenced principally by compression ratio and to a lesser extent the engine rotation speed. Duynslaegher suggested controlling turbulence in the cylinder with an appropriate geometry or admission phase could reduce this [31].

2.5.3 Compression ignition engines

Gray et al. [49] demonstrated ammonia in a CI engine without the use of additives or pilot fuels. At a compression ratio of 35:1 consistent ignition was achieved. Whilst the high compression ratio enables the ammonia

combustion, it is not suitable given the requirement for engines to operate at low loads, including idle. A variety of combustion initiators were investigated in order to limit the demand for the high compression ratio to provide the required ignition energy for ammonia. Pearsall and Garabedian [119] noted that although diesel CI engines operate excessively lean due to smoke limitations, the ammonia fuelled engine favoured operation closer to stoichiometric. This enabled better air utilisation and power output, surpassing diesel operation by up to 32%. Modifying the engine with preheated air intake, increased jacket temperature, larger ignition energies, and enriching the ammonia with hydrogen were suggested as significant ways to improve ammonia combustion. As highlighted by Dimitriou and Javaid [27], the literature for ammonia single-fuelled operation of a CI engine is very limited due to its unsuitable properties for CI. Although proven possible, the implementation of these engines is very difficult due to the extremely high compression ratios required.

2.5.4 Spark ignition engines

Tests were conducted on a single cylinder cooperative fuel research engine (CFR) by Starkman et al. [145], with compression ratios ranging from 6:1 to 10:1. The study suggested ammonia should be added to the engine as a vapour, and utilised ammonia's ability to break down into hydrogen and nitrogen to encourage combustion. The study further presented that a higher cylinder wall temperature promoted stable combustion and that the spark timing was similar to hydrocarbon fuels. Starkman et al. concluded that the decomposition of ammonia and corresponding intermediates linked the compression ratio and combustion temperature to the concentration of hydrogen formed. Duynslaeger however, disproved this theory by operat-

ing an ammonia fuelled engine without combustion, demonstrating that no hydrogen was released during the compression stroke. It was concluded that whatever the compression ratio, even if ammonia can be thermodynamically decomposed, the kinetics of the reaction are not fast enough in the engine [31]. Duynslaegher's study focused on using ammonia fuelling without the use of combustion promoters, instead assessing the effect of compression ratio, spark timing and equivalence ratios on the exhaust gas composition and engine performance. It was found that, as a result of the relatively low combustion temperatures, there were very little NO_x emissions present. Pearsall et al. [119] recognised that an effective way to facilitate combustion of ammonia in a SI engine was the use of high energy igniters as well as more compacted combustion chambers.

In more recent studies, Lhuillier et al. [94] successfully operated a modern single cylinder SI engine with ammonia only fuelling, achieving high power outputs with good efficiencies (37%). Similar to previous studies, they observed high NO_x (6000 ppm) and unburned ammonia (20000 ppm) in the exhaust stream as well as highlighting the need for additional treatment of the exhaust.

2.5.5 Dual fuel engines

Dual-fuelling, or co-fuelling, is a widely used technique found in much of the literature on ammonia engine testing. This technique uses a secondary fuel, usually with more favourable combustion characteristics, to overcome the difficult aspects of ammonia combustion and achieve stable engine operation. In early CI testing, Pearsall and Garabedian [119] conducted testing using dual-fuelling, in this case by supplying the ammonia vapour via the air intake and using diesel fuel to provide the ignition en-

ergy. A similar technique was demonstrated by Reiter and Kong [127] with a multi-cylinder, turbocharged diesel engine, achieving a maximum energy replacement of 95%. They found CO₂ emissions reduced monotonically for the same engine torque output as ammonia substitution ratio increased, as well as lower NO_x emissions provided the substitution ratio was below 60%. For SI engine dual fuel testing early studies, performed by Starkman et al. [145], partially decomposed the ammonia into hydrogen and nitrogen by running the fuel stream through an electrically heated catalysis of activated iron catalyst. They achieved an output of 71% compared to that of a hydrocarbon fuel with maximum nitric oxide concentrations of 4800 ppm using ammonia (3000 ppm at maximum power). Grannell et al. [48] recommended a compression ratio of 10:1 in the ammonia petrol dual fuelled engine with a standard mix of 70% ammonia and 30% petrol at normally aspirated wide open throttle. It was found that the maximum brake thermal efficiency was 32.0% at 10:1 compression and BMEP = 1025 kPa, compared to petrol at 24.6% at 9:1 compression ratio and a BMEP of 570 kPa. The operation was limited either by engine roughness as a result of excess ammonia or knocking as a result of excess petrol. Mørch et al. [111] investigated various ammonia-hydrogen mixtures, at a range of air fuel ratios within a CFR-engine. It was concluded that a dual mixture of 10 vol.% hydrogen performs the best with respect to efficiency and power. They also experienced high NO_x emissions(3500 - 5000 ppm) occurring with a high hydrogen content and an excess air-fuel ratio (λ) between 1.1 and 1.4.

Frigo and Gentili [39] investigated a four-stroke SI engine operating on an ammonia-hydrogen mixture with the intention of using an on-board catalytic reformer to crack the hydrogen from the ammonia. Again confirming the necessity of adding hydrogen to ammonia to improve ignition

characteristics and increase combustion velocity. Recommending similar substitution ratios to Mørch et al, Frigo and Gentili observed lower NO_x emissions of a maximum at 1700 ppm at low load and 3000 rpm as well as ammonia slip. The ammonia slip was only measured using a threshold alarming system which “did not give alarms with the final injection and ignition setting”, no further detail was given around this. Westlye et al. [164] focused their investigations on the emissions generated by a dual fuelled ammonia hydrogen engine, especially around the formation of NO_2 and N_2O as well as unburned ammonia. They operated on a fuel mix of 80% ammonia and 20% hydrogen by volume, varying the compression ratios and lambda values. They found the nitric oxide emissions will be lower than from hydrocarbon combustion near stoichiometric conditions, however under fuel lean conditions NO formation increases. Alongside this they concluded the N_2O concentration is sensitive to both the spark timing and the excess air ratio. They proposed a mechanism that provides an explanation of the formation of the various emissions which is based on the amount of trapped fuel within crevices. They stated an ammonia slip of 10 - 25 ppm. Lhuillier et al. [94] concluded that the addition of hydrogen was able to stabilise the operation of a SI engine provided the ignition timing was correctly advanced. They were able to achieve comparable engine characteristics to pure methane fuelled operation. Pochet et al. [124], successfully demonstrated a homogeneous charge CI engine with 70% ammonia 30% hydrogen and a compression ratio of 15.3:1. The compression ratio was recognised to be a trade-off between the high compression required to promote ammonia combustion but limited to prevent ringing occurring due to the hydrogen and its high combustion energy. It was also found that exhaust gas re-circulation EGR significantly reduced NO_x emissions however unburned hydrogen and ammonia measurements were not taken.

2.6 Summary

This literature review has explored ammonia's potential as a fuel for heavy-duty combustion engines by examining its chemical characteristics, production methods and historical usage. It has established a foundation for understanding ammonia's viability as a fuel, noting key advantages such as ease of storage and high energy density as well as disadvantages such as toxicity and current production carbon intensity. The review highlights future production methods that will be able to decarbonise ammonia production, enabling it as a low carbon fuel. Additionally, it details combustion and burning velocity fundamentals, focusing on the characteristics that arise when analysing ammonia and hydrogen flames. This section also links the fundamental combustion parameters to the engine performance within both compression ignition and spark ignition engines.

In supporting the constant volume combustion chamber study, the review of optical research on flame speed measurement provided valuable insights in to the design and development of the test rig. It was noted that most studies utilise central ignition electrodes, resulting in challenges comparing real-world ignition systems. Considering the multiple fuels intended for use within the chamber, further detail was drawn out comparing the multiple studies within literature on methane, ammonia and ammonia-hydrogen premixed flame studies. This provided a benchmark data-set for comparison with the new combustion chamber as well as highlighting the lack of studies on hydrogen-ammonia testing.

The review also examined literature on the use of ammonia as a fuel in compression ignition and spark ignition engines, including dual fuel operation with hydrogen and methane as combustion promoters. The insights

gained informed expectations for the engine study and identified key areas of interest such as ammonia slip and NO_x emissions. It concluded that most existing studies are outdated or were conducted on research engines, indicating the need for a modern engine retrofit demonstrator.

Chapter 3

Design of a Novel Optically Accessible Constant Volume Combustion Chamber

The primary objective of this research activity was to experimentally compare the combustion characteristics of various premixed air-fuel mixtures including methane, hydrogen, and ammonia, within an engine-like environments. A key aspect involved parametric studies of temperature, pressure, and air-fuel equivalence ratio to understand their influence on the combustion dynamics of these fuels, with a focus on both spark ignition (SI) and turbulent jet ignition systems (TJI). In order to effectively carry out this investigation, a novel optically accessible combustion chamber was designed in accordance to the British Standard, BSEN 13445:2021 [16] and PD5500 [18]. Detailed within this chapter are the steps taken to develop and manufacture the bespoke constant volume combustion chamber (CVCC) tailored to provide the environmental conditions required to assess ignition systems under dual-fuel operations. It is important to note that the conventional

central electrode ignition system commonly employed in fundamental combustion studies was not considered for the initial design as the design was chosen to attempt to replicate heavy-duty engine conditions and geometries with a specific emphasis on accommodating both SI and TJI configurations. The modular design enables future modifications to enable the central electrode system, but the side wall approach in this study enhances the relevance to real world systems. This chapter details the design and development of the optically accessible combustion chamber including the following sections;

- Design - a detailed walk through of the design process including the design verification work to ensure conformance to standards.
- Rig setup - the setup of the experimental rig enabling fine gas mixture controls for multi-fuel operation.
- Methodology - the experimental methodology and testing procedures for various gas mixtures.
- Data acquisition and processing - data acquisition setup and LabView control with processing for key information.

3.1 Design functionality and requirements

The following section details the fundamental considerations taken in the design alongside the calculations necessary to confirm the geometries and materials in the design. The requirements were developed using learning from both literature and prior engine test results. The requirements are shown in Table 3.1.

Table 3.1: Requirements for the Constant Volume Combustion Chamber

No.	Requirement
1	The chamber must be rated to withstand the combustion pressures of 100 bar at 100°C.
2	The chamber must be fabricated from materials that are compatible with all rated fuels - diesel, methane, ammonia, and hydrogen.
3	The chamber optical access must be maximised with clear sight of the flame initiation point from the front and side views.
4	The chamber must allow for both temperature measurement of the internal volume temperature and wall temperature.
5	The chamber must allow for high frequency pressure measurement (1kHz) to accurately record developing combustion pressures.
6	The system must provide fine control of the air and fuel quantities to provide an accuracy of fuel-air equivalence ratio within 1% error.
7	The system must provide control of the in-chamber temperature from 25 °C to 100 °C within 1°C.
8	The design must be able to accommodate spark ignition, turbulent jet ignition, and center ignition systems.
9	The chamber must be rated to BSEN 13445:2021[16].
10	The design must be modular to allow for the development of new methodologies.

In order to provide maximum optical access while still imitating the geometry of the cylinder and allowing for future studies, three optical ports were included in the design; two side views and one front view. This will support

chemiluminescence (“natural light” and intensified) imaging studies as well as future particle image velocimetry (PIV) and schlieren imaging.

Figure 3.1 shows a full render of the combustion chamber design. The intake gas port and thermocouple port can be seen on the top side of the chamber, as well as the bolted retaining rings for each of the windows. Figure 3.2, presents a cross-section of the chamber in spark ignition configuration. This provides further detail around the window sealing configuration mentioned later in this chapter.

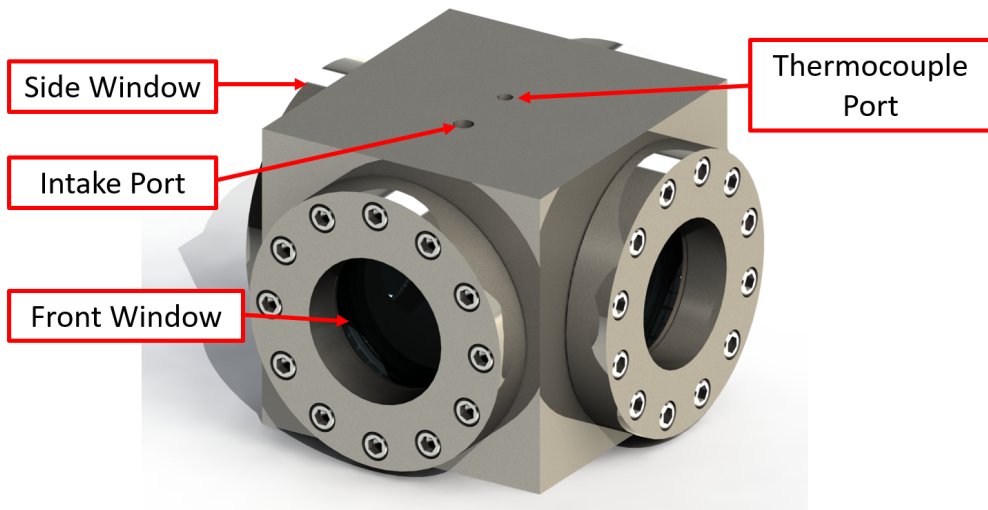


Figure 3.1: Render of the combustion chamber.

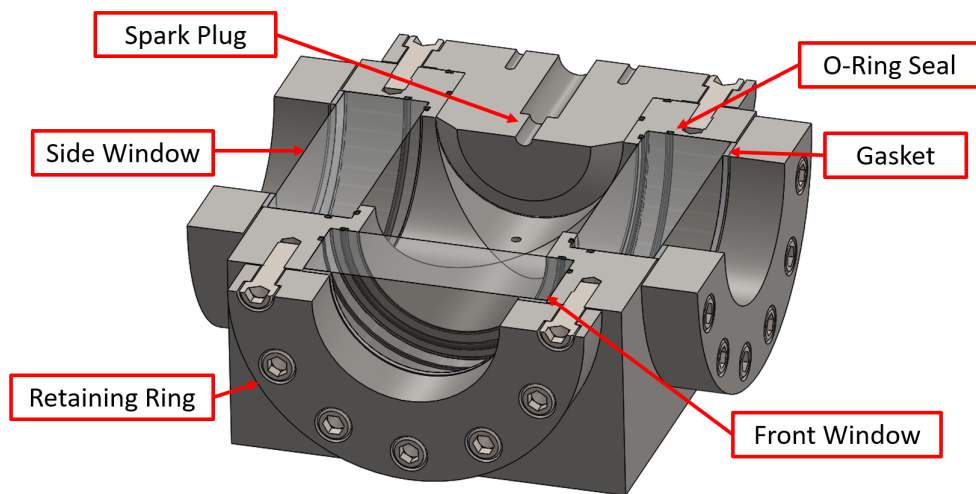


Figure 3.2: Cross-section of the combustion chamber.

3.2 Material selection and compatibility

The intention of the device is to be used to investigate the fundamental combustion characteristics of various fuels, as a result the chamber must be compatible with a wide range of fuels. The materials used in the assembly are listed in Table 3.2.

Table 3.2: List of parts used in the constant volume combustion chamber assembly with associated part numbers and materials.

Part Number	Part Name	Material
P001	Main Body	316 Stainless Steel (1.4401)
P002a/b	Ignition Cap SI/JI	316 Stainless Steel (1.4401)
P003	Window Cap	316 Stainless Steel (1.4401)
P005a	Optical Window	Fused Silica
P005b	Window Blank	316 Stainless Steel (1.4401)
P006	O-ring	NBR
P010	Gasket	PTFE

3.2.1 Main body

Every fuel must be taken into account for its compatibility with the main body of the chamber which will be subject to high pressures and temperatures and exposure to all fuels. For the chamber, type 316 stainless steel - a metastable austenitic alloy, containing molybdenum for improved corrosion resistance and high temperature strength - was selected as the suitable material. When exposed to hydrogen across a range of temperatures, little or no loss in ductility was observed. Its resistance to hydrogen embrittlement and general hydrogen compatibility is due to its high nickel and molybdenum content [135]. It is important to note that ammonia is corrosive to copper, brass, nickel, rubber, and some stainless steel alloys; however, it is compatible with type 316 [85, 137].

3.2.2 Optical access

There are two commonly used materials for optical access in literature for these apparatus; fused silica (quartz) and sapphire. Fused silica is composed of high purity SiO_2 in non-crystalline form. It is known to have exceptional optical, thermal, and mechanical properties. Due to its high purity, it is extremely inert and is compatible with all fuels that are being investigated [26]. Sapphire (Al_2O_3) is produced as a single crystal, it has a very high mechanical strength, thermal stability, and resistance to corrosion it is also compatible with all investigated fuels. Sapphire is not suitable for large windows or intricate designs due to the difficult and expensive manufacturing process.

Table 3.3: Comparison of the thermal and mechanical properties of fused silica and sapphire [72].

Material	Fused Silica	Sapphire
Molecule	SiO_2	Al_2O_3
Young's Modulus (GPa)	97.2 (para) 76.5 (perp)	335
Tensile Strength (MPa)	41	275
Operating Temperature ($^{\circ}C$)	950 – 1150	1200
Coefficient of Expansion ($10^{-6}/K$)	7.1 (para) 13.2 (perp)	8.4

The transmissivity of light must also be considered to ensure that the optical access would be suitable for both chemiluminescent imaging and future laser optical research. Reviewing the chart in Figure 3.3, it can be seen that fused silica has more than 90% transmissivity for the visible light range (400 - 700 nm).

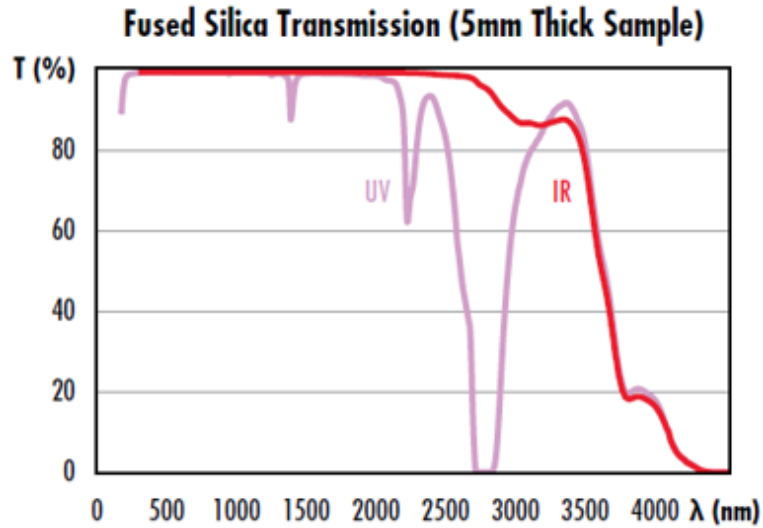


Figure 3.3: Transmission data for UV and IR grade fused silica for a 5mm thick sample without Fresnel reflections [25].

3.2.3 O-rings and gaskets

The o-rings used for sealing are made of nitrile rubber, a material that is frequently used in marine, automotive, and fuel structures due to its exceptional resistance to the majority of fuels, including those investigated in this study [100]. The gaskets used are PTFE, intended to equally distribute the bolting force throughout the window face whilst preventing glass to metal contact that can damage the windows, they are not exposed to any fuel mixtures.

3.3 Design calculations

The calculations needed to design the constant volume combustion chamber are described in depth in the following section. These consist of the thermal expansion calculations, the nominal design stress calculations, and the initial pressure approximation calculations.

3.3.1 Pressure approximation calculations

It is important to have an approximation of the post-combustion pressure that the combustion chamber will be exposed to to understand the maximum design pressure and the pressure release valve pressure. To do this approximation the following assumptions are made;

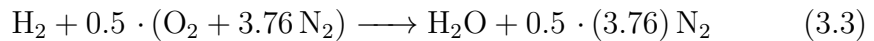
- The combustion is complete.
- No heat is lost to the surroundings.
- The gases are assumed to be ideal.

These assumptions will result in a significant overestimation of the final combustion pressure as heat will always be lost to the surroundings, other products being produced as a result of incomplete combustion will also take energy away, and the combustion efficiency will not be 100% so the total heat released will not be the maximum. The volume of the combustion chamber is set to 1.2 L. The following calculations are to provide the approximation for complete hydrogen combustion at 0.1 MPa, 273K in air. Initially the total number of moles, n_{total} , of gas within the chamber are calculated;

$$p_{int} * V = n_{total} * R * T_{int} \quad (3.1)$$

$$n_{total} = \frac{p_{int} * V}{R * T_{int}} \quad (3.2)$$

where the initial temperature and pressure are T_{int} and p_{int} respectively and R is the universal gas constant, 8.314 kJ/molK [113].



Using the combustion equations for the fuel, the moles of hydrogen can be calculated;

$$n_{H2} = \frac{1}{1 + 0.5 * (1 + 3.76)} \quad (3.4)$$

Fuel	Latent Heat of Vaporisation [MJ/kg]
Hydrogen	120
Ammonia	18.8
Methane	50

Table 3.4: Latent heat of vaporisation of the three fuels considered in this study, taken from NIST [113].

Table 3.4 presents the latent heat of vaporisation of the various fuels, this value takes into account the enthalpy of formation of water and can therefore be used to calculate the total energy released as a result of a complete combustion of the fuel in air. Using the calculated energy released, Q , assuming the entirety of the energy is transferred into heating the products, the change in temperature, ΔT can be calculated. The mass, m , is calculated from the moles and molar masses of the products.

$$Q = m * C_p * \Delta T \quad (3.5)$$

Rearranges to give,

$$\Delta T = \frac{Q}{m * C_p} \quad (3.6)$$

Figure 3.4 presents the approximate combustion pressure for multiple fuel mixtures at varying temperatures across a range of initial pressures. These values are significantly overestimated especially when considering the completeness of combustion with ammonia which will decrease the final combustion pressure. It does however provide a ballpark figure for the design pressure of the combustion chamber. For future studies, gradual increase

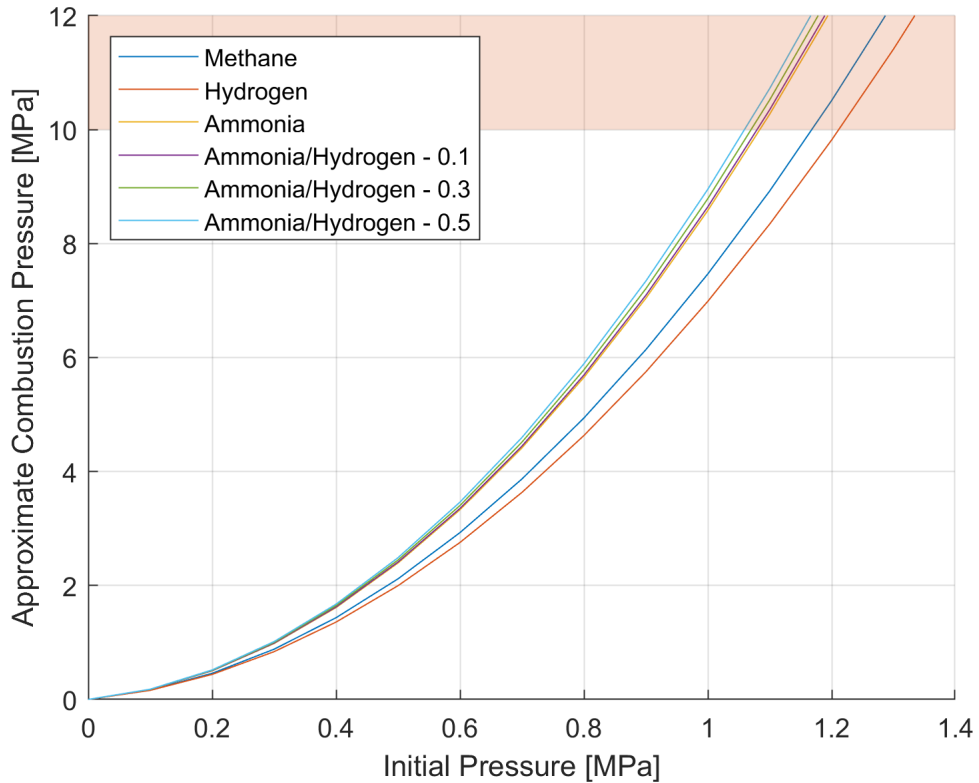


Figure 3.4: Plot of the approximate maximum post-combustion pressure for various fuel mixtures at 298K.

in the conditions from 0.1 MPa will allow for the maximum initial pressure to be achieved, accounting for incomplete combustion. A pressure relief valve will be used to prevent over-pressures.

3.3.2 Nominal design stress

BS EN 13445-3:2021 provides the necessary means to design by formula to ensure the main body is above the minimum required wall thicknesses for the desired pressure the calculations were then verified using Solidworks FEA modelling [17]. The designated operation of the device falls under Load Case 0, which includes considerations for the internal calculation pressure as defined in 5.3.10 as well as the maximum dead loads from 5.3.2.4.2.1 in the standard.

For an internal pressure, the maximum allowable pressure shall not be less than the differential pressure which will exist at the specified location in the chamber when the pressure relieving device starts to relieve (7.5 MPa adjustable up to 10 MPa). The absolute value of the design pressure shall not be smaller than the absolute value of the maximum allowable pressure. 316 Stainless Steel (1.4401) is an austenitic steel with a minimum rupture elongation of 40%. As a result the nominal design stress for normal operating load cases can be calculated from Section 6.5 of BS EN 13445-3:2021[17]. This states the nominal design stress shall not exceed the greater of the two values;

- The nominal design stress for normal operating load cases f shall not exceed f_d , the minimum 1% proof strength at calculation temperature, as given in the technical specification for the material, divided by the safety factor 1.5.

From Table 3.5, the minimum 1% proof strength at calculation temperature is 175 MPa and therefore the nominal design stress from this method is;

$$f_a = \frac{175}{1.5} = 116.6 \text{ MPa} \quad (3.7)$$

If a value of Rm/T is available, the smaller of two values:

- the minimum tensile strength at calculation temperature, as given in the technical specification for the material, divided by the safety factor 3.0; and
- the minimum 1% proof strength at calculation temperature, as given in the technical specification for the material divided by the safety factor 1.2.

From Table 3.6, the nominal design strength from this method is the smallest of the two following;

- The minimum tensile strength at calculation temperature is 390 MPa and therefore the nominal design stress is;

$$f_a = \frac{390}{3} = 130MPa \quad (3.8)$$

- Or the minimum 1% proof strength at calculation temperature is 175 MPa therefore the nominal design stress is;

$$f_a = \frac{175}{1.2} = 145.8MPa \quad (3.9)$$

Following the method from BS EN 13445-3:2021, the nominal design strength at the operating temperature of 100°C is given as $f_d = 130MPa$ [17].

Table 3.5: Minimum values for the 0.2% (Rp0.2) and 1.0% (Rp1.0) proof strength of stainless steel 316 (1.4401) at elevated temperatures in the solution annealed condition (100 – 300°C) from BS EN 10272:2016 [15]

Temperature [°C]	100	150	200	250	300
Minimum 0.2% proof strength [MPa]	175	158	145	135	127
Minimum 1.0% proof strength [MPa]	210	190	175	165	155

Table 3.6: Minimum values for the tensile strength of austenitic steels at elevated temperatures in the solution annealed condition from BS EN 10272:2016 [15]

Temperature [°C]	100	150	200	250	300
Tensile Strength Rm [MPa]	430	410	390	385	380

3.3.3 Cylindrical shell thickness calculations

Due to the nature of the design, the pressure vessel is not considered to be a thin cylindrical shell and therefore does not conform to methods from BS EN 13445-3 [17]. To verify the design of the vessel the hoop stress will be calculated from a simplified design. The design has a 210 mm square cross-section with a 100 mm bore cut out, therefore, to confirm the yield stress safety factor the hoop stress can be overestimated by assuming a thickness of 55 mm. The representative cross-section is shown in Figure 3.5. The maximum stress will be found at the inner wall when $r = 50$ mm.

$$\text{Hoop Stress, } \sigma_{\theta} = p \cdot \frac{r_i^2 + r_o^2}{r_o^2 - r_i^2} \quad (3.10)$$

Where r_i is the internal radius, r_o is the outer radius, and p is the internal pressure. Therefore, the maximum internal pressure of 10 MPa (100 bar) results in a maximum hoop stress of 15.86 MPa. Providing a safety factor of 9 when compared to the nominal design strength. This does not consider the axial forces as a result of the bolted end caps, or the additional counter-bored hole. These will be considered in Section 3.5. To verify the design completely a hydrostatic test was completed alongside a design review. The design review summary and hydrostatic test report are included in Appendix B.

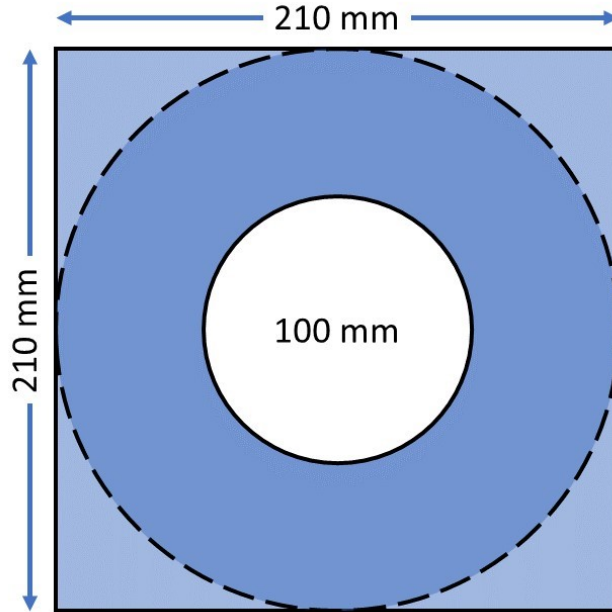


Figure 3.5: Representative cross-section used for stress calculations.

3.4 Optical window design

The optical access to the chamber is maximised to provide the ability to test with a variety of imaging techniques in the future. A common set-up for optical combustion chambers enables a top-down view of the ignition point and is useful for direct high speed chemiluminescent imaging of a flame. As the two bores of the chamber cylinders are 100 mm diameter, the maximum aperture of the window is 100 mm. This enables potential investigations into flame/wall interactions in the future. Schlieren imaging relies on a collimated light source passing through the region of interest, as a result this technique as well as other laser based techniques requires two opposing windows which will also be included in the design. This also provides future opportunity for multidimensional flame imagery. The windows must be specified to withstand the high temperatures and pressures associated with the combustion, whilst maintaining a strong seal.

3.4.1 Window thickness

The optical elements in this design will be in a “port-hole” style commonly used in optical combustion chambers. The window is a supported plane-parallel circular element so as a result the thickness can be derived from the calculated stresses and the desired safety factor. The maximum stress on a uniformly loaded window is given by

$$S_{max} = \frac{K \cdot D^2 \cdot P}{4 \cdot T^2} \quad (3.11)$$

Where S_{max} is the maximum stress, K is the empirical constant (0.75 for a clamped window) , D is the unsupported diameter for a circular window, and T is the thickness of the window. These variables are shown in the diagram in Figure 3.6. Since

$$S_{max} = \frac{F_a}{SF} \quad (3.12)$$

Where F_a is the apparent elastic limit of the material and SF is the safety factor. Rearranging these equations, the thickness of the window is given by

$$T = D \sqrt{\frac{SF \cdot K}{4}} \cdot \sqrt{\frac{P}{F_a}} \quad (3.13)$$

Considering the working pressure of 100 bar (10 MPa), the unsupported diameter of 100mm, K value of 0.75, and the allowable stress of 41MPa with a safety factor of 4 taken from Table 3.3.

$$T = D \sqrt{\frac{SF \cdot K}{4}} \cdot \sqrt{\frac{P}{F_a - \sigma_T}} \quad (3.14)$$

$$T = 100 \sqrt{\frac{4 \cdot 0.75}{4}} \cdot \sqrt{\frac{10}{41}} = 42.77mm \quad (3.15)$$

The final thickness of the optical windows was chosen to be 45 mm, this provided a SF of over 4 at a pressure of 100 bar.

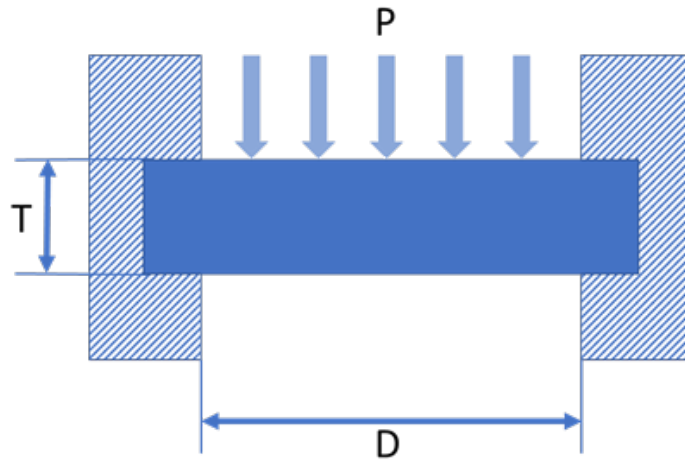


Figure 3.6: Representative diagram of a clamped pressure vessel window.

3.4.2 Sealing the window

The windows are sealed using two o-rings, the main seal is a static face sealed o-ring which seals the optical window against the main body as shown in Figure 3.7, this method is also used with the ignition caps. Following BS EN 4518, standard o-ring sizes were selected to suit the geometries [14]. This also provided standard groove dimensions to follow, providing a correct fitting o-ring. A back up axially sealing o-ring was also included, this has an additional purpose of supporting the window to prevent metal to window contact which can cause damage to windows. Table 3.7 provides the dimensions used in the design for the o-rings.

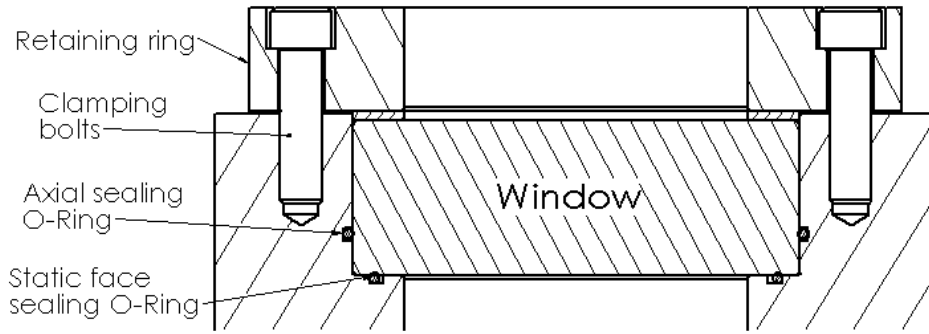


Figure 3.7: Cross-section showing the window sealing.

Table 3.7: O-ring selection and dimensions from BS EN 4518 [14].

O-ring Code	Internal Diameter [mm]	Cross Section [mm]	Location
1095-30	109.5 ± 0.5	3 ± 0.1	Ignition axial
1145-30	114.5 ± 0.5	3 ± 0.1	Window face
1195-30	119.5 ± 0.5	3 ± 0.1	Window axial

3.5 Bolt loading calculations

Each cap fixed to the main body will be subject to a pressure of 100 bar distributed across a 100 mm circular face. To account for the case in which an o-ring fails, the distribution used will be the full face of the window – 130 mm. The bolts are not pre-loaded and will be hand tightened. Further detail on assembly and disassembly is given in Appendix C.

$$Force = Pressure * Area \quad (3.16)$$

$$= 10.0 * 10^6 * \pi * (65 * 10^{-3})^2 = 132.2kN$$

This force is held by 12 equally spaced bolts, resulting in a force of 11.1 kN per bolt. Following the recommended design stress values from PD 5500 [18], alongside the metric bolt root areas in accordance with BS 3643-1:2007 [76], M12x1.75 Bolts were selected with a root area of $76.25mm^2$. The bolt design stress is,

$$\sigma = \frac{F}{A} = \frac{11.2 * 10^3}{76 * 25 * 10^{-6}} = 145.1MPa \quad (3.17)$$

This is within the recommended design stress values from Table 3.8-1 in PD 5500 for BS4882 grades B8MX at 100°C, 174 MPa therefore the safety factor is 1.18 [18]. Due to the fact the peak pressure will only be observed during combustion and will dissipate quickly, this was considered suitable.

3.5.1 Bolt elongation calculation

Due to the sealing arrangement a check was made to ensure the static face seal would not be broken in the maximum loading case as a result of elongations in the bolts.

$$dl = \frac{F \cdot L}{E \cdot A} \quad (3.18)$$

where F is the force on the bolts, L is the effective length, E is the Youngs' modulus, and A is the stress area.

$$dl = \frac{9.82 \cdot 45}{190 \cdot 76.25} = 0.0305mm \quad (3.19)$$

This is significantly lower than the extension required to break the o-ring seal as the o-ring is compressed by 0.8 mm.

3.6 Thermal expansion

The optical window is an area which needs to be considered in the case of thermal expansion. The clamped mechanism must constrain the window without causing additional stresses that may lead to cracking or a breakdown in the seals causing leaks.

Table 3.8: Combustion chamber material thermal expansion coefficients

Material	Thermal Expansion Coefficient (α m/m°C)
Stainless Steel 316	16×10^{-6}
Fused Silica	0.55×10^{-6}

The combustion chamber is rated to a temperature of 100°C. Assuming the chamber starts at room temperature, the change in temperature is 75°C. Using the following equations, the change in thickness and diameter can be calculated,

$$\text{Thermal Expansion, } \Delta l = \alpha \cdot l_o \cdot \Delta T \quad (3.20)$$

For the window clamping, in the axial plane (to the window) the compressibility of the o-ring and gasket sealing mechanisms allow for a large tolerance in assembly. The change in thickness at the maximum tolerance of the glass thickness of 45.5 mm results in a thickness increase of 1.88×10^{-3} mm which will be absorbed by compression in the sealing mechanisms. For the diameter of the window, the increase in diameter is 5.36×10^{-3} mm in comparison to the expansion of the stainless steel structure of 0.156 mm. The magnitude of the steel expansion coefficient is significantly larger than the fused silica, therefore the additional stresses caused by thermal expansion are avoided.

3.7 Simulation

A finite element analysis (FEA) of individual parts of the CVCC were completed alongside a full assembly simulation. Both the front window restraining cap and the side window restraining caps were analysed along with a blank ignition cap. The analysis was carried out with an internal pressure of 100 bar and a maximum design temperature of 150°C was assumed for each simulation. It was also assumed that the heating of the assembly was very gradual hence there are no thermal gradients across the wall thicknesses. There are a number of o-ring seals throughout the design which have not been modelled. The properties of the 316 stainless steel was modified to account for the elevated temperatures. Due to the temperature not exceeding 560 °C time dependent properties relating to creep were not considered.

Table 3.9: Material properties

Property	Value
Yield Strength 0.2% Offset	201 MPa
Tensile Strength	517 MPa
Elongation in 2"	53%
Reduction of Area	77%
Modulus of Elasticity (Tension) (Young's)	190 GPa
Modulus of Elasticity (Shear)	73 GPa

The maximum allowable design stress was calculated in 3.3.2 and given as 130 MPa. This section will describe the full assembly result for the FEA simulations. The single part results can be found in Appendix B.

3.7.1 Geometry

See Appendix A for the full unchanged geometry of the part. The geometry used has been simplified to improve the simulation results and avoid meshing singularities. The following details were removed; gas inlet and exhaust, o-ring grooves, instrumentation holes (thermocouple and pressure transducer) and a blank ignition plate was used. The whole assembly is sectioned to take advantage of symmetry to reduce computational time.

3.7.2 Boundary conditions, loading and meshing

All of the component parts are identified with contact interactions to ensure that when the load is applied it is transferred correctly. The inside face of the chamber is loaded with 100 bar pressure and the parts are connected to the main body via the bolt connection. The red arrows in the image represent the pressure load of 100 bar, the purple fixtures represent distributed bolt loading constraints, the yellow arrows represent a symmetry fixture, and the green arrows represent a fixed constraint.

Table 3.10: Mesh properties

Mesh Type	Solid Mesh
Element size	4 mm
Tolerance	0.2 mm
Mesh quality	High
Total nodes	788951
Total elements	547294
Maximum Aspect Ratio	27.342
Percentage of elements with Aspect Ratio < 3	99.9%
Percentage of elements with Aspect Ratio > 10	0.00164%

To understand the loading around points of interest such as the loaded faces

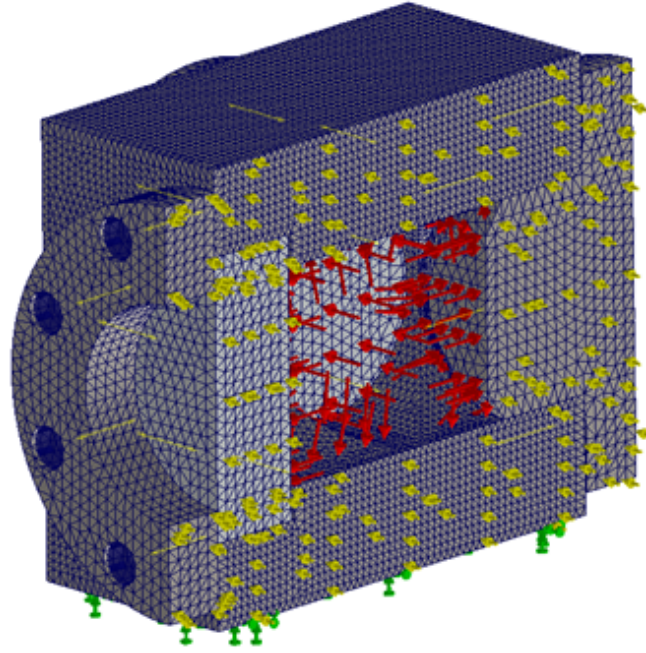


Figure 3.8: Boundary constraints, fixtures and loading constraints added to simplified main body assembly.

and bolts, the meshing was enhanced around these areas to 1.5 mm side length. This was performed after previous studies highlighted poor meshing in these areas of interest. This improved the percentage of elements with an aspect ratio of <3 from 96% to 99%. The meshing was prioritised on the main body with a 4 mm maximum element size.

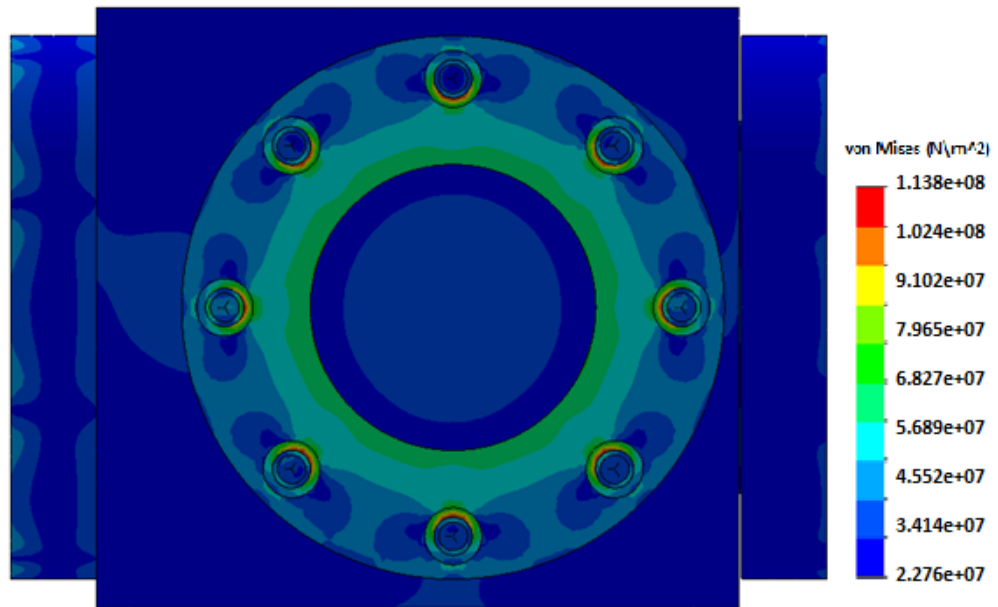
3.7.3 Results

Results of the stress concentration analysis is shown in Figure 3.9, the maximum stress observed by the assembly under 100 bar of pressure is 113.8 MPa, this was below the allowable design stress calculated previously of 143 MPa. It is important to note that the high values of stress are seen at the bolting positions, these are expected due to the modelling of bolt loads in the software causing singularities and are expected to be over-approximated by the simulation. The other more significantly stressed

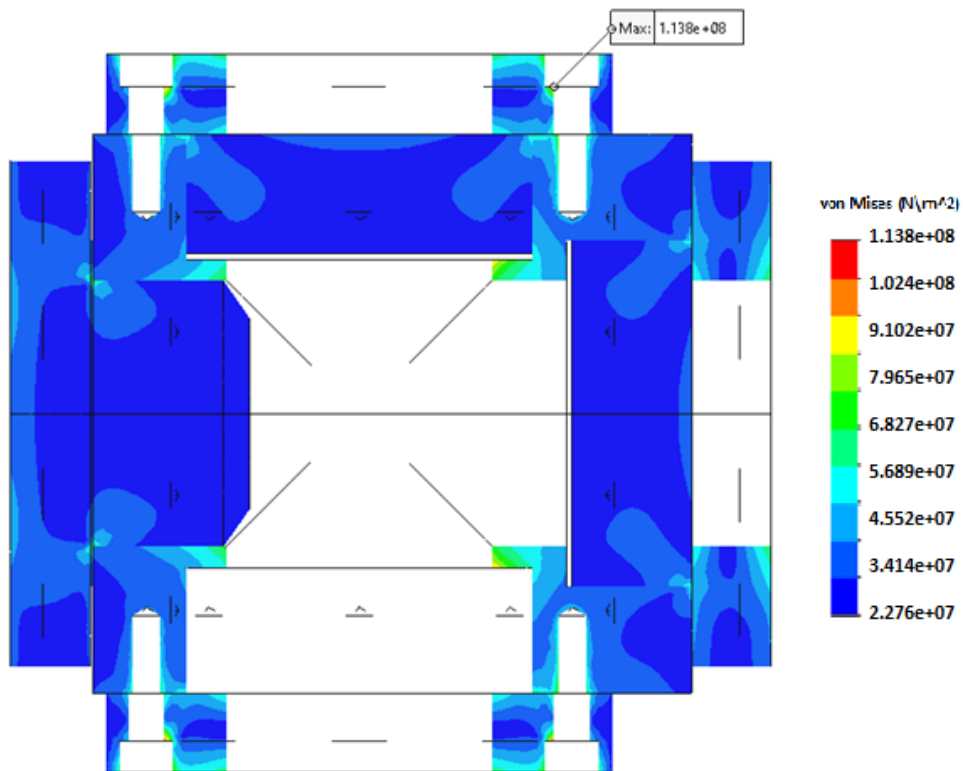
region was the inside corner of the main body between the front window and the side window. The maximum predicted stress was 89.7 MPa, equating to a safety factor of 1.7. Although lower than the general model, an overstress in the instance of a peak 100 bar pressure spike would not affect the sealing capacity of the system, nor put risk onto the user. As a result, this was decided to be sufficient. The deformations of the part are provided to illustrate how the structure will perform under load, shown in Figure 3.10, they are exaggerated to help demonstrate the mechanisms that cause these movements. They also provide a sanity check for the simulation result. Stress intensity is also shown throughout the analysis. The stress levels are compared against the allowable limits of stress intensity of the material. It was found that all of the components had stress levels below the limits given in 3.3.2. The lowest factor of safety for each component is tabulated below.

Table 3.11: Finite element analysis results per component.

Part No.	Component	Safety Factor	Max Stress [MPa]	Deflection [mm]
P001	Main Body	1.9	104.5	0.02226
P002	Ignition Cap	2.6	76.3	0.04021
P003	Side Window Cap	2.2	91.4	0.05775
P004	Front Window Cap	2.4	84.4	0.05424



(a)



(b)

Figure 3.9: Von Mises stress plots; (a) side view, (b) top-down section view.

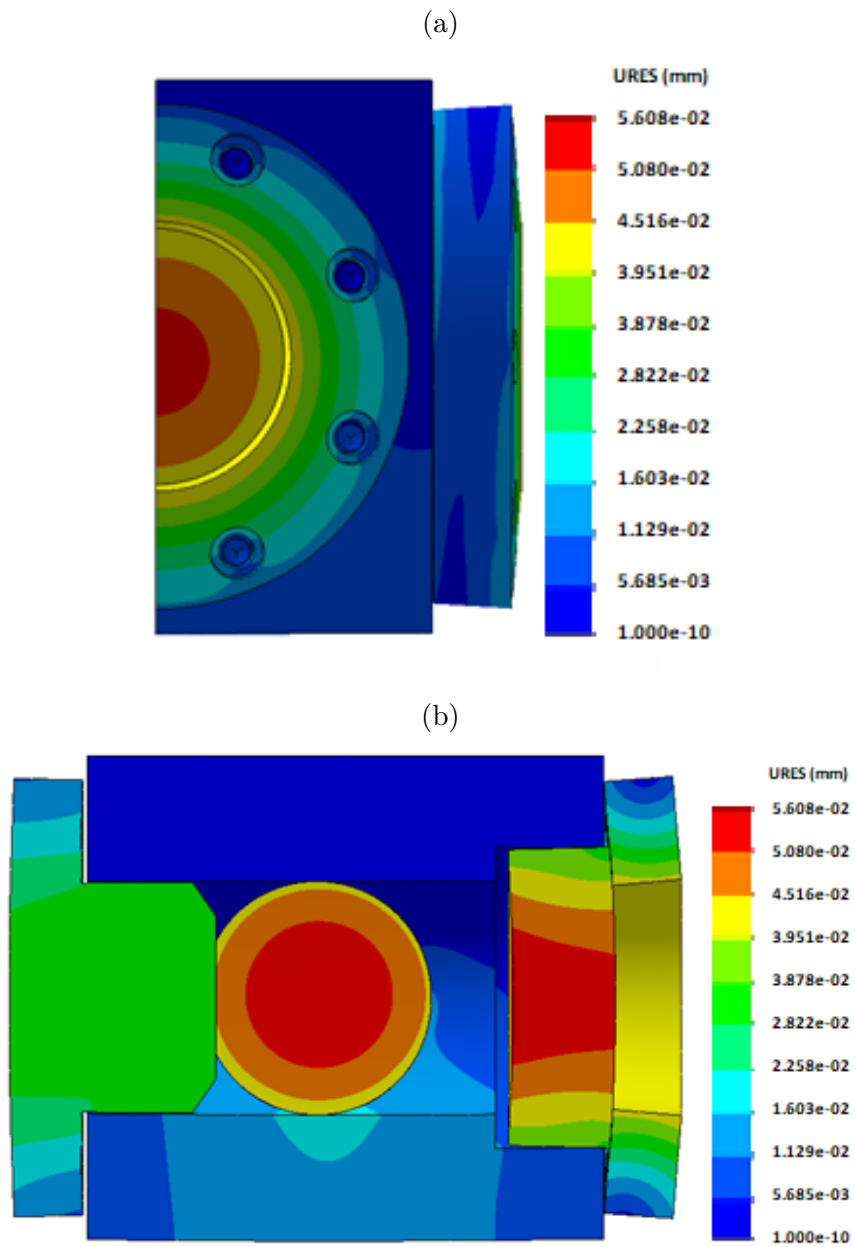


Figure 3.10: Exaggerated deformation plots (a)front view (b)side section view.

3.8 Instrumentation and control overview

In order to meet the design requirements, the test rig must provide sensitive gas mixture control, temperature control, and accurate instrumentation to support data acquisition. Alongside this the rig must be safe and provide a level of redundancy against potential over-pressures. The following section details the key design decisions that were made around the test rig as well as providing an overview of the instrumentation and control of the rig.

3.8.1 Air fuel mixture control

The equivalence ratio of the combustion mixture is controlled using Dalton's Law of Partial Pressures. This law states that, in mixture, the total pressure of a mixture of gases or vapours is equal to the sum of the partial pressures of its components. Utilising fine gas pressure controls alongside pressure transducers, the accuracy of the equivalence ratio control was within 1% of the desired target ratio. This technique is used in many examples of similar test rigs [98, 161, 173].

This principle relies on the initial volume of gases to be known in the mixture, as a result post combustion, the chamber must be prepared by flushing the system with nitrogen, then compressed air and then vacuuming down to ensure the level of contaminants in the volume was kept to a minimum. The flush, vacuum process was cycled three times to below 0.1 bar resulting in a contaminant concentration of less than 1% in the initial mixture. This assumes that the mixture is in a homogeneous state.

Table 3.12: Vacuum purge cycling contaminant concentration per iteration.

Contaminant Pressure	Flush Gas Pressure	Total Pressure	Vacuum Pressure	Contaminant Concentration
1	0	1	0.1	100%
0.1	0.9	1	0.1	10%
0.01	0.99	1	0.1	1%

Other experimental setups are known to use mass flow meters to dictate the quantity of fuel and air [41, 94]. In these setups, the desired fuel quantity is input into the system and the mass flowmeter will automatically fill the chamber to that point. This system is not as common and as mass flow controllers are intended for flow applications, not specific filling applications, the partial pressure method was chosen.

3.8.2 Temperature control

One of the systems requirements was to be able to control the temperature of the combustion air, ranging from room temperature up to 100°C, within a reasonable time frame of up to 1 hour. Various techniques have been documented in literature and the following methods are discussed in the subsequent section;

- Direct Charge Heating
- Passive Body Heating/Indirect Charge Heating
- Pre-combustion Heating

Direct charge heating utilises cartridge heaters placed inside the combustion chamber to rapidly heat the charge to a desired temperature in conjunction with a thermocouple [7, 40]. This method is suitable for some

applications however with highly combustible premixed volumes, the surface temperature of the cartridge can be an ignition source. Furthermore this method does not allow for accurate control of the wall temperature of the vessel. This lack of control can be alleviated using insulation and a longer warm up time however there is also risk of the heaters degrading faster due to their exposure to the combustion events.

Passive body heating or indirect charge heating utilises the thermal mass of the chamber to heat the internal volume. There are three ways that this can be done, placing the entire chamber into a temperature controlled environment such as an oven [52], fitting cartridge heaters into the wall and using external heaters pads/tape [128, 174]. This method is slower than using the direct heating however results in smaller temperature gradients and more homogeneous heating across the chamber. It also allow for better control of the wall operating temperatures. Embedding cartridge heaters into the chamber walls can cause some issues with large temperature gradients especially in designs with larger windows, this can result in warping and undesirable stresses in the window risking damage. The window ports can be designed to account for this with expansion spaces.

Pre-combustion heating is used more in fuel spray studies, it uses a preliminary combustion of a lean combustible mixture to cause a high temperature and pressure rise. In a short time after this, the fuel is then sprayed into the environment. This method can achieve high temperatures and pressures quickly however there is the added complexity of the post combusted products to account for in the charge mixture. As a result it is only suitable for fuel spray analysis [4]. The method that was selected was externally heating the chamber using heat pads, although the slowest method of heating due to the thermal mass, once up to temperature this method provides homogeneous wall temperatures which enables future studies into wall in-

teractions. The chamber was also wrapped in insulation to aid with the warm up speed and prevent heat loss to the surroundings.

In order to calculate the power of heaters required a simple calculation of the thermal mass of the combustion chamber was used. Stainless steel 316 has a specific heat capacity of 500J/kgK , assuming the chamber is a solid steel block of weight 80kg , the thermal mass is 40kJ/K . In order to raise the temperature from room temperature to $100\text{ }^\circ\text{C}$, the total heat energy required is 3000kJ , this is not taking into account any heat losses. To heat the chamber to this temperature in one hour, would require 1kW of heat input. Four 750W heaters were purchased, providing a total of 2.8kW of heating power. The heaters were overpowered to reduce utilisation and therefore increase longevity of the heaters as well as to account for heat losses. They were placed on the top and bottom side of the chamber with thermal paste between to enable effective heat transfer and improved temperature distributions. The temperature was controlled using a PID controller to maintain the correct temperatures. In addition to the heaters, during higher temperature trials the chamber will be wrapped in an insulating blanket.

3.8.3 Settling times

After the charge has been injected into a chamber, there is likely to be a presence of turbulent flows/swirls inside that volume that can affect the ignition event if not allowed time to dissipate. These flows lose energy quickly and only require a few minutes to settle as shown by Milton [110].

Furthermore, when filling the chamber, the internal gases will increase in temperature. As the equivalence ratio control is governed by Dalton's law

of partial pressures, an imbalance of temperatures between the gas filling will result in errors in the equivalence ratio. To minimise the errors, the temperature increase is reduced by slowly introducing the pressure into the chamber, this allows the rise in temperature to dissipate. The dwell or settling time is therefore constrained by the time taken for the temperature to decrease. Considering literature values for similar sized chambers, a settling time of 2 minutes was suitable [62, 80, 123, 140, 158]. The testing within this reported work was all completed at 25 °C. In order to achieve this, after the temperature increase as a result of the final compressed air filling step, the operator would wait until the in-chamber temperature would drop to 25 °C and then combust the mixture. For future work, in the case where the ambient temperature is too low to achieve this, the heaters may be used. In the rare instance where the ambient temperature is too high, the 25 °C testing cannot be completed.

3.8.4 Moisture control

Combustion events involving oxygen and hydrogen species will form water as one of the products, initially due to the flame temperature and pressure this water will exist in the form of water vapour. However when the water interacts with a cooler surface, it will condense into liquid form. It was found that this water built up enough to require removal after 3 cycles as the condensate on the window distorted the view. The residual water can potentially influence the concentration of the initial fuel mixture in cases where the fuel is soluble or can react with water. Ammonia is especially susceptible to this, forming an aqueous ammonia solution resulting in a decreased amount of ammonia able to combust leading to inaccuracies in fuel concentration. To alleviate this issue the temperature and vacuum were

used to remove the water. By vacuuming the chamber to less than 0.05 bar the resultant vapour pressure of water is 32°C. Once this temperature is achieved the water would evaporate and be captured in a water trap to protect the vacuum pump. The volume was then cycled once it was visibly dry to ensure correct concentrations of the initial mixture.

3.8.5 Ignition of the charge

The spark ignition system used consists of a NGK Racing Spark plug R0465B-10 used in conjunction with a P-100T Bosch Ignition Coil [9]. The ignition coil has four pins. Two pins are wired to a power supply that is able to alter the voltage, providing variability in the spark energy. The remaining pins are wired to the National Instruments DAQ NI9401 which sends a 5V TTL signal charging the coil. The coil will collapse and release the charge on the trailing edge of the TTL signal. The charge time is also variable providing another method to vary the spark energy.

3.8.6 Instrumentation

Figure 3.11, provides an overview of the locations of the chamber instrumentation. The following section details further information about the selection of said instrumentation;

- Four k-type thermocouples located 20 mm protruding into the chamber for in-chamber gas temperature measurements, 5 mm from the chamber wall for wall temperature measurements, under one of the heaters for external wall temperature measurements, and an ambient sensor.

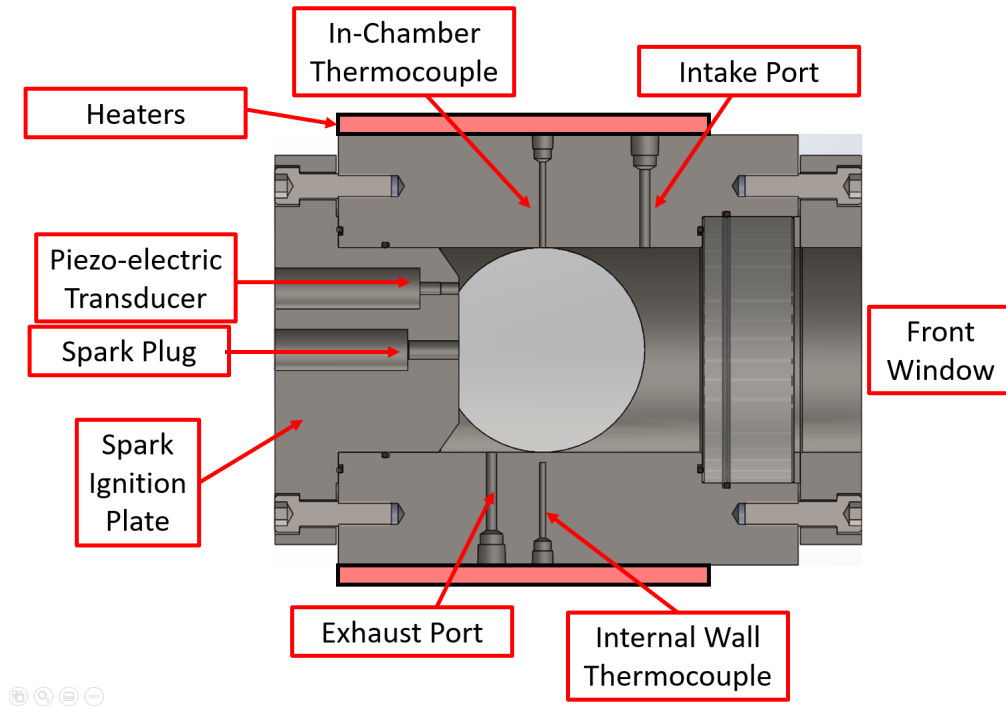


Figure 3.11: Side-on cross-section of the combustion chamber showing the location of key instrumentation and heaters.

- Two piezoresistive pressure transducers were used on the gas inlet system, one for measuring fine fuel pressures up to 0.7 bar, and one for the final mixture pressures up to 10 bar.
- A high frequency piezoresistive pressure transducer for measuring the combustion event at high speeds.

Mineral insulated k-type thermocouples were used, as there was no intention for fast gas temperature measurements in these experiments. The temperatures output by the thermocouples provide the user with information around gas temperatures, and initial temperatures pre-combustion. These have a response time of 0.300 seconds [148] and an accuracy of $\pm 1.5^\circ\text{C}$ following IEC60584-1. Chen [22] utilised numerical simulations to evaluate the impact of temperature fluctuations, showing that the laminar burning velocity deviated by $\pm 2\%$ under $\pm 3\text{ K}$ temperature variation.

The two piezoresistive transducers were used to monitor the gas inlet pressures. Both sensors were premium grade UNIK5000s with an accuracy of 0.04% of the full scale with a range of 0 - 0.7 bar for the fuel measurement and 0 - 10 for the initial combustion pressure measurements. The 0 - 0.7 bar transducer had an error of $\pm 2.8 \times 10^{-4}$ bar and the final mixture pressure, measured with the 10 bar transducer had an error of $\pm 4.0 \times 10^{-3}$ bar.

A PCB 112B05 piezoelectric transducer alongside an inline charge converter (PCB 422E53) was used in this set up. The output of the charge converter was 1 mV/pC with a ± 5 V output was connected to a power conditioning unit (PCB 480C02) to output to the DAQ module. This enabled pressure measurement up to 350 bar. Due to drift in the transducer measurements, prior to combustion the transducer will calibrate against the 10 bar UNIK5000 transducer. Considering the sensitivities of the piezoelectric transducer, the in-line charge converter and the power conditioning unit alongside the error in the UNIK5000 transducer, the combined error in this sensor was ± 0.063 bar. The sensor was flush mounted inside the combustion chamber, and due to its sensitivity to thermal shock and exposure to the high temperature flame front, the sensor was covered to ensure accurate measurements. Figure 3.12 shows the difference between two identical combustions, one with no protection for the transducer and the other with. As the graphs show, the uncovered sensor indicates a significant drop in pressure below zero, this is due to the piezoelectric crystal expanding as a result of exposure to the flame resulting in an inaccurate reading.

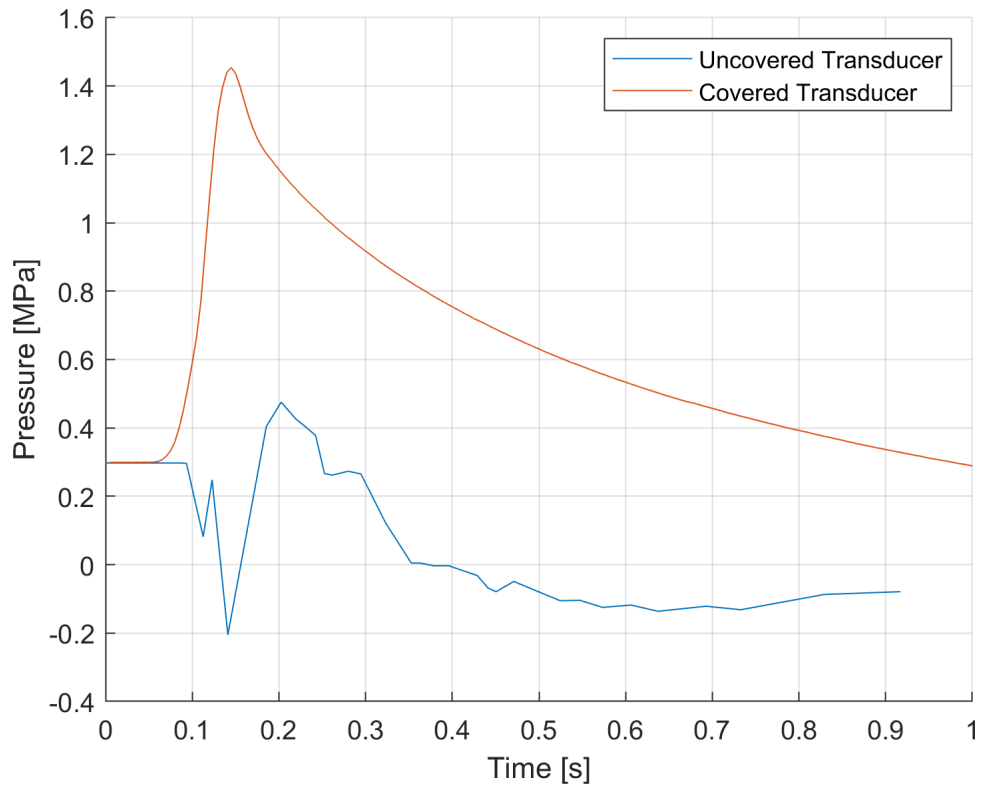


Figure 3.12: Comparison of two combustions with the pressure transducer protected from the thermal shock and uncovered.

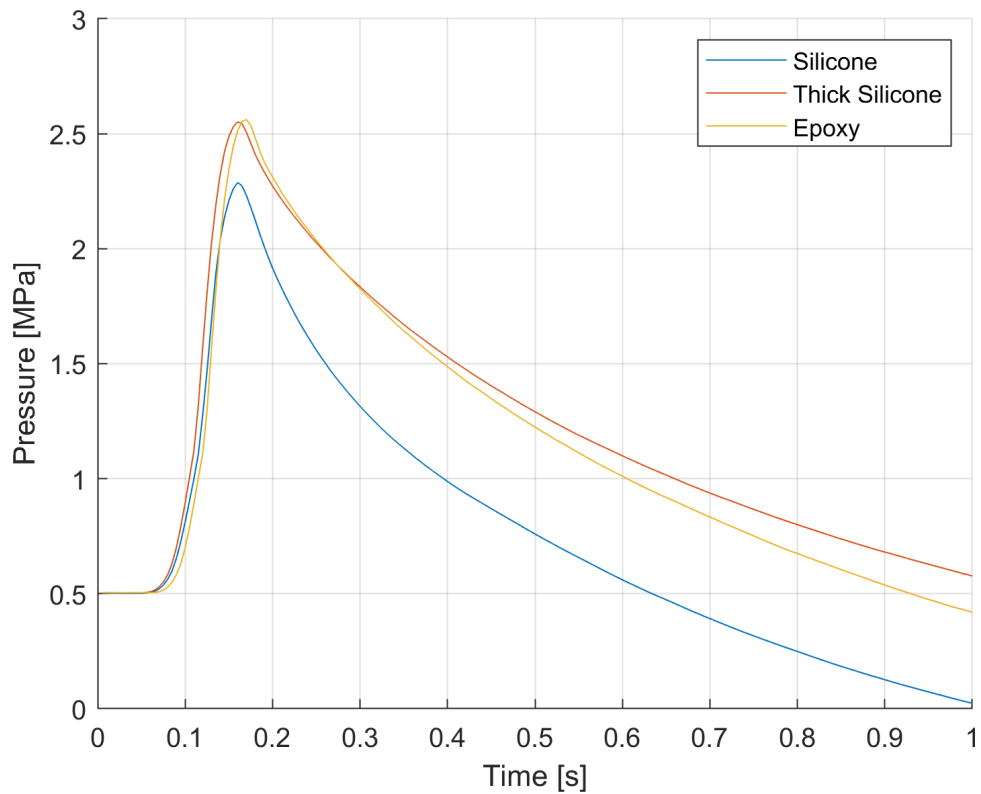
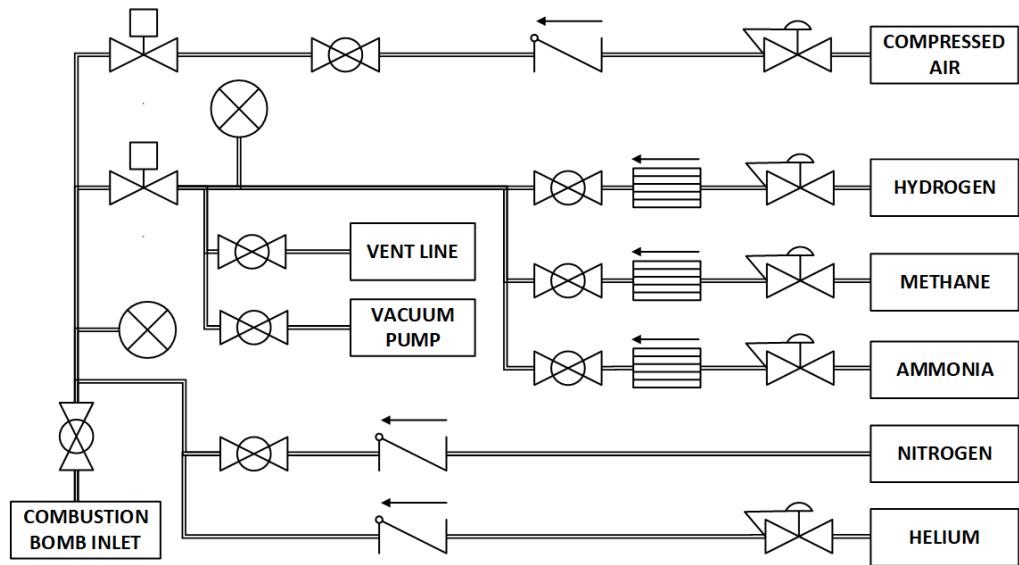


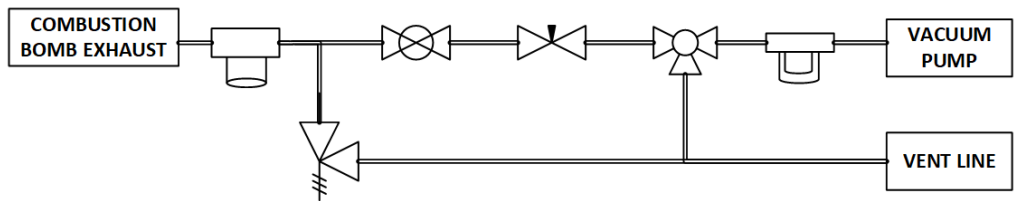
Figure 3.13: Comparison of different thermal shock protections used on the piezoelectric pressure transducer.

In order to ensure the covering used on the piezoelectric sensor was suitable, a number of tests were completed the results of which are shown in Figure 3.13. Three different materials were used to cover the sensor to understand their ability to prevent the thermal shock. The three materials used were; a thin layer of thermal silicone, a thin layer of epoxy and a thicker layer of silicone supported by a metal ring. The pressure traces show the ability of the materials to delay the thermal shock, allowing the pressure rise to be recorded before the heat transfer interferes with the reading. The thick silicone was selected as the cover.

3.9 System schematics

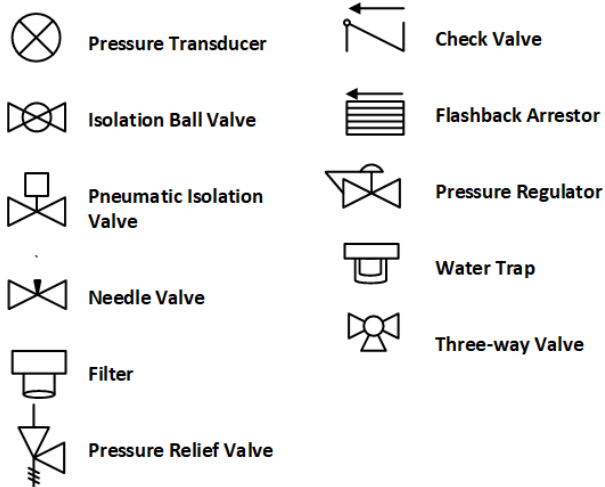


(a) Gas intake system.



(b) Gas exhaust system.

KEY



(c) Key for system schematics

Figure 3.14: Combustion chamber intake and exhaust schematics.

3.9.1 Intake System

The gas intake system must be able to handle both the oxidiser, in this case, compressed air, and the various fuels. It also required fine control and instrumentation of the gas pressures in order to minimise any errors in the equivalence ratio calculations using Dalton's law.

The system, shown in 3.14a consists of;

- two interlocked pneumatic valves to prevent unintended mixing of a fuel and an oxidiser in the line.
- a 0.7 bar pressure transducer on the fuel line to enable fine control of the fuel gas pressures when filling.
- a 10 bar pressure transducer just before the chamber inlet to control the pressure of the compressed air intake.
- flashback arrestors on each of the fuel lines to prevent any flames travelling back to the fuel source.
- a check valve on the compressed air line to prevent any back flow of gases.
- a nitrogen input to be used as an inert gas in purging fuel lines and the combustion chamber post combustion.
- a helium input to be used in the case where the combustion chamber has been dismantled. It is a very small molecule and used commonly for hydrogen leak testing.

The fuel line is able to be isolated from the combustion chamber, flushed with nitrogen and vacuumed down. This enables multi-fuel operation. The

pressure regulators were sized based on the requirements of a rich mixture of each fuel at 10 bar. This enabled fine control across the region of desired pressures whilst still allowing a maximum if needed.

Table 3.13: Gas pressure regulator settings

Gas Line	Pressure Setting [bar]
Compressed Air	10
Hydrogen	1.5
Methane	1.5
Ammonia	3.5

3.9.2 Exhaust system

The exhaust system must be able to handle high temperature and pressure post combustion gases as well as provide protection for the combustion chamber in the case of over-pressure. The system, shown in 3.14b, consists of;

- an inline filter, intended to remove any particulates from the gas flow, preventing damage to valves.
- a pressure relief valve set to 75 bar to prevent any risk of over-pressure in the chamber.
- an isolation ball valve to isolate the system during combustion events.
- a needle valve to enable controlled venting of high pressures post combustions.
- a three-way valve directing either to the vacuum pump or the vent line, this protects the vacuum pump from high inlet pressures.
- a water trap on the vacuum line to prevent any water vapor from building up in the vacuum pump.

3.10 Data acquisition and processing

A 4 channel, cDAQ-9174, CompactDAQ chassis from National Instruments was specified with modules that sample the pressures, temperatures, and output the signals for the camera and spark control. The unit held four modules detailed in Table 3.14. The thermocouple outputs were input directly into a dedicated temperature input module via mini-TC slots sampling at a rate of 70ms per channel which is significantly faster than the thermocouple response time. Each of the pressure signals were recorded using a 100 kS/s/ch simultaneous voltage input module, this provides high resolution pressure traces for the in-chamber combustion. Finally a 5V digital input output module with a 100 ns rate was used to send the TTL signals to both the camera and the spark plug, the high speed of the card provided extremely accurate control of the spark timing which was only required to be within 0.1 ms.

Table 3.14: National Instruments DAQ modules

Part No.	Description
NI9210	4-Channel Temperature Input Module for thermocouples
NI9215	± 10 V, 100 kS/s/ch, 16-Bit, Simultaneous Voltage Input, 4-Channel for each of the pressure signals
NI9401	5 V/TTL, 8 Bidirectional Channels, 100 ns Digital Module for camera trigger and spark trigger signal.

A dedicated LabView program was used to read the inputs from the DAQ via a USB connection; the dashboard is shown in Figure 3.15. The program makes it very simple for the user to set-up, initiate and record combustion events. It also includes a calculator to help the user determine the correct gas mixture as well as real time monitoring of temperatures and pressure conditions to fill the chamber to the desired amount. It is also possible to regulate the spark charge duration and the recording time.

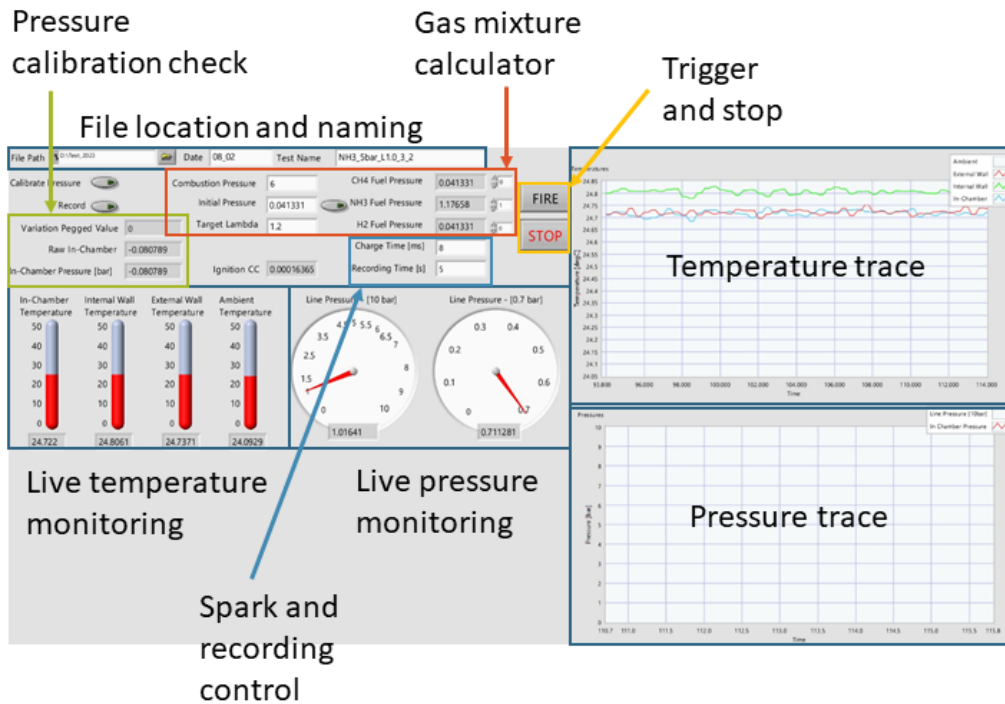


Figure 3.15: Screenshot of LabView dashboard.

3.10.1 Data processing

The LabView code outputs a .txt file with the recorded high speed data. The headings of this data are

- Time (s) - The time allows for both synchronised high speed data as well as synchronisation with the flame speed images.
- Line pressure (bar) - [10 bar] - This line pressure is used to ensure the initial combustion pressure is correct, it is isolated from combustion.
- Line pressure (bar) - [0.7 bar] - This line pressure provides the final fuel pressure, it is also isolated from combustion.
- Ignition current clamp (amps) - A current clamp is used for diagnosis to ensure the spark plug has fired.
- In-chamber pressure (bar) - This is the pressure output from the

piezoelectric in-cylinder transducer.

- Ambient temperature (°C) - This temperature is the monitor of ambient conditions.
- External wall temperature (°C) - This temperature allows monitoring of the heater control.
- Internal wall temperature (°C) - This temperature is from a thermocouple 5mm away from the chamber walls.
- In-chamber temperature (°C) - This is the in-chamber temperature, although slow sampling it provides a true reading for initial temperature.
- Initial pressure (bar) fuel 1 - This is trigger by the user to capture the fuel filling information to calculate equivalence ratio.
- Initial pressure (bar) fuel 2 - This is trigger by the user to capture the fuel filling information to calculate equivalence ratio for fuel mixes.

In order to process the data further, a MATLAB script is used. The code has multiple functionalities including processing the high speed data text file output, calibrating the image analysis code, importing and processing the high speed flame images, and post processing the results. The image analysis code will be described further in Chapter 4. When processing the high speed data, the code calculates initial fuel and air pressures to provide a true equivalence ratio value, it also find the maximum pressure from the in-chamber transducer. The pressure traces are able to be aligned to the flame images using this code.

3.11 Conclusion

The final design selected for the combustion chamber consisted of a 210 mm wide by 210 mm high by 225 mm deep block of 316 stainless steel which was machined to incorporate two 100 mm diameter bored cylinders. The internal volume of the chamber is 1.2 L. Detailed drawings of the design can be found in Appendix A. One side of the chamber was elongated to accommodate an ignition plate, from which the combustion is initiated. The chamber includes the option for three windows which are constrained using port-hole style retaining rings or end caps fixed using 12xM12 bolts. The window configuration enables multiple imaging techniques such as schlieren and laser based imaging techniques.

The chamber was verified to BSEN 13445:2021[16] using both simulations and hydro-static testing to 143 bar - see Appendix B for further detail. The over-pressure was to emulate the higher temperature properties of the steel. The materials of the chamber were selected with material compatibility in mind considering the desired fuels - ammonia, methane, hydrogen and diesel. Stainless steel 316 was chosen for the main body due to its high strength and high resistance to corrosion. The modular design allows for variation in the testing equipment with blank faces, quartz windows and instrumentation faces. It also allows for variation in the design of the ignition head enabling multiple ignition techniques to be investigated.

The chamber was fully instrumented with thermocouples measuring the temperature inside the chamber, at the chamber internal and external walls as well as ambient temperature. Alongside this the internal pressure is measured using a high frequency piezo-electric pressure transducer. The location of the instrumentation can be found in Figure 3.11. Two piezo-

resistive pressure transducers were situated on the fuel and air intakes to enable very fine control of the gas mixture and equivalence ratios - shown in Figure 3.14a. The heating system provides 2.8 kW of energy to the system, which is able to heat the chamber up to 100 °C using a PID controller which regulates the temperature to within 0.2 °C. This was verified with calculations, however future work will fully confirm this.

Chapter 4

Analytical Techniques

The optical access in the combustion chamber is key to developing a comprehensive understanding of the fundamental flame characteristics observed during the combustion events. This chapter delves into the analytical techniques employed for the flame speed analysis in the combustion chamber, offering insight into the methodologies developed to extract valuable information from the experimental data.

Provided in this chapter is detail about the imaging equipment used in the studies including the setup and calibration as well as walking through the image processing codes. The image processing codes were developed to extract meaningful data such as flame speed, vertical centroid movement, shape ratio, and wrinkle factor. A dedicated section focuses on uncertainty in the imaging, assessing potential sources of error and strategies for minimising their impacts.

4.1 Imaging setup

The combustion chamber was designed with multiple optical access ports, facilitating three different angles for flame capture. These ports will also enable advanced imaging techniques such as schlieren imaging. The design provides a degree of flexibility in capturing the flames from different perspectives, providing comprehensive insights into the combustion process. For the initial experiments, described in Chapter 5, natural light flame imaging was used. This techniques relies on the flame's inherent luminosity to capture its progress. Presented in Figure 4.1, the combustion chamber's optical setup with the high-speed camera.

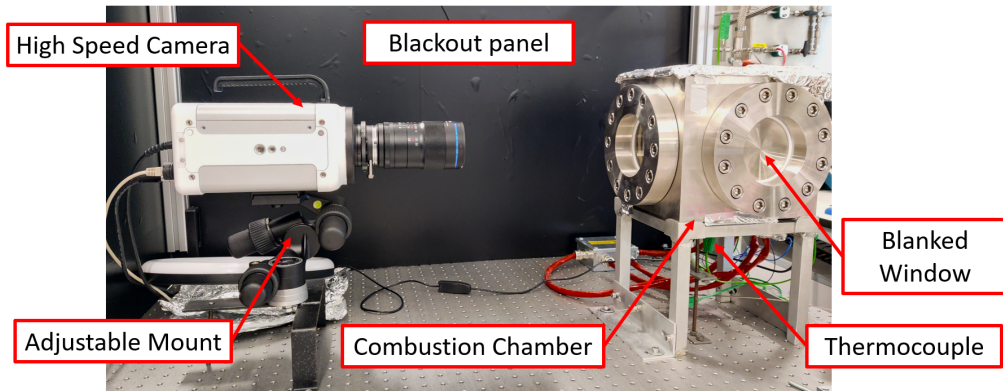


Figure 4.1: Image of the constant volume combustion chamber optical setup with the high speed camera.

Hydrogen flame speeds have been observed to be 1.5 m/s for room temperature and pressure flames at a stoichiometric ratio. As a result, a minimum frame rate of 5000 frames per second was set to capture at least 100 frames of the flame expansion [6]. A Photron FASTCAM NOVA S9 was selected, featuring a 1-Megapixel CMOS sensor capable of capturing 9,000 frames per second at full resolution (1024 x 1024) [122]. The square sensor maximised the number of useful pixels available in the images, as other options available were 16:9 aspect ratios which would lead to a higher number of

wasted pixels. The camera's light sensitivity was a crucial consideration. At high frame rates, there is less time for the shutter to capture the light from the event, this results in darker images. The selected camera operates in monochrome with an ISO of 64,000. The camera was also able to reduce resolution in order to capture at higher speeds, with 640 x 640 resolution being able to capture 20,000 frames per second.

The camera was positioned to give a field of view of 100 mm, which takes advantage of the camera's full resolution with a resultant pixel ratio of 0.100 mm/pixel. This resolution was more than sufficient for the flame imaging and similar to the majority of papers [10, 57, 139]. Three optical ports in the combustion chamber offer versatility. For the studies performed in this thesis the front facing view was used, as shown in Figure 4.3. While the front-facing view was utilised for initial studies, two side views enable potential setups for schlieren or laser measurements in future investigations.

The camera was connected to the control PC via an Ethernet connection, this enables control and configuration via the manufacturers PF4V software. The initial settings are prepared within this software including the frame rate, shutter speed, and filenames. Additional features include image measurement tools and focus assistance, ensuring optimal camera settings before initiating any testing.

During natural light flame imaging, in order to prevent any ambient light impacting on the imaging or introducing unwanted reflections, the chamber was enclosed in a blackout structure. This ensured the imaging was completed in darkness and the only light captured was from the flame. To eliminate any interference from ambient light or unwanted reflections, the chamber was enclosed in a blackout structure. This arrangement guaranteed that the imaging occurred in complete darkness, allowing the camera

to capture only the light emitted by the flame. The blackout panel can be seen in Figure 4.2.

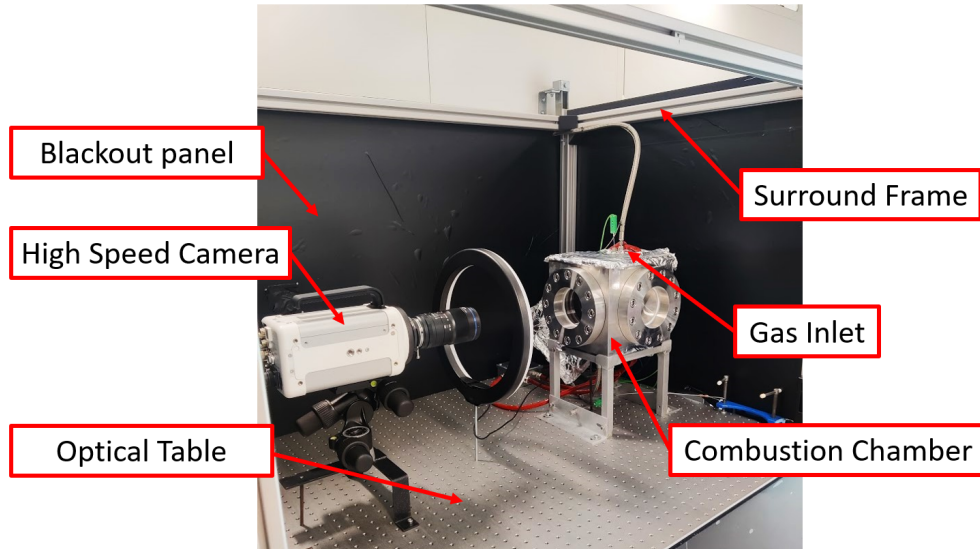


Figure 4.2: High-speed camera setup with blackout frame.

4.1.1 Image calibration

Image calibration is essential to account for any movements in the camera set up, ensuring consistency and accuracy in subsequent image processing. A calibration image was captured using the PF4V software. In order to provide a completely clear image of the bore and make it possible to identify important characteristics, the calibration image needed to have background illumination at appropriate levels. The image serves as a reference for the spatial resolution determination, the spark centre, the cropped region, and the diameter of the outer circle. Figure 4.3 shows the output from the calibration code.

Shown as the blue dashed square in the image, the search area was defined by the user for the spark plug and outer ring identification. The spatial resolution was calculated by binarising the image, and utilising MATLAB's

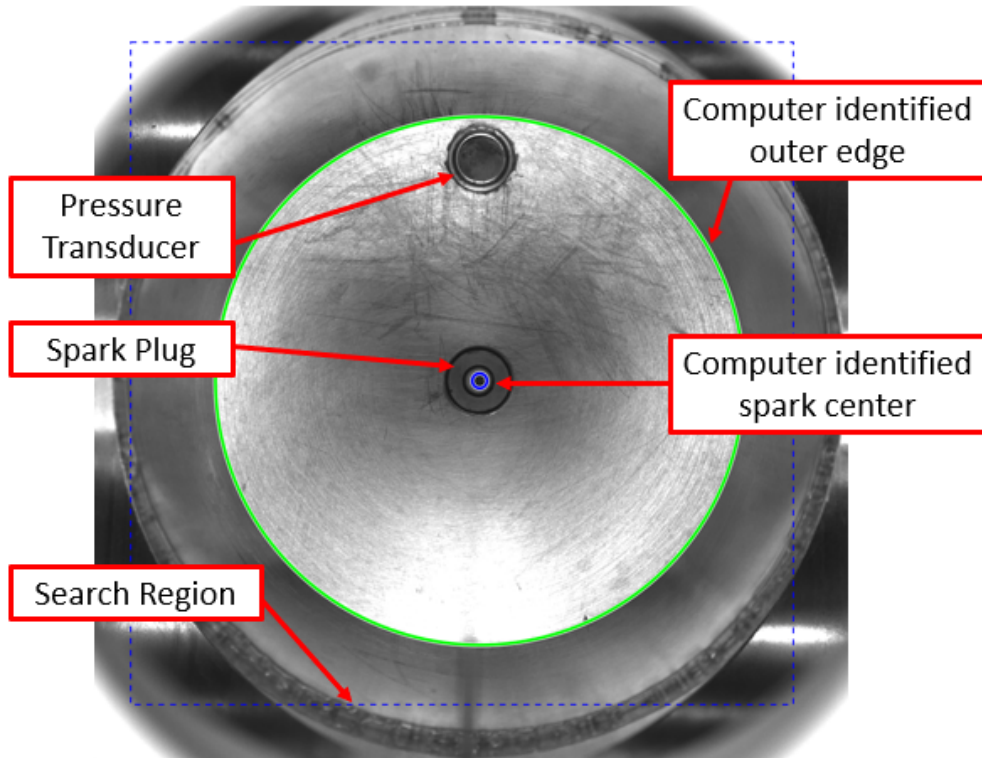


Figure 4.3: Pixel calibration and spark center check, calibration code output.

'**regionprops**' function to identify regions, their centres, and bounding boxes. The outer ring, identified by the code and shown as the green circle, was a known diameter of 72mm, this was used to determine the resolution in mm/pixel. The spark centre was also identified on the image as the blue circle, this was used in subsequent processing code to identify the spark initiation point.

4.2 Image processing

The following section outlines the computational steps involved in processing the flame images and extracting the relevant flame properties. After the initial flame image calibration, the code utilises the outputs to import, enhance, and interpret the raw TIFF files. The image processing code can

be split into the following sections; image adjustment and filtering, flame edge healing and binarisation, and flame property acquisition.

4.2.1 Image adjustment and filtering

In order to increase the computational speed of the code, the initial image is cropped and masked to remove any unwanted peripheral information and prevent reflections impacting the flame edge identification. The images are brightened using the **imadjust** function and a Canny edge filter is applied. The Canny edge detection algorithm applies a derivative of Gaussian filter to compute the image gradients. The method uses two threshold values to detect strong and weak edges, including the weak edges if they are connected to the strong edges. By using the two edges the method is less likely to interpret noise as an edge. Due to the nature of some of the flames, the coefficients were required to be adjusted for varying fuels and in some cases equivalence ratios. The steps taken are shown in Figure 4.4. A side-by-side comparison of an ammonia and ammonia-hydrogen flame is shown in Figure 4.5, there is a clear difference in both edge strength and flame brightness for the two. The interpreted flame edges were output to enable operator review and reconfiguration in the case of noise being interpreted, the flame edge can be seen in blue in Figure 4.6.

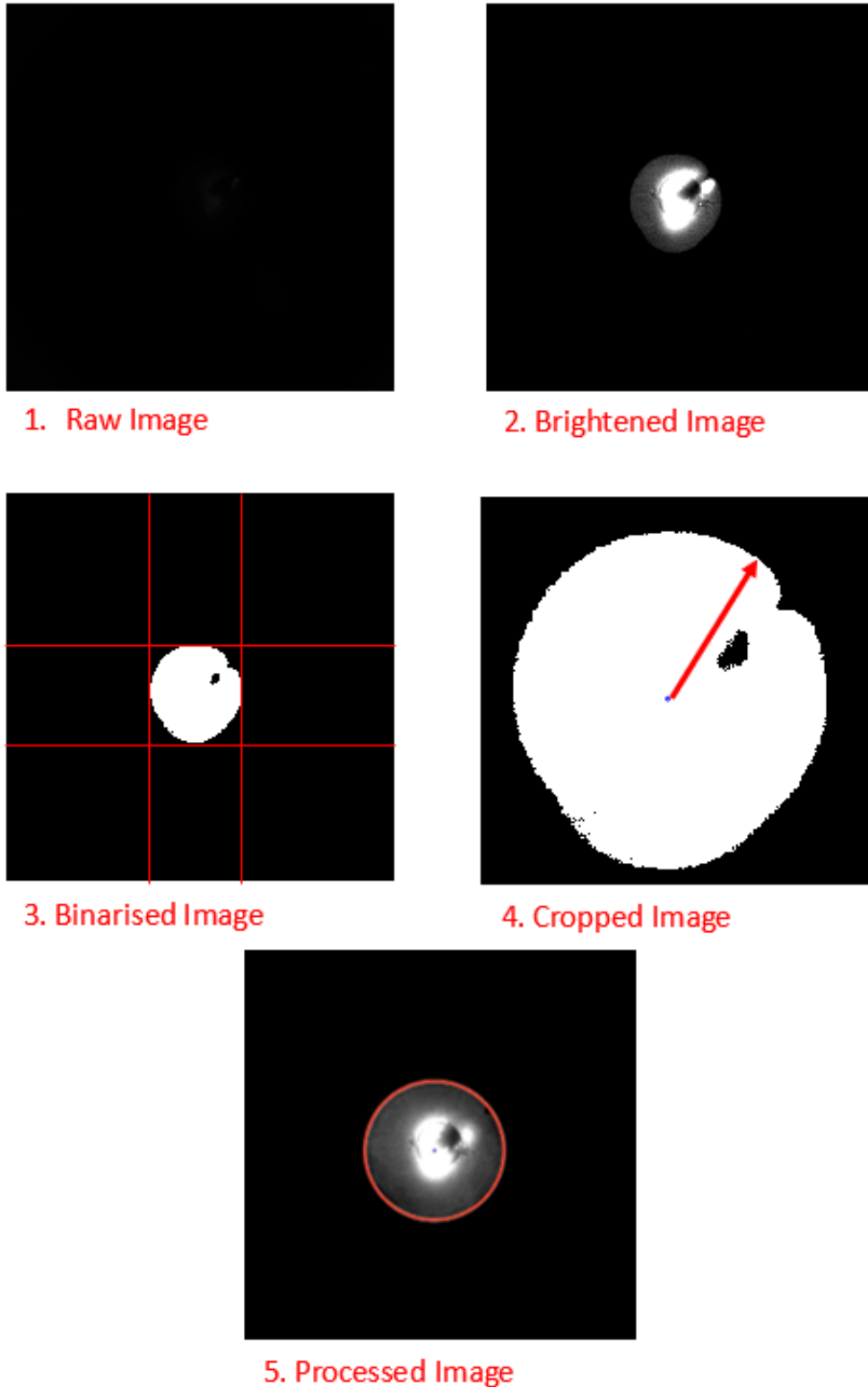


Figure 4.4: Image processing steps: 1.Raw TIFF image taken directly from high speed camera with no processing. 2.Image is brightened for ease of processing to find edge. 3.Image is binarised for edge detection and region-props function. 4.Flame boundary is identified to calculate wrinkle factor, radius and flame speed. 5.Processed image is output with flame edge identified for checking.

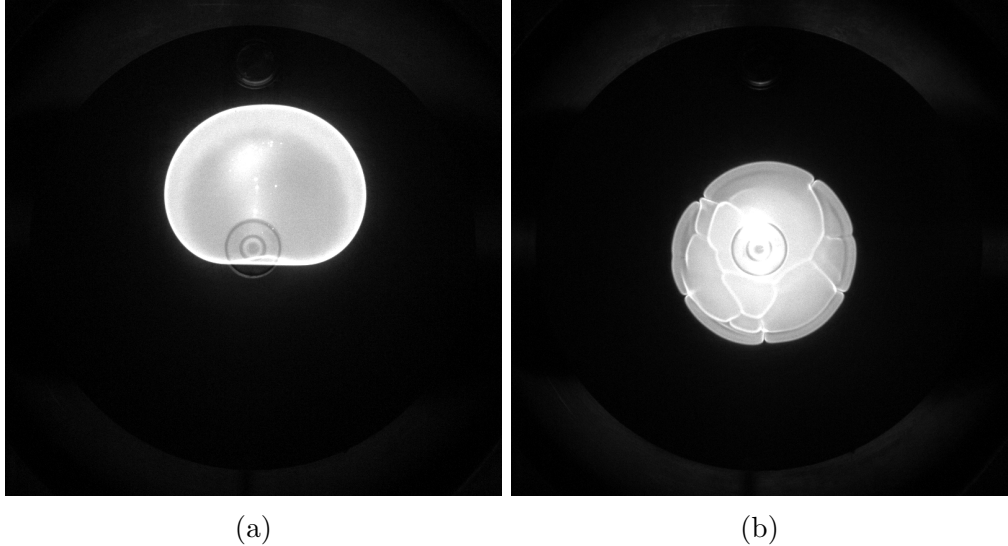


Figure 4.5: (a) Ammonia-air flame at 0.5 MPa, $\phi = 1.0$, (b) Ammonia-hydrogen-air flame at 0.5 MPa, $\phi = 1.0$, SR = 0.5.

4.2.2 Flame edge healing and binarisation

Due to some reflections on the pressure transducer, there were some instances where the flame was misidentified. To prevent this occurrence, the pressure transducer position was masked in the flame image, this excluded it from subsequent calculations. The masking of the transducer reflection provides accuracy for the flame speed measurements as it removes misrepresentation of the flame boundary. However it also will cause a small degree of inaccuracies in metrics that rely on the boundary definition of the flame such as wrinkle factor. It is important to note that in the future to remove this issue the raised section of the pressure transducer can be coated in a non-reflective paint to prevent or minimise the reflections. The flame was identified close to the edge of the mask and a straight line was drawn between the two points, averaging the flame front in this section. To address any irregularities in the flame edge, a dilation operation is performed. The flame is then filled, binarized, and eroded to separate the flame region from the background and provide an accurate representation

of the flame. Finally, a de-noise operation is completed to eliminate any unwanted artifacts or small features.

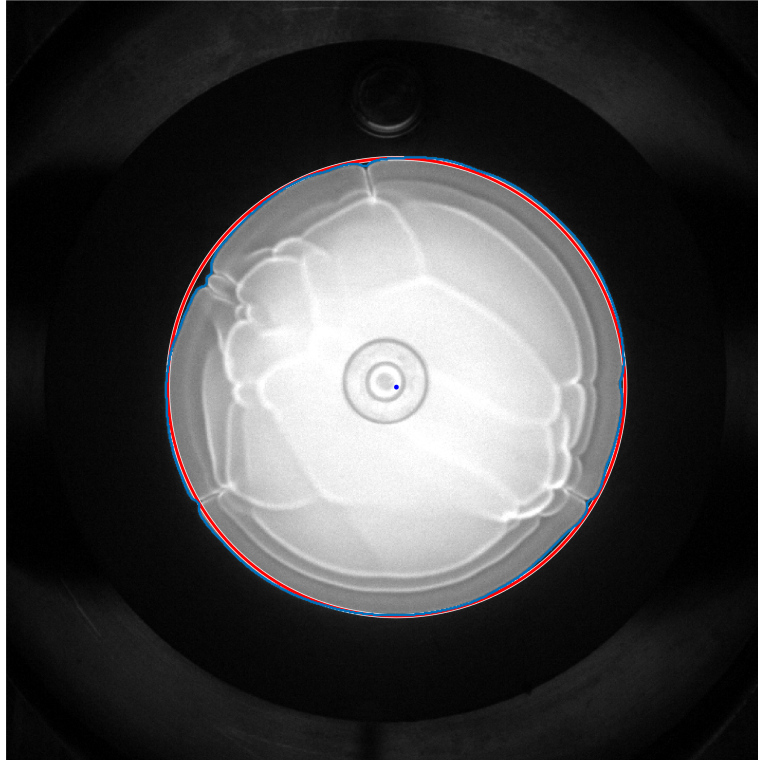


Figure 4.6: Ammonia-hydrogen-air(50:50) flame at 0.5 MPa, $\phi = 1.0$, with identification of flame centroid, flame outline (blue), and mean radius (red).

4.2.3 Flame property acquisition

The flame properties are defined using the **regionprops** function. This function returns the following information; area, bounding box, centroid, perimeter, and mean intensity. These outputs are used to derive the following properties;

- Flame area, centroid, and perimeter - taken directly from the function outputs.
- Wrinkle factor - quantifies the wrinkling or irregularities in the flame boundary by considering the flame perimeter against the flame area,

as shown in Equation 4.1. The higher the wrinkle factor, the more irregular the flame boundary is. There are some instances where the wrinkle factor is below one, this is a minor error in image processing resulting in the area appearing larger than it is.

$$WrinkleFactor, W_f = \frac{FlamePerimeter^2}{4 * \pi * FlameArea} \quad (4.1)$$

- AB shape ratio - is the ratio of the bounding box in the x and y axis, and highlighted in green in Figure 4.8. It is derived from the bounding box output.
- Luminosity - Matching the raw image to the defined region enables the average luminosity of the area to be taken from the mean intensity property.

The mean flame radius is calculated from the output of the **bwboundaries** function that identifies the pixels which are the boundary of the binarised region. The distance from the flame centroid for all values is then calculated and averaged to provide the mean radius. The boundaries are used to produce contour development plots that provide an understanding of the flame edge development as it propagates through the chamber, an example of this can be found in Figure 5.2.

4.3 Side combustion view

To investigate the flame wall interactions, the side on view camera configuration provides a different view of the combustion as seen in Figure 4.7. The same flame binarisation and processing codes are used to recognise the flame front, however the definition of the flame radii are changed to allow

for two apparent flame speeds to be defined, in the x direction (perpendicular to the wall) and y direction (parallel to the wall). The radius in the y direction is defined by the bounding box shown in green and the x radius is taken as the average of the distance of points defined in red from the centroid defined in yellow.

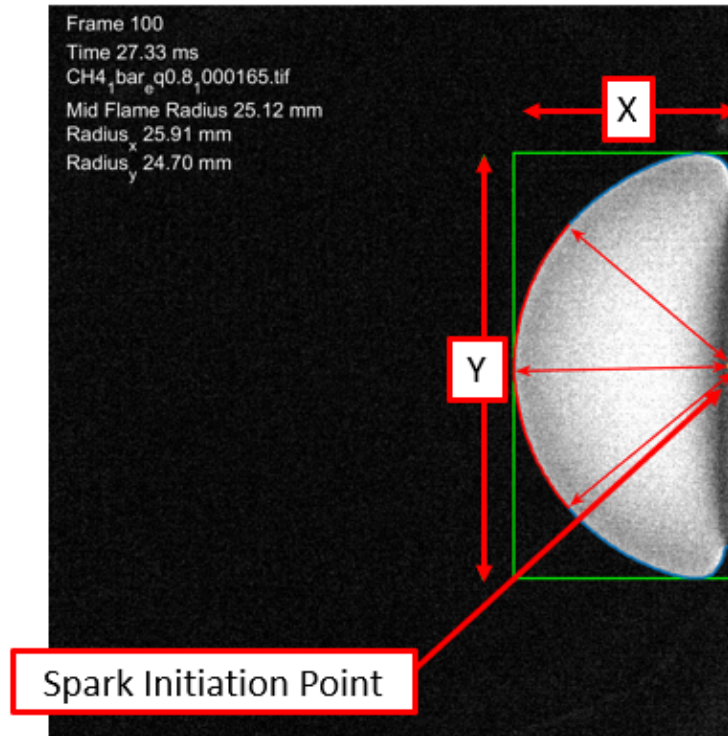


Figure 4.7: Side on configuration view of a combustion event.

4.4 Unstretched laminar burning velocity

As discussed in Section 2.2.2, the unstretched laminar burning velocity is calculated from the stretched flame propagation speed, S_n . The flame propagation speed is defined as the derivative of the flame radius with respect to time as the mixture is considered to be quiescent. Using the mean flame radius calculated from the flame images, Equation 4.2 is used.

$$S_n = \frac{dr}{dt} \quad (4.2)$$

where S_n is stretched burning velocity, r is the flame radius in mm and t is the elapsed time from ignition in ms. In the case of a spherically propagating flame, the flame front is stretched due to the curvature of the flame front, this stretch is found to influence the flame characteristics. The stretch rate is defined as the change in ratio of flame front area per unit time per unit area. In this instance, for a spherically propagating flame not influenced by buoyancy, it is defined using Equation 2.4. Stretch rate for buoyant flames are discussed in Section 4.4.1.

Various correlations have been discussed in literature with regards to the relationship of unstretched laminar burning velocity and flame stretch, these are discussed in more detail in Section 2.2.2. For the flame analysis used in these studies, assuming the flame is adiabatic and the propagation is quasi-steady, the flame propagation speed can be extrapolated using the non-linear correlation shown in Equation 4.3, proposed by Kelley and Law [83].

$$\left(\frac{S_n}{S_s}\right)^2 \ln\left(\frac{S_n}{S_s}\right)^2 = -2\frac{L_b\epsilon}{S_s} \quad (4.3)$$

For this correlation it can be shown that the $\ln(S_n)$ varies linearly with ϵ/S_n^2 , with the y intercept equal to $\ln(S_s)$ and a gradient equal to $-S_s L_b$. To reduce noise in the flame speed calculation, the data was down-sampled to 75 points. This was in line with Huo et al. who suggested a minimum of 30 points were required to be used in the extrapolation to remove random errors [66]. The laminar burning velocity, S_L^0 , is calculated from the continuity equation across the flame's surface, where the burned and unburned

densities, ρ_b and ρ_u , are calculated from thermo-transport data.

$$S_L^0 = \frac{\rho_b}{\rho_u} * S_s \quad (4.4)$$

4.4.1 Flame buoyancy

In some instances, especially with ammonia-air flames, the influence of buoyancy is significant. Figure 4.8 shows a well developed ammonia flame which has been misshapen due to buoyancy. As discussed in Section 2.2.5, Ronney et al. concluded the buoyancy affect can be considered negligible for flames above 15 cm/s [130]. For ammonia-air flames, some of the speeds observed are significantly less than this. The influence of buoyancy “squashes” the flame as the vertical movement adds to the vertical velocity of the flame moving above the spark and subtracts from the velocity below. This phenomena was detailed at length by Chen [23], who proposed a method to account for the buoyancy influence in laminar burning velocity measurements. This method was utilised for the ammonia-air flames.

Using the horizontal, a , and vertical bounding box, b , lengths as derived from the **regionprops** function, the variation rates are calculated and can be defined by Equations 4.5 and 4.6. It is assumed that the fuel consumption rate of the equivalent spherical flame and the buoyancy affected flame are equal.

$$\dot{a} = 2V_f + 2V_e \quad (4.5)$$

$$\dot{b} = 2V_f + V_{b1} - V_{b2} \quad (4.6)$$

Where \dot{a} and \dot{b} are the rate of change of bounding box lengths a and b respectively. V_f is defined as the propagation velocity of the equivalent spherical flame, V_b is the buoyancy induced vertical flame deformation at

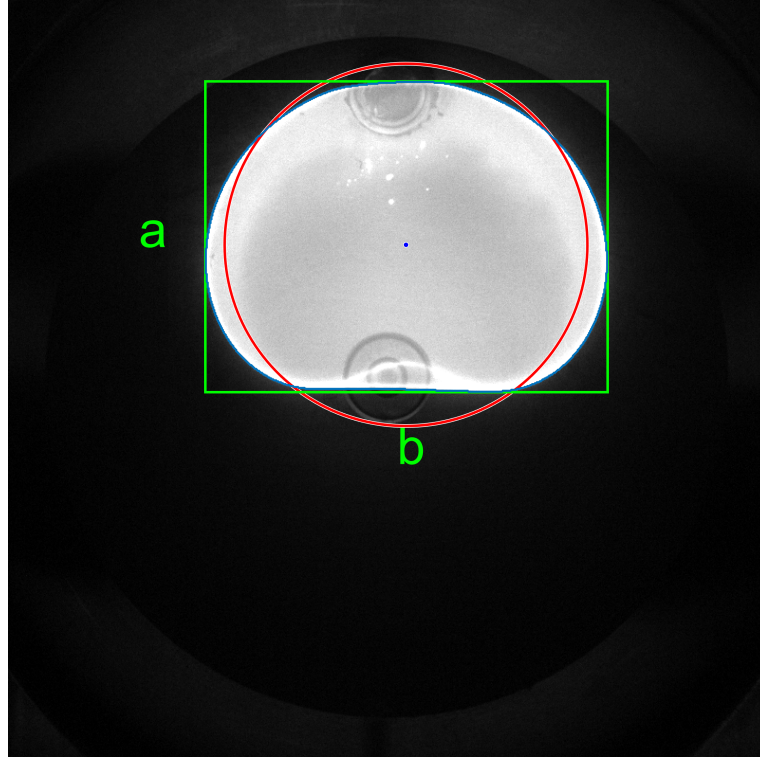


Figure 4.8: Ellipsoidal buoyancy calculation using the bounding box (green). Mean radius (red) from standard assumptions shown along with flame boundary (blue).

the ends of the horizontal axis with V_{b1} and V_{b2} being the buoyancy induced velocities at the upper and lower ends of the vertical axis, V_e is the buoyancy induced at the end of the horizontal axis deformation velocity at the ends of the horizontal axis in the horizontal direction. These values can be used to produce a better approximation of the flame radius r , flame propagation speed V_f , and stretch rate ϵ via Equations 4.7, 4.7, and 4.9 respectively.

$$r = \frac{1}{2} a^{\frac{2}{3}} b^{\frac{1}{3}} \quad (4.7)$$

$$V_f = \frac{dr}{dt} = \frac{1}{3} * \left(\frac{b}{a}\right)^{\frac{1}{3}} \dot{a} + \frac{1}{6} \left(\frac{a}{b}\right)^{\frac{2}{3}} \dot{b} \quad (4.8)$$

$$\epsilon = \frac{1}{A} \frac{dA}{dt} = \frac{2}{r} V_f = \frac{4}{3} \left(\frac{1}{a}\right) \dot{a} + \frac{2}{3} \left(\frac{1}{b}\right) \dot{b} \quad (4.9)$$

Once the flame propagation speed and the stretch were defined, the non-

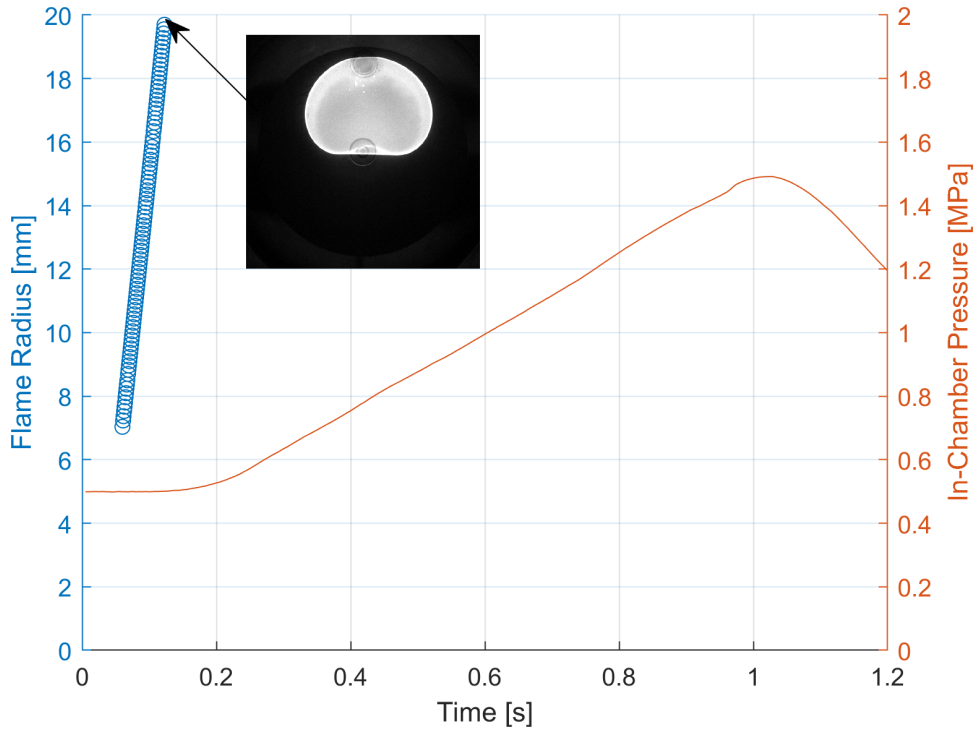
linear correlation from Equation 4.3 was used to extrapolate the flame propagation speed to the zero stretch condition and then the burned to unburned density ratio was used to find the laminar burning velocity.

4.5 Uncertainty

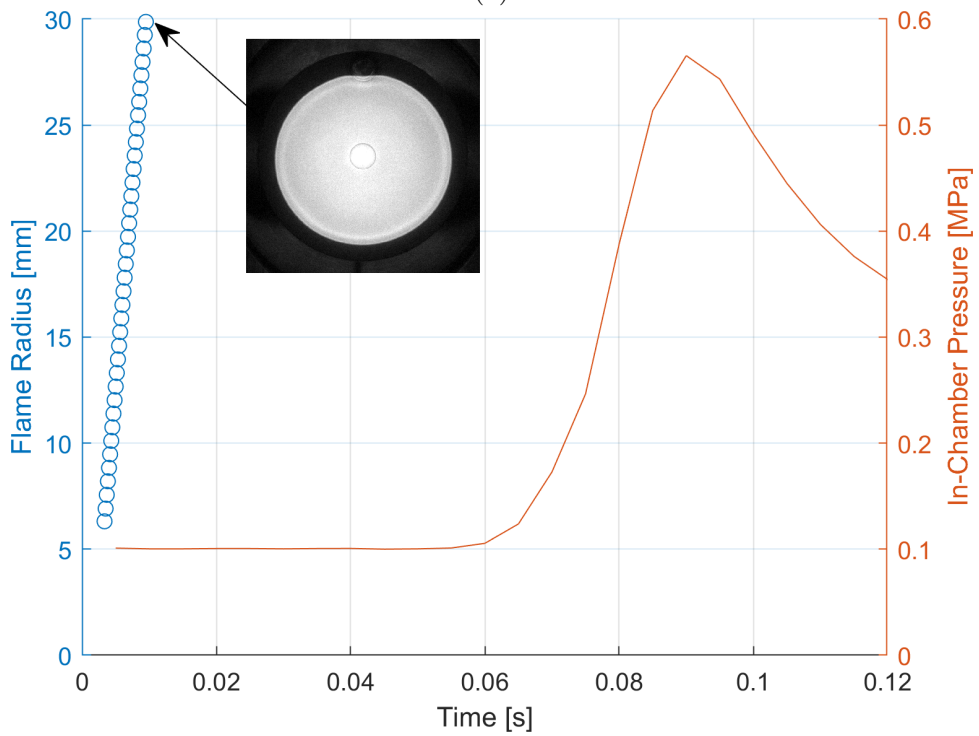
In their review of the accuracy of laminar burning velocity measurements of methane-air flames, Chen [22] highlighted multiple sources of uncertainty including confinement, flame instability, ignition energy, buoyancy, non-linearity of flame speed-stretch relationships. Drawing on the conclusions by Burke et al. [19], the confinement effect of the non-spherical (cylindrical) geometry on the evolution of the flames was minimised by limiting the considered flame radius to 0.3 times the wall radius or 30 mm. This minimised the error to within 3%.

Preliminary experiments, using a standard j-type spark plug, saw strong influence on local flame growth as a result of heat transfer from the ground electrode which caused a crack in the flame fronts. The spark plug was then changed to a central ignition spark plug which no longer influenced the initial flame propagation via heat transfer. It was noted that there was variation in the spark plug depending on where the arc occurred. With a j-type plug, the spark gap is set as the closest point and therefore the arc consistently occurs at the tip of the electrode. With the central electrode the spark gap is a circular space around the tip of the electrode, as a result the arc is able to occur at any point within that circle. This influence was minimal in the early stages of propagation and therefore did not impact the flame speed measurements. Following the assumption introduced by Bradley et al.[13], the influence of the ignition energy on the flame prop-

agation speed is avoided in the reported results by only considering flame radii above 6 mm in the calculation of laminar burning velocity.



(a)



(b)

Figure 4.9: Pressure rise plot with flame radius progression for;(a)Ammonia-air flame at 0.5 MPa, $\phi = 1.0$ (b)Ammonia-hydrogen-air flame at 0.5 MPa, $\phi = 1.0$, SR = 0.5.

As the inner diameter of the chamber is sufficiently large in comparison to the maximum flame diameter considered, the rise in chamber pressure during the recording of the flame propagation is avoided. Figure 4.9 shows the chamber pressure rise and the flame radius development of two combustion events, a relatively fast ammonia-hydrogen-air combustion and a relatively slow ammonia-air combustion. The chamber pressure rise across the entire recorded flame development is negligible, therefore the pressure can be assumed to be constant within the observation range. In some instances, cracks originating from the spark initiation were observed on the flames, these cracks can lead to uncertainty in the measured flame speed. The propagation and development of these cracks may lead to a cellular structure that enhances the flame speed due to the increase in flame area and therefore reaction area. In the case of cracks which do not propagate and remain stable throughout the flame expansion the effect is not easily quantifiable and can be considered negligible [117].

Chapter 5

Constant Volume Combustion Chamber Results

Using the bespoke optical combustion chamber described in Chapter 3, the findings of four optical combustion experiments are presented within this chapter alongside a discussion of the results. The intention of the investigations were;

- To benchmark the novel optical combustion chamber using methane-air flames.
- To understand the equipment's ability to measure ammonia-air flames.
- To investigate the influence of hydrogen substitution on the shape, cellularity and apparent flame speed of ammonia-air flames.
- To understand the impact of the “real world” engine ignition systems and compare to literature investigations.

Methane-air flames were used as the initial benchmark combustion testing due to the maturity and extent of the literature investigations avail-

able. Following this, due to specific interests in ammonia-air and ammonia-hydrogen-air combustion events, an investigation into the capability to measure ammonia-air flames was completed as well as a hydrogen-enriched pressure sweep, providing further detail into the influence of hydrogen substitution on characteristics of ammonia-air flames. The initial tests described were all completed with a wall-mounted automotive spark plug with a front facing view of the combustion, this enables future comparison of similar wall mounted combustion systems. In this configuration only one window was installed with side windows blanked using metal inserts. The system deviates from the standard central ignition design seen throughout literature which are intended to minimise influence of the chamber walls to produce laminar burning velocity results. However, a key output of the studies conducted was a baseline set of repeatable results that establish the novel combustion chamber as a future platform for “real-world” combustion systems such as turbulent jet ignition (TJI) which will be able to be directly compared to the spark ignition (SI) results. If the central ignition system was used in this studies, it would be significantly harder to draw comparisons.

Recognising the chambers alternative geometry to standard literature combustion chambers, especially around the spark initiation point, a further investigation was conducted with a side-on view of combustion to understand the influence of the closeness of the wall on the various flame mixtures.

5.1 Key experimental parameters

Discussed in the following section are key calculations that define the experimental conditions as well as the mixture properties used. For the methane

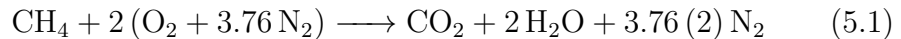
benchmarking and ammonia-air testing the equivalence ratio and initial pressures were varied, whereas for the ammonia-hydrogen-air investigations the equivalence ratio was kept at 1.0 and the substitution ratio by molar ratio (hereby referred to as SR) was varied from 0 - 0.5. The conditions for each of these experiments can be found in Table 5.1. As shown in Section 4, there was no pressure rise in the chamber during the period across which the flame images were recorded in all experimental conditions. As a result the measurements can be considered to be completed at the initial temperature and pressure. All experiments were run at 298K. Variations in in-chamber temperatures across the test conditions were kept to ± 3 K.

Fuel	Substitution Ratio, SR	Pressure [MPa]	Equivalence Ratio ϕ
CH_4	-	0.1, 0.3, 0.5	0.8 - 1.3
NH_3	-	0.1, 0.3, 0.5	0.9 - 1.1
NH_3/H_2	0-0.5	0.1, 0.3, 0.5	1.0

Table 5.1: Experimental conditions used in this study.

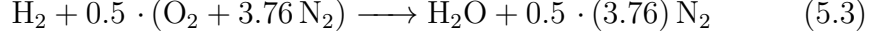
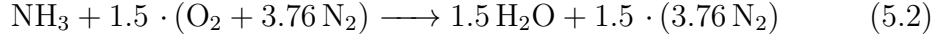
5.1.1 Properties of mixtures

The control of the mixture quantities was based on Dalton's Law of Partial Pressures, to calculate this the oxidation equation of each fuel was used. Equation 5.1 describes the oxidation reaction for methane, from this reaction the stoichiometric molar air fuel ratio was calculated as 1:9.52.

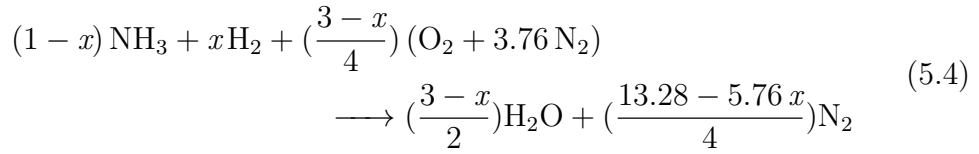


For ammonia and hydrogen, Equations 5.2 and 5.3 describe the oxidation reactions with a stoichiometric molar air fuel ratios of 1:3.57 and 1:2.38

respectively.



These equations can be combined for multi-fuel mixtures, for example;



where x is the molar SR of hydrogen in ammonia. The equivalence ratio ϕ is defined in Equation 5.5. For dual-fuel ammonia-hydrogen-air mixtures the global equation is also defined Equation 5.6.

$$\phi = \frac{\text{fuel} - \text{to} - \text{air ratio}}{\text{fuel} - \text{to} - \text{air ratio}_{stio}} = \frac{n_{\text{fuel}}/n_{\text{air}}}{(n_{\text{fuel}}/n_{\text{air}})_{stio}} \quad (5.5)$$

$$\phi = \frac{\left(\frac{X_{\text{H}_2} + X_{\text{NH}_3}}{X_{\text{Air}}}\right)_{\text{real}}}{\left(\frac{X_{\text{H}_2} + X_{\text{NH}_3}}{X_{\text{Air}}}\right)_{\text{stio}}} \quad (5.6)$$

The Tables D.1, D.2, D.3 in Appendix D show the properties of mixtures used in each of the studies. The burned and unburned densities were evaluated from gas equilibrium calculations with thermo-transport data of Tian et al [151].

5.2 Methane benchmarking study

In order to benchmark the combustion chamber in measuring ammonia and hydrogen flame characteristics, which have relatively limited literature relevant to this experimental set up and conditions, the chamber was used to measure well-known methane-air flames. The intention of this study was to investigate the capabilities and limitations of the combustion chamber utilising a fuel with well developed literature values, and a common source of validation of experimental equipment, to compare the results to. As shown in Table 5.1 the equivalence ratio, ϕ , was varied between 0.8 - 1.3 across three initial pressures 0.1 MPa, 0.3 MPa and 0.5 MPa.

Figures 5.1, 5.4, and 5.7 present the progression of each flame front at various radii and equivalence ratios. For ease of review, for each pressure the grid of images are brightened to the same degree, this provides the ability to see the relative change in intensity for each test condition. Figure 5.1 shows the varying flame progression for methane at 0.1 MPa. The time stamps on the images show that as the equivalence ratio increased from $\phi = 0.8$ the flame speed increased until $\phi = 1.2$ where it then decreased again at $\phi = 1.3$.

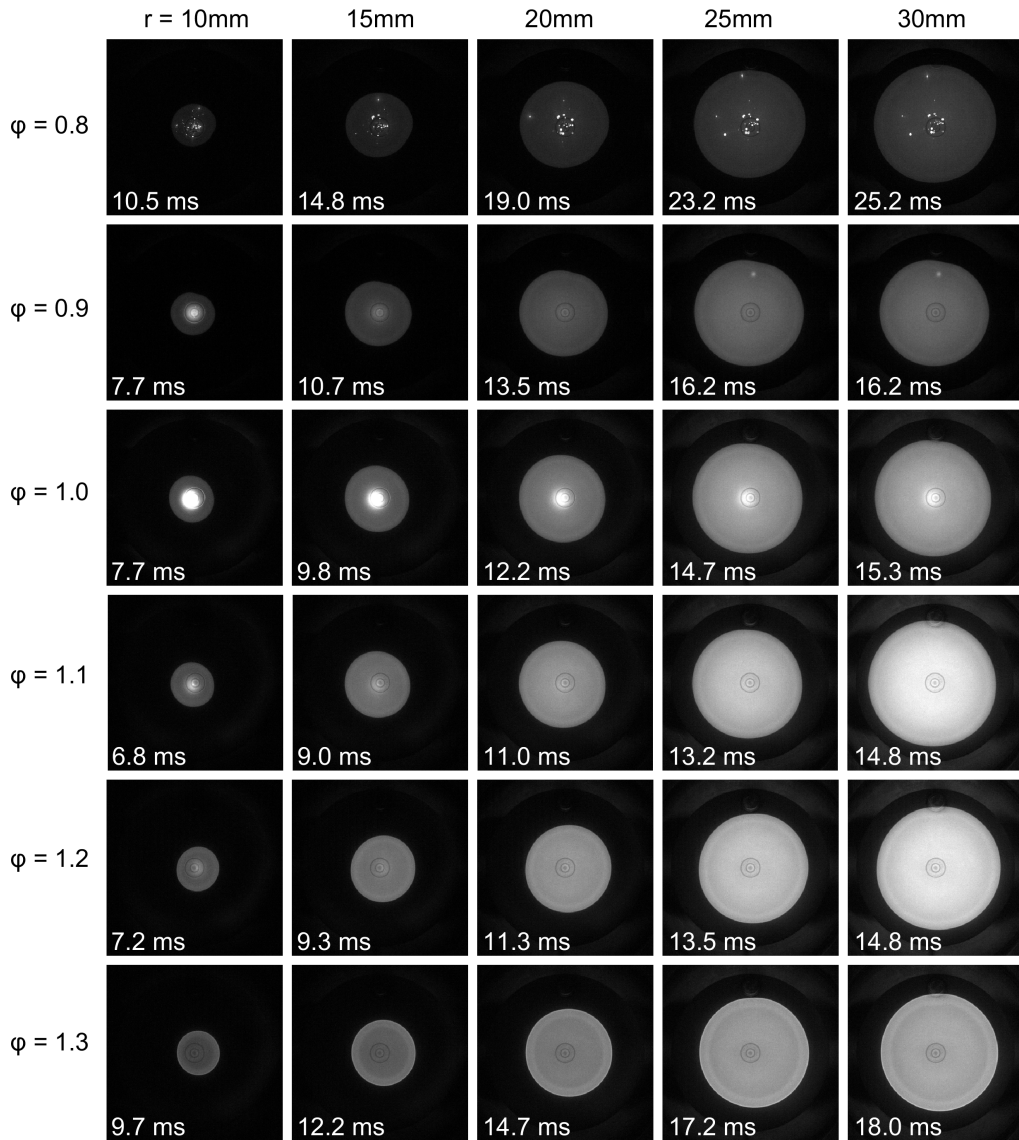


Figure 5.1: High speed images of spherically propagating methane pre-mixed flame at an initial pressure of 0.1MPa with varying equivalence ratios.

The plots in Figure 5.3 present the shape ratio and wrinkle factor of the mean flames at various equivalence ratios against the radius. Across all equivalence ratios the flame front was smooth, well-defined, and there was no evidence of cellularity. The shape ratio's for all of the flames remained between ± 0.05 around 1.0 indicating very little distortion to the flame shape. The wrinkle factor plot shows evidence of the flames stability against the initial spark influenced region by showing the initial high value, converging to close to 1. This is also observed in Figure 5.2, the smaller central

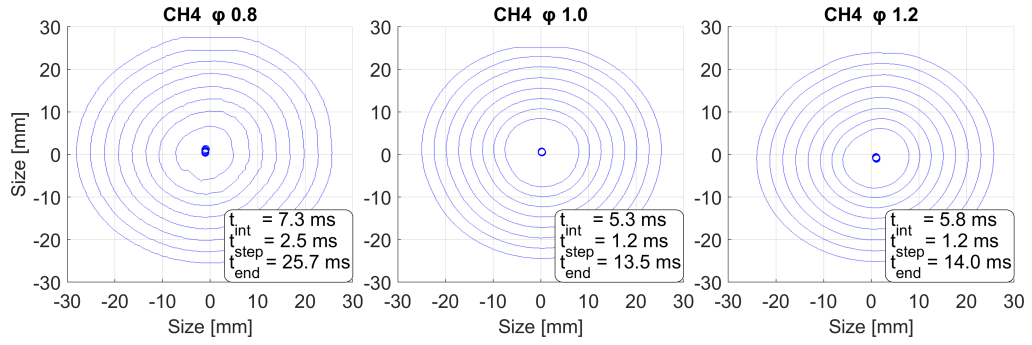


Figure 5.2: Flame contours of methane air flames at 0.1 MPa at different equivalence ratios.

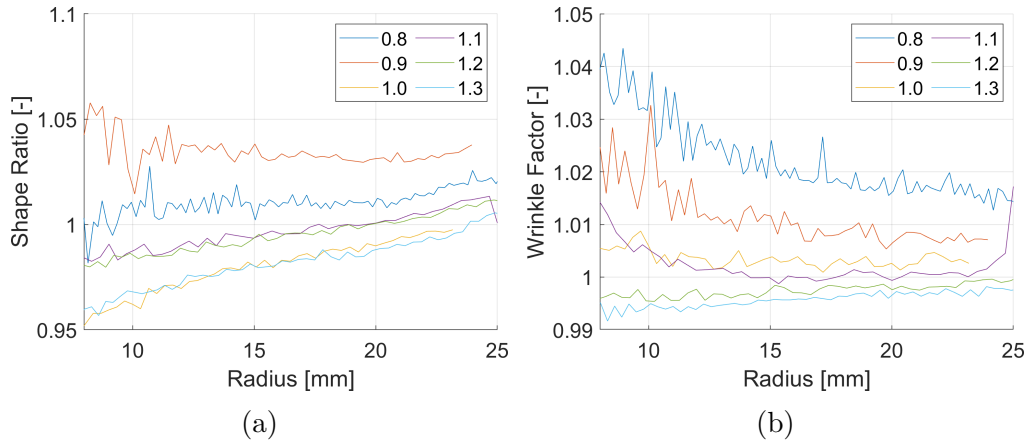


Figure 5.3: Plots for the 0.1 MPa methane-air test condition for the average of each equivalence ratio for; (a) shape ratio, (b) wrinkle factor against radius.

flame contours were initially non-circular but as the flame developed the shape became circular. The figure shows the initial spark time t_{int} , the time between each contour t_{step} and the final contour time t_{end} . The maximum centroid deviation observed across the measured flame expansion was 1 mm vertically and 0.14 mm horizontally.

Figure 5.4 shows the varying flame progressions for methane air flames at 0.3 MPa, once again the flame speed shows a similar correlation to equivalence ratio as conditions at 0.1 MPa, this is presented in Figure 5.15. There appears to be a stronger influence from the spark plug on the initial flame shape that propagated across the entire measure time. This was especially clear at $\phi = 1.1, 1.2,$ and 1.3 . This influence led to cracks

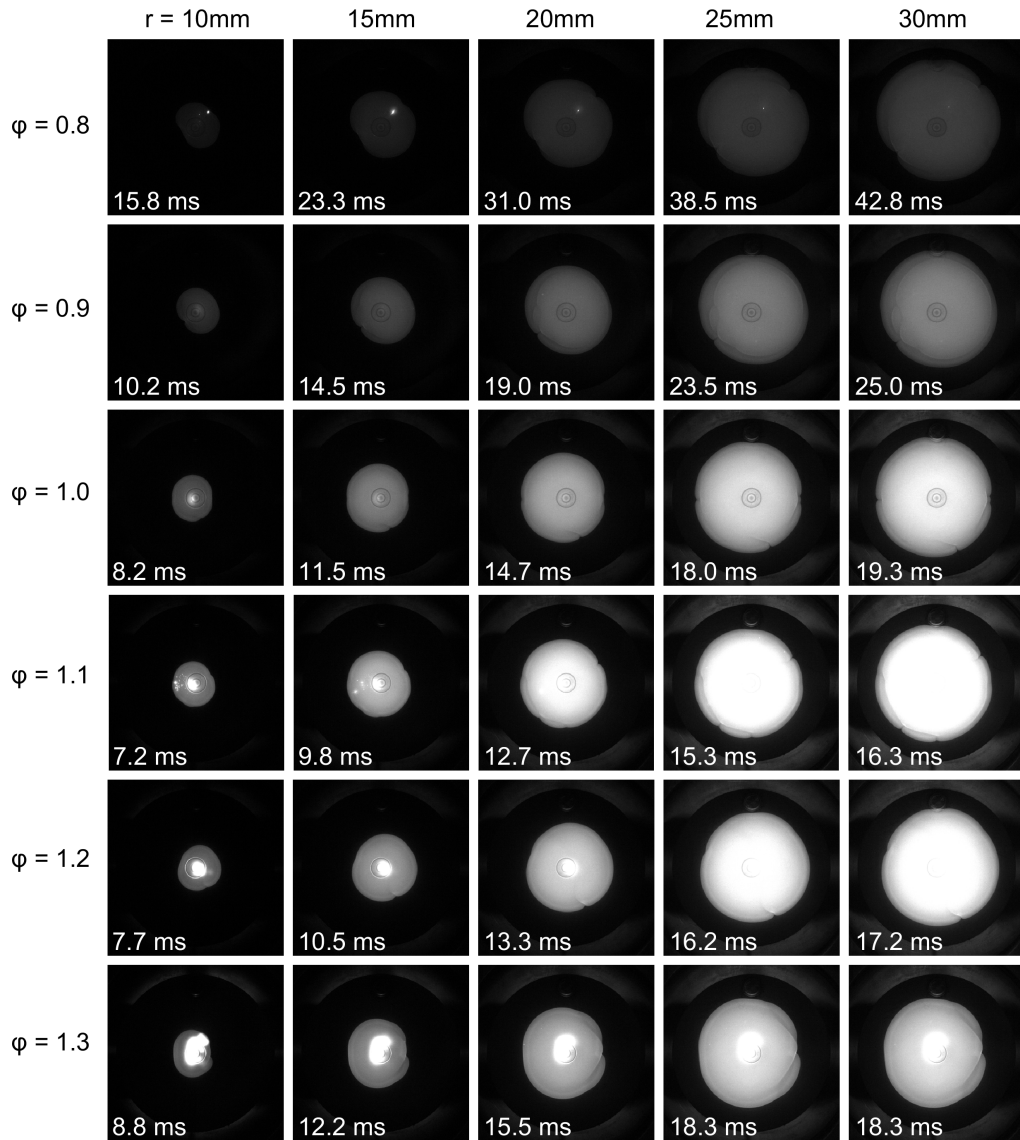


Figure 5.4: High speed images of spherically propagating methane pre-mixed flame at an initial pressure of 0.3MPa with varying equivalence ratios.

and wrinkles in the flame shape that were not seen in conditions at 0.1 MPa. Additional cells/cracks did not develop over the flame propagation suggesting the flame surface wasn't tending towards full cellularity. The wrinkle plots for these flames converge above 1.0 indicating there were wrinkles however they were not developing, shown in Figure 5.6 as well as the flame contour plots, Figure 5.5.

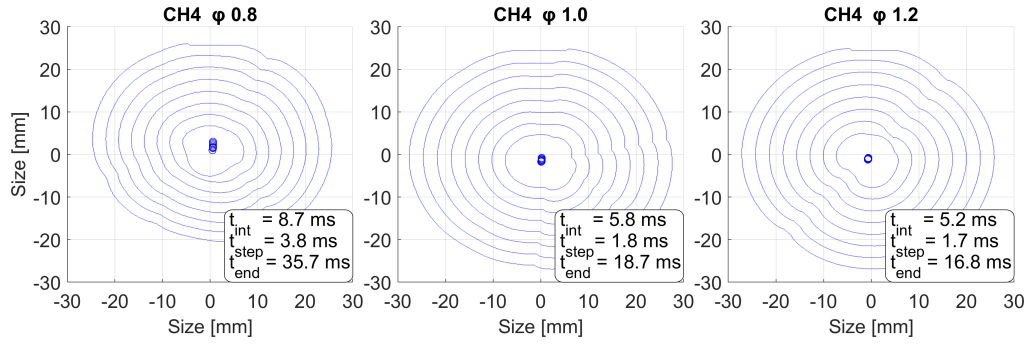


Figure 5.5: Flame contours of methane air flames at 0.3 MPa at different equivalence ratios.

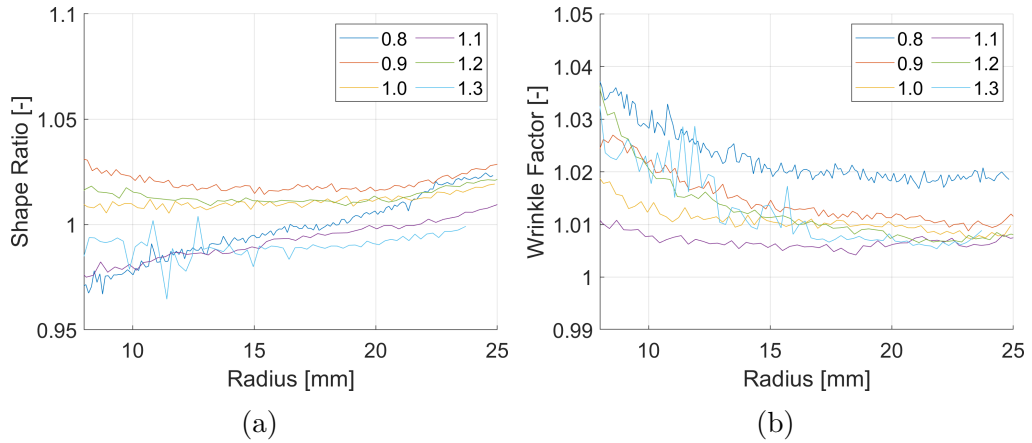


Figure 5.6: Plots for the 0.3 MPa methane-air test condition for the average of each equivalence ratio for; (a) shape ratio, (b) wrinkle factor against radius.

Figure 5.7 shows the final methane test case of 0.5 MPa. Across all equivalence ratios at this pressure condition there was evidence of cellularity observed from the spark initiation throughout the flame propagation. As the equivalence ratio increased, the relative flame luminosity increased up to $\phi = 1.2$ then begins to decrease, this is depicted in 5.12a. In some conditions the cells on the flame surface began to develop. Figure 5.8 presents the changes in the flame contour as the flame develops. The “pinch points” indicate the edges of the cells. The centroid of the flames were also plotted with the flame contours, as the equivalence ratio decreased the centroid movement became more pronounced. This was clear at $\phi = 0.8$ where not only was the flame centroid travelling upwards, the shape of the flame

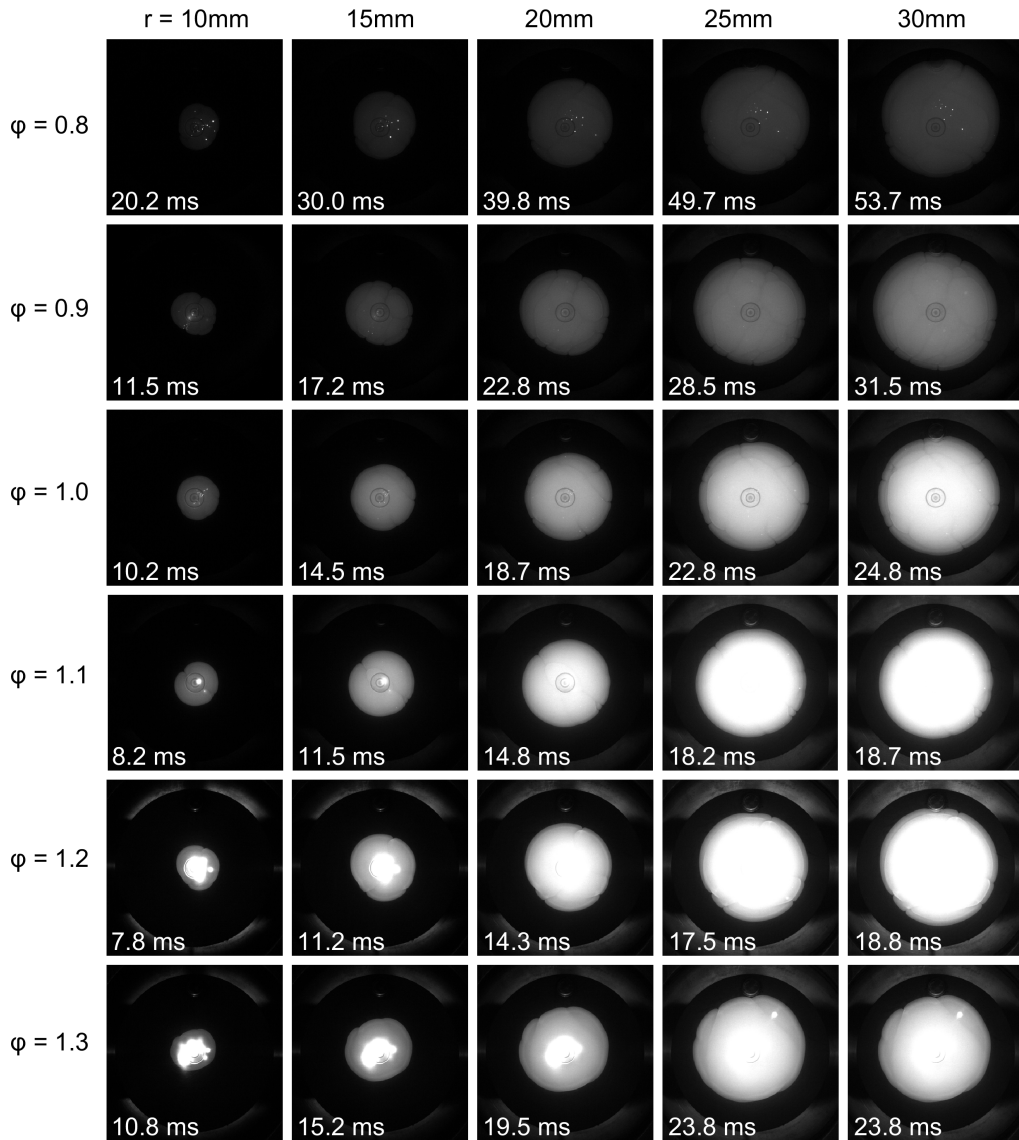


Figure 5.7: High speed images of spherically propagating methane pre-mixed flame at an initial pressure of 0.5 MPa with varying equivalence ratios.

was more ellipsoidal. The maximum centroid deviation observed across the measured flame expansion was 2.3 mm vertically and 0.5 mm horizontally.

For the 0.5 MPa pressure condition, the shape ratio shown in Figure 5.9a presents a gradual increase across the flame radius, this indicates the flame shape was becoming more deformed as it expanded. The deformation was calculated as the width of the flame front divided by height as discussed in Section 4.2, therefore an increase ratio indicates the flame increasing

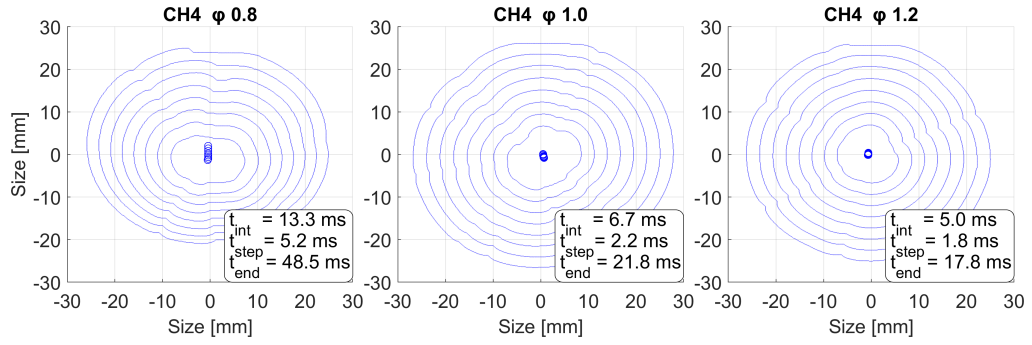


Figure 5.8: Flame contours of methane air flames at 0.5 MPa at different equivalence ratios.

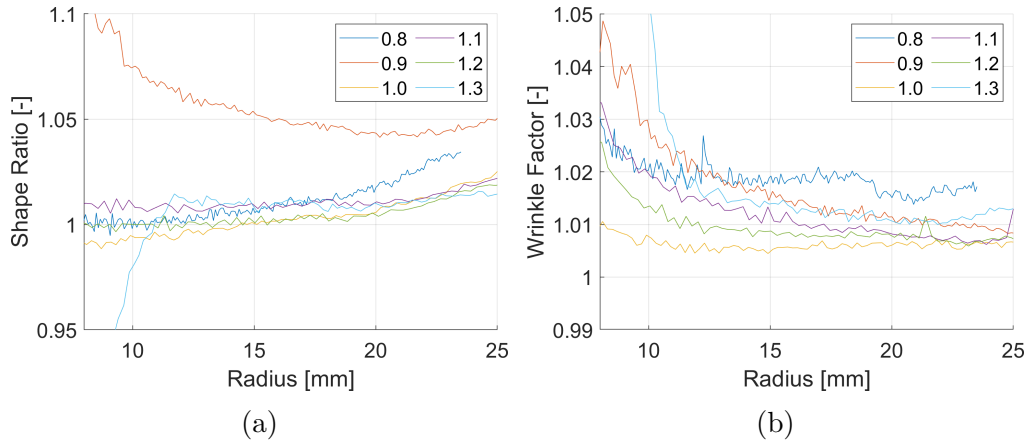


Figure 5.9: Plots for the 0.5 MPa methane-air test condition for the average of each equivalence ratio for; (a) shape ratio, (b) wrinkle factor against radius.

in width faster than in height. This is an indication of the influence of buoyancy on the flame. At $\phi = 0.9$, the shape ratio plot presents a trend different to the other equivalence ratios with an initial high value converging towards a shape ratio of 1.05.

Figure 5.9b presents the wrinkle factor of the flame fronts at each equivalence ratio against radius. During initial flame propagation there was a high wrinkle factor to begin with which then reduced as the flame expanded. The wrinkling remained above 1.0 indicating the wrinkles remain throughout the propagation. As a flame expanded, the wrinkle factor reduced as there was a larger perimeter flame front, for the 0.5 MPa pressure condition, as seen in Figures 5.7 and 5.8 the cells remained in the flame

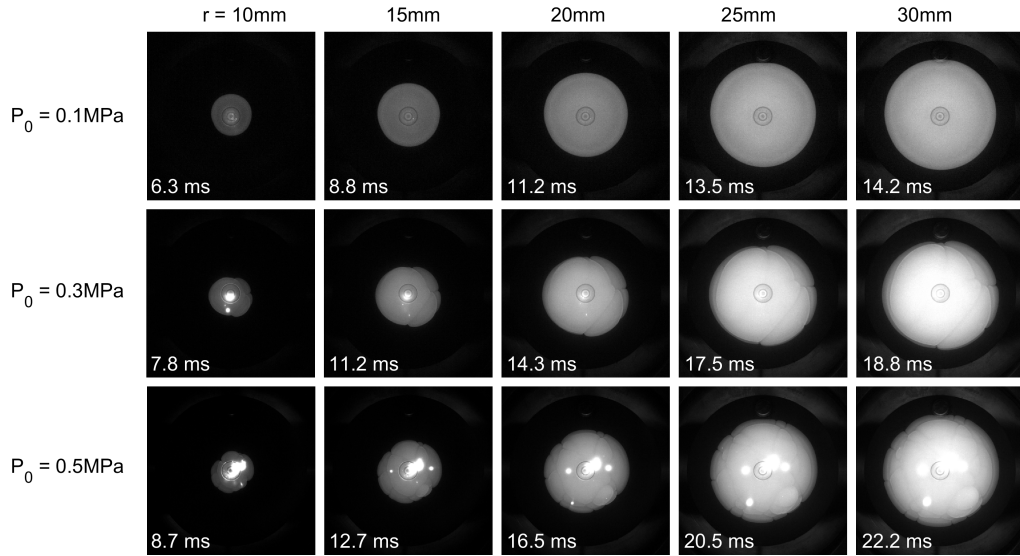


Figure 5.10: High speed images of spherically propagating methane pre-mixed flame at an equivalence ratio of 1.0 across different pressures.

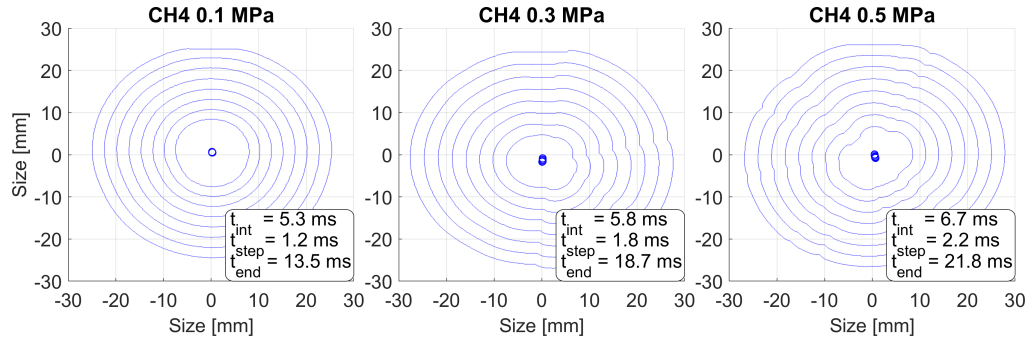


Figure 5.11: Flame contours of methane-air flames at various pressures at an equivalence ratio of 1.0

front and in some cases such as $\phi = 1.0$ continued to develop. The maximum centroid deviation observed across the measured flame expansion was 3.6 mm vertically and 0.5 mm horizontally.

Figure 5.10 shows the changing flame contours at $\phi = 1.0$ for each pressure condition 0.1 MPa, 0.3 MPa, and 0.5 MPa. This figure shows the influence of pressure on flame shape and cellularity, with an increasing pressure resulting in wrinkles in the flame front as well as a decrease in flame speed and movement of the flame centroid. Reviewing the flame contour maps shown in Figure 5.11, the wrinkles can be clearly seen in the 0.3 MPa condition however they did not continue to develop, as the radius increased.

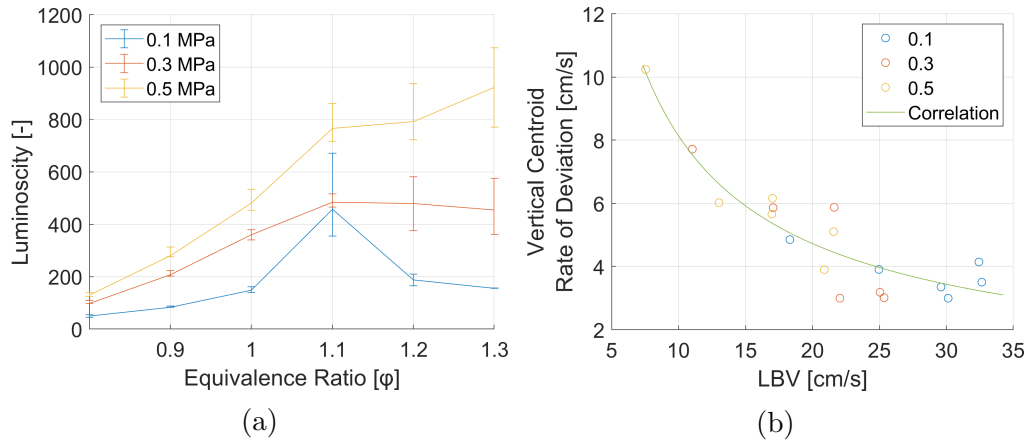


Figure 5.12: Plots presenting (a) flame luminosity at a radius of 20 mm for each of the methane air test conditions, and (b) flame centroid deviation rate against laminar burning velocity (LBV) for each pressure condition for methane-air flames.

This was unlike the 0.5 MPa pressure condition where the cells continued to develop.

Figure 5.12a presents the flame luminosity of each test condition at a radius of 20 mm at each equivalence ratio and pressure. As highlighted in previous sections the flame luminosity is weakest at the lean conditions with $\phi = 0.8$, slightly richer conditions such as at $\phi = 1.1$, the flames are at their brightest. The pressure also has a significant influence on the luminosity, as the pressure increases the luminosity of the flame increases.

To detect the influence of buoyancy in the flame measurements, the centroid deviation rate of each flame was plotted. In the horizontal direction this varied very little, a maximum of 0.5 mm deviation across all tests. The rate of vertical deviation is plotted in Figure 5.12b against varying laminar burning velocity for each of the pressure conditions. This plot shows the rate of deviation was minimal for all flames apart from 0.5 MPa in lean conditions when the flame was at its slowest.

Table 5.2: Measured unstretched laminar burning velocity and corresponding Markstein Length at 0.1 MPa methane-air flames.

ϕ	S_l [cm/s]	Range of scatter from the mean S_l [cm/s]		L_b [mm]	Range of scatter from the mean L_b [mm]	
0.79	18.31	-0.64	0.71	0.53	-0.04	0.02
0.89	24.96	-0.70	1.03	0.61	-0.10	0.13
0.97	29.60	-0.56	0.90	0.51	-0.15	0.08
1.08	32.65	-0.52	0.55	0.56	-0.04	0.04
1.19	32.43	-2.33	1.90	0.73	-0.17	0.16
1.28	30.14	-0.10	0.06	0.80	-0.10	0.12

Table 5.3: Measured unstretched laminar burning velocity and corresponding Markstein Length at 0.3 MPa methane-air flames.

ϕ	S_l [cm/s]	Range of scatter from the mean S_l [cm/s]		L_b [mm]	Range of scatter from the mean L_b [mm]	
0.80	11.03	-0.30	0.52	0.55	-0.09	0.06
0.89	17.06	-0.64	0.51	0.28	-0.15	0.09
0.99	21.62	-0.57	0.83	0.26	-0.01	0.02
1.09	25.05	-0.11	0.12	0.40	-0.09	0.08
1.20	25.35	-1.52	1.27	0.56	-0.27	0.24
1.29	22.05	-1.05	1.17	0.68	-0.24	0.14

Table 5.4: Measured unstretched laminar burning velocity and corresponding Markstein Length at 0.5 MPa methane-air flames.

ϕ	S_l [cm/s]	Range of scatter from the mean S_l [cm/s]		L_b [mm]	Range of scatter from the mean L_b [mm]	
0.80	7.54	-0.21	0.35	0.25	-0.34	0.29
0.90	13.02	-0.69	0.76	0.12	-0.21	0.36
0.99	16.97	-0.08	0.14	0.33	-0.41	0.23
1.10	20.89	-0.73	0.84	0.24	-0.15	0.10
1.19	21.58	-1.27	1.49	0.42	-0.29	0.34
1.29	17.02	-0.72	1.17	0.57	-0.43	0.38

The mean results of the unstretched laminar burning velocity calculations are presented in Tables 5.2 - 5.4, these were obtained from at least three experimental repetitions at each condition. The average scatter in the measured unstretched laminar burning velocity measurements was 4.3% of the average value, with the maximum observed being 6.9%.

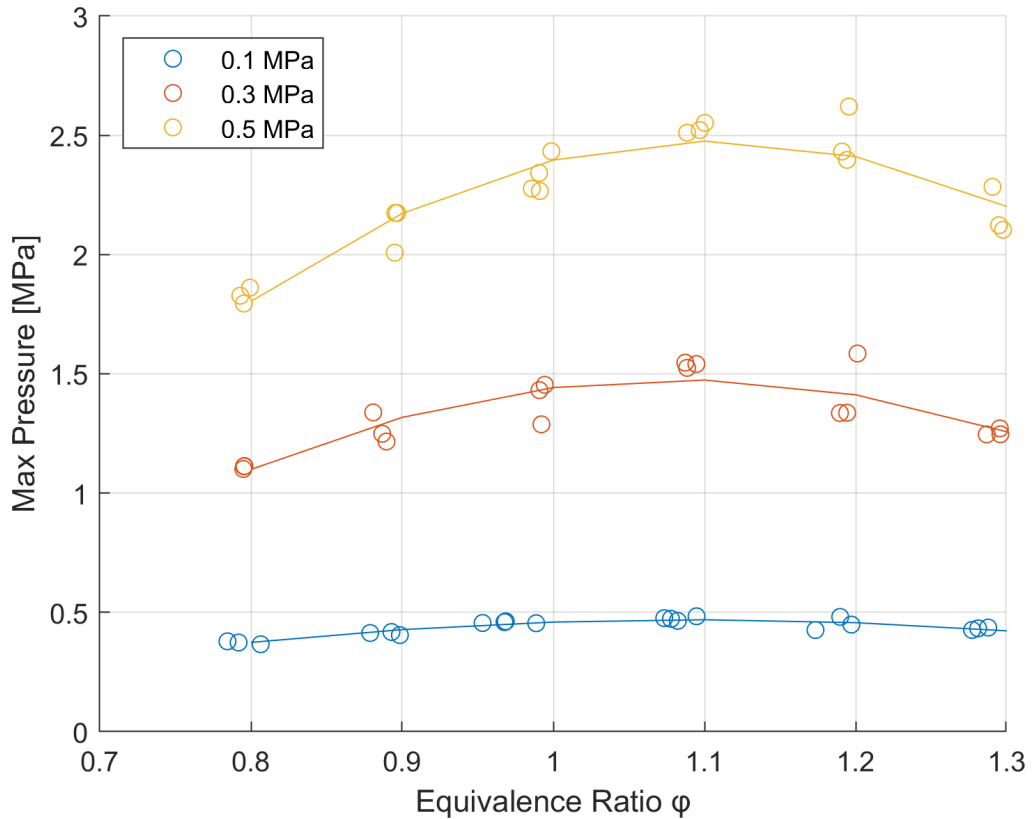


Figure 5.13: Maximum pressure vs equivalence ratio for premixed methane-air combustion

Figure 5.13 shows the influence of initial pressure and equivalence ratio on the peak combustion pressure. For all conditions the combustion pressure peaked at an equivalence ratio of 1.1, with a dramatic overall increase as the initial pressure was increased. The peak at 1.1 can be expected as a result of the dissociation effects. When the equivalence ratio is slightly above 1.0, there is a surplus of oxygen in the mixture. The excess oxygen can increase the combustion temperature, leading to disassociation of the combustion products, releasing additional energy into the chamber.

Figures 5.14 - 5.16 present the comparison of the data with experimental literature data previously identified from Section 2.4. Figure 5.14 presents the results for 0.1 MPa methane-air laminar burning velocities, the data showed a strong correlation with an r-squared term of 0.962. The shape of the correlation is very close to matching the literature correlation, the

equivalence ratio appears to be offset in the data by 0.1 equivalence ratio. This is also seen in the 0.3MPa and 0.5MPa pressure condition. At the 0.3 MPa initial pressure condition the experimental data has a strong correlation with an r-squared term of 0.971. Figure 5.15 shows the experimental data plotted against the equivalent literature data at this condition. In these test cases there were wrinkles present in the flame front as well as some degree of cellularity development.

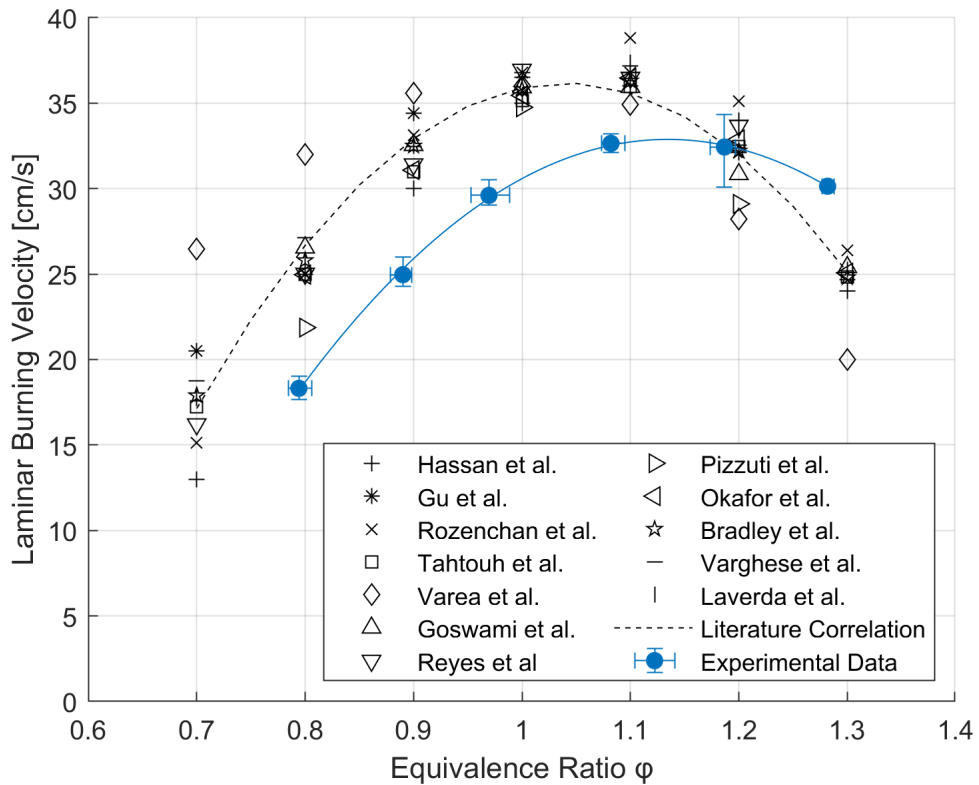


Figure 5.14: Laminar burning velocity vs equivalence ratio for premixed methane-air combustion at 0.1 MPa initial pressure compared to literature.

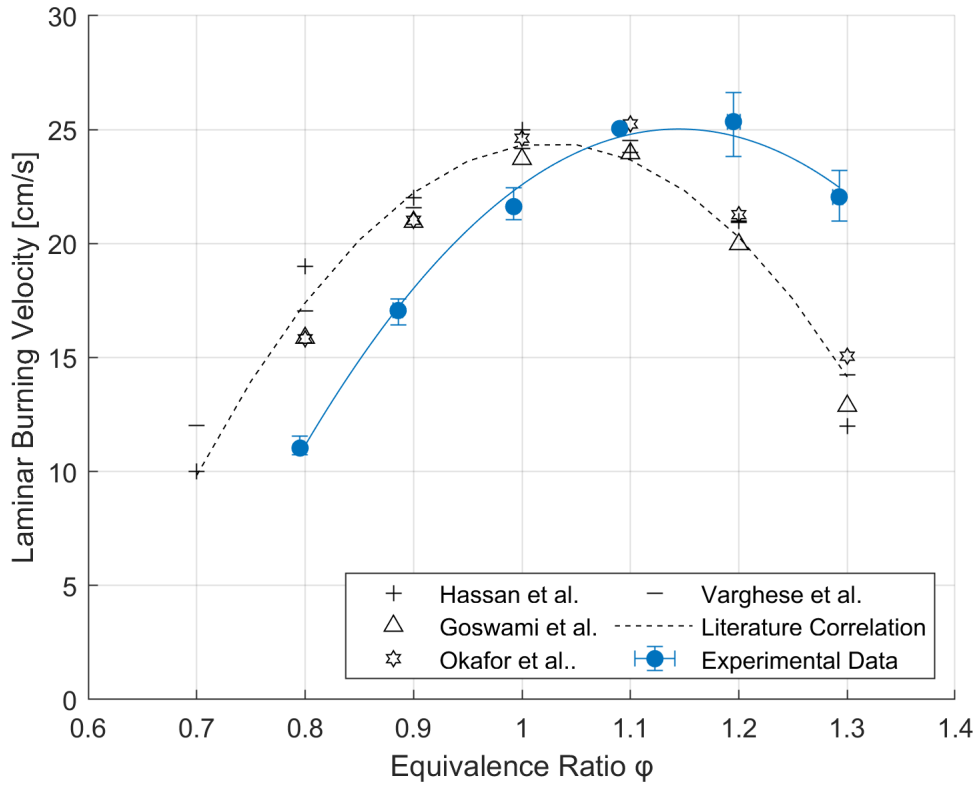


Figure 5.15: Laminar burning velocity vs equivalence ratio for premixed methane-air combustion at 0.3 MPa initial pressure compared to literature.

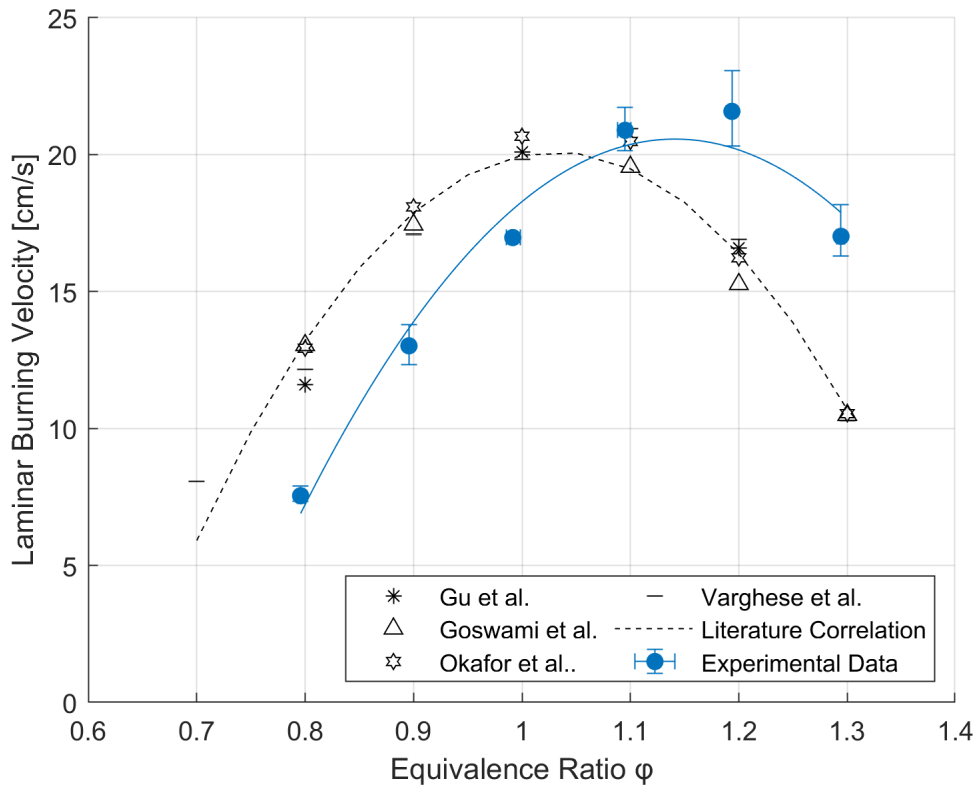


Figure 5.16: Laminar burning velocity vs equivalence ratio for premixed methane-air combustion at 0.5 MPa initial pressure compared to literature.

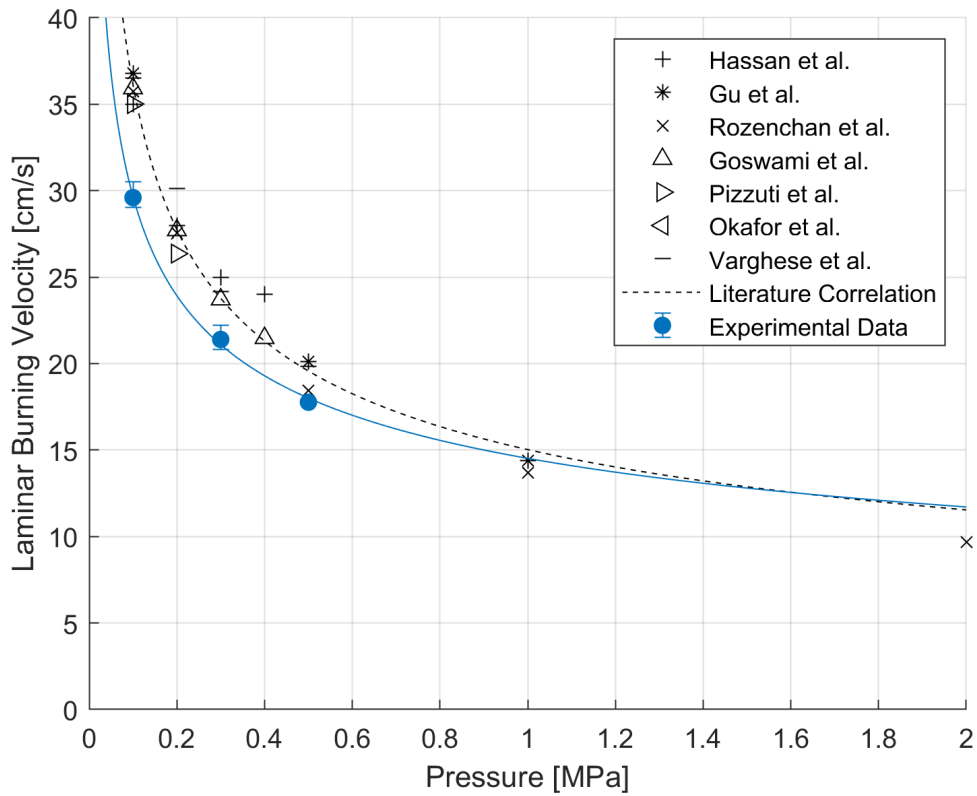


Figure 5.17: Laminar burning velocity vs initial pressure for premixed methane combustion at 1.0 equivalence ratio compared to literature values.

Figure 5.16 presents the final pressure case for methane-air flames, 0.5 MPa, against the relevant literature values. The r-squared value for this data set was 0.931. Once again cellularity was observed throughout the range of flame equivalence ratios. Figure 5.17 presents the comparison of the affect of increased pressure on the laminar burning velocity for the experimental and literature values. There is a reasonable correlation between the two data sets although all of the values are lower than literature, this is discussed further in Section 5.6.1.

5.3 Ammonia testing

The following section describes an investigation of ammonia flame measurements conducted with the combustion chamber. Due to the low laminar burning velocity of ammonia, the measurements are significantly more susceptible to technique dependent uncertainties that are exacerbated by instability phenomena described in Section 2.2. Ammonia has a relatively narrow flammability range, equating to an equivalence ratio range of 0.72 - 1.46. With the geometry and spark condition used in this study the combustion was limited to equivalence ratios between 0.9 - 1.1, and the initial pressure limited to 0.3 MPa and 0.5 MPa. Each of the following data sets was repeated a minimum of three times. The thermal and transport properties used in this study are shown in Table D.2.

Figure 5.18 presents the flame progression of an ammonia-air flame at 0.3 MPa. As the flame propagated through the mixture, the shape was deformed to a mushroom shape, there was also a clear vertical velocity component that was not strongly observed in the methane-air flames. The bottom edge of the flame appeared to invert at the $\phi = 0.9$ condition, showing significant deformation as a result of buoyancy. This is also seen in Figure 5.19, which presents the flame progression for 0.5 MPa ammonia-air flames across different equivalence ratios. For both pressure conditions the richer flames were significantly faster and showed less deformation. As a result of the rising flame observed in each pressure condition, the available volume for flame speed measurement was reduced hence the measured radius only reaching 20mm.

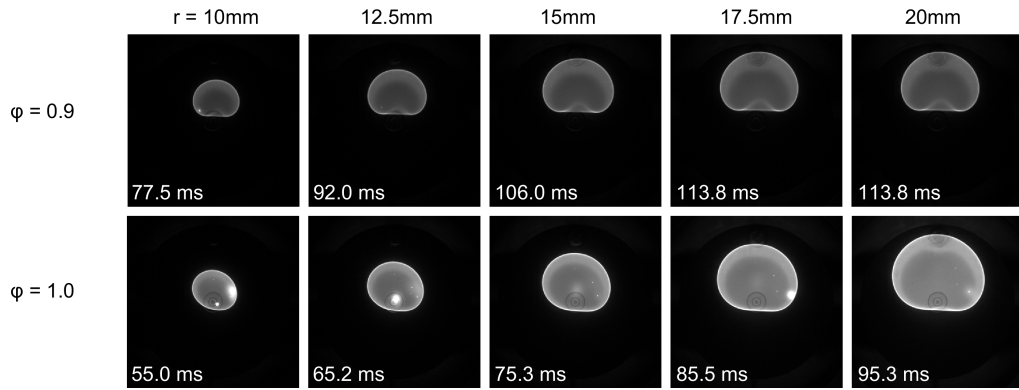


Figure 5.18: High speed images of spherically propagating ammonia pre-mixed flame at an initial pressure of 0.3MPa with varying equivalence ratios.

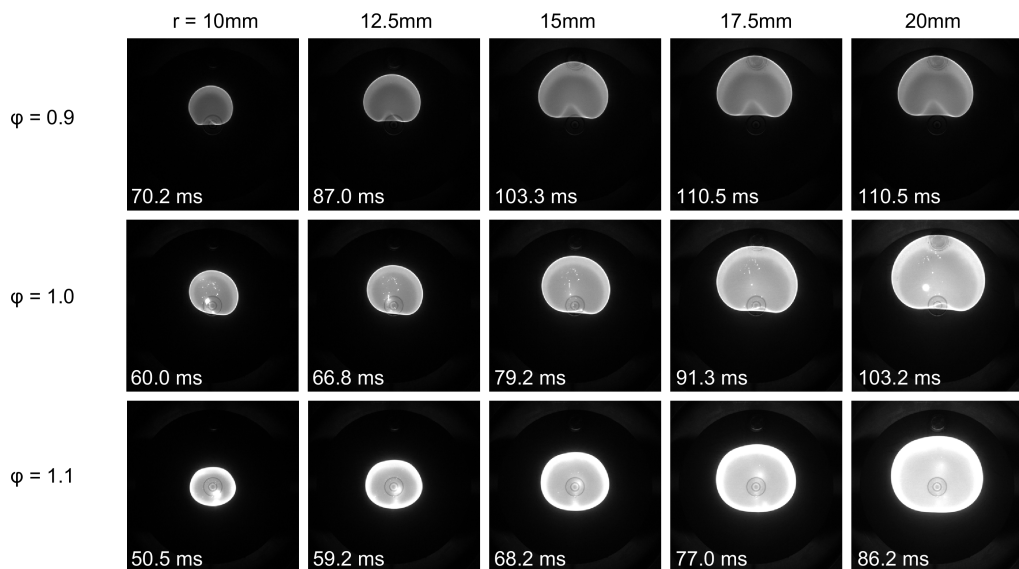


Figure 5.19: High speed images of spherically propagating ammonia pre-mixed flame at an initial pressure of 0.5MPa with varying equivalence ratios.

Figure 5.20 demonstrates the progression of each flame at the 0.5 MPa test condition at three equivalence ratios, at richer conditions the flame speed increased and the impact of buoyancy was reduced. This is indicated by the times presented as well as the general flame shape. The vertical centroid movement can also be observed in these plots. The maximum horizontal deviation observed was 0.6 mm, the maximum vertical deviation was 9.4 mm with a velocity of 18.4 mm/s. The flames shown have no evidence of cellularity of cracking, and the influence of the initial kernel shape seemed

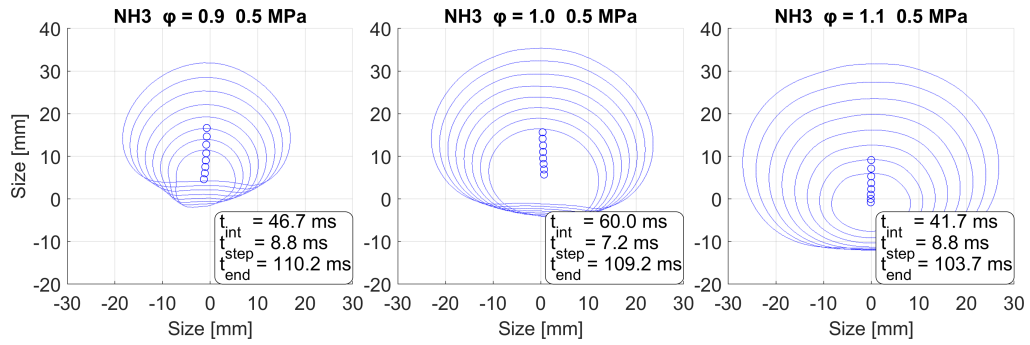


Figure 5.20: Flame contours of ammonia-air flames at 0.5 MPa at varying equivalence ratios.

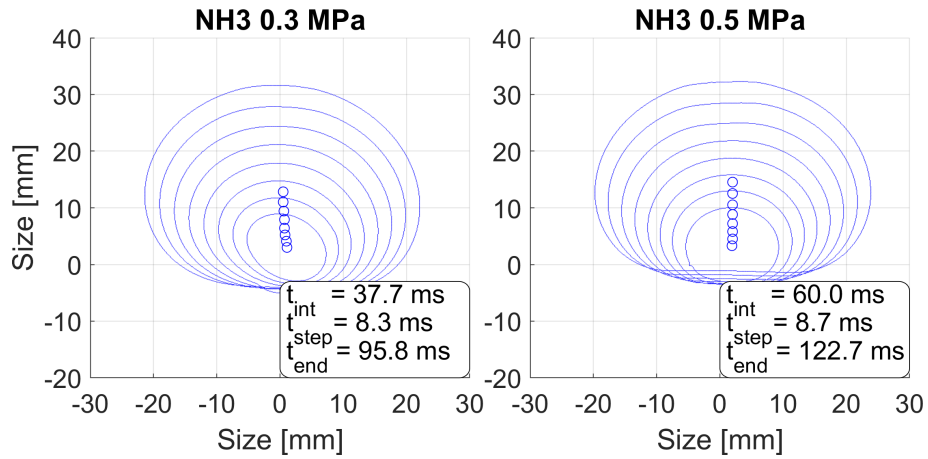


Figure 5.21: Flame contours of ammonia-air flames at various pressures at an equivalence ratio of 1.0.

to be overcome as the flame expanded as shown by the flame at $\phi = 1.1$.

Figure 5.21 compares the flame contours of two ammonia-air flames at an initial pressure of 0.3 MPa and 0.5 MPa at an equivalence ratio of 1.0. The change in flame velocity due to the difference in initial pressure is indicated by the time points presented in the figure. In addition the centroid movement is plotted showing a clear upwards velocity across the entire recorded propagation.

Figures 5.22 and 5.23 present the change in shape ratio and wrinkle factor against flame radius for the 0.3 MPa and 0.5 MPa pressure conditions for ammonia-air flames. For both flames there was a clear trend of increasing shape ratio with radius, indicating that as the flames expanded the shape

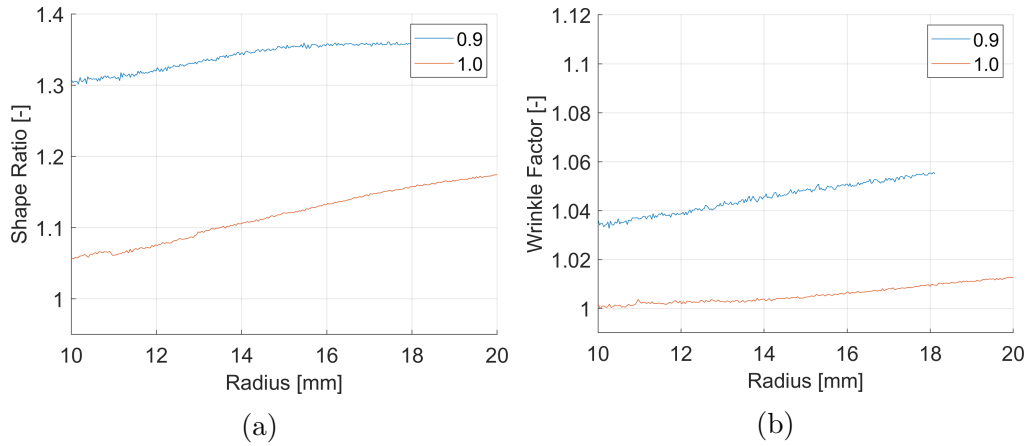


Figure 5.22: Plots for the 0.3 MPa ammonia-air test condition for the average of each equivalence ratio for; (a)shape ratio, (b)wrinkle factor against radius.

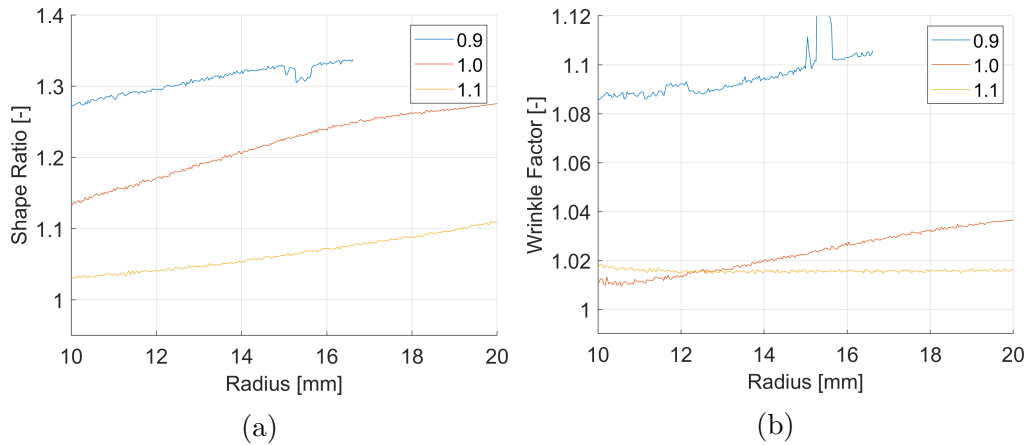


Figure 5.23: Plots for the 0.5 MPa ammonia-air test condition for the average of each equivalence ratio for; (a)shape ratio, (b)wrinkle factor against radius.

became more compressed as buoyancy influenced the flame. For all of the equivalence ratios presented, the relationship plateaued as the flame developed. The wrinkle factor for all conditions also gradually increased with radius, this was as a result of the flame shape becoming less circular due to the flat edge on the underside of the flame.

The plot shown in Figure 5.20 and 5.21 also show the position of the centroid against time as each flame progresses. The maximum horizontal deviation observed was 0.3 mm and the maximum vertical deviation was 11.3 mm with a vertical velocity of 20.2 mm/s. To understand this further, the

vertical velocity of the centroids at different conditions are shown in Figure 5.24a. Although there are limited tests, there was a negative correlation between the flame speed and the vertical centroid velocity. It is difficult to form many conclusions from the luminosity plot of the ammonia-air flames presented in Figure 5.24b this is due to the limited range of equivalence ratios tested. Similar to the methane luminosity plots, the luminosity increases from $\phi = 0.9$ to $\phi = 1.1$.

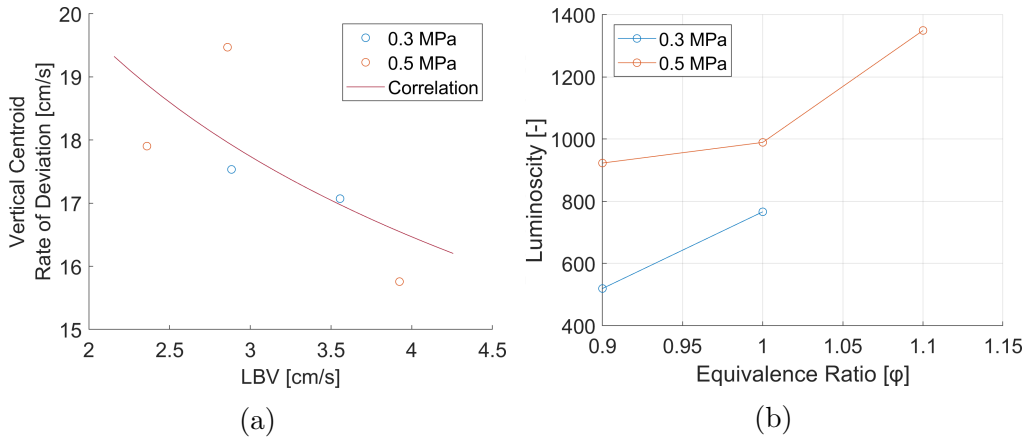


Figure 5.24: Plots presenting (a) flame centroid deviation rate against LBV for each pressure condition for ammonia-air flames, and (b) flame luminosity at a radius of 20 mm for each of the ammonia air test conditions.

Table 5.5: Measured unstretched laminar burning velocity at 0.3 MPa - ammonia-air flames.

ϕ	S_l [cm/s]	Range of scatter from the mean S_l [cm/s]	L_b [mm]	Range of scatter from the mean L_b [mm]
0.89	2.88	-0.04 0.08	0.52	-0.08 0.17
0.99	3.56	-0.25 0.30	0.27	-0.42 0.30

Table 5.6: Measured unstretched laminar burning velocity at 0.5 MPa - ammonia-air flames.

ϕ	S_l [cm/s]	Range of scatter from the mean S_l [cm/s]	L_b [mm]	Range of scatter from the mean L_b [mm]
0.90	2.53	-0.12 0.18	0.52	-0.23 0.12
1.00	2.99	-0.08 0.12	0.58	-0.35 0.36
1.10	3.97	-0.24 0.41	0.03	-0.38 0.55

The mean results of the pure ammonia-air flame mixtures are presented in Tables 5.5 and 5.6, obtained from at least three experimental repetitions of each condition. The scatter of the laminar burning velocity measurements and the Markstein lengths are presented. The average scatter of the laminar burning velocity results was 5.8%. Due to the number of conditions available for testing, it was difficult to form a correlation around the pressure values presented in Figure 5.27a.

The influence of buoyancy is very clear across all ammonia-air flames, in order to understand the influence, two techniques described from literature are used with the experimental data from this study and presented in Figure 5.25. The techniques used are described in detail in Section 2.2.5.

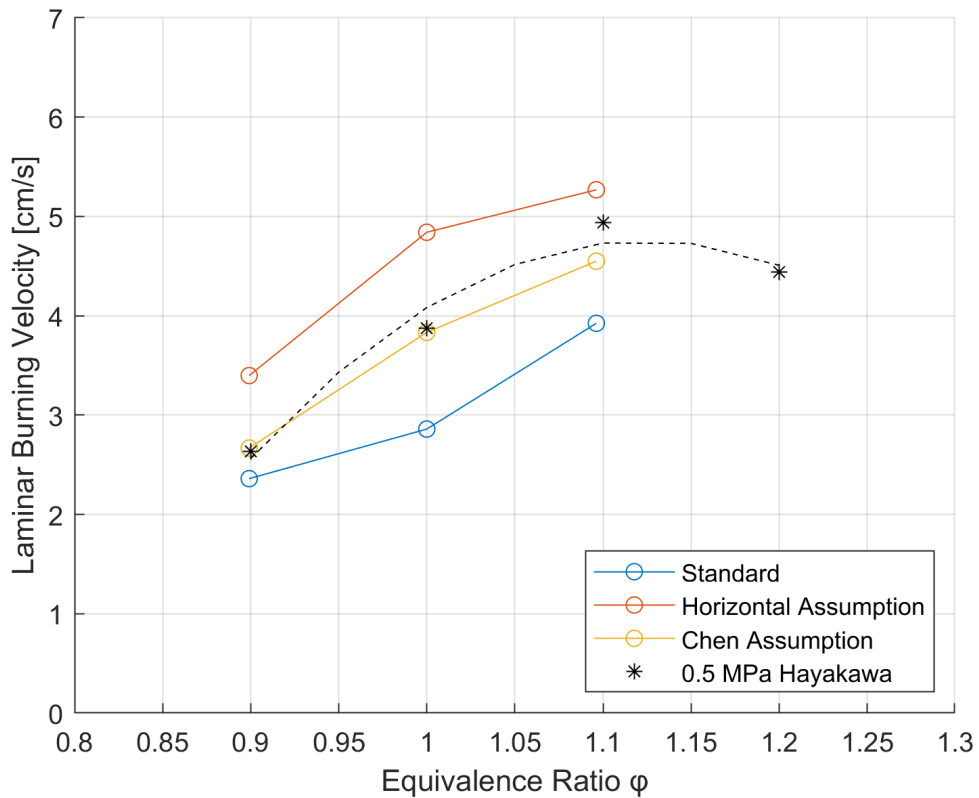


Figure 5.25: Laminar burning velocity vs equivalence ratio for premixed ammonia-air combustion at 0.5 MPa initial pressure compared to literature. Three techniques compared to account for buoyancy as described in Section 4.4.1.

Figure 5.26 presents the experimental equivalence ratio sweep against LBV

for the ammonia-air premixed flames alongside a similar study performed by Hayakawa et al. [57] for both 0.3 MPa and 0.5 MPa initial pressures. There is good alignment with literature for the 0.5 MPa condition, however for the 0.3 MPa condition there are not enough points to see a strong relation.

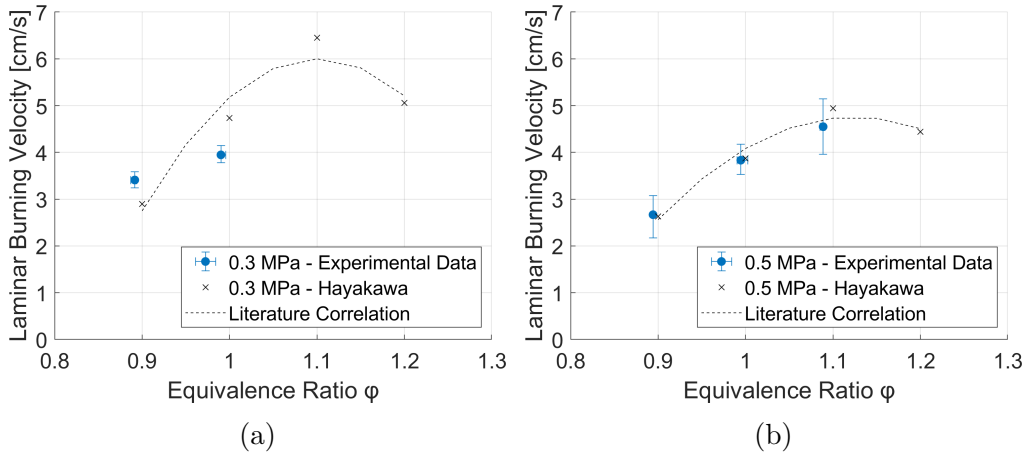


Figure 5.26: Plot presenting the buoyancy adjusted laminar burning velocity against equivalence ratio for the 0.3 and 0.5 MPa pressure conditions.

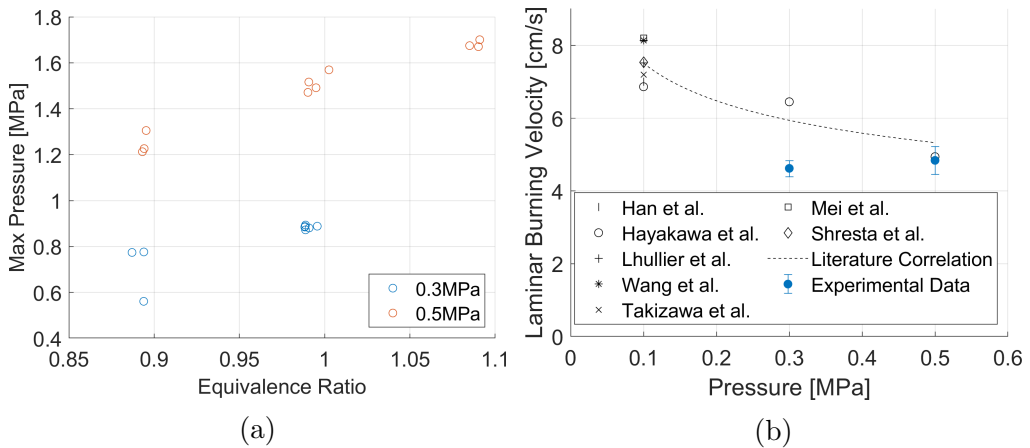


Figure 5.27: Plots presenting the (a)Max pressure vs equivalence ratio for premixed ammonia combustion at 0.1 MPa - 0.5 MPa initial pressure and (b)the laminar burning velocity results against literature for ammonia-air flames at varying pressures.

5.4 Ammonia/hydrogen testing

This iteration of combustion chamber experiments involved understanding the influence of hydrogen on ammonia flame structures and characteristics. With hydrogen acting as a combustion promoter, results were taken across three pressures, 0.1 MPa, 0.3 MPa, and 0.5 MPa at an equivalence ratio of 1.0 with varying hydrogen substitution ratios (SRs). The SR, based on the stoichiometric molar ratio, is defined in Section 5.1.1.

Figure 5.28 presents the combustion results at 0.1 MPa for varying hydrogen SRs. At this pressure condition, $SR = 0$ and 0.1 were unable to be achieved. The flame luminosity decreased as the hydrogen concentration increased and the flame speed increased substantially between $SR = 0.2$ and 0.5. The centroid showed little movement, less than 0.6 cm/s for all flames. The contour plot, Figure 5.29, presents three contour plots for the ammonia 0.1 MPa condition. The flames remain stable with no cellularity observed. Some movement of the centroid position was observed however it was not to a high degree, a maximum of 1.3 mm in the vertical direction and 0.2 mm horizontally.

Figure 5.30a presents the plot of shape ratio against flame radius for the 0.1 MPa initial pressure condition. The values of shape ratio are relatively low and close to 1.0, for $SR = 0.2$ and 0.5 conditions the ratio remained almost constant, which is reflected in Figure 5.30b. This indicates the flames were very spherical and not wrinkled. The $SR = 0.3$ conditions showed decreasing values towards 1 for both the shape ratio and the wrinkle factor. This is also shown in the flame contour plot, Figure 5.29.

The results from the 0.3 MPa test condition are presented in Figure 5.31. The SR was successfully varied from $SR = 0 - 0.5$ molar ratio of hydrogen.

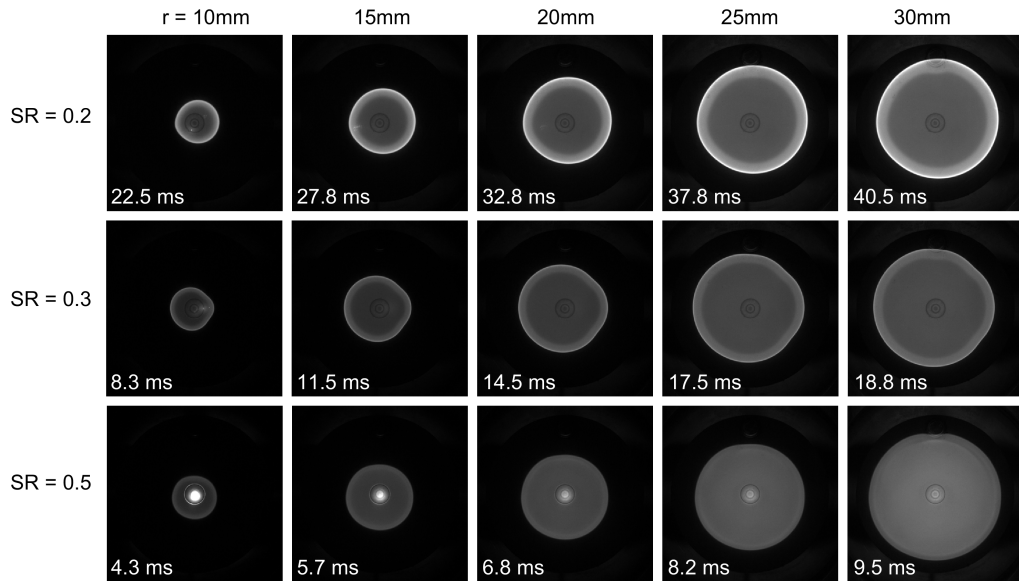


Figure 5.28: High speed images of spherically propagating ammonia-hydrogen-air premixed flame at an initial pressure of 0.1 MPa with varying SRs at an equivalence ratio of 1.0.

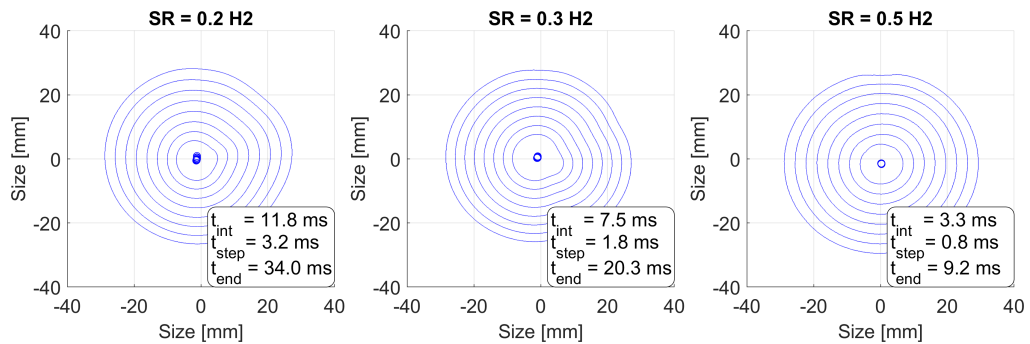


Figure 5.29: Flame contours of ammonia-air flames at 0.1 MPa at varying SRs.

The time stamps on the frames show the increase of speed with increasing hydrogen substitution as well as a decrease in the influence of buoyancy. At $SR = 0.3$ and 0.5 there was a presence of cracks on the flame front as indicated by the contour plots, Figure 5.32. The maximum centroid deviation observed was 5.4 mm vertically and 0.2 mm horizontally, this is not accounting for the $SR = 0$ flame which is discussed in the previous section. The cracks initiated early on in the propagation did not develop for the $SR = 0.3$ condition, however for $SR = 0.5$ the cracks developed further as the flame expanded.

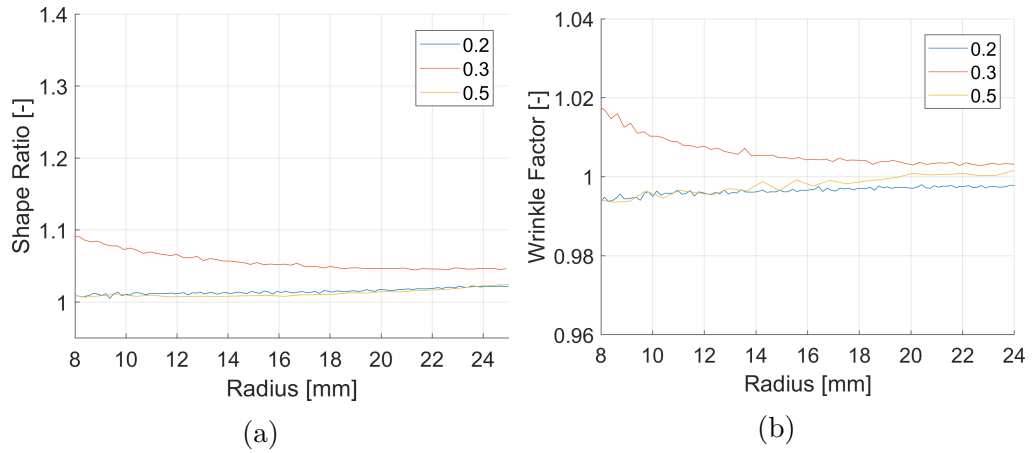


Figure 5.30: Plots for the 0.1 MPa ammonia-hydrogen-air test condition for the average of each SR for; (a)shape ratio, (b)wrinkle factor against radius.

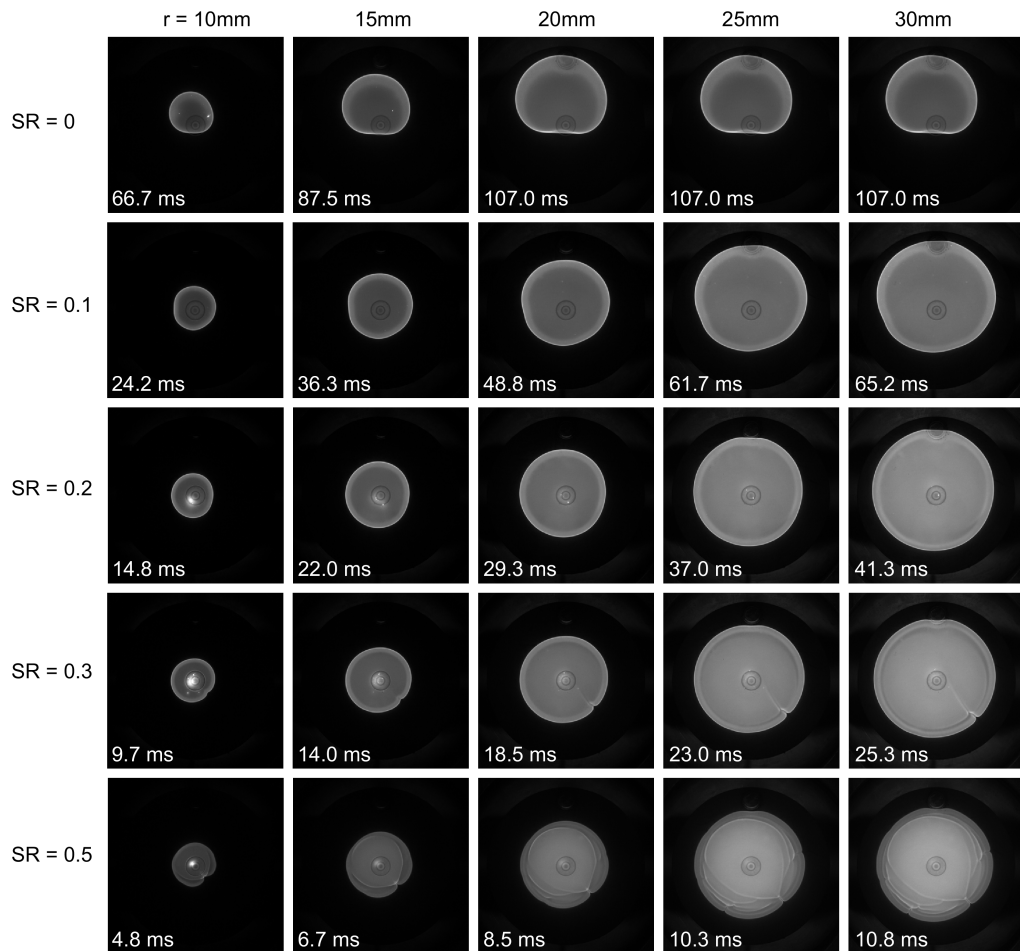


Figure 5.31: High speed images of spherically propagating ammonia-hydrogen-air premixed flame at an initial pressure of 0.3MPa with varying SRs at an equivalence ratio of 1.0.

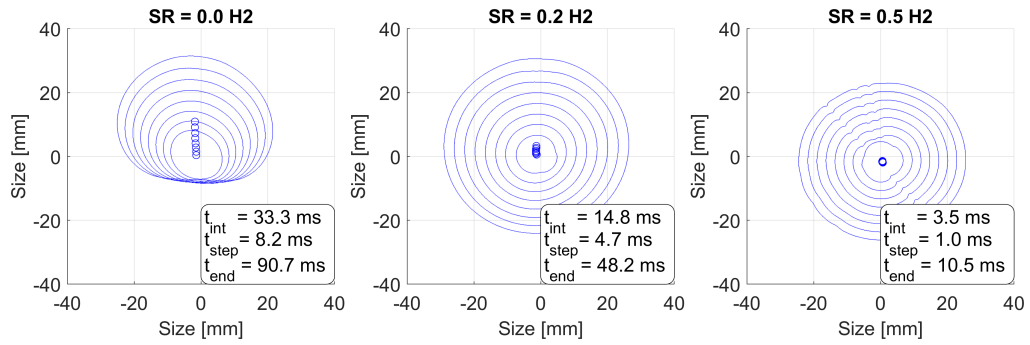


Figure 5.32: Flame contours of ammonia-air flames at 0.3 MPa at varying SRs.

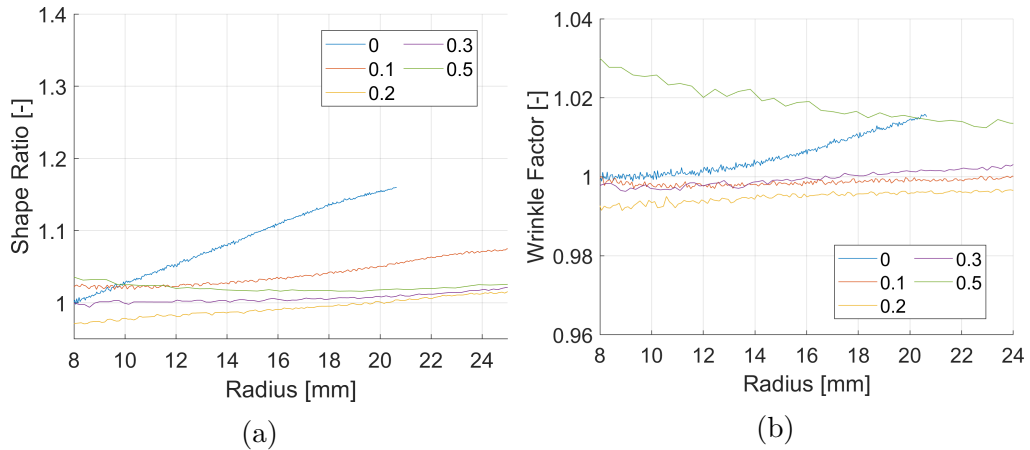


Figure 5.33: Plots for the 0.3 MPa ammonia-hydrogen-air test condition for the average of each SR for; (a)shape ratio, (b)wrinkle factor against radius.

The shape ratio plot presented in Figure 5.33 shows the results for the 0.3 MPa test condition. For $SR = 0$ and 0.1 , the flames showed clear influence of buoyancy on the flame shape as indicated by the increasing shape ratio over radius. The other SRs remained relatively constant throughout the propagation. The wrinkle factor plot shows the $SR = 0$ plot gradually increasing due to the misshapen nature caused by buoyancy, it also shows a relatively high value for $SR = 0.5$, this is as a result of the cellularity seen throughout the expansion.

Figure 5.34 presents the 0.5 MPa test condition. In this condition the onset of cellularity appeared at a lower SR of 0.3 hydrogen with some level appearing at 25 mm flame radii at $SR = 0.2$. The contour plots,

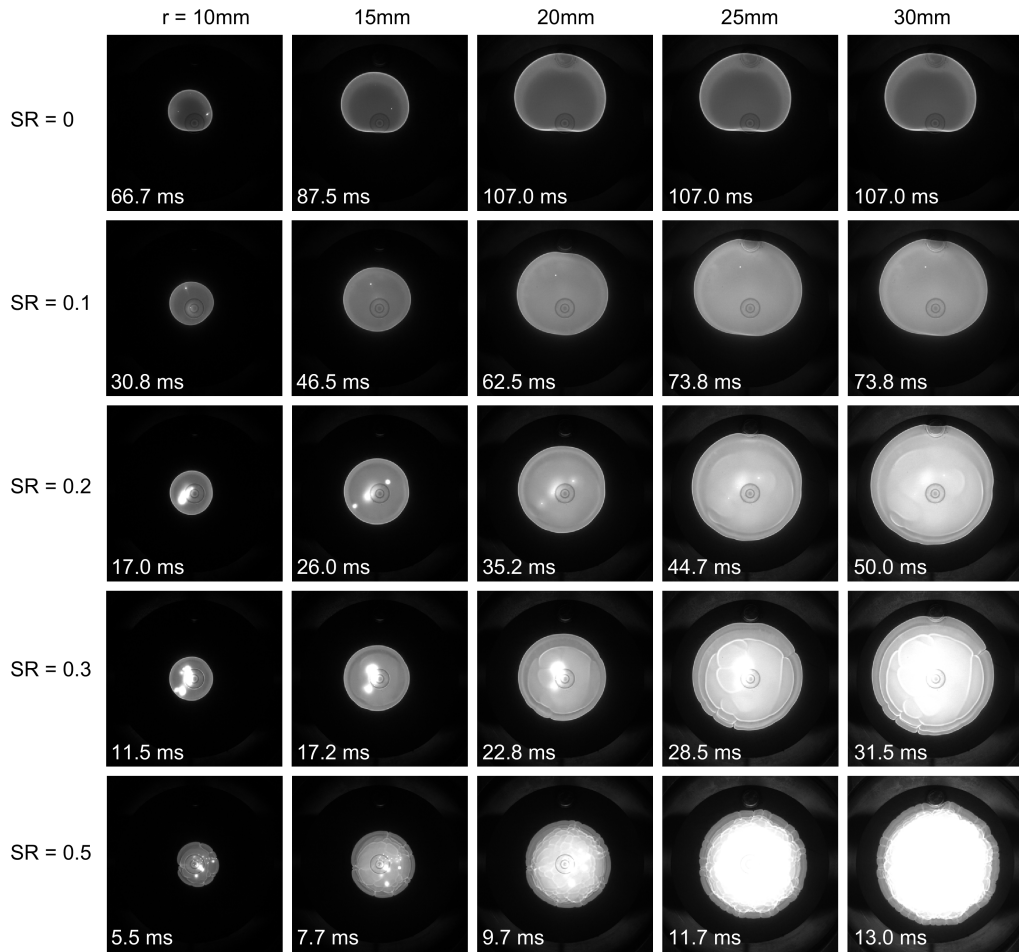


Figure 5.34: High speed images of spherically propagating ammonia-hydrogen-air premixed flame at an initial pressure of 0.5MPa with varying SRs at an equivalence ratio of 1.0.

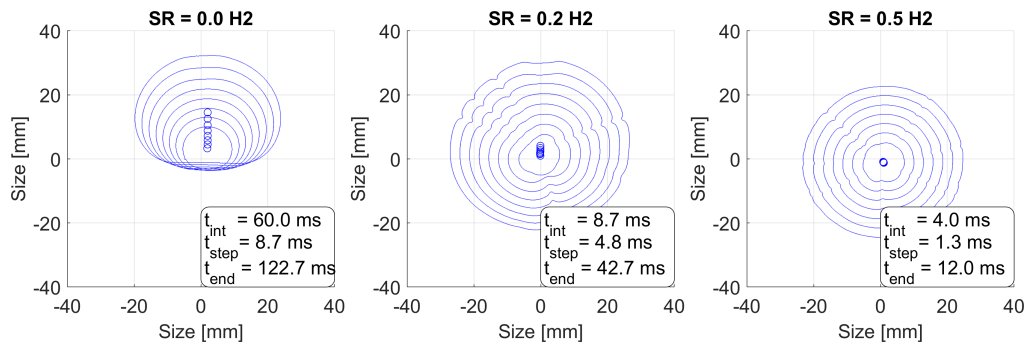


Figure 5.35: Flame contours of ammonia-air flames at 0.5 MPa at varying SRs.

presented in Figure 5.35, show the onset and development of cellularity in both the SR = 0.2 and 0.5 flame conditions. It also shows that the SR = 0.2 flame was slightly influenced by buoyancy as indicated by the rising

centroid value. The maximum observed deviation was 6.7 mm vertically and 0.2 horizontally, once again not accounting for $SR = 0$. The shape ratio plot, Figure 5.36a, shows the clear deformation of the flame for the $SR = 0$ and 0.1 flames as the ratio increased for both conditions. The ratio remained constant for the other three conditions. The wrinkle plot for this test condition, Figure 5.36a, show an upwards trend for each of the SR , indicating the flame fronts were becoming more wrinkled as they expanded. Figure 5.37 shows the correlation of rate of centroid deviation against the laminar burning velocity, there is a very strong trend showing the exponential increase of centroid movement at decreasing speeds.

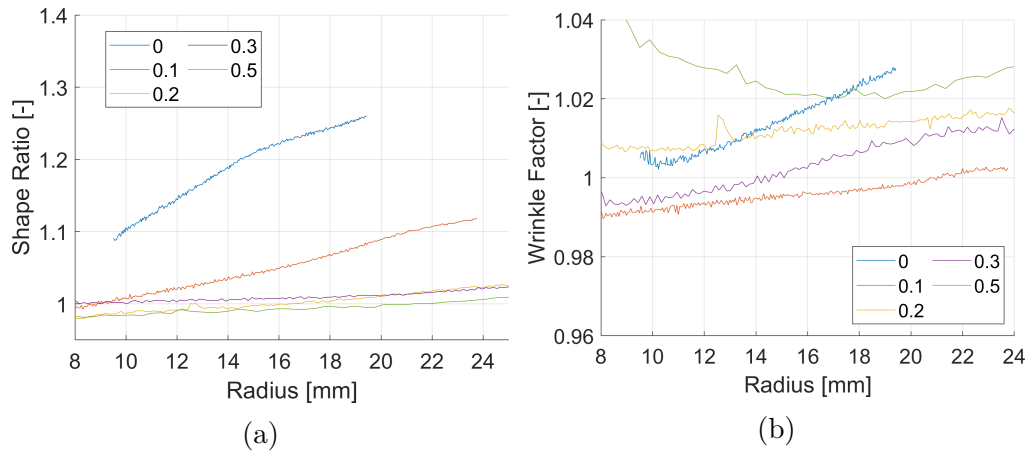


Figure 5.36: Plots for the 0.5 MPa ammonia-hydrogen-air test condition for the average of each SR for; (a) shape ratio, (b) wrinkle factor against radius.

Both the 0.1 and 0.3 MPa pressure conditions show similar luminosity relationships with $SR = 0.2 - 0.5$ as presented by Figure 5.38a. The 0.5 MPa condition deviated from the trend and continued to increase the luminosity gradually with SR . Figure 5.38b, shows that across all three pressure conditions the maximum combustion pressure observed increased as the SR increased.

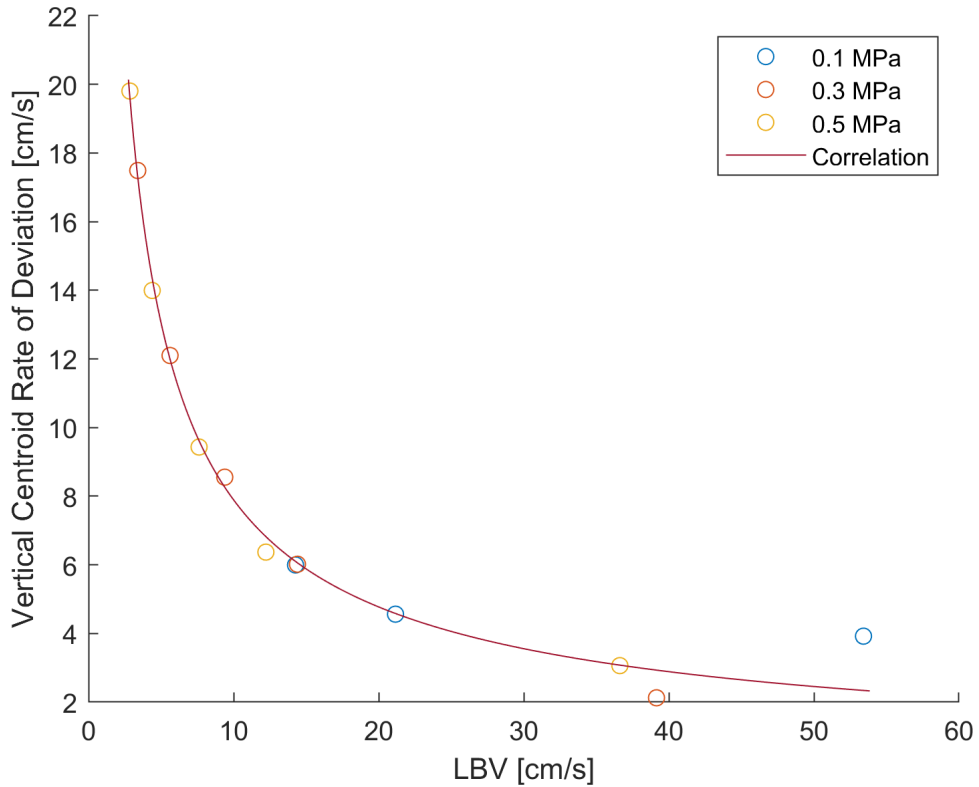


Figure 5.37: Plot of flame centroid deviation rate against LBV for each pressure condition for ammonia-hydrogen-air flames.

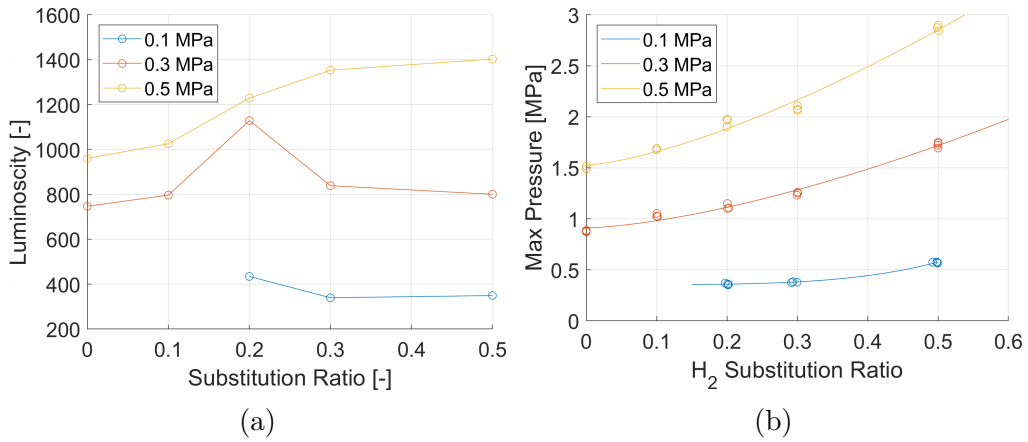


Figure 5.38: (a) Plot of flame luminosity vs hydrogen SR of an ammonia-air premixed flame at an initial pressures of 0.1, 0.3, and 0.5 MPa at an equivalence ratio of 1.0. (b) Max pressure vs SR for premixed ammonia-hydrogen-air combustion at 0.1 MPa - 0.5 MPa initial pressure.

Tables 5.7 - 5.9 present the measured unstretched laminar burning velocity of premixed ammonia/hydrogen mixtures of varying SRs across the three pressure conditions, 0.1 MPa, 0.3 MPa, and 0.5 MPa. Each test condition was repeated a minimum of three times, with the means being presented

in the tables. The range of data scatter from the mean laminar burning velocity is also presented. Across all of the data sets the average scatter was 3.5%.

Table 5.7: Measured unstretched laminar burning velocity at 0.1 MPa with varying ammonia/hydrogen SRs.

SR	S_l [cm/s]	Range of scatter from the mean S_l [cm/s]		L_b [mm]	Range of scatter from the mean L_b [mm]	
0.00	-	-	-	-		
0.10	-	-	-	-		
0.20	14.27	-0.52	0.50	0.41	-0.36	0.36
0.30	21.36	-1.83	1.36	-0.04	-0.12	0.14
0.50	53.26	-0.75	0.51	-0.07	-0.08	0.09

Table 5.8: Measured unstretched laminar burning velocity at 0.3 MPa with varying ammonia/hydrogen SRs.

SR	S_l [cm/s]	Range of scatter from the mean S_l [cm/s]		L_b [mm]	Range of scatter from the mean L_b [mm]	
0.00	3.45	-0.09	0.06	0.23	-0.27	0.17
0.10	5.64	-0.19	0.22	0.01	-0.22	0.19
0.20	9.39	-0.27	0.26	0.20	-0.30	0.38
0.30	14.60	-0.70	0.57	-0.52	-0.13	0.08
0.50	39.26	-0.96	0.82	0.24	-0.15	0.19

Table 5.9: Measured unstretched laminar burning velocity at 0.5 MPa with varying ammonia/hydrogen SRs.

SR	S_l [cm/s]	Range of scatter from the mean S_l [cm/s]		L_b [mm]	Range of scatter from the mean L_b [mm]	
0.00	2.98	-0.07	0.14	0.63	-0.26	0.15
0.10	4.42	-0.21	0.15	-0.02	-0.63	0.48
0.20	7.63	-0.48	0.66	-0.11	-0.19	0.22
0.30	11.90	-0.31	0.44	-0.38	-0.16	0.17
0.50	34.26	-2.40	2.25	0.42	-0.17	0.10

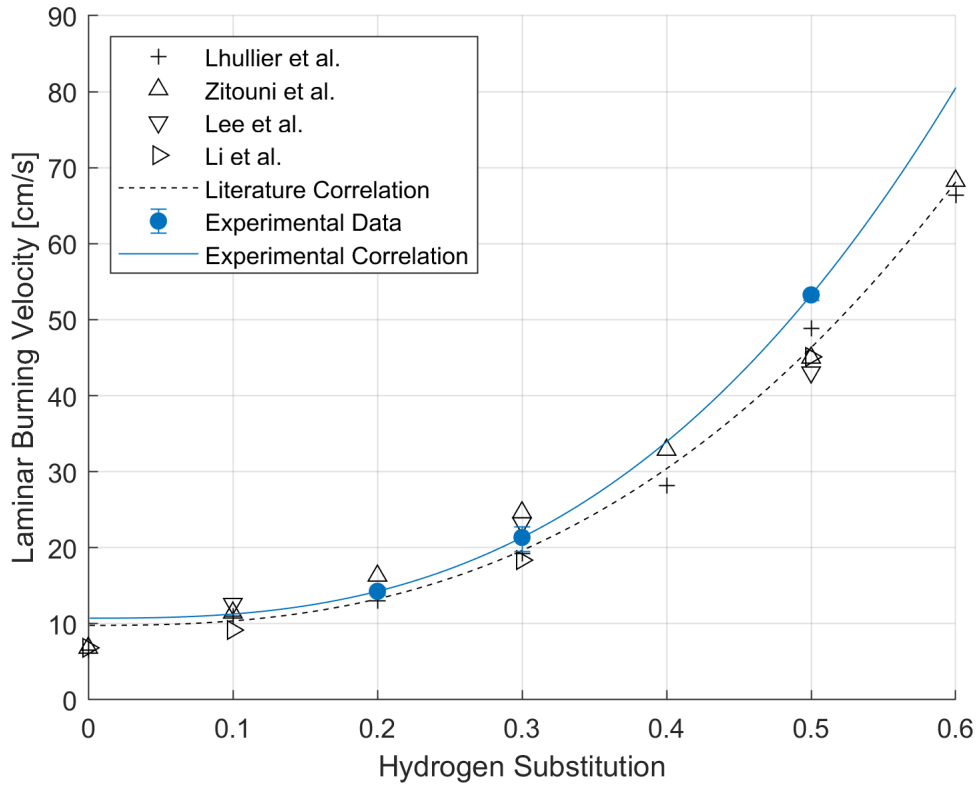


Figure 5.39: Laminar burning velocity vs SR for premixed ammonia-hydrogen-air combustion at 0.1 MPa initial pressure

Figures 5.39 - 5.41 shows good alignment to the literature values for the conditions achieved. The experimental data at the 0.1 MPa pressure condition shows excellent alignment to literature. The 0.3 and 0.5 MPa conditions deviate from literature after $SR = 0.3$.

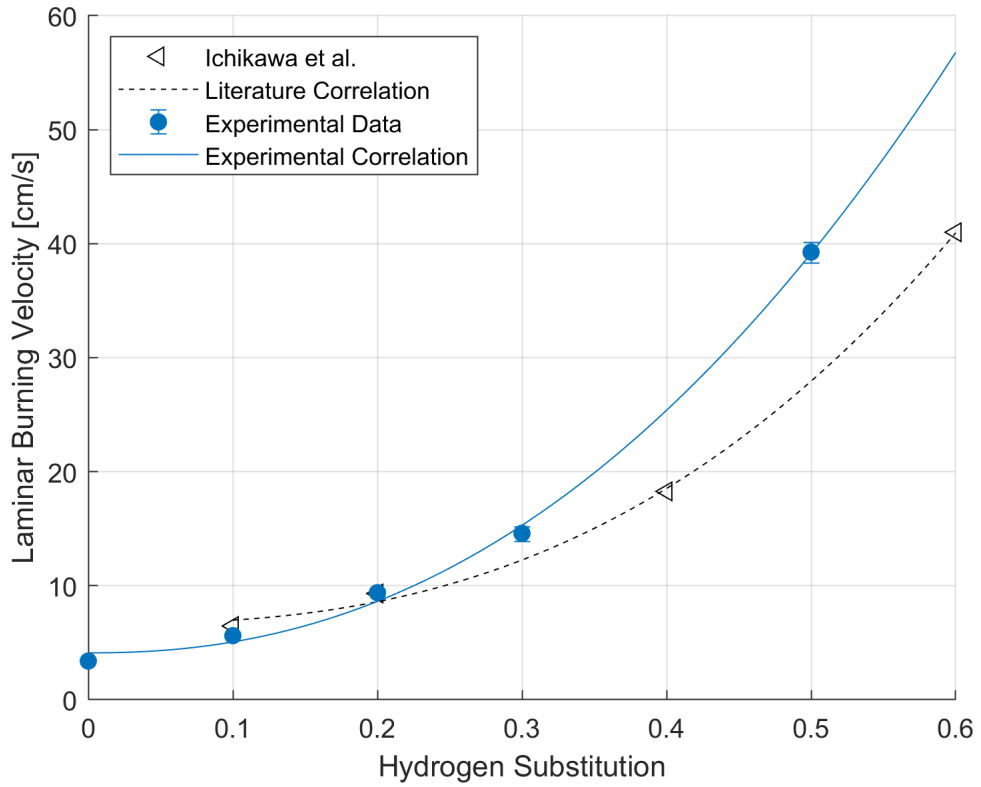


Figure 5.40: Laminar burning velocity vs SR for premixed ammonia-hydrogen-air combustion at 0.3 MPa initial pressure

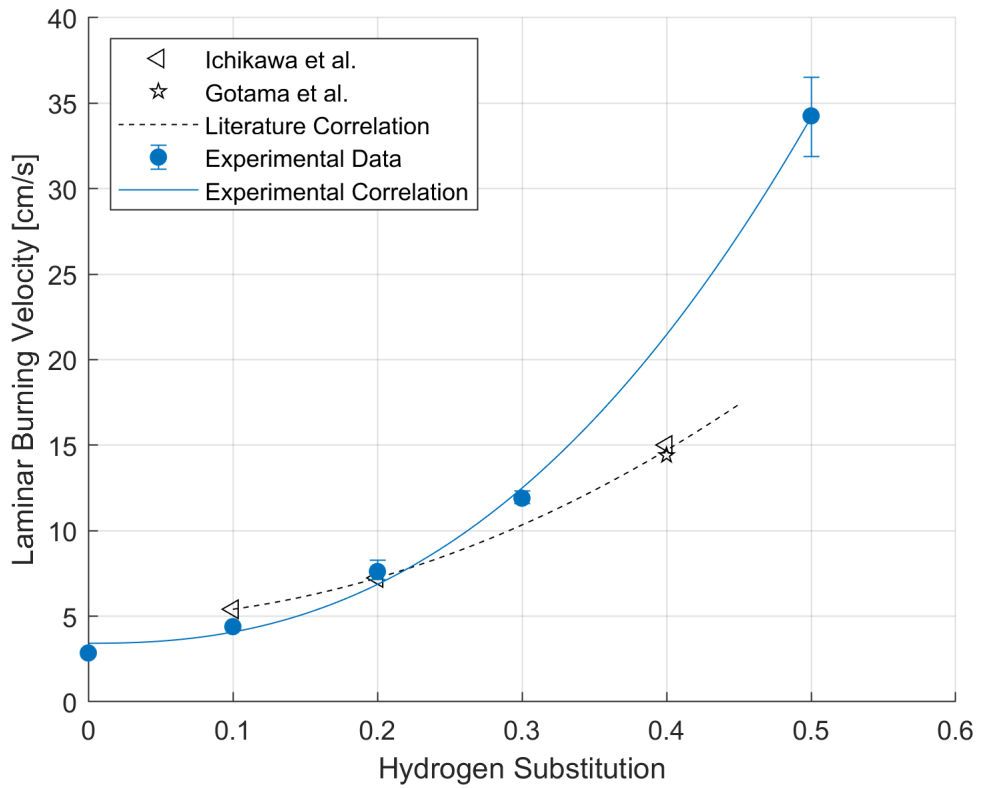


Figure 5.41: Laminar burning velocity vs equivalence ratio for premixed ammonia-hydrogen-air combustion at 0.5 MPa initial pressure

5.5 Side combustion imaging results

The intention of the final set of testing completed was to understand the impact of the wall mounted spark initiation point further and to attempt to address the deviation from the literature. To do this, the experimental setup was adjusted and the side windows were added to the combustion chamber to allow for a side-on view of the combustion. This enabled a comparison to be made of the flame speed against the wall to the flame speed at the furthest point to the wall. The experimental conditions investigated in this study are shown in Table 5.10. The properties of the mixtures used in this study are taken from Table D.1.

Fuel	Pressure [MPa]	Equivalence Ratio ϕ
Methane	0.1	0.8, 1.0, 1.2

Table 5.10: Experimental conditions of the side imaging testing

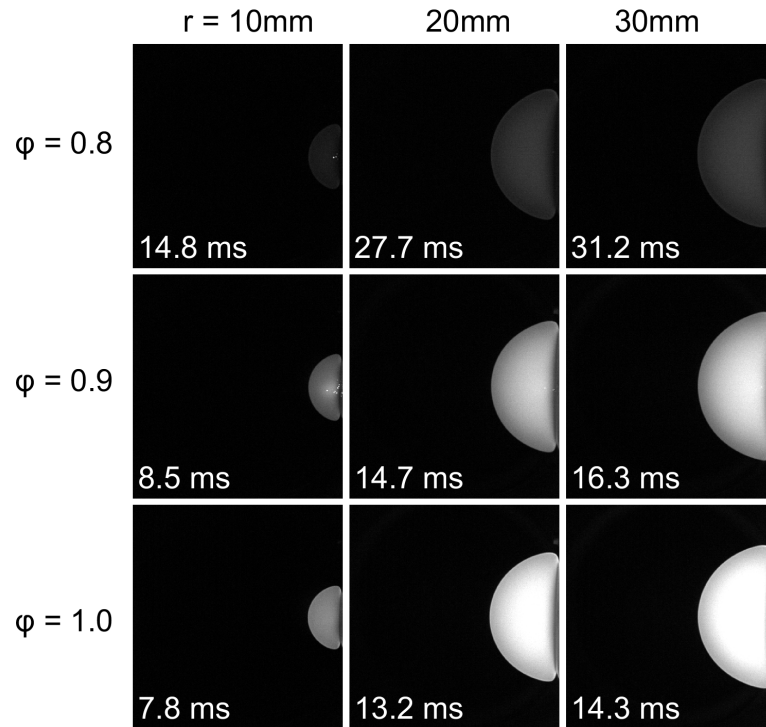


Figure 5.42: High speed images of spherically propagating methane pre-mixed flame at an initial pressure of 0.1MPa with varying equivalence ratios, side-on view.

Figure 5.42 presents the combustion results of the methane condition with the varying equivalence ratios and radii. Once again to allow for relative comparison of flame brightness, the image grids are brightened to the same degree. The development of the radius measured in the horizontal and vertical directions against time is plotted in Figure 5.43 alongside the apparent flame speed. The apparent speeds appear to be similar for the initial propagation however the wall effected speed slows as the flame propagates. This indicates the flame was slowed by the wall.

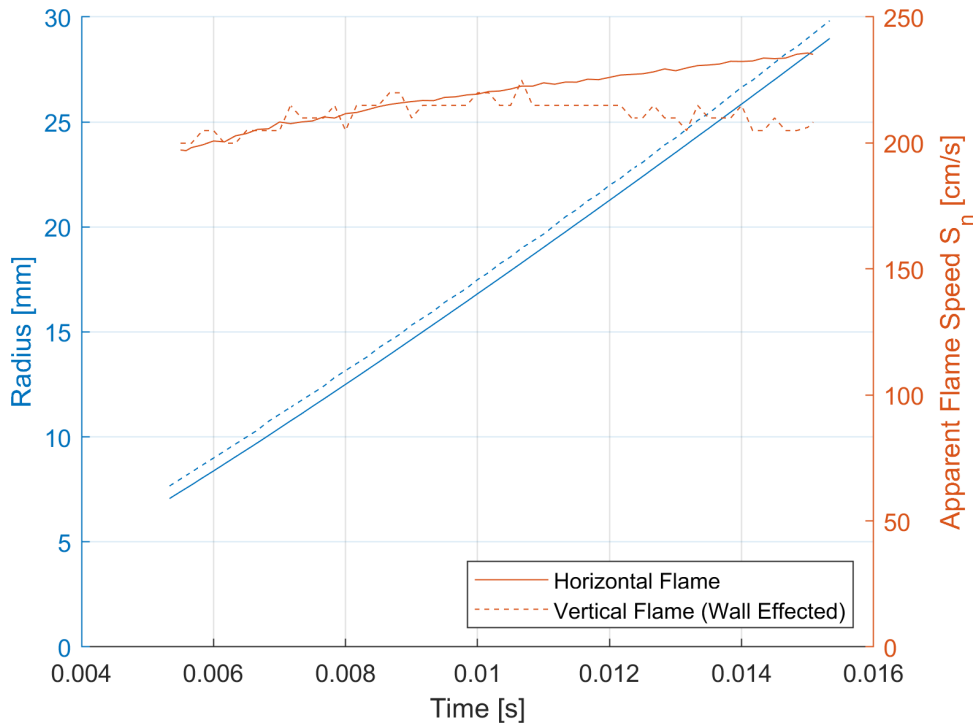


Figure 5.43: Plot of flame radius and apparent flame speed in horizontal and vertical direction against time for methane-air flames at 0.1 MPa, equivalence ratio $\phi = 1.0$.

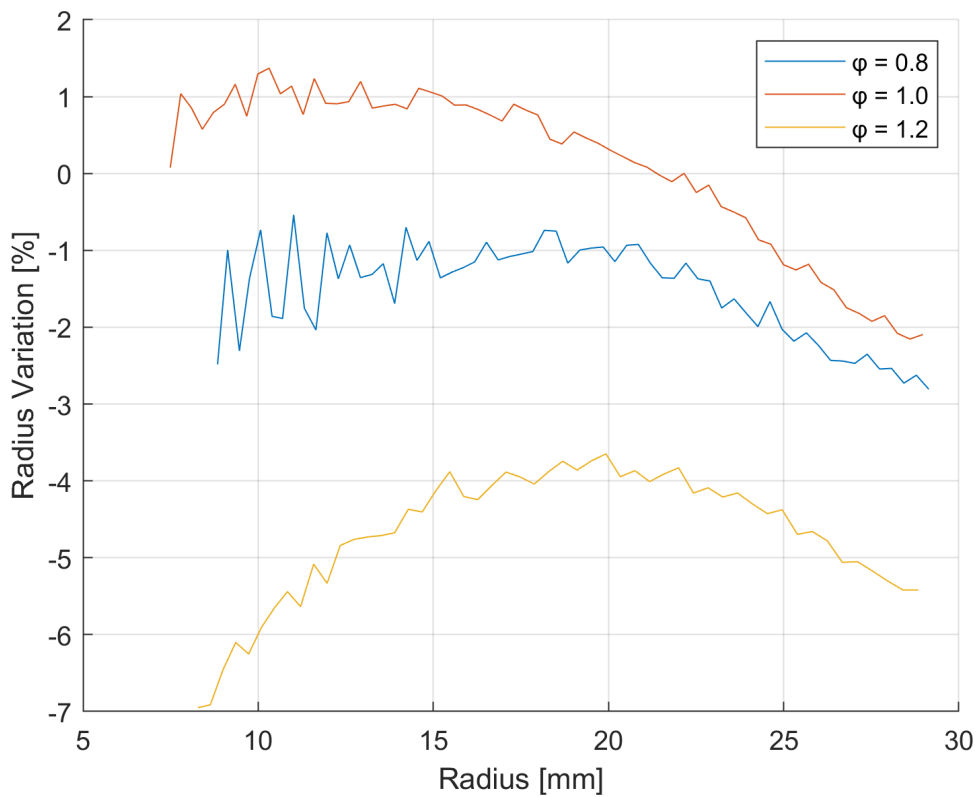


Figure 5.44: Plot of the variation in radius between the horizontal and vertical radii for different equivalence ratios.

Comparing the two calculated flame radii can provide insight into how the influence changes over the flame expansion. Figure 5.44 presents the comparison of each equivalence ratio measured. The radius variation is calculated as the difference between the horizontal radius and vertical radius divided by the horizontal. To understand the influence of the wall further, the two measured apparent flame speeds were plotted against radius for each of the equivalence ratios, the results are shown in Figure 5.45. The influence of the wall appears to change with equivalence ratio, with the influence at its highest at larger radii. In order to compare the equivalence ratios, the apparent laminar burning velocities are calculated from the unstretched flame speeds using the non-linear stretch extrapolation and presented in Figure 5.46. The impact of the wall appears to influence the higher equivalence ratio values more significantly. The lower equivalence ratios are relatively unaffected.

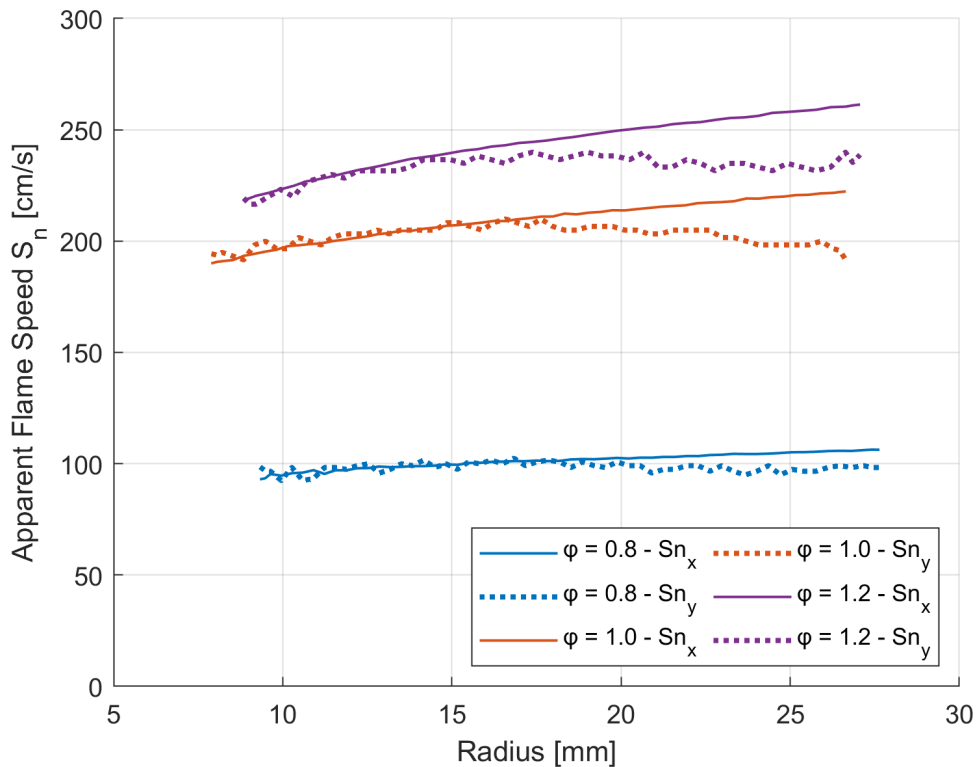


Figure 5.45: Plot of the apparent flame speed against the flame radius for various equivalence ratios considering both the horizontal flame S_{n_x} and vertical (wall influenced) flame S_{n_y} .

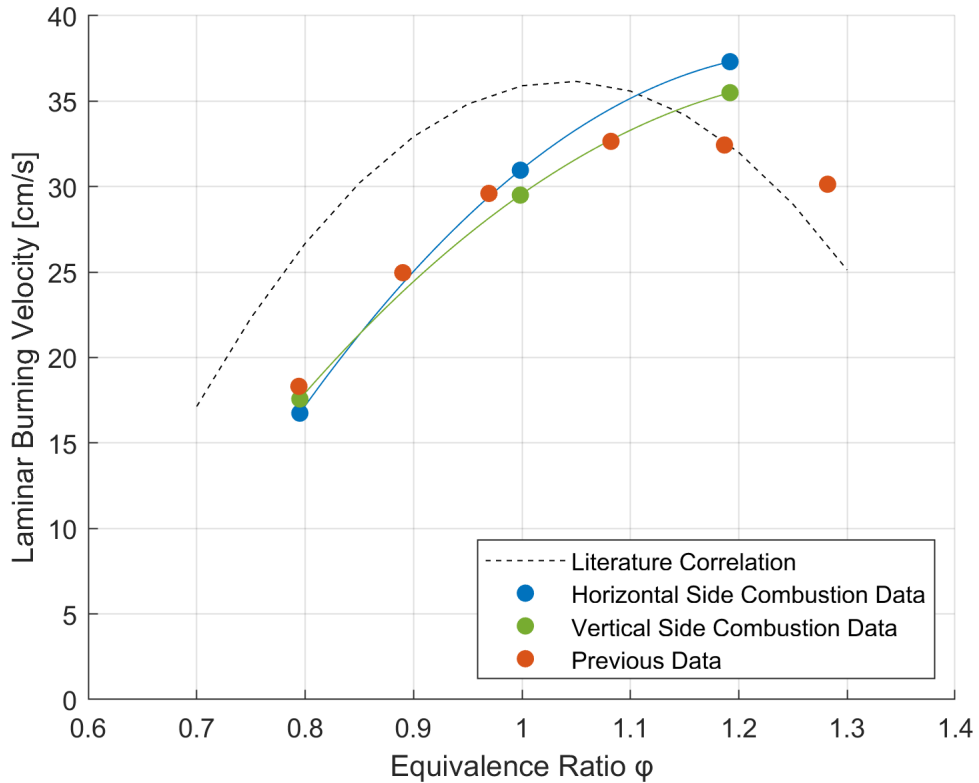


Figure 5.46: Plot of side combustion laminar burning velocities with literature data and previous data.

5.6 Discussion

5.6.1 Methane benchmarking

The methane benchmarking study used the novel combustion chamber to measure methane-air flames with the aim of validating the chamber in measuring ammonia-air and ammonia-hydrogen-air flame characteristics. Given the limited literature results relevant to the experimental set up and conditions, the intention was to understand the capabilities and limitations of the combustion chamber using a fuel with well established literature values and a common source of validation of experimental equipment to compare the results to.

The methane-air 0.1 MPa pressure condition sweep produced very clean

flame images with the one exception to this at $\phi = 0.8$ where there are some residuals post the SI observed in Figure 5.1. These bright spots were regularly observed during the first test of the day, and resulted in an update to the operating procedure to spark the chamber with no fuel five times before testing, this reduced the occurrence. It was suspected that the presence of the bright spots were caused by small pieces of the spark plug being released into the chamber post ignition, these were significantly more apparent in less bright flames such as $\phi = 0.8$. Where the bright spots have been observed, there was no discernible change to the flame front therefore did not impact final laminar burning velocity calculations.

The shape ratio plot for 0.1 MPa, Figure 5.3a, showed very little change other than a slight uplift at higher radii, this suggests the flame front was stable and only very slightly influenced by buoyancy. This was confirmed by the wrinkle plot, Figure 5.3b, which shows across all equivalence ratios a tendency to approach 1.0 as the flame developed, indicating a smooth flame front. The luminosity of the flames were also measured and presented in Figure 5.12a, for the 0.1 MPa pressure condition there was a rise in luminosity at $\phi = 1.1$, this is expected at a leaner condition due to the disassociation effect caused by increased oxygen, however the luminosity then drops off. For the other pressures, the spread in measurements becomes very high as the equivalence ratio increases, for the 0.3 MPa pressure condition the luminosity appears to remain steady above $\phi = 1.1$. For the 0.5 MPa condition the luminosity increases slightly.

Unlike the 0.1 MPa pressure condition, the 0.3 MPa condition presented flames with wrinkles across every equivalence ratio, as seen in Figure 5.4. The wrinkles or cracks that were seen in the flames appeared to originate from the spark initiation as opposed to developing when the flame propagated as shown in the wrinkle plot, Figure 5.6b. This suggested the flame

fronts were still relatively stable, however they were more likely to be influenced by the spark in comparison to the 0.1 MPa condition. The flame contour plots presented a similar story, Figure 5.5, the first contour step from the central point for all equivalence ratios was not circular. The early contour shape was sustained across the flame expansion. The shape ratio plot, Figure 5.6a, alongside the contour plots showed the progression of buoyancy on each of the flames. The buoyancy impacted the $\phi = 0.8$ flame the most significantly, this was seen by the ellipsoidal flame shape and rising flame centroid as well as the positive gradient shape ratio plot. This was also the slowest flame in the comparison.

The 0.5 MPa pressure condition presented a cellular flame across the majority of equivalence ratios, $\phi = 0.8 - 1.1$, at the richer values, $\phi = 1.2$ and 1.3, the flames still presented with cracks that developed but the cells appeared to be significantly larger, as shown in Figure 5.7. The influence of the SI is once again observed in the early flame propagation and sustained throughout the propagation. The contour plots, Figures 5.8, show an even higher degree of centroid vertical movement for $\phi = 0.8$, continuing to strengthen the correlation that buoyancy has a significantly greater impact on slower flames. In addition to this, the development of flame wrinkles in the contours was observed in all of the flames, indicating developing instability/cellularity as the flames expand. The influence of buoyancy was clearly seen by the positive gradients of the shape ratio against radius plots, Figures 5.9a, especially for $\phi = 0.8$ and 0.9.

When comparing to literature, the results of the three pressure conditions show a very similar correlation shape to the data taken from literature, however the results appear to be shifted by 0.1 equivalence ratio. There are a few potential reasons that this variation has occurred. In the case that the shift was as a result of experimental setup error this would suggest

the filling process was making the mixture richer than intended. The error required for this to occur is in the region of 15% between the two pressure transducers which have been re-calibrated to check for any variation. The transducers read identical values when exposed to a common volume indicating this is not the error.

Comparing the general experimental setups between literature and the novel combustion chamber, two main differences can be identified. The first is the optical imaging methods, natural light imaging is not commonly used in laminar burning velocity results due the flame front identification being dependent on the brightest point of the flame. The true position of the flame front is better approximated by the temperature and therefore using schlieren imaging which captures density gradient which is a function of the temperature will improve the accuracy of the flame measurements. Natural light imaging will underestimate the position of the flame front and the changing luminosity as a result of the equivalence ratio can result in loss of flame front definition.

The other variation from literature for this chamber is the geometry and spark initiation, the chamber is a cylindrical design with a counter-bored cylinder to allow for optical access, this may have some influence on the flame propagation but this is minimised by taking a small volume as the active window to avoid the influence of the chamber outer walls. However the spark initiation point is directly on a side wall, this is due to the chamber being designed as a platform to compare the effectiveness of various engine ignition technologies such as TJI with alternative fuels. The closeness to the wall was expected to cause a deviation from the literature values, to understand this further the side view combustion experiments were completed.

5.6.2 Ammonia testing

Across multiple literature studies with ammonia-air flames, adaptation has been made to the SI electrodes including varying the spark gap and spark energy to improve combustion initiation. The combustion chamber will be able to accommodate variable SI systems including the central electrode system, however for the following studies the same SI setup was used throughout. As a result of this, for difficult to combust mixtures such as those with ammonia, the study was limited as the spark energy was not increased and the initiation point was close to the wall. The pressure was varied from 0.1 MPa to 0.5 MPa however the 0.1 MPa condition did not combust. The equivalence ratio was varied from $\phi = 0.9 - 1.1$, once again limited by the inability for combustion.

Following the standard method to avoid the influence of the chamber walls on the flame shape, the resultant range of radii available for measurement will be dependent on the rate of vertical deviation from the centroid. Across the majority of the ammonia-air flames, this equated to 20 mm radius. Figure 5.20, presents the flame contour plots for the 0.5 MPa pressure condition at three different equivalence ratios, here the impact of buoyancy can be seen clearly as well as the relationship between buoyancy and flame speed. The upwards trends on the shape ratio and wrinkle factor plots, Figures 5.22b and 5.23b, show the flame continuing to be impacted by the buoyancy across the entire expansion.

Due to the very slow laminar burning velocity of pure ammonia-air flames, the presence of buoyancy was significant across all of the testing regime. In order to account for this, there have been multiple techniques used in literature, as discussed in Section 2.2.5. Two methods seen in literature,

one used by Pfahl et al. [120], which takes the flame horizontal expansion as the radius, ignoring any vertical influence of buoyancy, and the other developed by Chen et al. [23] simplifies the flame into an ellipsoidal shape, considering the influence of buoyancy across the entire flame front. These methods were applied to the experimental data and compared to known literature values produced by Hayakawa et al. [57] who used a different technique finding a quasi-static region where the flame propagation and shape ratio were constant. These various techniques are plotted in Figure 5.25, firstly the data where no buoyancy is accounted for, shows an underestimation of the flame speed, this is due to accounting for the bottom of the flame dramatically reduced velocity. The “horizontal assumption” used by Pfahl et al, over estimates the flame speed due to considering the horizontal component of buoyancy caused by the flame being squashed as part of the burning velocity. The technique used by Hayakawa is discussed in Section 2.2.5, although a good way of recording the laminar burning velocity without the influence of flame buoyancy, the number of points are limited to the non-buoyancy affected region. Finally the “Chen assumption” used by Chen et al. shows a very good alignment to the method used by Hayakawa et al. suggesting both methods provide good representations of flame speed measurements without buoyancy influence.

Figure 5.26 presents the correlation with literature data, there is some degree of correlation for the 0.5 MPa pressure condition and 0.3 MPa pressure condition. Due to the limitations introduced by the spark plug configuration, a range of equivalence ratios of ammonia air mixtures were unable to combust within the chamber, therefore comparisons are difficult to draw especially for 0.3 MPa. One discrepancy which isn’t quantified is the spark plug wall positioning, it is suspected that there is a high impact of heat loss on the flame. The low laminar burning velocities result in a higher

susceptibility to technique-dependent uncertainties as well as the chamber geometry, this is due to there being more time for the flames to be exposed to the issues. For example when considering the heat loss to the walls, there is a much longer time of exposure in comparison to a methane flame that is five times faster.

5.6.3 Ammonia hydrogen testing

The ammonia-hydrogen-air testing was completed with the aim of understanding the influence of hydrogen as a combustion promoter for ammonia. Three pressure conditions were considered, 0.1, 0.3, and 0.5 MPa, with an equivalence ratio fixed at stoichiometric $\phi = 1.0$. The SR of hydrogen by molar ratio was varied from SR = 0 to 0.5.

During the pure ammonia-air testing at 0.1 MPa there was no combustion observed at any equivalence ratio, with hydrogen SR = 0.2 reliable combustion was achieved. Figure 5.28 presents the flame images for the 0.1 MPa pressure condition, these images show the progression of the flame from $r = 10\text{mm}$ to $r = 30\text{ mm}$ for each of the SRs. An interesting point to note is the change in flame intensity gradient as the hydrogen SR increases, at SR = 0.2 the flame had a bright edge and thick border which decreased as the hydrogen ratio increased. At SR = 0.5 the bright border was no longer obvious and the flame was less bright. This is expected of hydrogen which has little light emission at stoichiometric mixtures. The plots of shape ratio and wrinkle factor, Figures 5.30, show very little change for SR = 0.2 and 0.5, this indicates very stable and smooth flames at these conditions. The SR = 0.3 condition initially is high at a small radius before tending to 1.0 for both the wrinkle factor and shape ratio. This suggests some level of spark influence on the flame shape which is then stabilised as the flame

propagates through the mixture. There is very little evidence of buoyancy observed across the flames in Figure 5.29, this is due to the high velocity overcoming the buoyancy affect.

The full substitution range was achieved for the 0.3 and 0.5 MPa pressure conditions. Figure 5.31 presents the flame images for the 0.3 MPa pressure condition across the SRs. A similar relationship around the flame edge brightness as the hydrogen ratio increases can be observed however it appears more gradually. The increase in flame speed was dramatic as the hydrogen SR increased with the impact of buoyancy being present strongly in the $SR = 0$ flame and slightly in the $SR = 0.1$ flame. At higher SRs, $SR = 0.3$ and 0.5 , the presence of wrinkles and cracks in the flame front is observed in the contour plots, Figure 5.32. For the $SR = 0.3$ condition the crack appears to originate from the point of ignition and remain throughout the propagation, other cracks did not form unlike the $SR = 0.5$ condition where there was clear cell development in the flame. Confirming the observations around the impact of buoyancy, the shape ratio plots, Figures 5.33a, depict a clear shape change as the radius increases for $SR = 0$ and 0.1 . The large influence of buoyancy on the flame shape can be seen to read across into an increasing wrinkle factor as well which highlights the wrinkle factor does not just indicate flame wrinkles in some cases. Within Figure 5.33b, the $SR = 0.5$ case shows true flame wrinkling and therefore a high wrinkle factor throughout, the gradual decrease is as a result of the increasing flame radius.

The appearance of cellularity occurred at a lower SR for the 0.5 MPa pressure condition, this is expected as the flames will be more prone to Darrieus-Landau and thermodiffusive instabilities resulting in flame wrinkling [12]. Figure 5.34 presents the progression of the flames at the 0.5 MPa pressure condition across all SRs. At $SR = 0.2$ some degree of cel-

lularity can be observed in the 25 and 30 mm frames, at $SR = 0.3$ and 0.5 the cellularity is significantly more pronounced. As the hydrogen ratio increased, the cells reduced in size and appeared earlier in the propagation. The high cellularity of these two conditions will result in higher flame surface areas and will increase the flame speed significantly. The shape ratio plots indicate the influence on buoyancy at the $SR = 0$ and 0.1 conditions, Figure 5.36a, with the higher SR conditions remaining stable. The influence of cellularity on the wrinkle factor shown in Figure 5.36b shows the high or increasing value for all conditions, although noting a similar case of buoyancy shape change but no wrinkling for the $SR = 0$ plot.

The apparent increase in flame speed as a result of cellularity is seen to affect the correlation with literature across all three laminar burning velocity against SR plots shown in Figures 5.39, 5.40, and 5.41. Each of the fits show good alignment to the literature with an overestimation occurring when the flames tended towards cellularity. The increase in cellularity as a result of the hydrodynamic and thermodynamic instabilities results in self acceleration of the flame as the surface area and therefore reaction area increases significantly [84].

Although presented for each fuel, the relationship of buoyancy to laminar burning velocity is compiled in Figure 5.47 for all fuels in the study. The figure presents the flame centroid vertical rate of deviation against laminar burning velocity, indicating the influence of buoyancy on flames with low burning velocities. The relationship goes exponential as the laminar burning velocity decreases with a relationship of,

$$\frac{dy_{cent}}{dt} = 3.817 * S_L^{-0.634} \quad (5.7)$$

where dy_{cent}/dt is the centroid vertical deviation with time and S_L is the

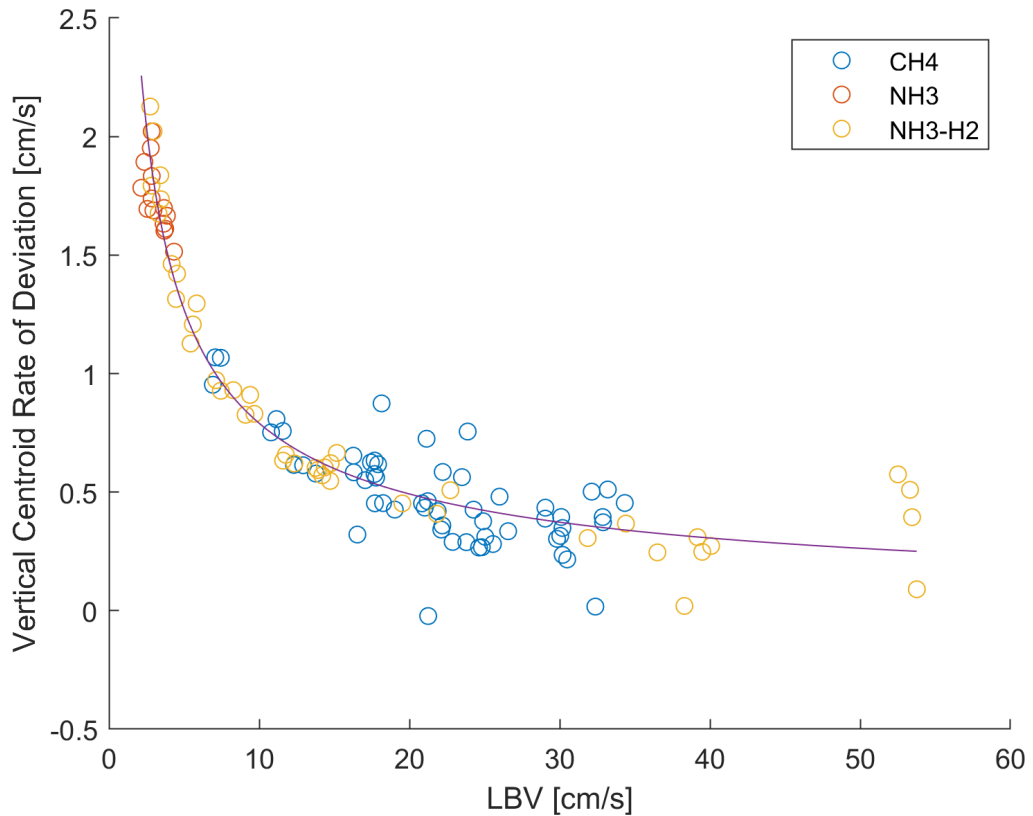


Figure 5.47: Plot of flame centroid deviation rate against LBV for each pressure condition for all flames measured.

unstretched laminar burning velocity. Ronney and Wachman proposed the limit at which buoyancy could be ignored to be 15 cm/s [131] which in this instance suggests a centroid velocity of 0.69 cm/s.

5.6.4 Side combustion study

The intention of the side combustion study was to further investigate the shifted methane laminar burning velocity measurement. One hypothesis for the shifted values was as a result of the wall influence. To understand this further the camera was moved to a side position to be able to understand if there was a variation between the flame progression near to the wall and furthest from the wall. The study found that the influence varied across equivalence ratios, with the richer flames being affected more than the

leaner flames albeit not enough to show good alignment to literature. The influence of heat transfer to the wall resulting in the flame slowing can be seen clearly in the apparent flame speed plots in Figure 5.45. It shows as the flame radius increases, the velocity of the flame close to the wall decreases. This appears to be correlated to the equivalence ratio as the $\phi = 1.2$ is more impacted in comparison to $\phi = 0.8$. The other influence is around the stretching of the flame, due to it not being completely spherical, the flame stretch assumption that it is expanding in all directions as a sphere will be impacted especially at the walls as the flame cannot expand towards the wall.

The misalignment with literature is still present and is suspected to be as a result of the wall interactions, although the side combustion study provided details around the flame expansion against the wall in comparison to away from the wall, the initiation of the flame still occurs very close to the wall. This can result in the flame losing temperature as seen in the ammonia flame testing where equivalence ratios reached by literature were not able to be replicated with the chamber as well as the early stages of flame propagation being strongly influenced by the wall which will influence the later flame. The intention of the combustion chamber was to build a platform able to compare “real-world” combustion systems within a controlled, quiescent environment. The literature laminar burning velocity results provide a comparison for the chamber however due to its design, the results were not expected to match literature. The results obtained in the investigations provide a baseline set of findings to be used in comparison with future work to understand how modern combustion systems can improve the combustion of alternative fuels such as ammonia.

Chapter 6

Experimental Engines

The experimental test rig and setup utilised for the ammonia-hydrogen dual fuelling engine testing is described in the following chapter. It contains information about the test bed instrumentation and control, the data acquisition, and technical specifications of the engine. The base engine used was a 2017 Volvo D8 diesel engine, which was upgraded to be able to operate on multiple fuels including ammonia and hydrogen. The two new fuelling systems are described in detail alongside the engine control unit upgrade that was required.

The intention of the engine testing was to evaluate the performance of a dual fuel heavy-duty engine at low loads and explore the viability of retrofitting of diesel engines.

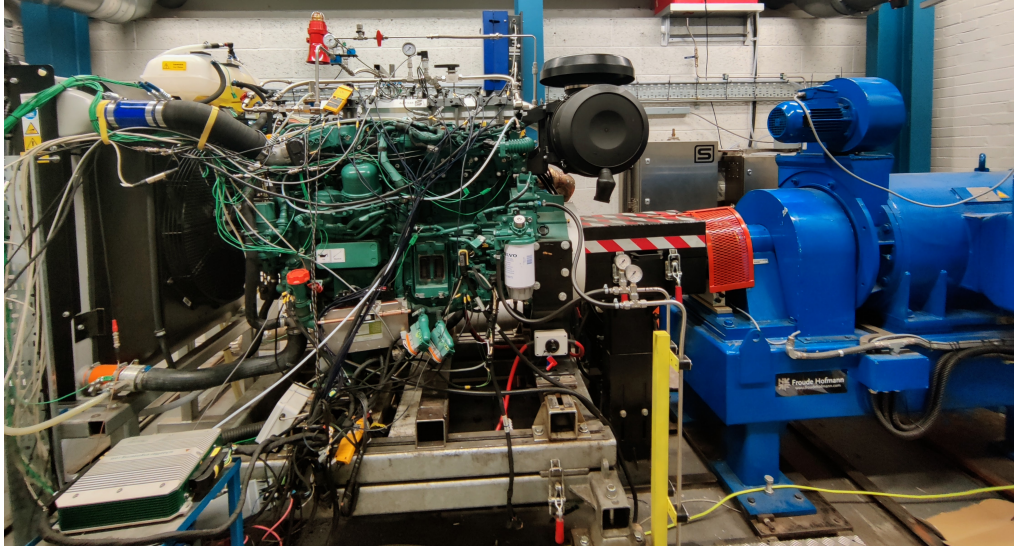


Figure 6.1: Volvo engine test rig.

6.1 Background

Chapter 1 highlights there is a clear direction that the marine industry has identified that sustainable low/zero carbon ammonia will be part of the future energy mix by 2050. As a result, many larger industry players are priming their future engines to be able to operate either partly or fully on ammonia. Decarbonisation solutions for engines above 0.1 MW are needed, this will be relevant not only for shipping but also for agricultural and industrial plant equipment. As discussed in Section 2.5, further research is needed to understand the viability of ammonia as a fuel for these areas especially around fuel control and emissions, however the combustion characteristics and engines performance must also suit the application.

6.2 Engine test facilities

The engine test facility shown in Figure 6.1, includes a fuel metering and conditioning unit, exhaust gas analysis, and an industry standard dy-

namometer. The engine used is an in-line 6 cylinder, 4 stroke Volvo PENTA (Model number: TAD873VE). It is described as an off-road diesel engine with 235 kW brake power or 320 HP, rated at 2,200 rpm. It has a 7.7 L cylinder displacement and operates using a common rail fuel injection system, with a variable geometry turbo (VGT). The engine operates with a dual radiator, one designated for the inter-cooler and the other for engine coolant, and a cooled exhaust gas re-circulation (EGR) system. A small modification has been made on the coolant circuit to provide cooling for the exhaust side pressure transducers.

The combustion chamber of the engine was based upon a “Siamese” port design, with the geometry designed to induce a degree of swirl (with one port relatively curved). The piston was based upon a typical “Omega” bowl geometry, with squish flats around the periphery to also induce increased in-cylinder turbulence. The engine was compliant with Stage V off-road emissions regulations, being procured as the stationary generator set version. The hardware level (diesel common rail, external EGR, VGT) was however typical of that expected in current diesel engines across automotive, marine and off-road. The engine calibration was irrelevant during the currently reported work, as the testing was all undertaken using an open ECU at steady state with the emissions after-treatment disabled.

6.2.1 Dynamometer

The engine is mounted on a testbed and connected to a Froude Hofmann Dynamometer with a rated capacity of 460 kW at 7500 rev/min. The dynamometer is powered by an ABB AC drive unit able to both motor and absorb the engine output throughout its entire operating range. This is controlled using a D3000 Digital Dynamometer Controller that is capable

Volvo Penta - TAD873VE	
No. of cylinders	6
Capacity	7.7 liters
Cooling system	Water cooled
Induction system	Turbocharged, Intercooled
EGR system	Electronically controlled EGR system
Bore	110 mm
Stroke	135 mm
Compression ratio	17.5:1
Rated power	235 kW @ 2200 rpm
Maximum torque	1310 Nm @ 1450 rpm
Fuel injection system	High-pressure common-rail
Common rail pressure	2000 bar
Valves per cylinder	2 intake; 2 exhaust

Table 6.1: Main specifications of the test engine used in the present work.

of maintaining constant speed against varying engine torque throughout the cycle as well as being able to vary the engines speed whilst maintaining torque. These are known as speed mode or torque mode. For safety the dynamometer is oversized to the engine, this enables it to safely control the engine and ramp down in the case of an emergency stop.

6.3 Diesel fuelling system

Figure 6.2 provides a schematic of the diesel supply system used to fuel the engine test rig. The diesel is pumped using a lift pump into the Sierra FuelTrak Transient metering and conditioning system. The pump operates on a fixed voltage, so the back pressure is managed with a return needle valve routed back into the tank to meter the flow. The FuelTrak system includes two Coriolis flow meters which provide instantaneous tracking of the feed and return flow rates which in-turn provide a instantaneous fuel consumption. There is also an option of steady state operation using an integrated weighing rig.

Coriolis flow meters operate on the principles of motion mechanics, the device splits the working fluid and directs it via two vibrating tubes driven by a drive coil. The tubes oscillate in opposition to one another at their natural frequency. The fluid is forced to accelerate as it meets the peak-amplitude vibration and decelerate as it moves away from this. The result is a twisting reaction of the flow tube during flowing conditions, this influences the vibrating tube and the time delay between the two is directly proportional to the mass flow rate.

The fuel is also conditioned by this system, maintained at 15 °C using a dedicated coolant circuit. The conditioning liquid is cooled using a MTA TAE Evo M10 Chiller. Once conditioned the fuel is pumped to the engine, with another back pressure relief using a needle valve linking into the engine return line. This line also has a pressure gauge to allow the operator to ensure delivery pressure is sufficient to the engine specifications. It is then taken through the engine's stock primary filter with a water separator and pressurised via the Denso HP4 high pressure pump. Finally, the high-pressure diesel is injected into the cylinders via a common rail using the original equipment manufacturers (OEM) diesel injectors. Any fuel not used by the engine is returned via the return lines to the Sierra FuelTrak Transient to enable accurate fuel consumption measurements, by measuring the inflow and return mass flow rates. The diesel fuel used in the engine must conform to EU EN590US D975, 1-D and 2-D(Max 15ppm sulphur and 7% fatty acid methyl ester). The fuel flow rate was validated by measuring the flow rate at 600 rpm idling at multiple points throughout testing.

The Sierra Fuel Trak System is monitored and controlled by a dedicated PC in the engine control room, this enables control of the conditioning variables and flow rates.

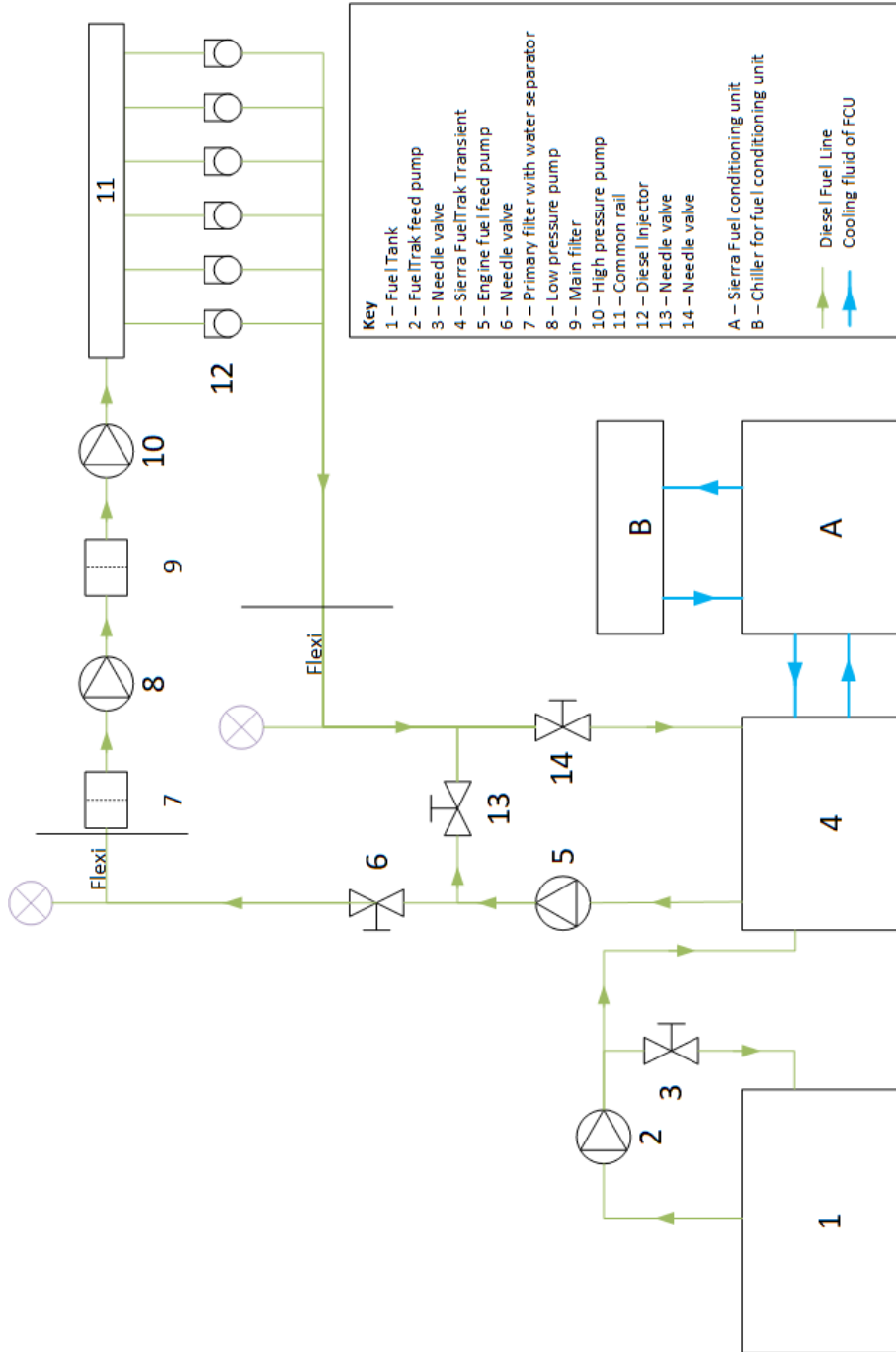


Figure 6.2: Volvo Engine Diesel Fuelling System

6.4 Instrumentation

To ensure accurate data linked directly to the shaft position, a Hohner Optical shaft encoder is used to monitor the crankshaft position and as a trigger for the data acquisition (crank angle time domain). The encoder has a resolution of 0.5 CAD, this means it will produce 720 pulses per revolution and 1440 per cycle. The top dead center (TDC) offset was set statically using markings on the engines flywheel, the encoder was then aligned using an oscilloscope and connected to the engine. Accurate measurement was required since small errors in the TDC measurement can result in large calibration errors in IMEP [107]. This alignment was checked by motoring the engine to observe the position of the peak cylinder pressure. Due to design constraints with the engine, a TDC probe was not able to be used. The angle of thermodynamic losses was set at -0.7 CAD.

Each cylinder is fitted with a Kistler 6125C quartz pressure transducer to accurately record the in-cylinder pressures of each of the cylinders. A trigger signal from the optical encoder is used as a clocking signal to ensure the measurements are specific to the crank angle degree. These transducers were connected to Kistler 5064D charge amplifiers to convert the incoming charge signals into readable voltages. These voltages are fed back to the NI9205 module. Piezoelectric pressure transducers tend to drift with little/no change in pressure, as a result, it is required to include piezoresistive pressure transducers to reference the signals. For this, a Kulite EWCT-12-312M pressure transducer was used to provide the manifold absolute pressure given at bottom dead centre of every intake cycle. The signals from this pressure transducer and another piezoresistive pressure transducer measuring the exhaust manifold pressure are fed back to a NI9220 module directly as they output a voltage relative to the pressure exerted

on them. During the intake stroke, the manifold pressure is equal to the in-cylinder pressure, at this point the output of the piezoelectric transducer is calibrated to this pressure preventing a drifting signal.

FLUKE current clamps were used to record various electrical signals around the engine, the signals triggering the diesel injection pulse, and the ammonia injection pulse are recorded as well as the ECU fuel injection pulse and Optimiser fuel injection pulse. This is a diagnostic mechanism to ensure the engine is operating in the correct mode but also that the optimiser is reading the ECU signals and converting them into the correct signals for the fuel injection. These also fed back to the NI9220 module.

Thermocouples were placed throughout the engine and test environment to monitor and record temperatures of various parts. In total there are 32 K-type thermocouples. The signals from the thermocouples feedback into a NI9213 thermocouple module that reads analogue voltage inputs.

6.5 Data acquisition and processing

A National Instruments modular Compact cDAQ-9179 system is used for the data acquisition on the engine. Table 6.2 presents a description of each module used in this system.

The system can sample data at specific resolutions driven by hardware triggered input signals, as well as time, triggered boards, this enables the use of the shaft encoder as a trigger for the pressure signals whereas other measurements such as temperatures were recorded at 100Hz from time-triggered boards.

The signals from the National Instruments DAQ are received into a Lab-

Table 6.2: National Instruments DAQ modules.

NI Code	Module Description
NI9220	Voltage Input Module – Slow card for measuring incoming piezoresistive pressure signals, current clamp signals, emissions, and flow meter signals at 100 kS/s.
NI9205	Voltage Input Module – Fast Card for measuring incoming piezoelectric pressure signals at 250 kS/s.
NI9401	Digital I/O – receives the incoming optical shaft encoder signals.
NI9213	Thermocouple Input Module – receives the thermocouple signals.
NI9862	CAN Interface Module – to interface with the engine ECU.

VIEW code, here the data is interpreted in real-time to calculate engine variables and are subsequently displayed on a configurable dashboard. This allows the user to monitor the engine using virtual instruments and can record the data for a time.

When recording data on the engine there are three files produced, one that presents the “slow” or low-frequency data such as the temperatures of various parts, one that presents the raw unfiltered “fast” data from the engine pressure gauges and finally a recording of cyclic data. Each of these files has various outputs that can be used to comprehensively understand the engine’s operating conditions,. The following section details the base calculations performed by the LabVIEW code to enable the operation of the engine as well as output the desired variables for the experiments performed. The outputs of the LabVIEW are also post processed in MATLAB to compare multiple test conditions.

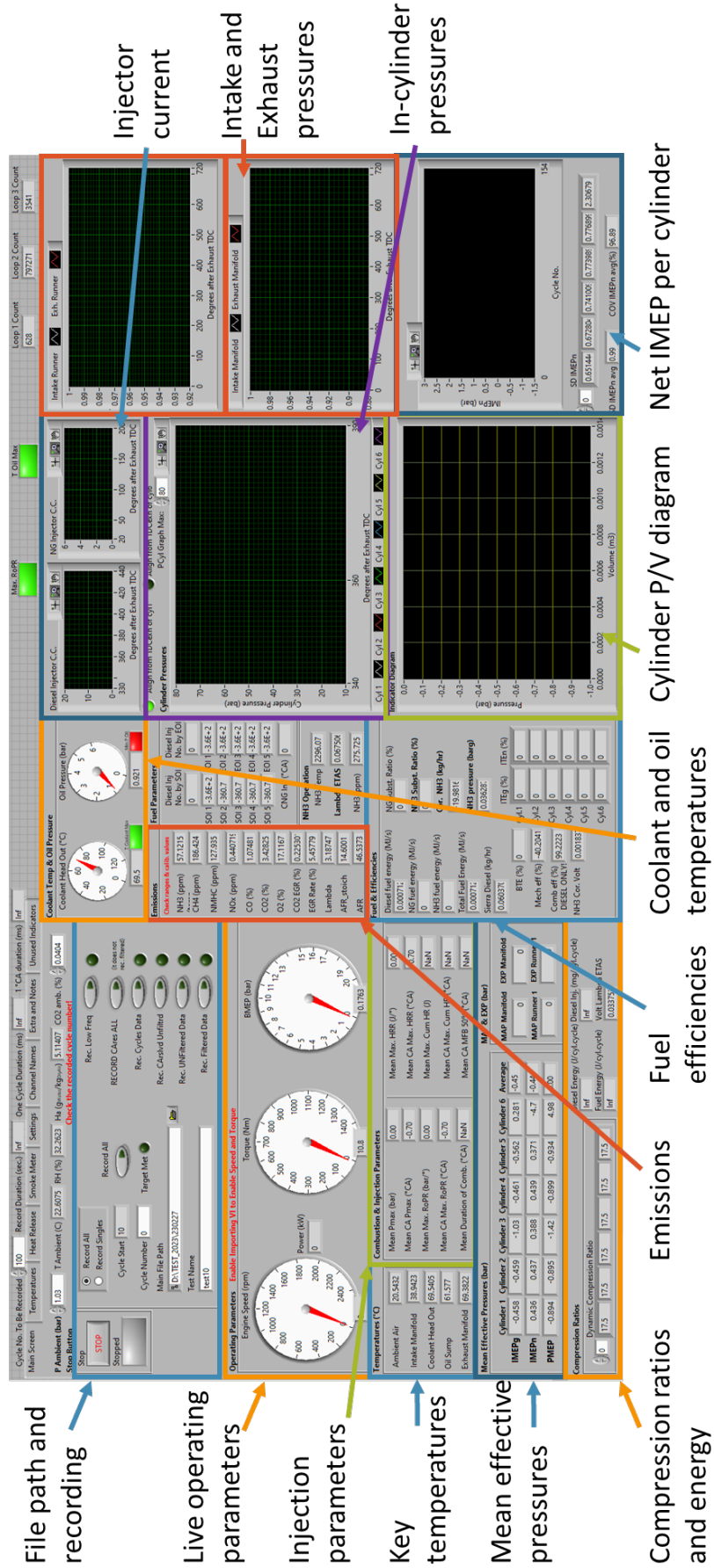


Figure 6.3: Main LabVIEW dashboard used during engine operation.

6.5.1 Mean effective pressure (MEP)

The mean effective pressure is a theoretical parameter that is used to measure the performance of an engine. It can be defined as the average pressure in the cylinder for a complete engine cycle. Indicated mean effective pressure (IMEP) is considered of particular importance when analysing engine performance, it is defined as the work per cycle per unit of swept cylinder volume [60]. This means it can be used as a parameter to compare engine performance regardless of engine displacement. IMEP can be categorised into gross IMEP ($IMEP_g$) referring to the work delivered to the piston over the compression and expansion stroke per unit swept volume (closed part of the cycle), and net IMEP ($IMEP_n$) referring to the work delivered to the piston over the complete engine cycle. The difference between the two values is referred to as the pumping mean effective pressure ($PMEP$), this represents the pumping work done by the engine in the intake and exhaust strokes. These parameters have units of pressure (force per unit area) and are expressed in bar ($10^5 N/m^2$). The pressure transducers were calibrated using a dead weight tester with the amplifiers and cables used in the test rig.

Combustion variations in the cylinders have the potential to cause wave motion in the intake and exhaust pipes that can lead to fluctuations in the cycle-by-cycle pumping work. As a result, the $IMEP_g$ is considered more suitable as a measure of engine performance as this is not included. The gross indicated work output per cycle ($W_{c,ig}$) is obtained by integrating pressure between the bottom dead centre of the intake stroke (BDC_{intake}) and the bottom dead centre of the expansion stroke ($BDC_{expansion}$).

$$W_{c,ig} = \int_{BDC_{intake}}^{BDC_{expansion}} p dV \quad (6.1)$$

Assume the swept volume, V_s remains constant, the gross indicated work per cycle can be divided by the swept volume to give the IMEP_g.

$$IMEP_g = \frac{W_{c,ig}}{V_s} = \frac{\int_{BDC_{intake}}^{BDC_{expansion}} p dV}{V_s} \quad (6.2)$$

The volume of the cylinder, V , can be calculated from the crank position, θ , at any timing using the method derived in Heywood [60].

$$V = V_c + \frac{\pi B^2}{4}(l + a - s) \quad (6.3)$$

Where V_c is the clearance volume, B is the bore, l is the stroke length, a is the crank radius, and s , the distance between the crank axis and the piston pin axis, can be expressed in the equation below.

$$s = a \cos \theta + \sqrt{(l^2 - a^2 \sin^2 \theta)} \quad (6.4)$$

The previous mean effective pressures are only related to the combustion based on the in-cylinder pressure trace and instantaneous cylinder volume. The brake mean effective pressure (BMEP) is calculated from the dynamometer power, this represents the actual output of the engine at the crankshaft, taking into account the full engine efficiency and incorporating friction losses. The equation is derived below.

$$BMEP = \frac{W}{V_d} = \frac{2 * \pi * n_s * T}{V_d} \quad (6.5)$$

$$W = \frac{P_b * n_s}{N} = 2 * \pi * n_s * T \quad (6.6)$$

Where, W is the work done per cycle, V_d is the engine displacement, n_s is the number of revolutions per power stroke, T is the measured torque, and P_b is the brake power.

6.5.2 Combustion stability indicator

The coefficient of variance in IMEP_g (CoV_{IMEP_g}) is used to indicate cycle-by-cycle variability in the combustion work output. It is defined as the ratio of the standard deviation of IMEP_g to the mean value of IMEP_g over total fired cycles. The mean value of IMEP_g is taken over 200 cycles and can be expressed as $\overline{IMEP_{g200}}$, and the standard deviation, σ_{IMEP_g} , is given by:

$$\sigma_{IMEP_g} = \sqrt{\frac{1}{n-1} \sum_{i=1}^n (IMEP_{gi} - \overline{IMEP_{g200}})^2} \quad (6.7)$$

CoV_{IMEP_g} is expressed as the standard deviation of IMEP_g as a percentage of mean IMEP_g and is given by:

$$CoV_{IMEP_g} = \frac{\sigma_{IMEP_g}}{\overline{IMEP_g}} * 100 \quad (6.8)$$

The cyclic variability and the standard deviation of both the gross and net IMEP are also calculated. These values provide a measure of engine stability and vehicle drive-ability. This value varies with speed and load, at idle around 10% is expected with less than 5% at higher loads.

6.5.3 Cylinder charge heat release rate

The heat release rate or rate of fuel burning can be defined as the rate at which the chemical energy of the fuel is released into sensible internal energy. The analysis of this can provide information about the magnitude, phasing and variation of heat release. It can be derived from the cylinder pressure vs crank angle data taken over the compression and expansion stroke. Following Heywood [60], the Traditional First Law method has

been applied. Understanding that a diesel engine can be modelled as an open system that is quasi-static, so uniform in pressure and temperature, the first law for this system is given as,

$$\frac{dQ_{net}}{d\theta} - p\frac{dV}{d\theta} + \sum_i \dot{m}_i h_i = \frac{dU}{d\theta} \quad (6.9)$$

Where $dQ_{net}/d\theta$ the heat transfer rate across the system boundary into the system, $p\frac{dV}{d\theta}$ is the rate of work transfer done by the system due to system boundary displacement, \dot{m}_i is the mass flow rate into the system across the system boundary at location i , h_i is the enthalpy of flux i entering or leaving the system, and U is the energy of the material contained inside the system boundary. When considering the system described, it can be said that the only mass flows across the system boundaries during the closed part of the cycle are the fuel and the crevice flow. Therefore, the equation becomes,

$$\frac{dQ_{net}}{d\theta} - p\frac{dV}{d\theta} + \sum_i \dot{m}_f h_f = \frac{dU}{d\theta} \quad (6.10)$$

Where \dot{m}_f is the fuel mass flow rate into the system, h_f is the sensible enthalpy of the injected fuel, and U is the sensible internal energy then $dQ_{net}/d\theta$ becomes the difference between the heat released by combustion of the fuel and the heat transfer from the system. The volume occupied by the injected fuel quantity compared to the cylinder volume can be assumed to be negligible.

This equation indicates the apparent net heat release rate, $dQ_{net}/d\theta$, which is the difference between the apparent heat release rate and the heat transfer rate to the walls. This is equal to the rate at which work is done on the piston plus the rate of change of sensible internal energy of the cylinder contents. If the cylinder contents are considered as an ideal gas, then the

equation becomes,

$$\frac{dQ_{net}}{d\theta} = p \frac{dV}{d\theta} + mC_v \frac{dT}{d\theta} \quad (6.11)$$

Using the ideal gas law, it can be expressed as,

$$\frac{d(pV)}{d\theta} = mR \frac{dT}{d\theta} \quad (6.12)$$

Substituting to eliminate the temperature (T) term, to get,

$$\frac{dQ_{net}}{d\theta} = p \frac{dV}{d\theta} + \frac{C_v}{R} \frac{d(pV)}{d\theta} \quad (6.13)$$

which can be expanded to,

$$\frac{dQ_{net}}{d\theta} = \left(1 + \frac{C_v}{R}\right)p \frac{dV}{d\theta} + \frac{C_v}{R}V \frac{dp}{d\theta} \quad (6.14)$$

The C_v/R term can be substituted for the ratio of specific heats, $\gamma = \frac{C_p}{C_v}$, and the equation becomes,

$$\frac{dQ_{net}}{d\theta} = \left(\frac{\gamma}{\gamma - 1}\right)p \frac{dV}{d\theta} + \left(\frac{1}{\gamma - 1}\right)V \frac{dp}{d\theta} \quad (6.15)$$

This gives the final net heat release rate equation, the equation relies on the instantaneous in-cylinder pressure, cylinder volume and gamma γ . For a diesel combustion event, typically the value is within the range of 1.3 – 1.35 [60]. The gross heat release rate is obtained by accounting for the energy exchange of heat transfer to the cylinder walls, this is discussed in later sections.

$$\frac{dQ_{gross}}{d\theta} = \left(\frac{\gamma}{\gamma - 1}\right)p \frac{dV}{d\theta} + \left(\frac{1}{\gamma - 1}\right)V \frac{dp}{d\theta} - \frac{dQ_{ht}}{d\theta} \quad (6.16)$$

6.5.4 Cylinder charge heat transfer

Heat transfer, Q_{ht} , is described as a parasitic process that removes energy from the engine cylinders in the form of thermal energy. It results in a loss in efficiency and can remove a significant fraction of the fuels chemical energy that would otherwise have been converted into useful work. Heywood states that heat transfer typically accounts for 15 – 20% of the gross cumulative heat release[60]. Inside the cylinder, convection occurring near the walls is the most dominant transfer mechanism.

$$Q_{ht} = -h_c A \Delta T \quad (6.17)$$

where h_c is the heat transfer coefficient, A is the cylinder surface area at a given time and ΔT is the temperature difference between the cylinder charge and the cylinder wall. The mean bulk temperature is calculated using the ideal gas law at each 0.5 CAD whilst the cylinder wall temperature remains constant. The Hohenberg correlation was used to determine approximate values of h_c , because the coefficients used are readily available from the recorded engine data [63].

$$h_c = 130 * P^{0.8} T^{-0.4} V^{-0.06} (\overline{S}_p + 1.4)^{0.8} \quad (6.18)$$

Where P is the instantaneous cylinder pressure in bar, T is the mean gas temperature in Kelvin, V is the instantaneous cylinder volume in m^3 and \overline{S}_p is the mean piston speed in m/s .

6.5.5 Cycle efficiencies

Engine efficiency calculations provide an indication of how well the fuel is utilised and transferred into useful work. The indicated combustion efficiency is a measure of how much fuel is burnt per cycle, calculated using the following formula,

$$\eta_c = \frac{GrossHR_{cum}}{q_{fuel} * Q_{LHV}} * 100 \quad (6.19)$$

Where $GrossHR_{cum}$ is the cumulative gross heat release in Joules, q_{fuel} is the fuel quantity injected per cycle in mg, and Q_{LHV} is the lower heating value of the fuel in MJ/kg. The lower heating value used in this was 42.5 MJ/kg. The thermal efficiency is how effective the chemical energy in the burnt fuel is transferred to $IMEP_g$, this is given by,

$$\eta_t = \frac{IMEP_g * V_s}{GrossHR_{cum}} * 100 \quad (6.20)$$

Where $IMEP_g$ is the gross indicated mean effective pressure and V_s is the swept volume. The product of the two efficiencies gives an indication of how well the fuel injected is converted to $IMEP_g$ called the fuel conversion efficiency.

$$\eta_f = \frac{\eta_c * \eta_t}{100} \quad (6.21)$$

6.5.6 Brake specific fuel consumption

Specific fuel consumption, sfc is a normalized parameter that is defined as the fuel flow rate per unit power output. It is a measure of how efficiently an engine is using the fuel supplied to produce work as a specific operating

condition.

$$sfc = \frac{\dot{m}_f}{P} \quad (6.22)$$

where, \dot{m}_f is the fuel mass flow rate in g/s and P is the engine power output in kW. For compression ignition engines the best values are lower around 180 g/kW.hr. This value can also be related to the fuel conversion efficiency by the Equation 6.23.

$$\eta_f = \frac{1}{sfc * Q_{LHV}} \quad (6.23)$$

The engine data in later sections were operated at a steady-state, therefore the speed and load remain constant across the cycles at 1000 rpm and 100 Nm of torque. Using these values the power output can be calculated.

$$P = 2\pi NT = 2\pi * \left(\frac{1000}{60}\right) * 100 * 10^{-3} = 10.47kW \quad (6.24)$$

6.6 Emissions analysis and smoke meter

The exhaust emissions are sampled from the exhaust plenum. To avoid local condensation inside the main distribution unit, which may harm the hot sample analysers that measure total hydrocarbons and nitric oxides (NO_x), the sample gas is conditioned to 198 °C before entering. Carbon monoxide and carbon dioxide are measured using non-dispersive infra-red absorption. In this system a heat source provides infra-red radiation which is interrupted by a rotating filter. The resulting series of pulses are directed through a cell containing the sample gas. The variation in signal is detected as the wheel rotates, this is amplified and subsequently output.

Paramagnetism is used to detect oxygen content in the exhaust by dis-

Target Gas	SIGNAL Analyser Model	Measuring Princi- ple	Measuring Range [vol]
Carbon Monoxide, <i>CO</i>	7000FM	Electromagnetic Spectrum	10%
Carbon Dioxide, <i>CO</i> ₂	7000FM	Electromagnetic Spectrum	20%
Oxygen, <i>O</i> ₂	8000M	Paramagnetic Spectrum	10%
Total Hydrocarbons, <i>THC</i>	SOLAR S4	Flame Ionisation Detector	0.4%
Nitrogen Oxides, <i>NO</i> _x	4000VM	Chemiluminescent	0.1%
Ammonia, <i>NH</i> ₃	NEBULA	Tunable Diode Laser Spectrometry	1%

Table 6.3: Summary of emissions analysers used in conjunction with the Volvo test rig including measuring principles, range and model.

placing a dumbbell filled with nitrogen in a magnetic field using oxygen molecules that are drawn to the field. A current is generated to move the dumbbell back to the original position which is in turn used to derive the oxygen concentration present in the sample. Levels of unburnt hydrocarbons are measured using fast-response flame ionisation detection, this technique is based on the detection of ions formed during combustion of organic compounds in a hydrogen flame. The combustion takes place in an electrostatic field in which the oppositely charged components of the combustion are driven towards electrodes resulting in a current proportional to the number of molecules of hydrocarbon present. The NO_x emissions are analysed using a chemiluminescent detector, this technique utilises a reaction between nitric oxide, NO and ozone to produce photons of light which are subsequently detected. The amount of light produced enables the concentration of NO_x to be deduced.

An AVL 415 Smoke meter is also used to analyse the engine exhausts specifically looking at the Filter Smoke Number (FSN) determined using

the filter paper method according to ISO 10056 and the soot concentration given in mg/m^3 . The device measures a range of 0 to 10 FSN with a detection limit of 0.002 FSN. Tunable diode laser spectroscopy is used to measure the ammonia emissions in the exhaust. Similar to the CO and CO_2 measurement, it uses the interaction of gas molecules with infra-red light to determine the concentration of the target gas. This method uses a collimated laser directed onto a photo diode, the diode is tuned to the characteristic absorption of the target gas.

6.7 Engine control unit (ECU) development

Initial testing with the engine was controlled via the OEM ECU, dictating injection parameters, EGR rates, AdBlue consumption, and many other variables. The conversion of the engine to be able to operate in dual fuel mode requires fine control of the engine injection signals. The Optimiser Diesel SuperEmulation sits between the OEM ECU and the diesel injectors. As the current pulse comes from the ECU to the injectors, the optimiser provides a dummy load and gives the ability to shorten or eliminate the pulses. Alongside this, the optimiser simultaneously operates the injectors for a secondary fuel, with the principle that it will provide the same power that was removed from the diesel injection pulse and replace it with secondary fuel. The engine's operation should be maintained and the total power unaffected. It was found that this system resulted in challenges during which the OEM ECU would operate in different modes depending on temperature and other parameters to perform standard operation processes such as increasing exhaust heat to burn off soot in the exhaust filters. This resulted in a difficulties in operation and experimental recording due to fluctuating conditions. The diesel injector signals are shown in Figure 6.4.

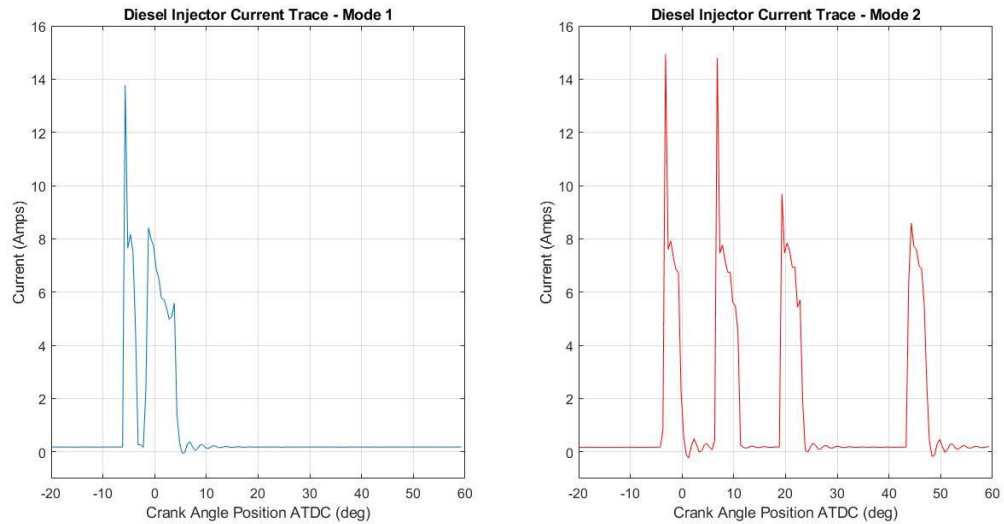


Figure 6.4: Diesel injector current clamp comparison for two injection modes.

Early testing with ammonia was performed using this system alongside a dedicated controller for ammonia injection, with the diesel fuel quantity being controlled using the optimiser device. This limited the degree of optimisation of the engine parameters and emission levels with the engine only operating at baseline conditions. The results of the testing in this condition are detailed in Chapter 7, described as the first iteration testing.

The engine was upgraded to operate using MAHLE Powertrain's Flexible ECU, replacing both the OEM ECU and the optimiser to a fully integrated whole engine control system. This allows for finer control of all engine operating parameters and fuelling controls. Specifically, control of the fuel injection duration and positioning was key for dual fuel operation as well as the ability to fix engine conditions removing the variability observed using the OEM ECU. The new ECU provided the capability to operate multi-pulse diesel injection control, alongside 2 sets of 6 injectors for ammonia and hydrogen fuelling.

6.8 Ammonia upgrade

The following section presents the steps taken to safely upgrade the test cell and engine to enable safe operation with ammonia fuelling. The general test cell upgrades are detailed along with the engine fuelling system upgrade.

6.8.1 Test cell upgrade

The test rig was upgraded with a complete gas detection system. The system incorporated NH_3 sensors mounted at different locations within the test cell to ensure operator awareness of high concentrations at any point. The sensors were connected to a central control panel which monitors the concentration of ammonia in the room. The low-level alarm was set at 25 ppm, and the high level at 35 ppm. When the high level alarm is triggered, a shutdown process is initiated. This includes stopping injection to the engine, shutting off ammonia supply to the test cell as well as audible and visual alarms.

Operational procedures designed to protect all operators working around the test cell were introduced, including pressure drop testing the ammonia lines before testing, purging with nitrogen before and after testing, and limiting access to the test cells during ammonia operation. Alongside this, engine operators were provided with personal handheld sensors that provided a real-time reading of ammonia concentration as well as alarming when dangerous levels were exceeded.

6.8.2 Calculations for the ammonia flow rate

When initially developing the ammonia fuelling system, a maximum flow rate of ammonia needed to be defined in order to size the system. To do this the specification sheet was used, using the provided maps of specific fuel consumption and assuming a substitution ratio of 90% and a combustion efficiency of 90% a target operating condition was selected as 1250 rpm and 20 bar IMEP load, using the diesel fuel consumption at this point, the value of 198 g/kWh was taken. Using the lower heating value of diesel (42.6 MJ/kg) assuming complete combustion gives the energy consumption at that point to be 8.43 MJ/kWh.

The power at the target operating condition is calculated,

$$EngineWork = \frac{IMEP}{V_d} = \frac{20 * 10^5}{0.0077} = 15400J \quad (6.25)$$

$$BrakePower = Work * Speed = 15400 * \frac{1250}{2} = 160kW \quad (6.26)$$

The brake specific fuel consumption of ammonia is calculated, assuming ammonia accounts for 90% of the fuel mixture,

$$BSFC_{NH_3} = \frac{EnergyConsumption}{LHV_{NH_3}} = \frac{8.43 * 0.9}{18.6 * 10^3} = 415.8g/kWh \quad (6.27)$$

Taking into account the combustion efficiency, this equates to a fuel flow rate of 72 kg/hr. This flow rate provided a benchmark for the ammonia fuelling system.

6.8.3 Fuel delivery system

The ammonia supply provides fuelling for two engines, as a result a large liquid ammonia tank was purchased for the facility with a maximum quantity of 530 kg. Due to ammonia's relatively low pressure liquid point, the tank existed at an equilibrium based on the ambient temperature. The ammonia was able to be extracted from the tank either as a liquid or a gas. For this testing, port fuel injection was selected, as a result gaseous ammonia was required. The port injection location was based upon prior natural gas injection layout developed in partnership with Clean Air Power for optimised mixing (albeit proven with natural gas). The relatively long injection durations with ammonia may have reduced pre-mixing.

Figure 6.5 presents the process flow diagram of the ammonia fuel delivery system. The fuel line throughout all of the circuits was 316 stainless steel to prevent any compatibility issues. The pressures in the line were monitored across the circuit. The external circuit consisted of a pressure gauge, filter, pneumatic shutoff, manual shutoff, flashback arrestor, and three way valve for directing the fuel to either engine. Early in this system is a check valve enabling nitrogen to be used as an inert venting gas. The internal system consisted of another manual shutoff valve, a Coriolis flow meter, e-shutoff valve, and further pressure and temperature monitoring.

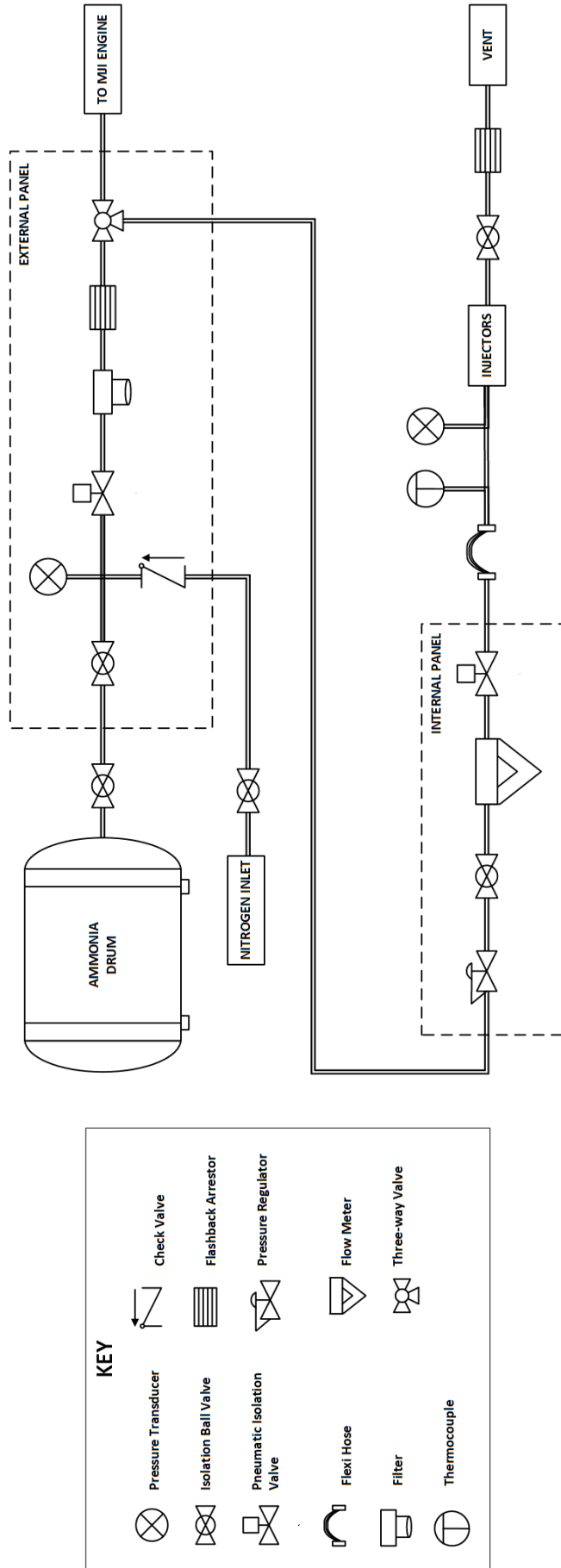


Figure 6.5: First iteration of the ammonia fuelling design.

The initial design of the system did not incorporate a pressure regulator. However during initial operation, it was found that the draw from the tank would reduce temperature and therefore pressure. To prevent this from influencing the ammonia injection and to stabilise the fluctuating line pressures, a pressure regulator was added before the Coriolis flow meter. Another limitation of the initial delivery system was the phase changes occurring within the line. It was found that at certain points of flow restriction the ammonia was condensing and accumulating at various points in the line. This was discovered due to a number of anomalies occurring during operation, the first being large spikes in the flow rates read by the Coriolis flow-meter. The flow meter relies on known values of density and temperature to calculate the flow rate. Due to the existence of liquid in the line the higher density suggested very high flow rates. The removal of the initial fuel filter on the external panel as well as the introduction of the pressure regulator removed the high readings on the flow meter.

6.8.4 Ammonia injection rail

Figure 6.6 shows the first iteration of the ammonia injection rail, highlighted in red. This system consisted of a single side fed rail with Parker Series 9 High-Speed Pulsed Solenoid Valves with a custom built adaptor to connect to the pipework for port fuelling. The rail was 1/2 in diameter pipework however was stepped down before the injectors to 1/4 in diameter. The initial injection system was selected due to its high pressure rating, up to 60 bar, which opened up the potential for future liquid ammonia injection studies, as well as proven ammonia compatibility from the manufacturer.

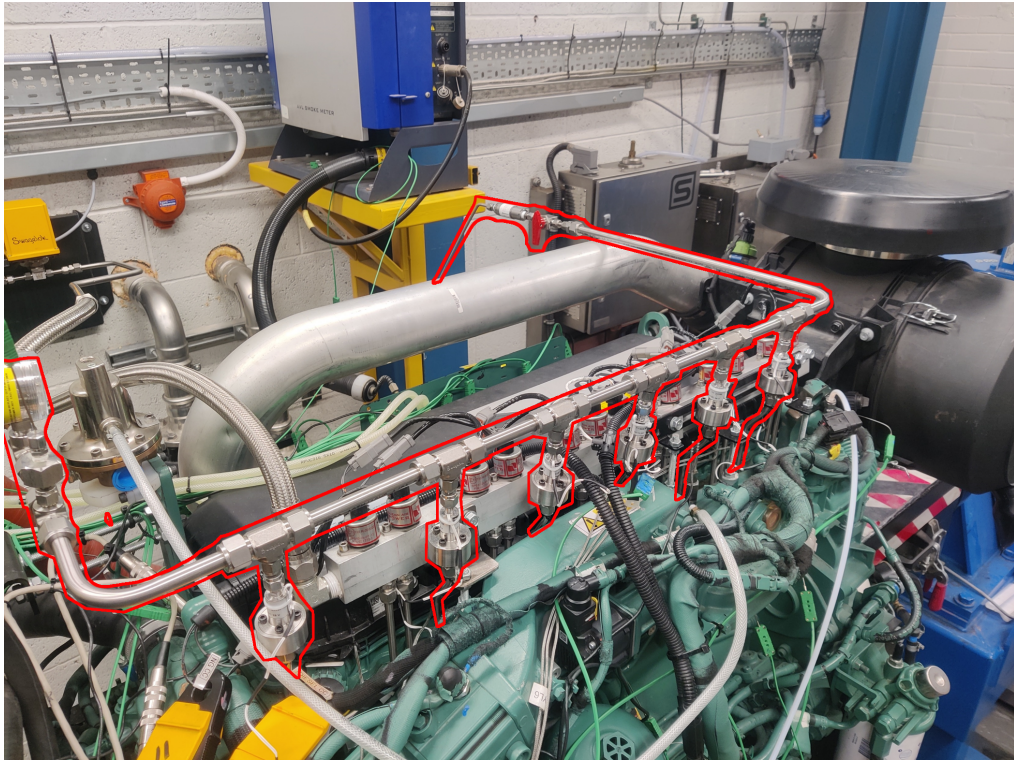


Figure 6.6: First iteration ammonia port fuel injection rail highlighted in red. Ammonia feed from the left side and venting from the right.

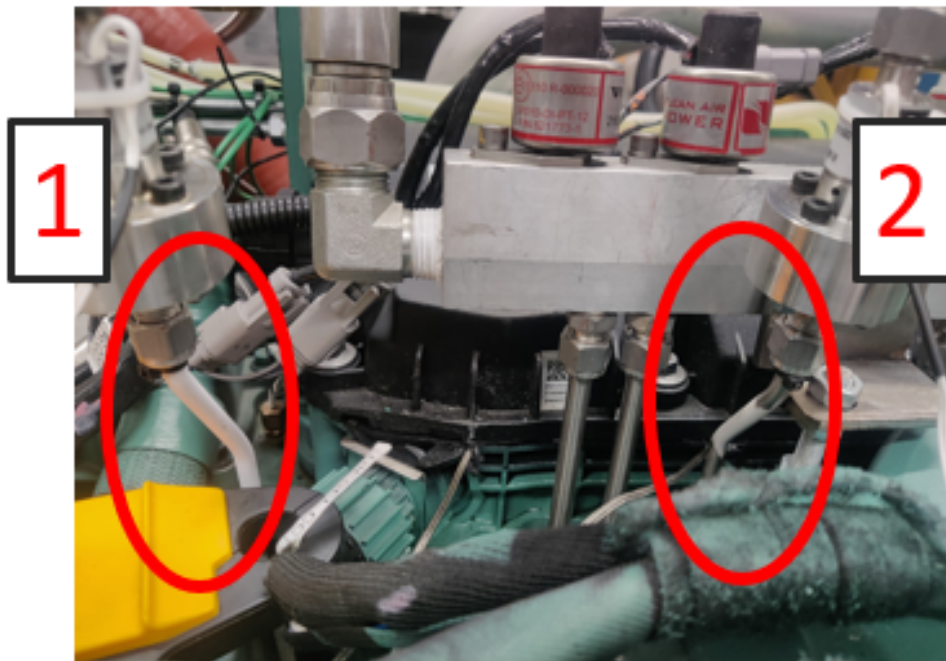


Figure 6.7: Image of Icing on Cylinder 1 and 2 injection pipes.

This first iteration of the ammonia injection rail presented some significant challenges around injection and liquefaction of ammonia. Due to the presence of liquid ammonia in the line, the first injector (left side into cylinder 1) was acting as a liquid catch for the rest of the rail. This resulted in large cylinder to cylinder variations, as well as icing around the injectors. The impact of this is discussed in Section 7.1. The unintentional injection of liquid ammonia resulted in an interesting phenomena shown in Figure 6.7. It was found that after a short period of injection, icing would appear on the port fuelling pipework. This is the result of the liquid ammonia absorbing heat from its surroundings and changing to a gas as it enters the intake manifold. In addition to this, it was found during testing that at higher speeds and load, the ammonia injection was flow limited.

The second iteration ammonia injection rail upgrade included new high flow port fuel injectors from Clean Air Power to improve the fuel flow as well as targeting and timing. The increased bore resulted in a more reliable injection of ammonia with no presence of icing observed. The new rail was supplied from both sides with a larger bore pipe work. The dual feed means that the ammonia would travel less in the pipework to reach the central injectors, balancing the fuel flow across the injectors. The increased bore, increased the volume of the fuelling rail, reducing the impact of single injections on the rail volume. This helps to maintain the rail pressure and therefore contributes to more homogeneous injections across all cylinders. The new dual feed and rail are shown in Figures 6.8 and 6.9. The results of this upgrade are discussed in Section 7.2.

6.9 Hydrogen upgrade

The updated fuel rail, shown in Figure 6.8, combines the ammonia rail with a new hydrogen rail. The same Clean Air Power injectors were used for both systems, although unlike the ammonia rail the hydrogen was fed from a single side and vented out of the other. The reason for this was that the hydrogen will remain a gas throughout the system and will be at a higher pressure so the impact of one injection was not significant on the total rail volume.



Figure 6.8: New integrated NH_3 and H_2 rail.

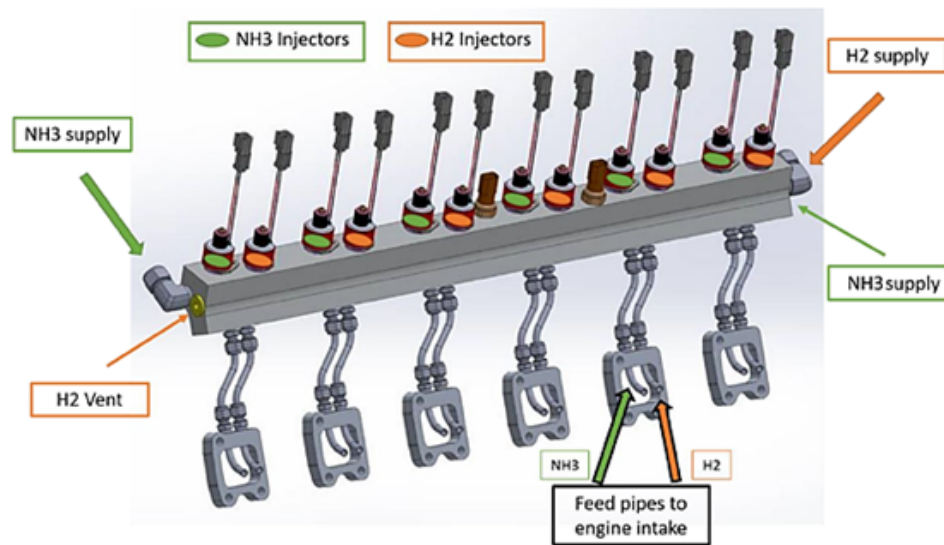


Figure 6.9: CAD schematic of new rail incorporating ammonia and hydrogen Clean Air Power injectors.

6.9.1 Test cell upgrade

Alongside the ammonia sensors installed in the test rig, further hydrogen sensors were added. The alarms for these were set at 100 ppm for the low alarm and 400 ppm for the high alarm. In the event of a high alarm the hydrogen injection will cease and the supply shut off automatically. The function of these sensors was to prevent an explosive environment from forming as a result of a leak. Due to the buoyancy of hydrogen, the sensors were placed on the ceiling of the lab where the hydrogen would accumulate in the event of a leak.

6.9.2 Hydrogen flow rate calculations

Using the previously calculated test condition energy consumption of 8.43 MJ/kWh, from Section 6.8.2, the lower heating value of hydrogen can be used to estimate the maximum flowrate required. The lower heating value of hydrogen is 120.0 MJ/kg, equating to an engine hydrogen demand of 12 kg/hr. It is important to note that the low end of the scale will also be used, especially in instances of hydrogen enrichment testing (circa 5% substitution ratios).

Due to its very low density, hydrogen presents a challenge when sizing mass flow meters for the fuel line. Coriolis flow meters are set to vibrate at a known frequency which is then shifted as a result of mass flowing through the system. In the case for hydrogen gas, the high maximum flow rates will result in inaccuracy on the low end of the measurements. As there is a need for accuracy across both the high and low end of the measurement, four Alicat CODA KM Series High Accuracy Mass Flow Meters[2] were installed in the system to enable measurement accuracy across the entire

Full-scale Flow [kg/hr]	Minimum Flow with 1% Error [g/hr]
30	1500
3	150
300 [g/hr]	15
40 [g/hr]	2

Table 6.4: Hydrogen flow meter sizing information and minimum flow rate with 1% error.

range with a maximum error of 1%. Table 6.4 presents the key information about the flow meters with the minimum accuracy measurement of each. This system also supports a smaller single cylinder engine, hence the very low 40 g/hr meter.

6.9.3 Fuel delivery system

The hydrogen is supplied from a manifolded 130 m^3 cylinder pack at 172 bar. This is stepped down to 100 bar at the cylinder pack which maximises the flow meters pressure range. Check valves were also installed after the flow meters to prevent backflow which can cause inaccuracies. The hydrogen is then regulated to 50 bar depending on the specific testing requirements, this contributes to maintaining a stable flow measurement and prevents the influence of process demand on measurements. The delivery system consists of the external panel and venting section, the fuel supply board and the internal panel, more detailed schematics are shown in Figure 6.10. There are e-shut offs incorporated to stop the flow of hydrogen in the case of an emergency.

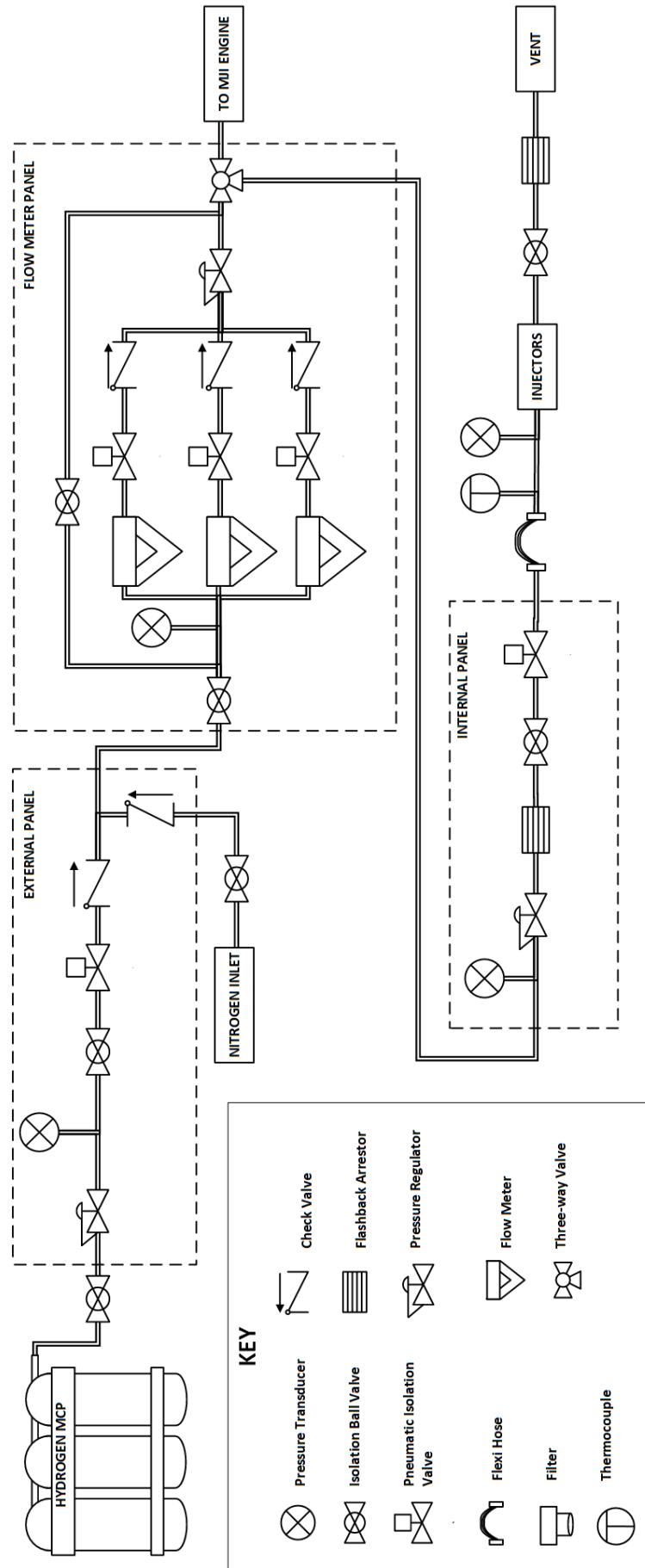


Figure 6.10: Hydrogen fuel delivery system.

Chapter 7

Dual Fuel Results

The intention of these experiments was to investigate the practicality of converting a standard 6-cylinder heavy-duty diesel engine to operate with ammonia dual fuel operation using diesel as a co-fired pilot fuel. The testing consisted of multiple stages as a result of learning and adjustments needed to incorporate the fuels effectively. The experimental setup including the two iterations of development are described in Chapter 6, alongside a justification of the changes. The initial “first iteration” testing can broadly be defined as ammonia fumigation substantially upstream of the intake ports whilst the “second iteration” testing consisted of a more-targeted port fuel injection of ammonia with a higher degree of control provided by the upgraded systems.

7.1 First iteration: Ammonia fumigation

The initial ammonia testing was completed using a single-side fed ammonia rail with high-speed solenoid valves controlled by a bespoke injector controller. The set up is further discussed and shown in Section 6.8.4. The

initial testing was performed at 160 Nm at 600 rpm, which represents 25% of the load at that speed with a BMEP of 2.5 bar. These tests were constrained by limited engine control, the diesel fuel quantity was controlled using a third-party controller which piggy-backed the original signals from the OEM ECU, restricting the degree of optimisation of the engines operation for best performance or emissions levels. Diesel injection was fixed, injected in two-pulse mode (pilot and main), whilst ammonia was fumigated into the ports. Due to the first iteration fuel system not having a pressure regulator within the line, the ammonia rail pressure was dictated by the vapour pressure of the ammonia tank. The rail pressure was not digitally recorded for this testing, the digital recording was added for the next iteration of fuelling system. The pressure before testing was measured from an analogue gauge to be 7 bar. The injection duration of ammonia was varied from 0 ms to 50 ms and three configurations of active cylinders were investigated;

- All cylinder injection.
- Cylinder 3 and 4 injection.
- Cylinder 6 only injection.

To begin with, all 6 injectors were active for testing at 600 rpm. At this condition the testing was limited to 36 CAD injection duration due to increasing instability in the combustion and large variation between cylinders which will put the crankshaft under high stresses. Figure 7.1 presents the change in $IMEP_n$ against the injection duration of ammonia. The variation in $IMEP_n$ from the baseline is also presented in Figure 7.2. For cylinder one the $IMEP_n$ increases with increasing ammonia, however for the remaining cylinders it decreases.

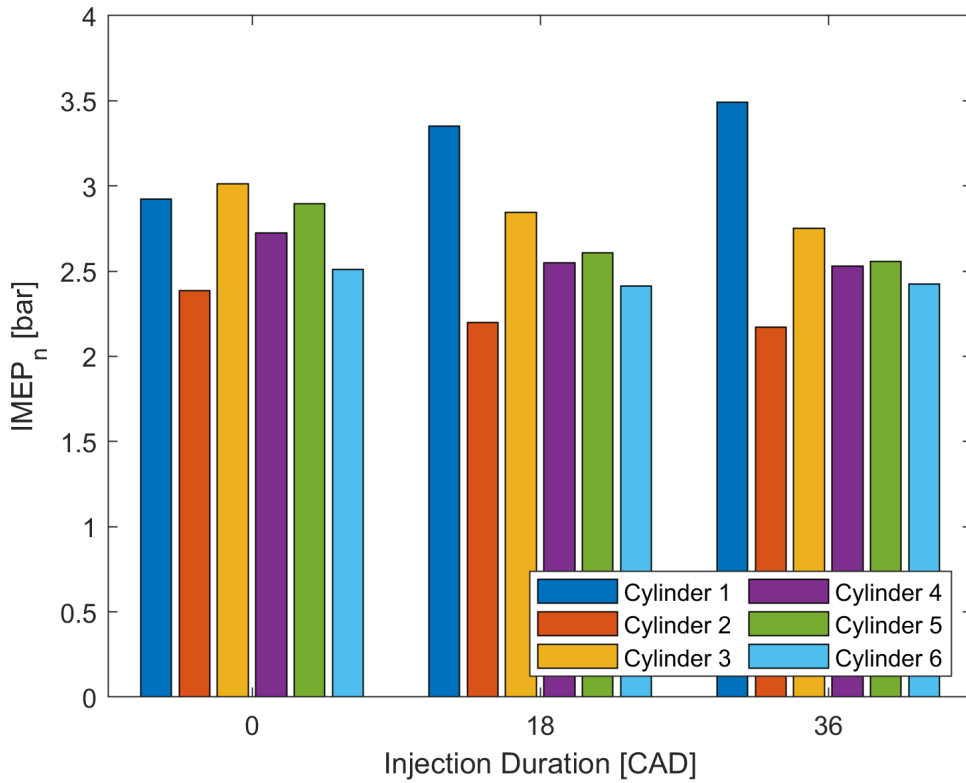


Figure 7.1: Plot of the IMEP_n for each cylinder against injection duration in CAD for the fixed point testing - all cylinder injection active.

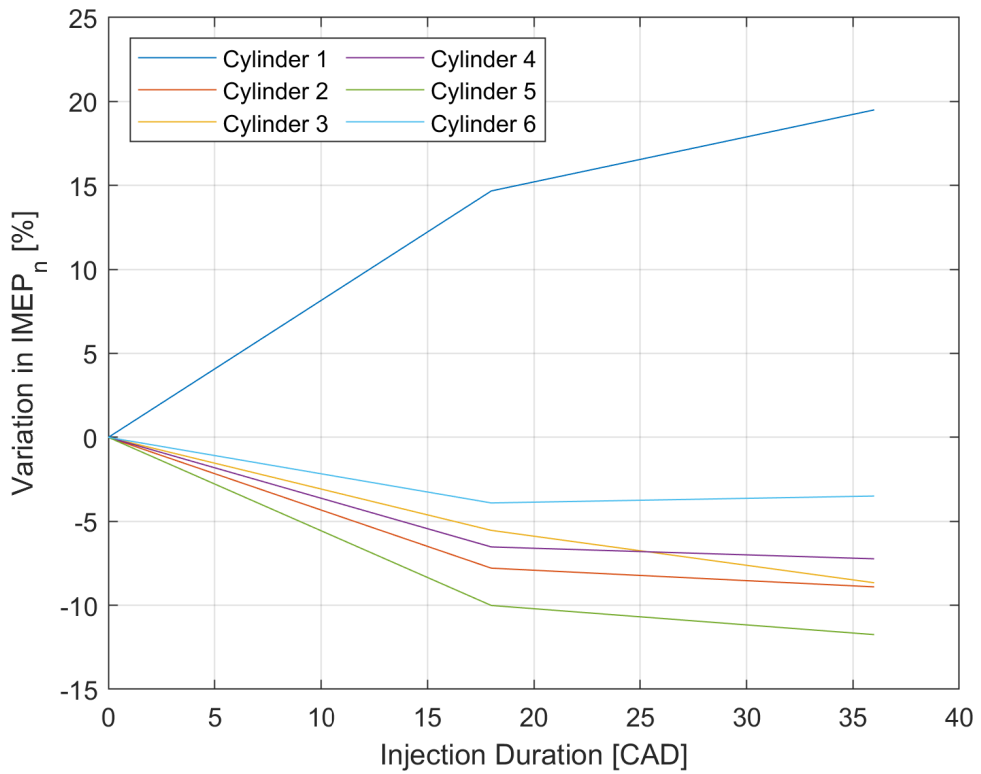


Figure 7.2: Plot of the change in IMEP_n for each cylinder against injection duration for the fixed point testing - all cylinder injection active.

Considering the $IMEP_n$ presented previously, an assumption can be made that the diesel mass flow reduction is entirely as a result of ammonia injection into the first cylinder. This is not entirely accurate as the reduction across each cylinder is not constant, suggesting a degree of ammonia injection into the other cylinders, however it provides an approximation of the substitution ratio (SR) achieved. Figure 7.3 shows the diesel fuel flow rates during the testing as well as an approximate ammonia SR observed in cylinder 1, the reduction in diesel fuel flow rate is as a result of the ammonia injection as the engine targets 160 Nm load.

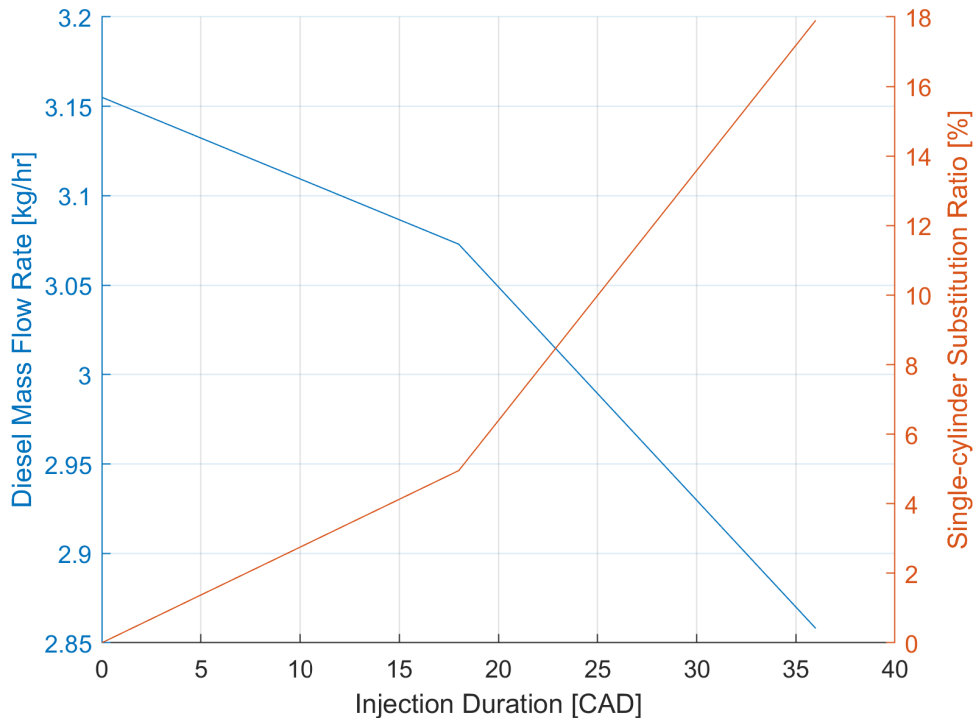


Figure 7.3: Diesel mass flow rate and cylinder one approximate ammonia SR against injection duration - all cylinder injection active.

The impact of the ammonia injection and resultant instability is shown in the in-cylinder pressure plots for cylinder one, Figures 7.4 and 7.5, showing the baseline and 36 CAD injection for 500 cycles respectively. There are some failed combustions as well as large pressure spikes observed in cylinder 1 with ammonia injection.

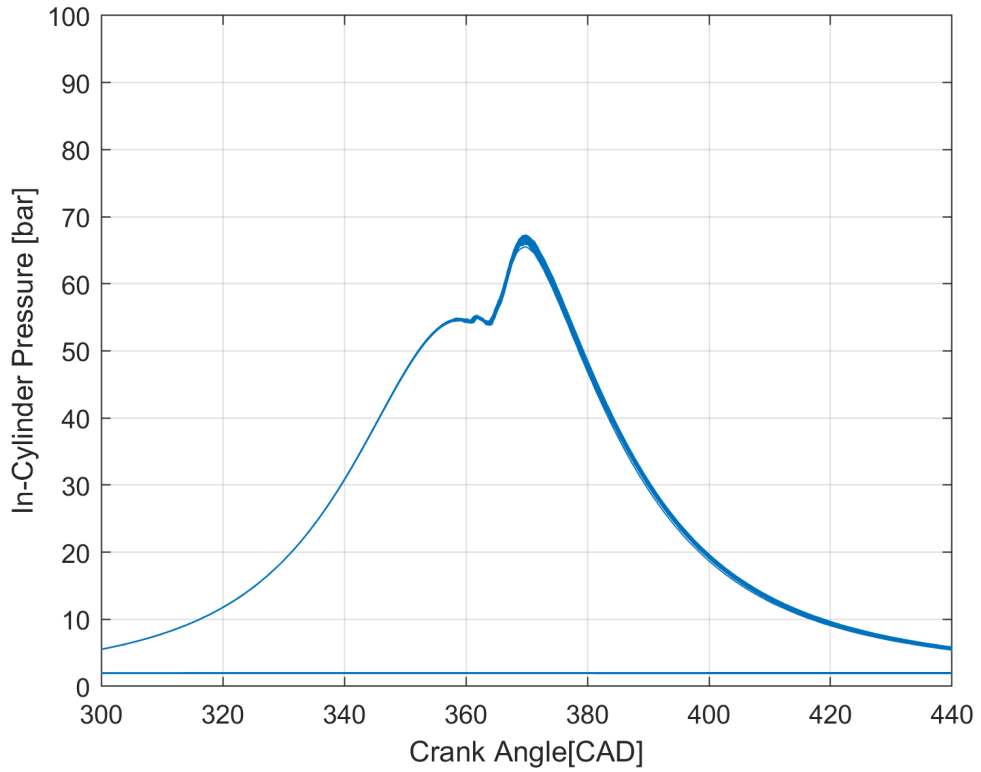


Figure 7.4: Plot for the fixed point ammonia engine testing - all cylinder injection active, of in-cylinder pressure for 500 cycles against crank angle for baseline - no ammonia injection

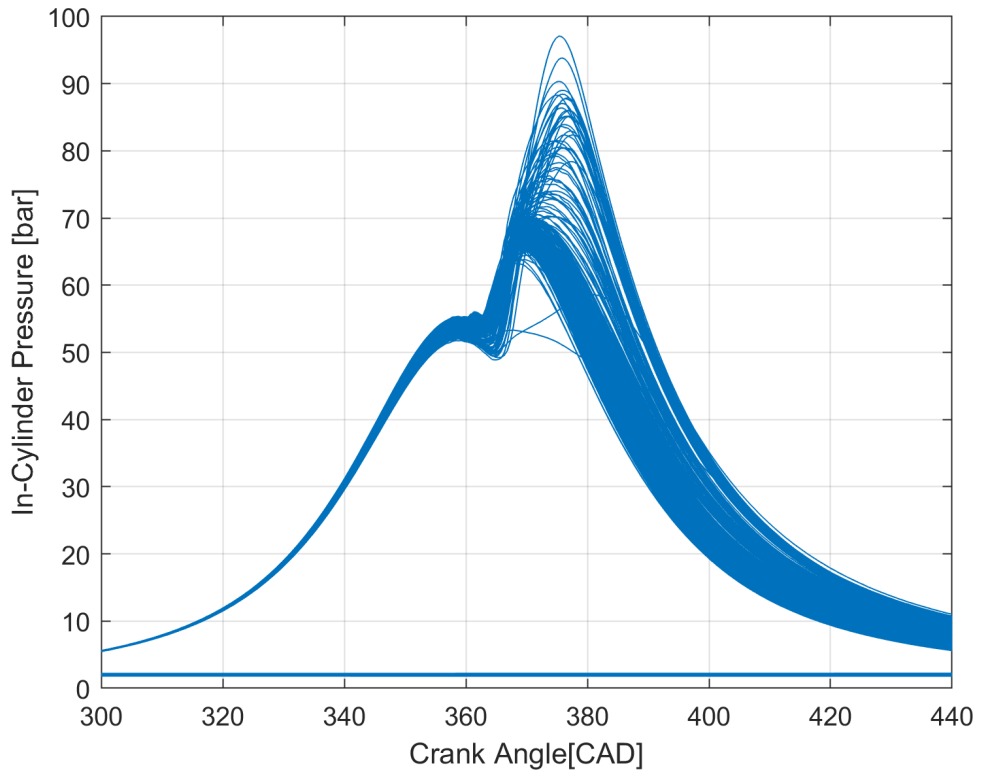


Figure 7.5: Plot for the fixed point ammonia engine testing - all cylinder injection active, cylinder 1 in-cylinder pressure for 500 cycles against crank angle for 36 CAD ammonia injection.

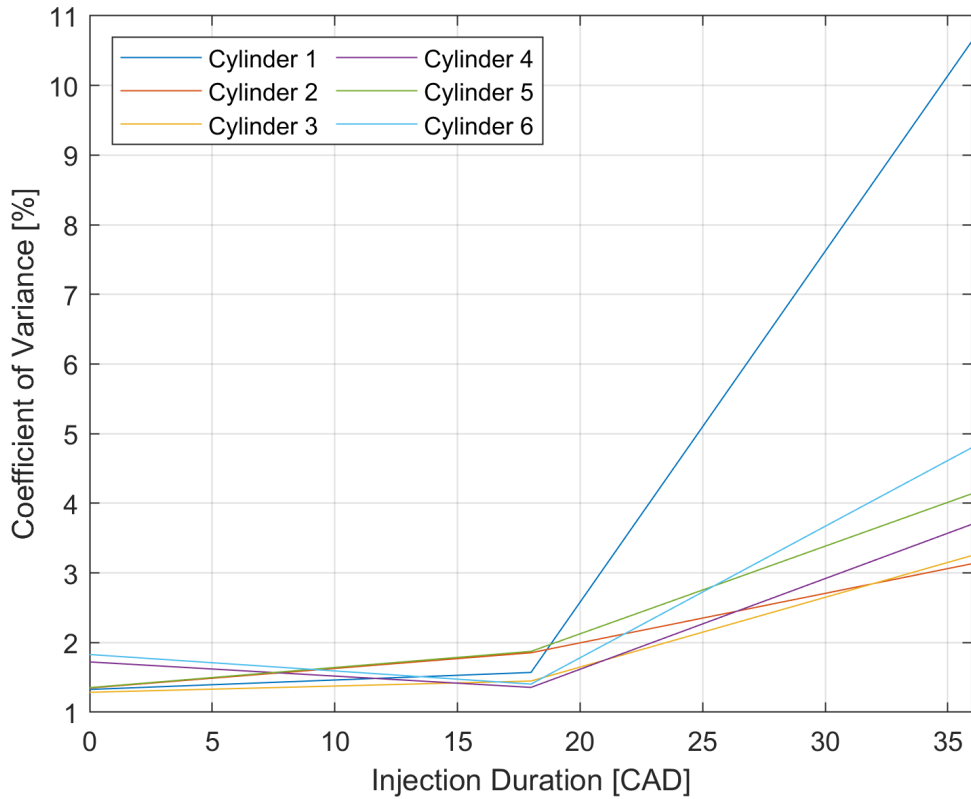


Figure 7.6: Plot of CoV of IMEP_n against ammonia injection duration for each cylinder - all cylinder injection active.

An effective way of measuring the cycle-by-cycle variation in an engine is using the coefficient of variance (CoV), this is an indication of engine stability the calculation of which is discussed in Section 6.5.2. Figure 7.6 presents the CoV for the three test conditions recorded for each of the cylinders with increasing ammonia injection duration. The plot shows the impact of the ammonia favouring cylinder 1, introducing combustion instability strongly in that cylinder but also in the other remaining cylinders.

The rate of heat release plot provides insight into how ammonia was burning within cylinder one. Figure 7.7, presents the changing rate of heat release curve against crank angle for the three conditions investigated. The initial peak shown represents the diesel pilot heat release, this remained fixed throughout testing, hence very little change observed throughout. Prior to the initial peak, there is a negative area which is indicative of the heat loss

as a result of the fuel injection. The main premixed peak reduces due to a reduction in diesel fuelling as the ammonia injection duration increases. On the tail of the premixed peak, there is clear ammonia involvement in the combustion, delaying the combustion as the ammonia SR increases.

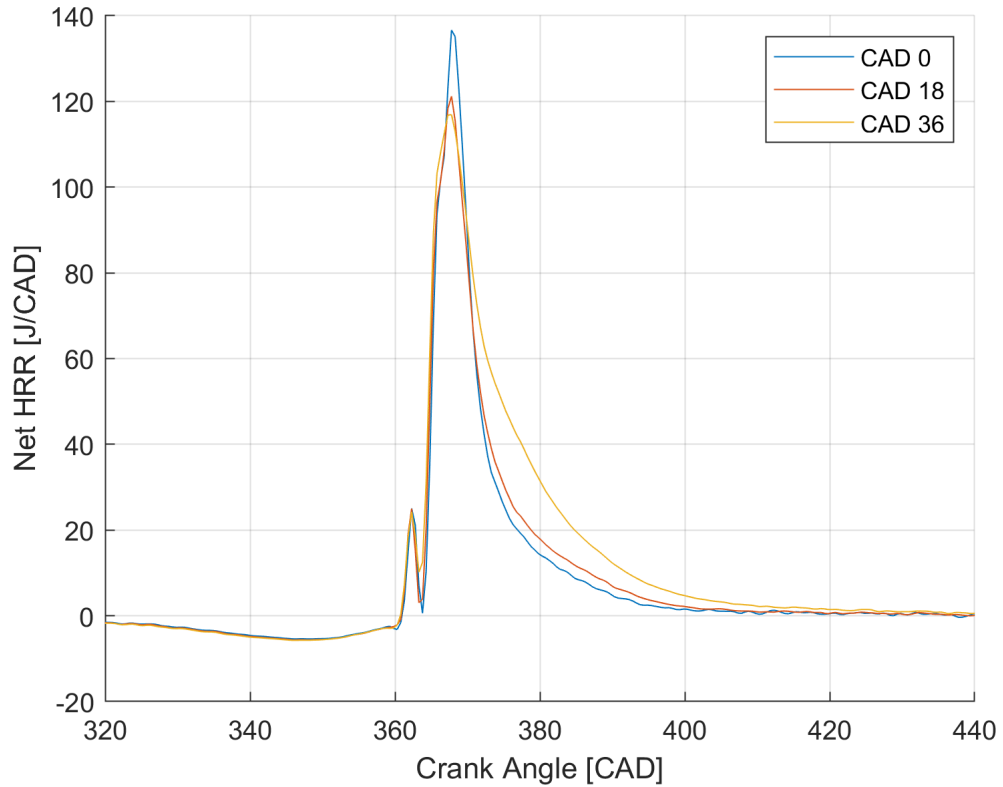


Figure 7.7: Rate of heat release against crank angle degree in cylinder 1 for various ammonia injection durations - all cylinder injection active.

To investigate the fuelling system further, two more ammonia injection modes were considered, cylinder 3 and 4 injection only and cylinder 6 injection only. These were chosen due to the firing order of the engine, 1-4-2-6-3-5, the intention for firing only cylinders 3 and 4 was to balance out the theorised fluctuating fuel pressures observed in the all cylinder firing mode and prevent the ammonia favouring cylinder 1. All cylinders remained fuelled by diesel throughout. The $IMEP_n$ and $IMEP_n$ variance across all cylinders are shown in Figures 7.8 and 7.9 respectively.

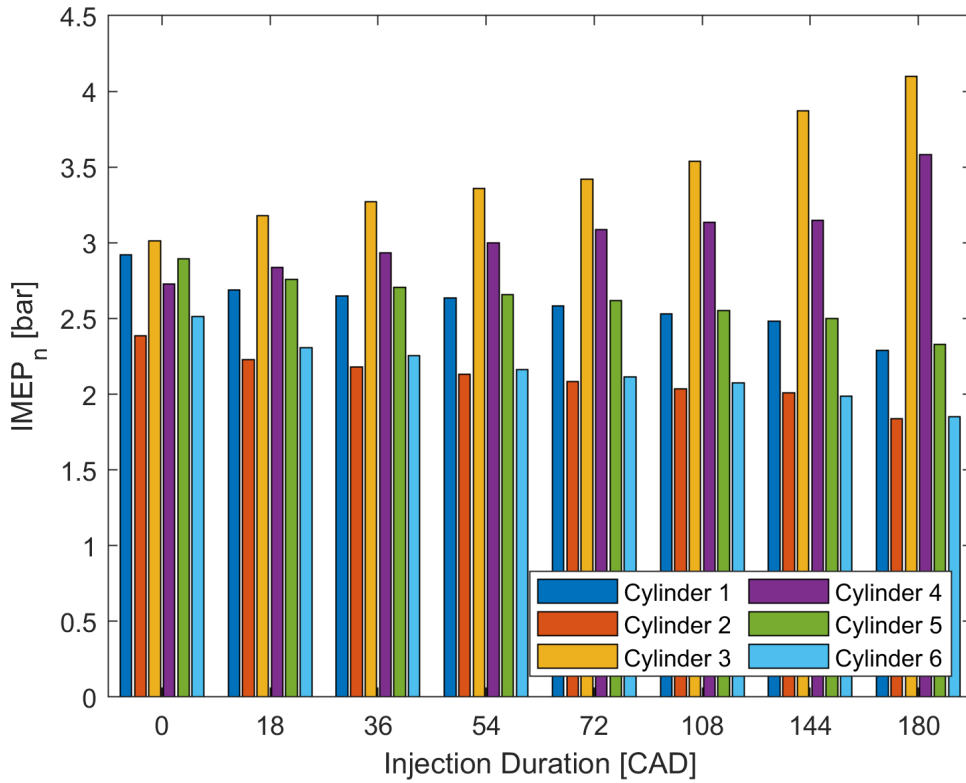


Figure 7.8: Plot of the IMEP_n for each cylinder against injection duration in CAD for the fixed point testing - cylinder 3 & 4 injection active.

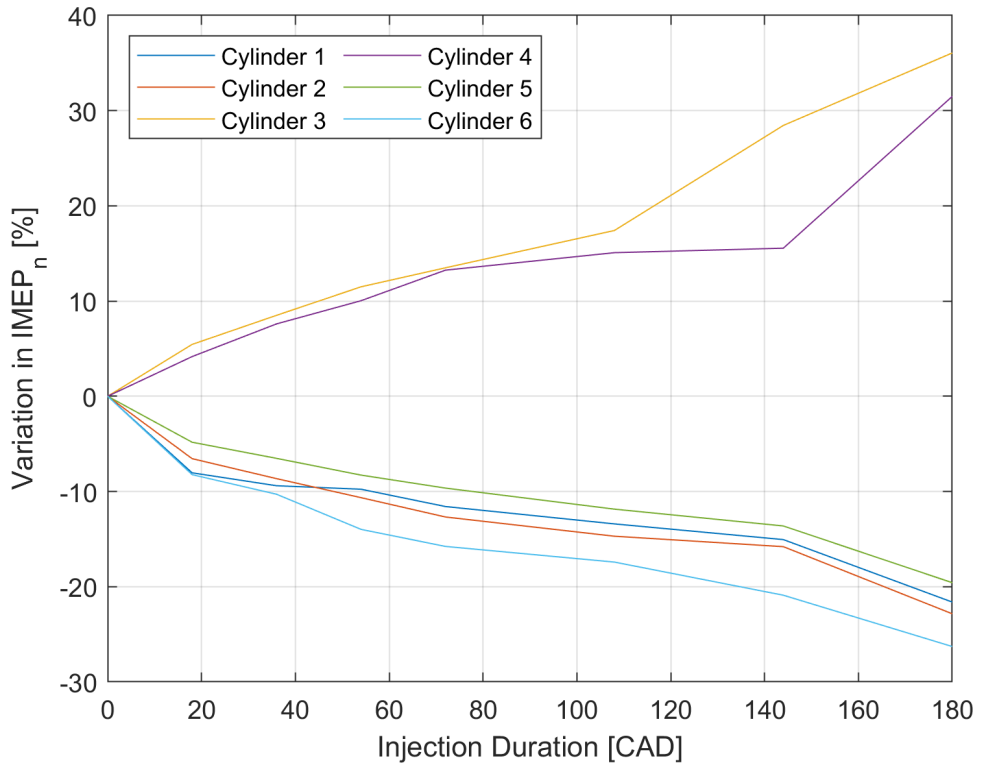


Figure 7.9: Plot of the change in IMEP_n for each cylinder against injection duration for the fixed point testing - cylinder 3 & 4 injection active.

Fuelling two cylinders with ammonia was more successful, a longer injection duration was able to be achieved up to 180 CAD. Once again the CoV increased with increasing ammonia injection duration except at 180 CAD where the variance drops to near baseline levels, as shown in Figure 7.10. Again the diesel mass flow rate was considered to understand the true substitution, Figure 7.11 presents the reduction of diesel mass flow rate as the injection duration of ammonia increases. In this case however as there are two cylinders clearly showing an increase in $IMEP_n$ as a result of ammonia injection the calculation considers two cylinder fuelling for the flowrate. A significantly lower SR was achieved for this test condition, it was predicted that this was a result of flow rate limitations.

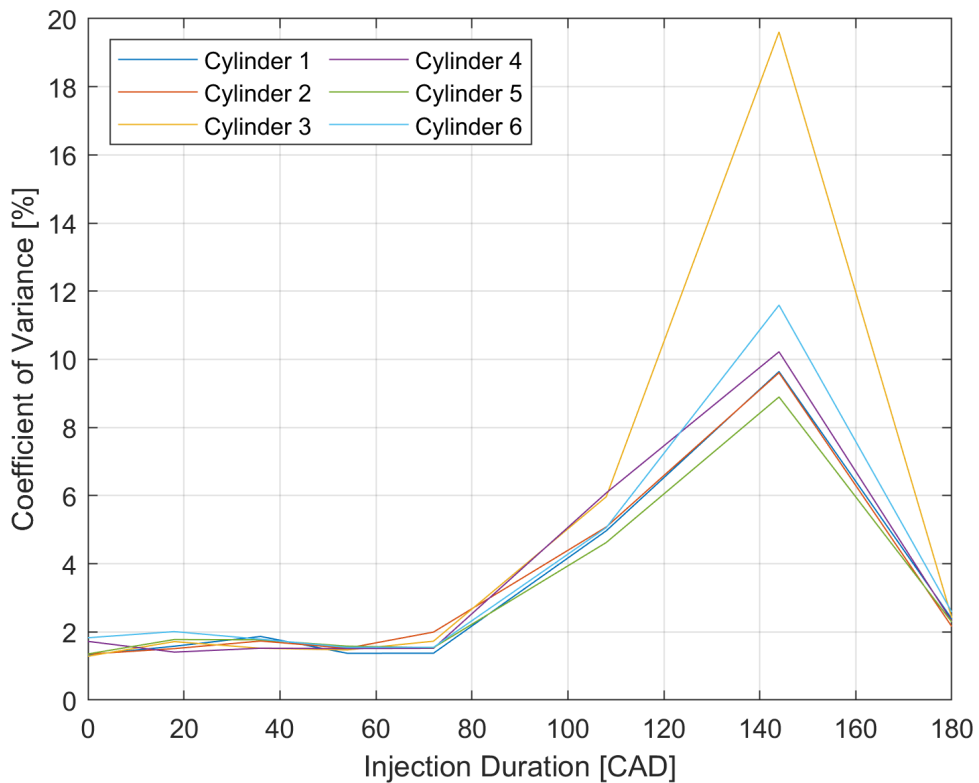


Figure 7.10: Plot of CoV of $IMEP_n$ against ammonia injection duration for each cylinder - cylinder 3 & 4 injection active.

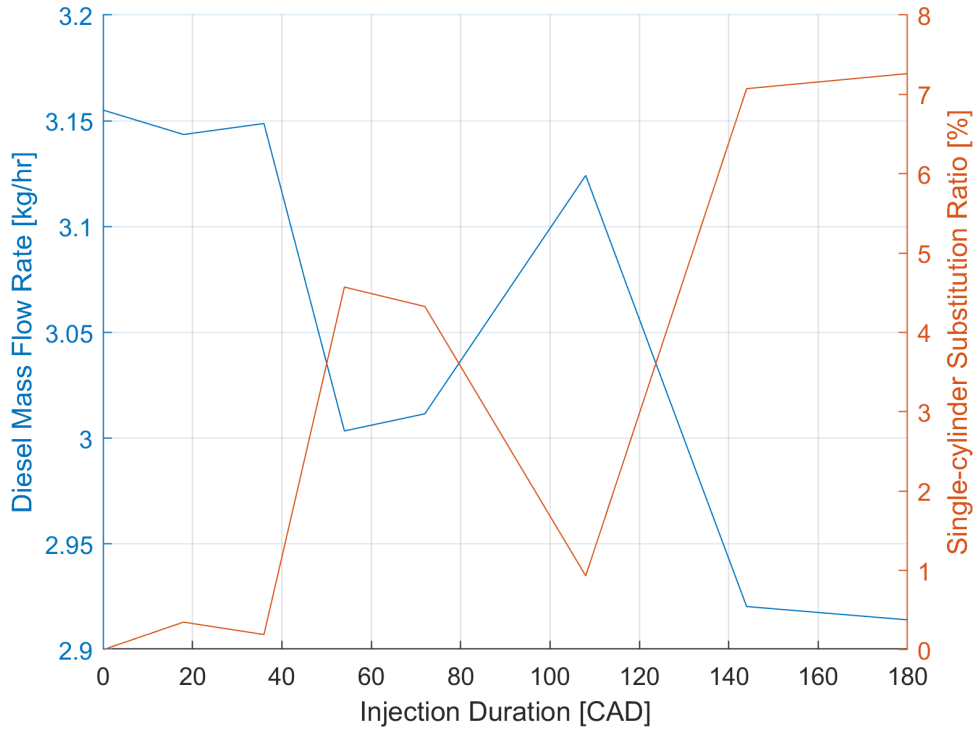


Figure 7.11: Diesel mass flow rate and average cylinder approximate ammonia SR against injection duration - cylinder 3 & 4 injection active.

The net heat release rate (HRR) for cylinder three presents a similar story, that the ammonia flow rate becomes a limiting factor at an injection duration of 180 CAD. Figure 7.12 presents the heat release rate as the injection duration increases. Once again as the ammonia duration increases the height of the diesel premixed peak decreases and the combustion is extended. However it appears at CAD 144 and CAD 180 the extension of combustion is very little.

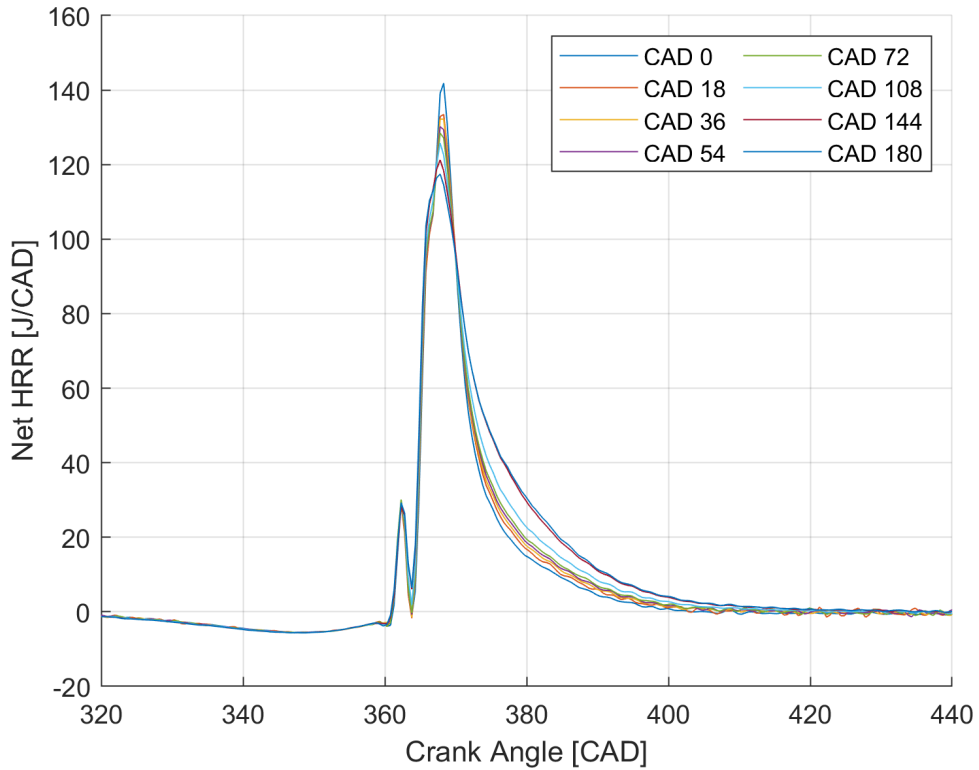


Figure 7.12: Rate of heat release in cylinder 3 against crank angle degree for various ammonia injection durations - cylinder 3 & 4 injection active.

In order to further investigate the impact of the suspected ammonia liquid in the line for the testing with all cylinder injection activated, a series of tests were performed with only cylinder 6 active. This was the furthest cylinder from the ammonia supply, potentially resulting in the other injectors acting as catches for the liquid ammonia in the line. For this set of testing an injection duration of 180 CAD was achieved. The increase in $IMEP_n$ and variance from the benchmark are plotted in Figures 7.13 and 7.14 respectively. They show a close to linear increase in the $IMEP_n$ for cylinder 6 and a decrease for the other cylinders as the engine compensated by reducing the diesel flow to the cylinders.

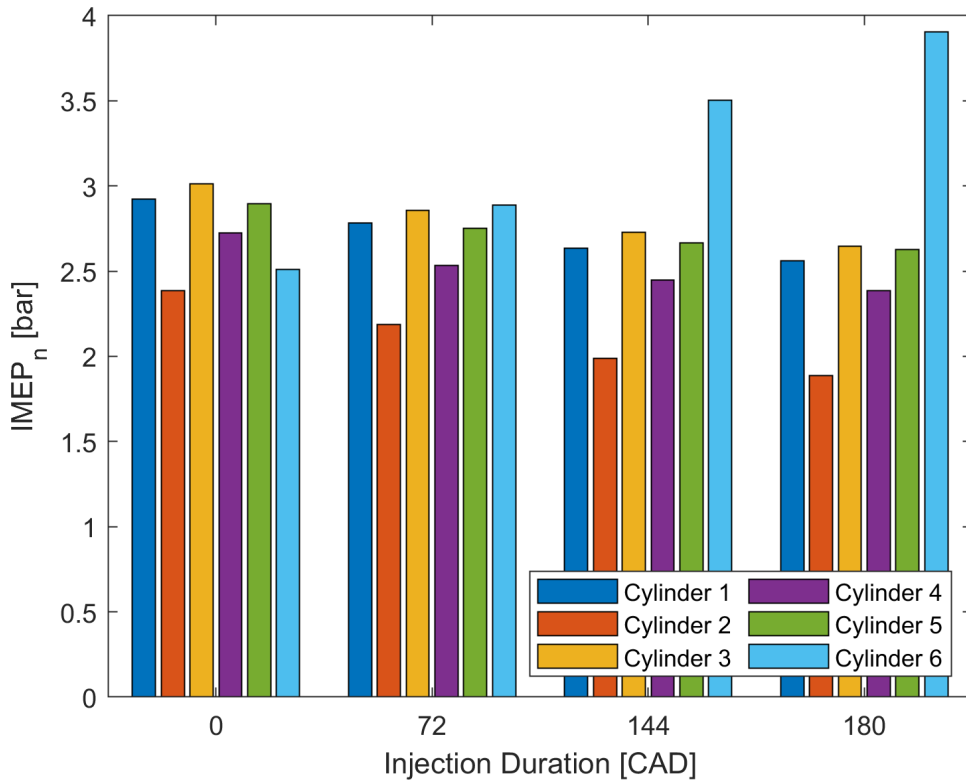


Figure 7.13: Plot of the IMEP_n for each cylinder against injection duration in CAD for the fixed point testing - cylinder 6 injection active.

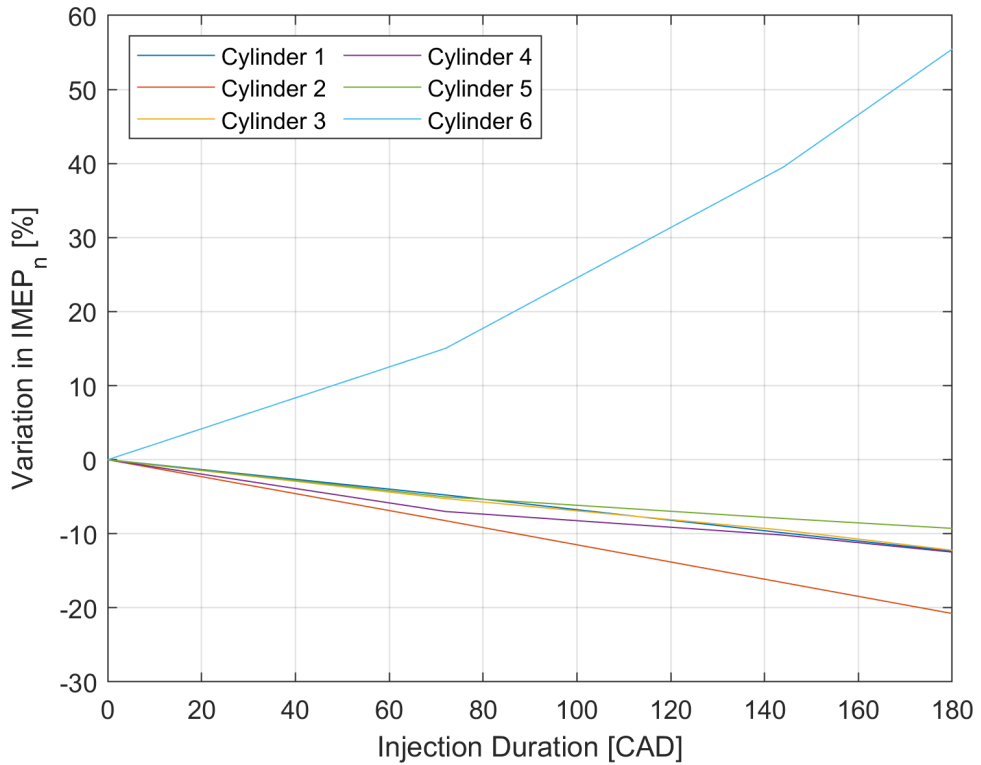


Figure 7.14: Plot of the change in IMEP_n for each cylinder against injection duration for the fixed point testing - cylinder 6 injection active.

The change in CoV is presented in Figure 7.15, showing a similar trend to the cylinder 3 and 4 active testing. The CoV increases with injection duration and then begins to decrease. For the cylinder 6 case this appears to occur earlier, peaking at 72 CAD instead of 144 CAD.

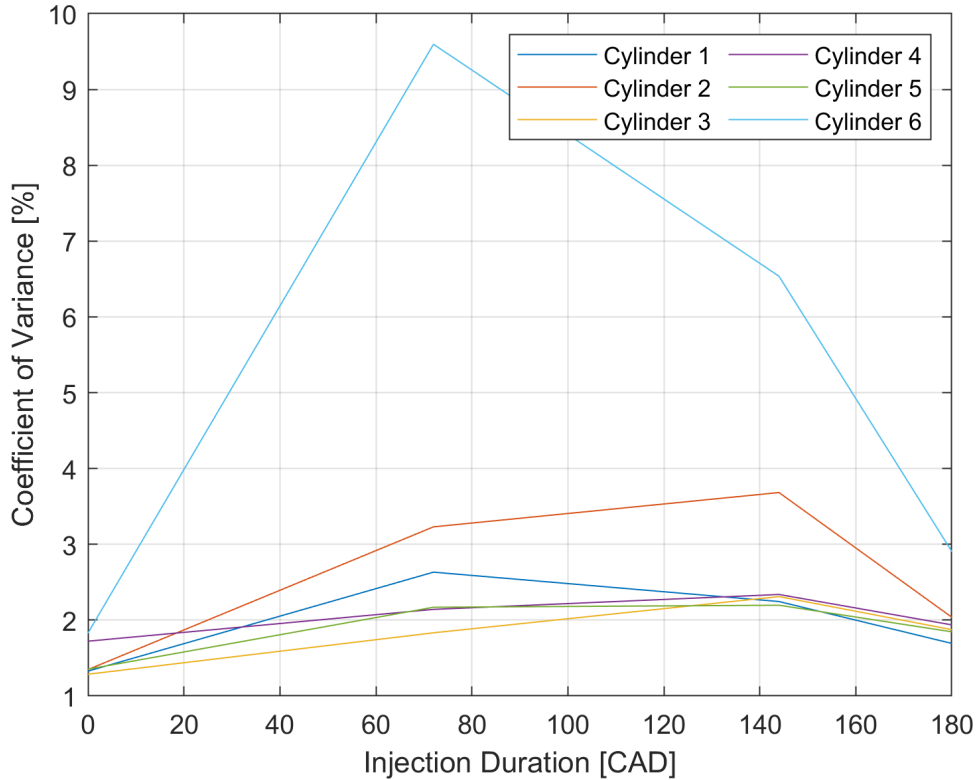


Figure 7.15: Plot of CoV of IMEP_n against ammonia injection duration for each cylinder - cylinder 6 injection active.

The change in diesel flow rate with injection duration alongside the approximate cylinder SR are presented in Figure 7.16. A drop off is observed in the cylinder SR at 180 CAD. The net heat release for cylinder 6, shown in Figure 7.17, presents the extension of combustion caused by ammonia as seen in the other test conditions.

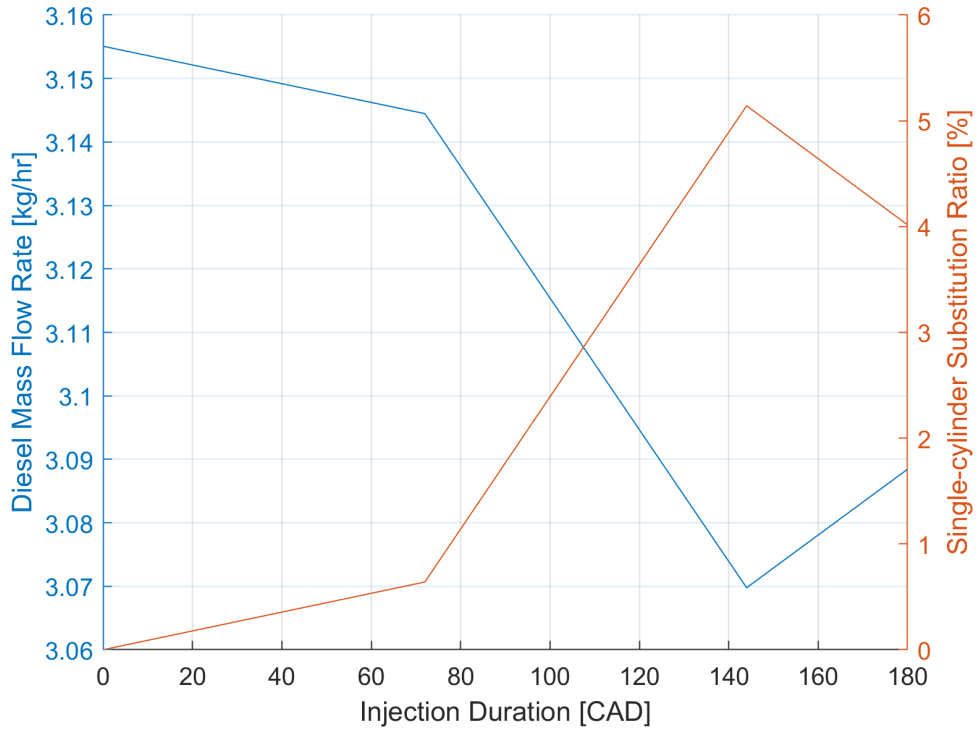


Figure 7.16: Diesel mass flow rate and cylinder approximate ammonia SR against injection duration - cylinder 6 injection active.

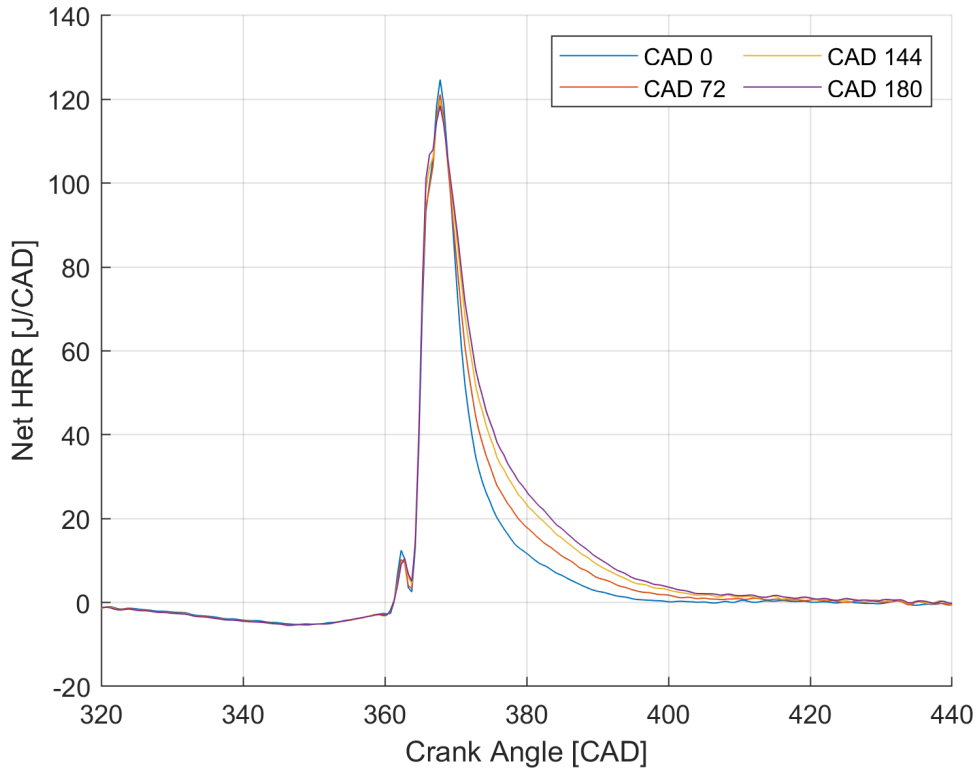


Figure 7.17: Rate of heat release in cylinder 6 against crank angle degree for various ammonia injection durations - cylinder 6 injection active.

7.2 Second iteration: Ammonia port-fuel injection

This testing was enabled by the upgrade of the ammonia fueling system and engine ECU as described in Chapter 6. Three different investigations were carried out, each targetting maximum ammonia SR.

- Unthrottled fixed speed (600 rpm) load sweep.
- Throttled (10%) fixed speed (600 rpm) load sweep.
- Unthrottled fixed load 9 bar BMEP speed.

Initial testing utilising the newly upgraded ammonia fuelling system continued to focus on the 600 rpm region, the lowest operating speed of the engine. Throughout testing the diesel injection strategy was fixed as a split injection at the minimum value required to idle the engine at operating speed, measured as 1 kg/hr, while the engine load was increased via increasing the ammonia injection quantity. At this speed, up to 55% ammonia SR by energy was achieved, with 100% throttle (full throttle). At 100% throttle, the air-fuel ratios observed were similar to diesel air-fuel ratios, presented in Figure 7.18. This resulted in poor ammonia combustion indicated by high levels of unburned ammonia in the exhaust albeit relatively low levels of NO_x as shown in Figure 7.19.

The ammonia fuel rail pressure was regulated down to 5 bar and remains within 0.5 bar for all testing except at the highest SR of the 100% throttle testing where the pressure drops to 4.32 bar indicating the rail was becoming flow limiting. With the new ECU the control of the engine was significantly improved, for this set of testing the external EGR was set to

0% to reduce noise, this will result in increased NO_x emissions and lower efficiencies. The variable geometry turbo was closed due to the lack of exhaust mass flow.

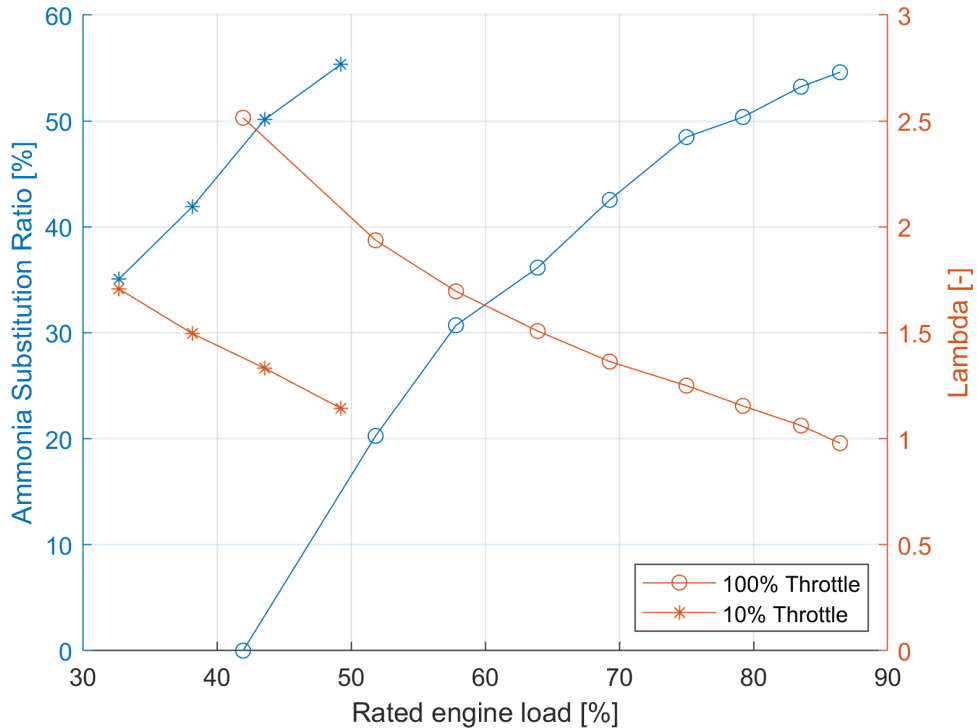


Figure 7.18: Plot of maximum SR (energy basis) achieved at 600 rpm and measured lambda across various engine rated loads - unthrottled (100% throttle) and throttled (10% throttle).

Another load sweep was performed at 600 rpm with the throttle set to 10%, this was intended to investigate methods to achieve more favourable ammonia combustion at lower loads. As ammonia combustion favours close to stoichiometric operation, throttling the engine provided the ability to operate the engine at close to stoichiometric for lower load operation. In this case, at 50% rated load at 600 rpm, the combustion was close to stoichiometric, achieving a reduced ammonia slip albeit higher NO_x emission.

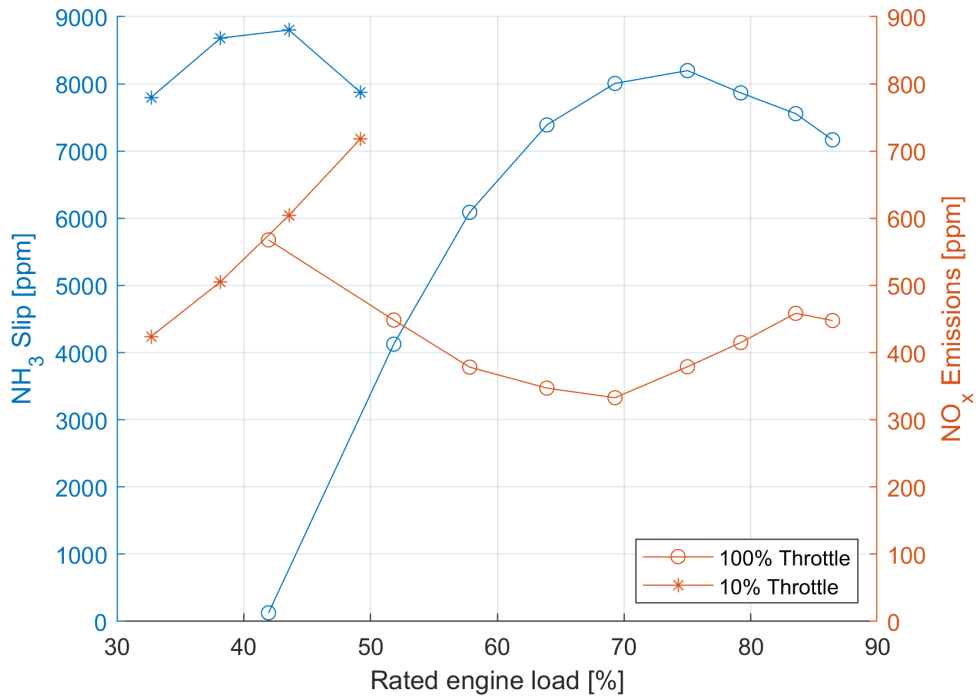


Figure 7.19: Plot of ammonia slip and NO_x emissions at 600 rpm across various engine rated loads - unthrottled (100% throttle) and throttled (10% throttle).

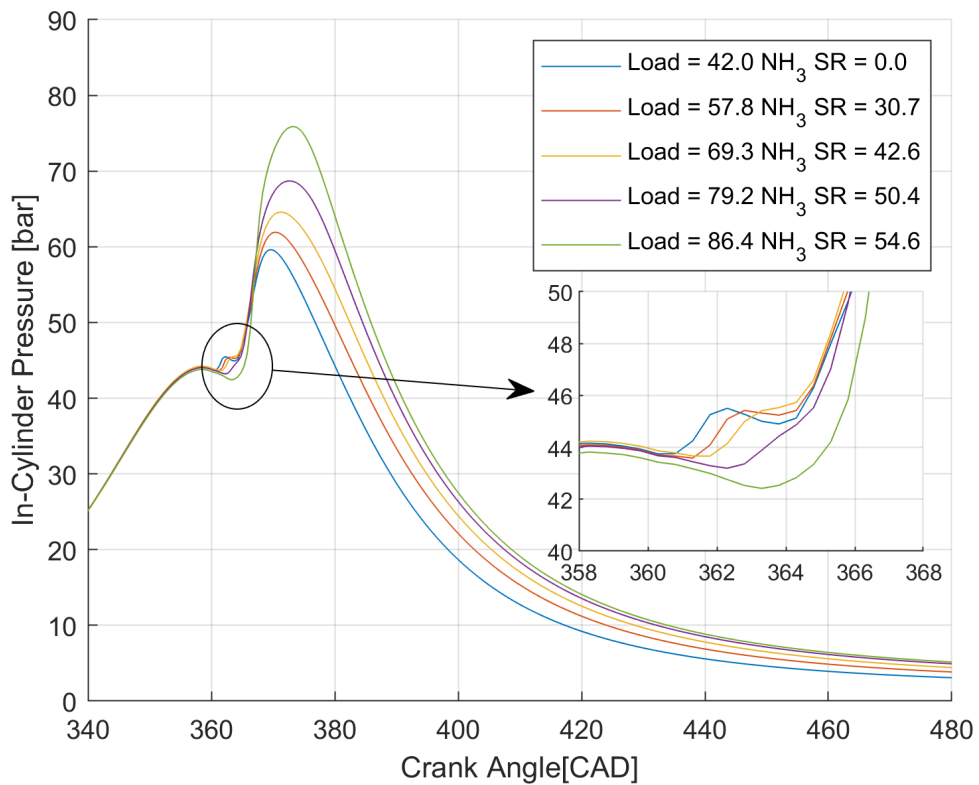


Figure 7.20: Plot of in-cylinder pressure at 600 rpm across various engine rated loads - unthrottled (100% throttle).

The reduction in air flow decreased the combustion gas temperature at ignition due to the reduction in trapped mass in the compression stroke. This impacts the effectiveness of ammonia and diesel combustion. The colder combustion temperatures at ignition result in a slower ammonia burn, increasing the slip and generally resulting in poor combustion. Figures 7.20 and 7.21 show the pressure against crank angle for the 100% and 10% throttle testing respectively. For the 100% throttle test condition the loss of the pilot diesel burn can be observed for the 79% and 86% rated engine load cases where the SRs on an energy basis were 50% and 55% respectively, this is highlighted in the magnified plot in Figure 7.20. For the 10% throttle condition, there is no presence of the pilot diesel burn in the plots.

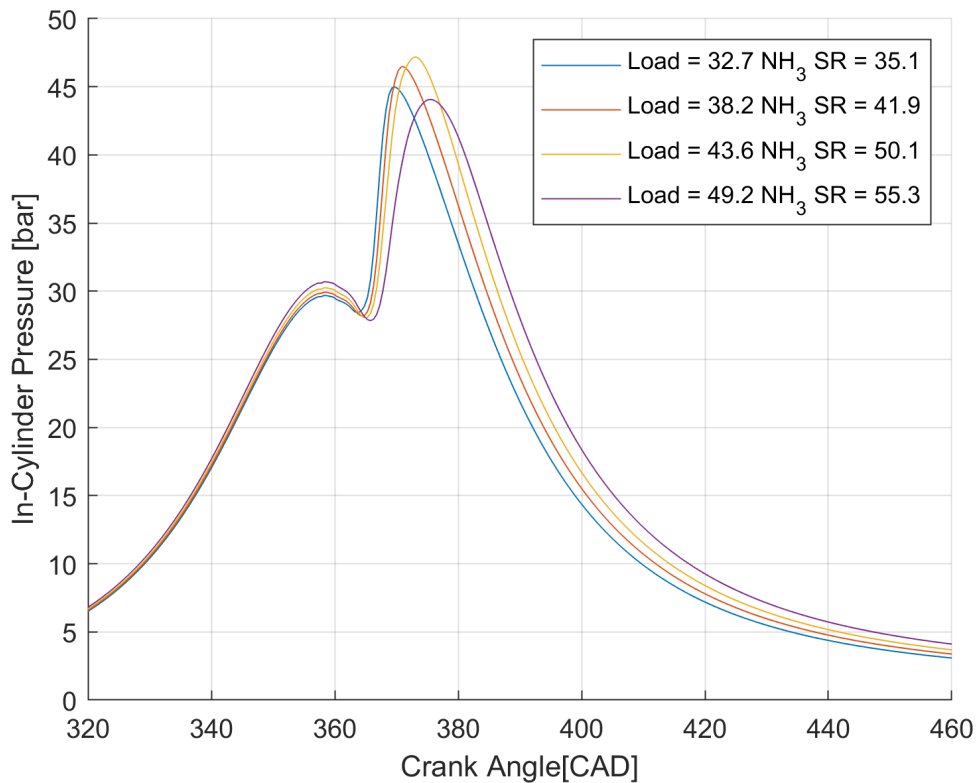


Figure 7.21: Plot of in-cylinder pressure at 600 rpm across various engine rated loads - throttled (10% throttle).

For the first iteration testing, the variation in IMEP_n is measured as the variation in IMEP_n from a measured baseline with no ammonia injection. For the testing completed for the second iteration, as the target was maximum substitution at increasing load points, the variation was defined as the variance from the average of all cylinder IMEP_n for that test point relative to the no ammonia injection point, presented in Figure 7.22. These results still present a degree of bias towards cylinder one, two and six, although it is significantly reduced in comparison to the first iteration design.

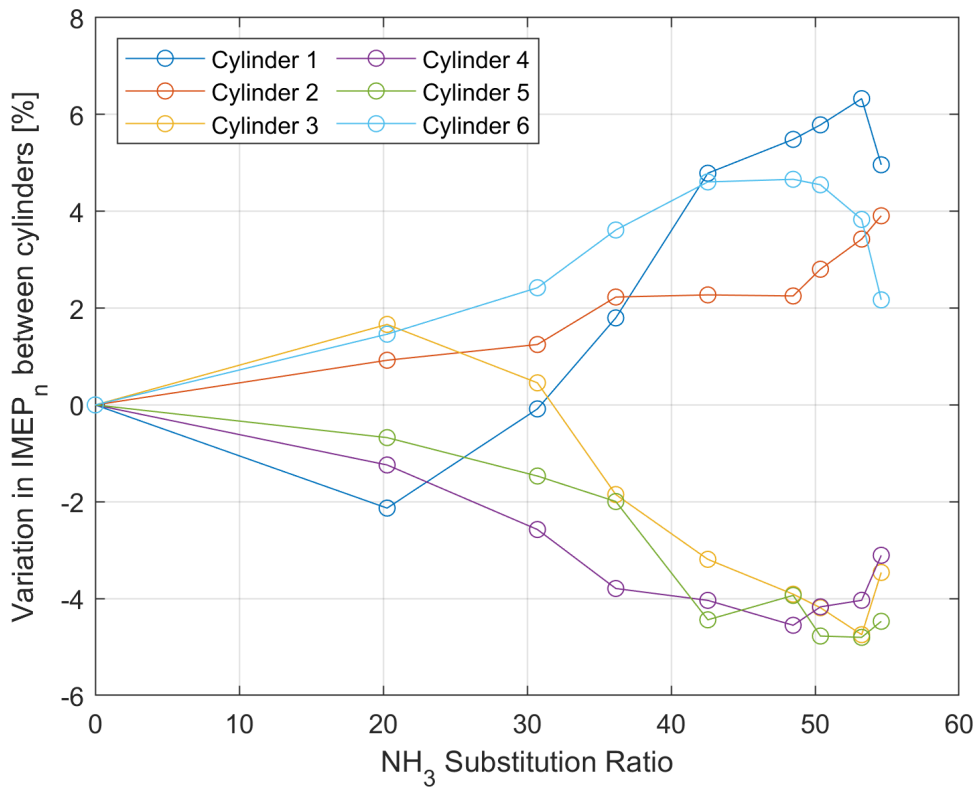


Figure 7.22: Plot of IMEP_n variation from the mean for each cylinder with varying SR and load - unthrottled (100% throttle).

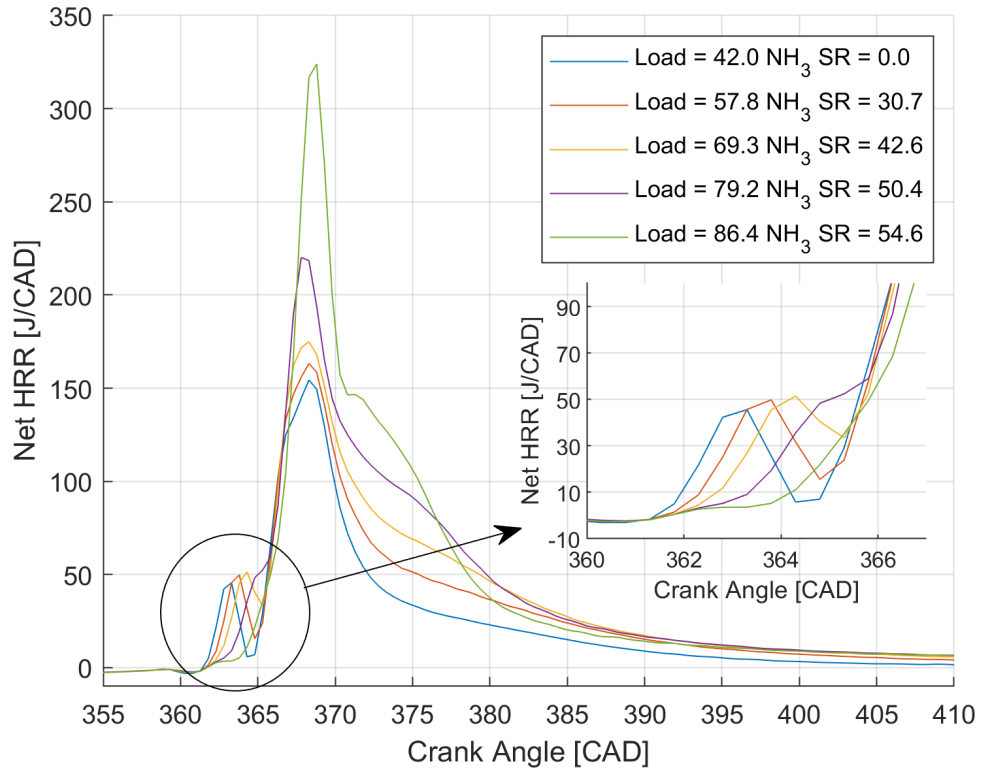


Figure 7.23: Plot of net heat release at 600 rpm across various engine rated loads - unthrottled (100% throttle).

The net heat release rate plots, shown in Figure 7.23, present the heat release curve against crank angle degree for the increasing load and ammonia SR. As the ammonia SR increases, as observed in previous cases, the duration of combustion increases shown by the more gradual tail end of the premixed diesel peak. At the highest SR, 54.6%, the combustion appears to increase in speed, this is suspected to be as a result of the conditions reaching close to stoichiometry and indicates further need for optimisation to improve this combustion further. The magnified section of the plot shows the impact of the ammonia injection and increasing load on the diesel pilot injection. The pilot was a fixed injection at 0.5 CAD before top dead centre, as the ammonia increases the combustion delays until at the highest SR and load where the pilot merges with the diesel premixed peak.

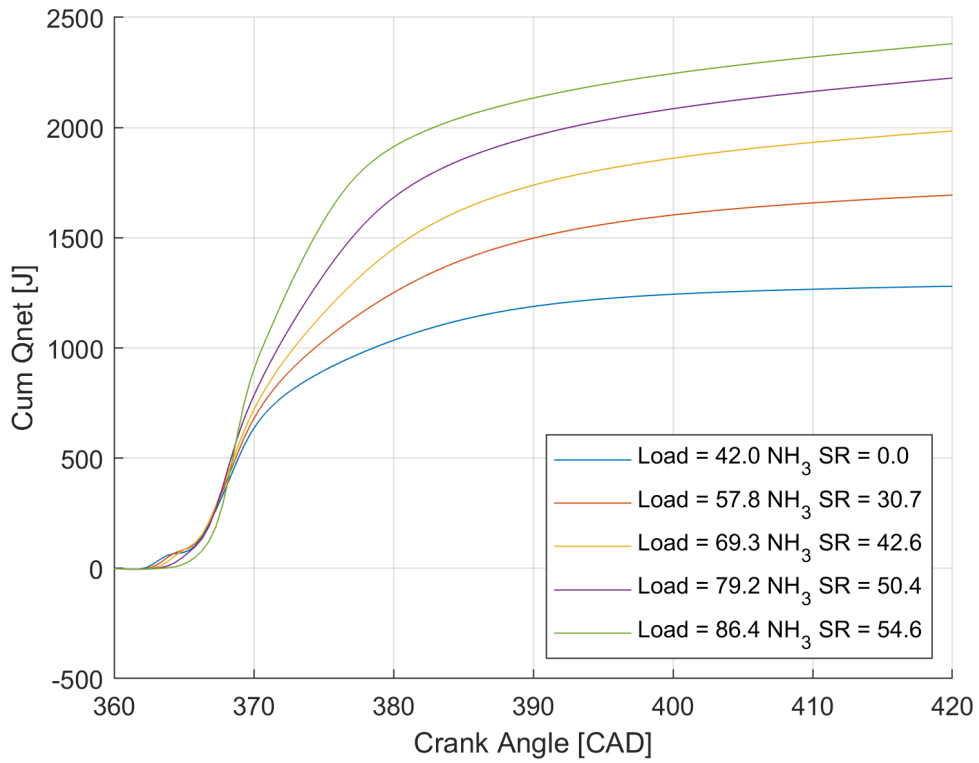


Figure 7.24: Plot of cumulative heat release at 600 rpm across various engine rated loads - unthrottled (100% throttle).

The cumulative net heat release curve, shown in Figure 7.24, for the unthrottled test condition show the contribution of ammonia to the combustion energy. The initial pilot combustion can be observed for all but the two highest SRs. After the initial diesel increase, there appears to be a slight inflection and subsequent linear increase post 370 CAD for the 50 and 55% ammonia SR points. The gradient of the inflection increases between the two points, suggesting a higher quality of combustion of ammonia at the higher load point - closer to stoichiometric.

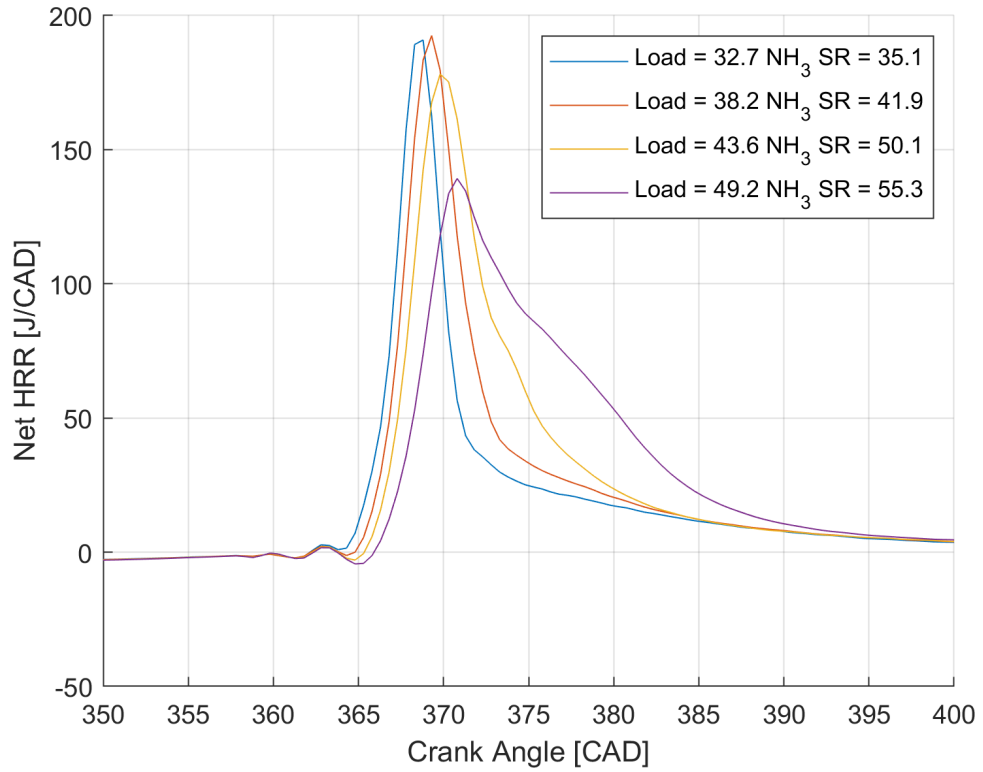


Figure 7.25: Plot of net heat release at 600 rpm across various engine rated loads - throttled (10% throttle).

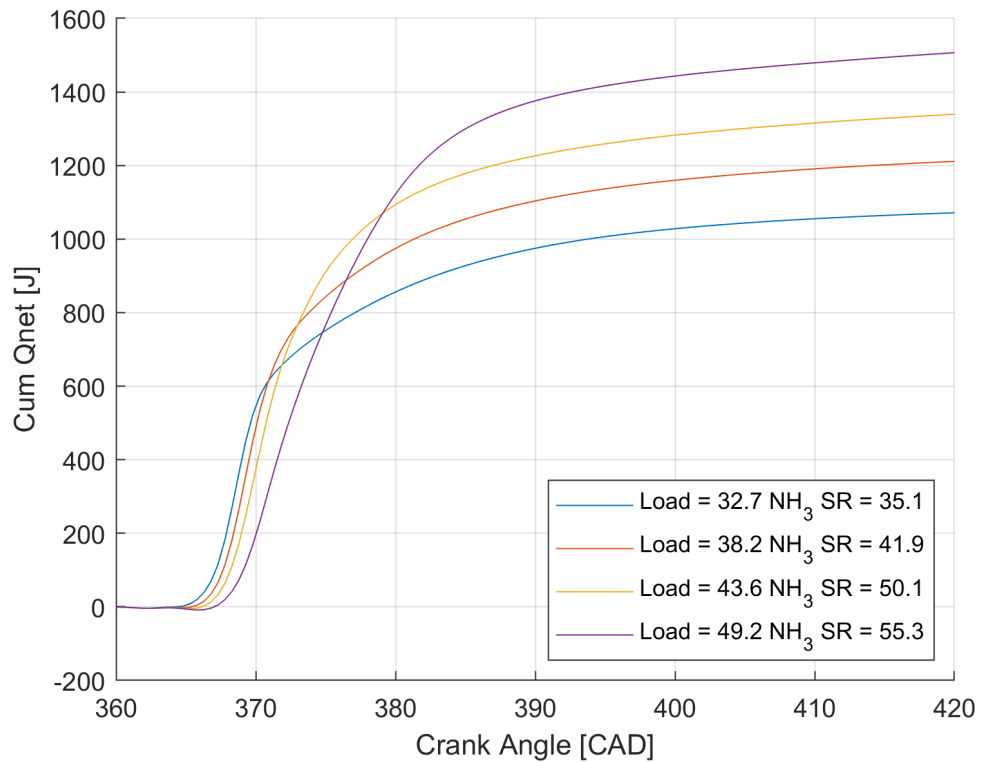


Figure 7.26: Plot of cumulative heat release at 600 rpm across various engine rated loads - throttled (10% throttle).

For the throttled test condition, the increase in load and ammonia SR delays the premixed diesel peak as well as extending the entire combustion as shown in the net heat release plot and cumulative heat release plots, Figures 7.25 and 7.26 respectively. Unlike the unthrottled test condition, there is no evidence of an inflection and linear increase, this suggested the diesel and ammonia combustion is better aligned, keeping the combustion duration relatively fast. At the highest load/SR condition there is a significant delay to combustion as a result of a lack of air in the chamber for the diesel fuel to ignite with.

In the final set of testing, the maximum ammonia SR at 9 bar BMEP for varying engine speeds was investigated. A SR of about 90% was achieved at both 600 and 800 rpm at 9 bar BMEP, this equates to maximum load at 600 rpm and 70% load at 800 rpm. At 1000 rpm, a SR of 73% was reached, in this instance the load is 54% of the engine rated load at that speed. Figures 7.27 and 7.28, present the SR achieved and the mass flow rates measured for ammonia and diesel for the various speeds.

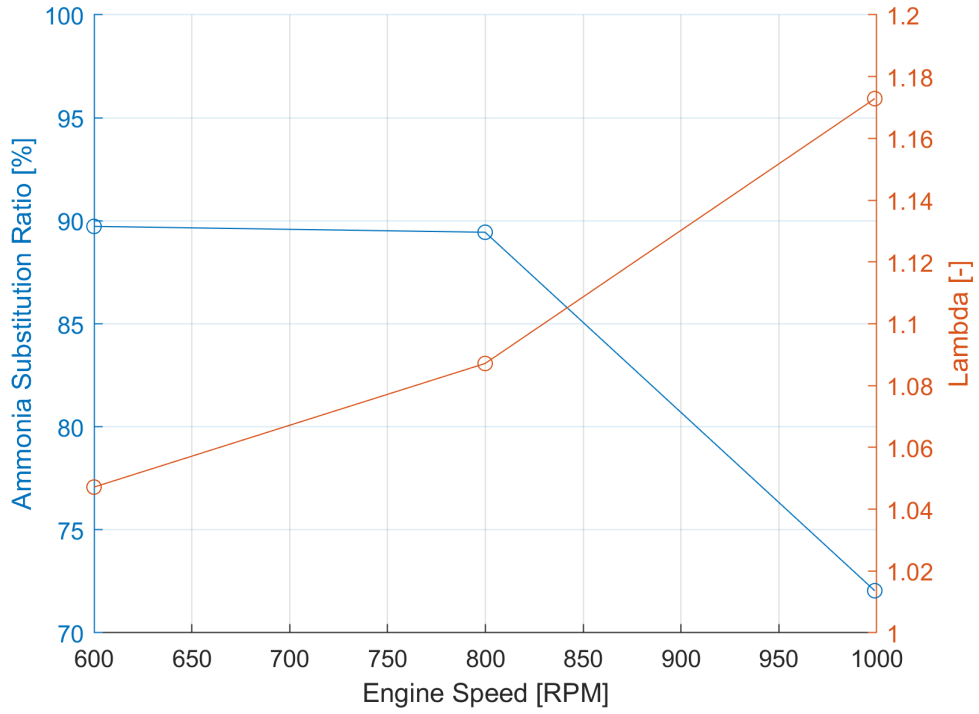


Figure 7.27: Plot of maximum SR (energy basis) achieved at 9 bar BMEP and measured lambda across various engine speeds.

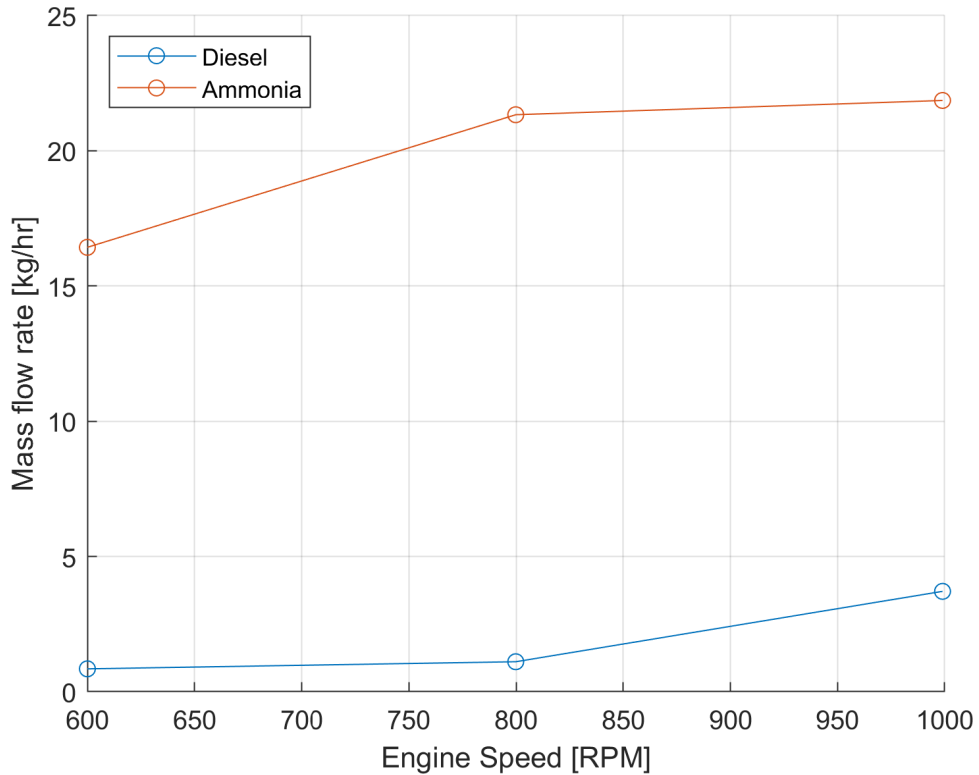


Figure 7.28: Plot of ammonia and diesel mass flow rates achieved at 9 bar BMEP at various engine speeds.

The increase in diesel fuelling and lambda observed at the 1000 rpm test condition suggests a fuel flow rate limitation at this condition. Throughout testing the brake thermal efficiency remained at 37% and the CoV was below 1.5% for all tests. Figure 7.29 presents the average in-cylinder pressure measurement for the three test points recorded. The net heat release plots shown in Figure 7.30, show a change in the diesel combustion as a result of increased diesel mass flow rate. The highest speed condition shows the increased diesel fuelling causing a premixed peak and a mixing-controlled burning phase, in other testing the diesel injection quantity has been low enough that the diesel charge is consumed within the first premixed phase of combustion.

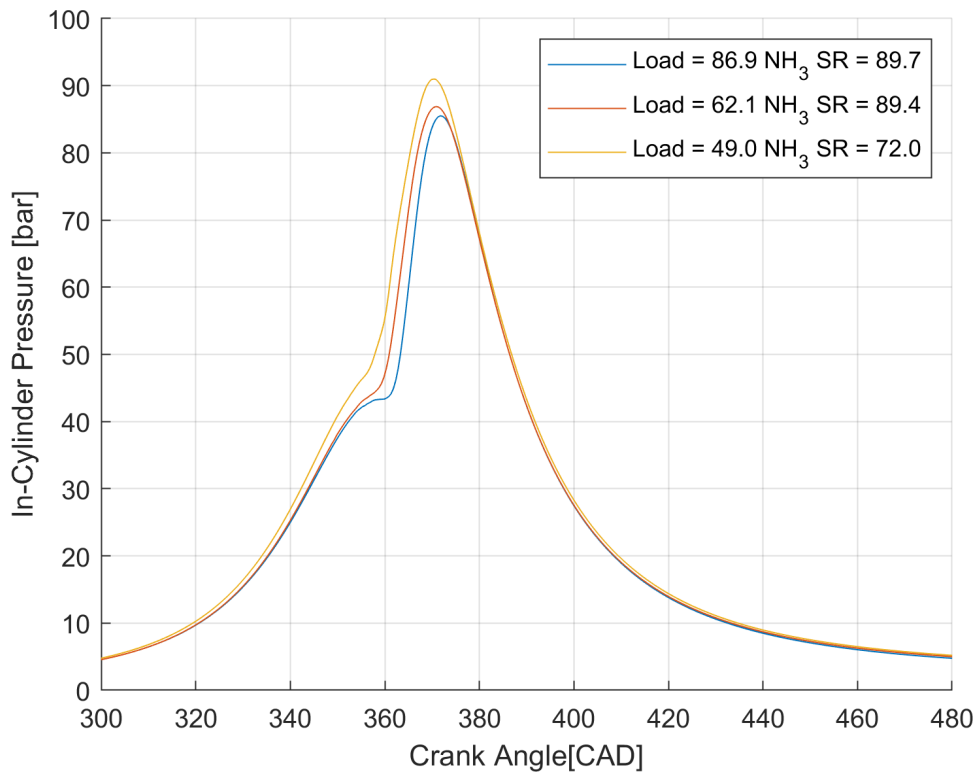


Figure 7.29: Plot of in-cylinder pressure against crank angle at 9 bar BMEP for various engine speeds.

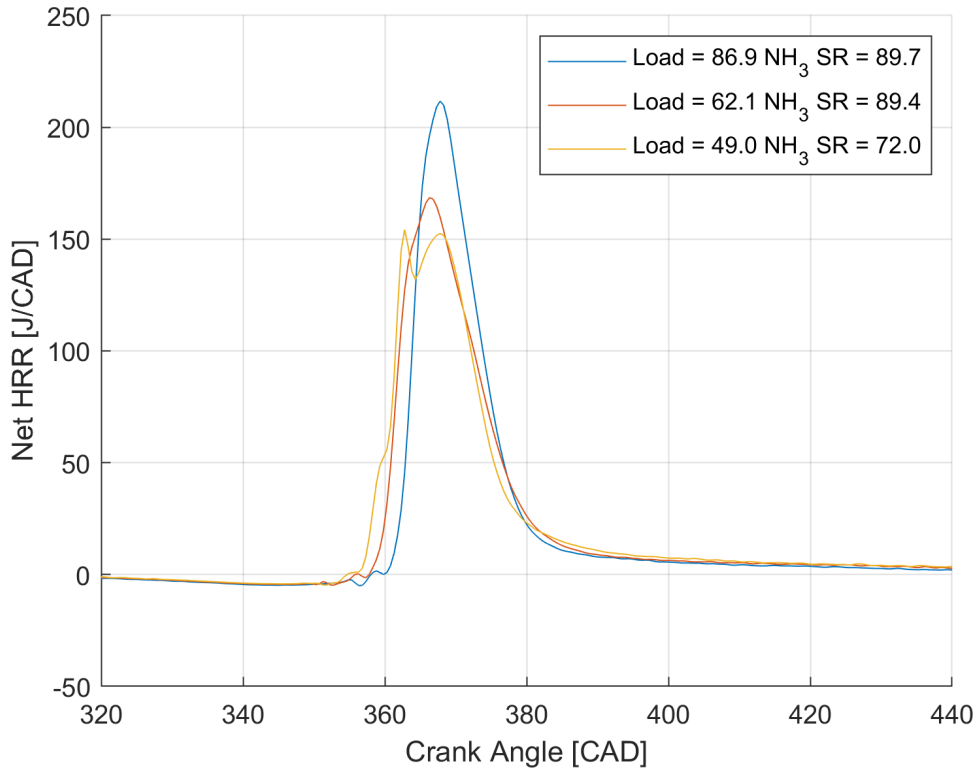


Figure 7.30: Plot of net heat release against crank angle at 9 bar BMEP for various engine speeds.

7.3 Discussion

Early ammonia testing was performed with the initial ECU and optimiser setup described in Chapter 6, the tests were carried out at 600 rpm - the minimum engine speed to aid in ammonia combustion due to its slow burning velocity - and 25% load at that speed. Diesel was injected in a two pulse mode (pilot and main) with ammonia fumigated into the chamber upstream of the ports. Fixing the engine load, the ammonia injection time was increased as the diesel injection quantity was reduced. The contribution of the ammonia addition to the total heat release of the combustion cycle was then calculated to determine the apparent energy SR. This SR accounts for the true quantity of ammonia combustion however the intricacies of ammonia slip as well as the influence on the combustion efficiency

lead to a high degree of uncertainty around the combustion.

The first set of testing consisted of an all-cylinder injection ammonia injection sweep. The testing revealed that not only was cylinder 1, the nearest injection site, receiving the majority of the ammonia flow, calculated from the variation in $IMEP_n$, but also that the fuelling to that cylinder was extremely unstable based on the CoV recorded. As a result of the instability, the testing was limited to a short injection duration to avoid stressing the engine crankshaft due to the cylinder-to-cylinder imbalance. The high instability alongside the observation of icing on the fuel lines shown in Section 6.8.4 suggest the presence of liquid ammonia in the fuelling line, this was also the suspected cause of the ammonia flow meter reading fluctuating significantly. Observing the cylinder heat release, Figure 7.7, the impact from the ammonia injection can be seen as the diesel premixed combustion peak reduces and the combustion duration is extended. The difference between no ammonia injection and CAD 18 injection duration is small in-comparison to CAD 36, it is suspected that at the shorter injection duration the ammonia was not able to combust at such low concentrations.

Two more ammonia injection options, cylinder 3 and 4 injection only and cylinder 6 injection only, were investigated in order to investigate the ammonia fueling impacts further. The injection strategies were selected in accordance with the engines firing sequence. By firing only cylinder 3 and 4, the goal was to counteract the rail favouring cylinder 1 as well as balance the injections between two cylinders. It was found that the stability of the engine improved significantly, with the two cylinders having a variation in $IMEP_n$ of 30% at in injection duration of 180 CAD in comparison to cylinder 1 injection variation of 20% at 35 CAD. The CoV of each cylinder was measured, remaining relatively low around 2% up to an injection duration of 72 CAD. The variance peaks at an injection duration of 144 CAD with

all but cylinder 3 showing around 10%. Cylinder 3 was close to double this at 20%, it was suspected that this was as a result of liquid in the line still reaching the cylinder. Interestingly the CoV recovers close to baseline levels at an injection duration of 180 CAD, considering the diesel fuel flow rate remains steady between the two points, it is suspected at this point the ammonia fuelling is flow limited as shown by the little change in both SR and heat release. The recovery could also be as a result of the extended duration injection providing enough time for any liquid ammonia injected to evaporate and reduce impact on the CoV.

When isolating injection to only cylinder 6, the intention was to attempt to remove the variation fully as a result of the liquid ammonia entering the chamber. This appeared to work as the variation in $IMEP_n$ from the baseline was 10% lower than the cylinder 1 testing. The CoV in $IMEP_n$ showed a peak at an injection duration of 72 CAD and then a recovery to close to baseline levels at the maximum duration of 180 CAD. The recovery was suspected to be as a result of the increased duration whilst being flow limited causing a reduction in rail pressure reducing the quantity of ammonia liquid. Unfortunately this iteration did not have digital rail pressure monitoring to prove the theory in its entirety. Lower single-cylinder SRs are observed for this injection strategy. This suggests the strategy was successful in reducing the ammonia liquid being injected into the line.

The initial testing utilising the first iteration ammonia fuelling rail provided key insights into the design of future fuelling systems, the following conclusions and subsequent upgrades were realised;

- Liquid ammonia was present in the fuelling line, impacting both the fuel instrumentation (fuel flow meter) and the in-cylinder combustion. A regulator was included in the new fuelling line to step down

the ammonia pressure, moving it away from the phase change and reducing the chance of it condensing.

- The single side fuelling design resulted in the fuel favouring the first cylinder. As a result the fuelling line was reconfigured to have a dual feed of ammonia as well as an increased rail volume to reduce the impact of a single injection on the total rail fuel quantity.
- At high injection duration, the ammonia flow rate became limiting. The volume of the ammonia fuelling system was altered to allow for higher flow rates as well as a larger injector nozzle diameter to increase the flow rate into the port per crank angle duration.
- Finer control of the injection strategy was required, this would allow for further optimisation of the ammonia combustion and improve SRs.

Together with the new fully integrated whole engine control system from MAHLE Powertrain, the upgraded ammonia fuel delivery system and rail, detailed in Section 6.8.4, improved the overall fuel flow and enabled greater control over fuel targeting and timing. These two upgrades combined enabled the engine's operating conditions to be optimised to favour ammonia-appropriate combustion conditions as well as precise control over the injection timing and quantity.

The first set of testing completed on the upgraded system was a 600 rpm unthrottled load sweep, for this testing the diesel pilot and main injections were fixed at the minimum load (idle) and speed condition whilst the ammonia injection quantity was gradually increased. A higher SR of 55% ammonia with 45% diesel by energy was achieved in this testing, showing a significant improvement on the first iteration testing. The in-cylinder

pressure and net heat release curves show a gradual shift of diesel pilot injection as the SR increases, it is suspected that this is due to a reduced combustion gas temperature as a result of the ammonia injection impacting the diesel combustion quality and increasing the ignition delay. At the higher end SRs, 50% and 55%, the combustion speed increases as shown by the higher ammonia peak post the diesel premixed phase with a sharper drop off, this is due to the close to stoichiometric conditions favouring the ammonia combustion. A large improvement on the variation in $IMEP_n$ was seen for this test condition with a maximum of 6% observed at the maximum SR as shown in Figure 7.22. As the ammonia SR increases, the variation increases for cylinders 1, 2, and 6, indicating a degree of fuelling imbalance between the cylinders. The drop off in variation at the test point indicates a maximum flow rate has been reached, which is confirmed by the drop in fuel rail pressure. It is important to note diesel engine intake manifolds are not developed to the same high level of cylinder-to-cylinder air flow accuracy that is required for SI engines. This becomes problematic when operating with dual fuel gaseous port fuel injection which necessitates fuel balancing capabilities in order to precisely control cylinder-to-cylinder air fuel ratios. This balancing capability would improve the stability of the engine and dual fuel operation. Future work will need to address the individual injector balancing and/or utilise an new intake manifold design with improved cylinder-to-cylinder air flow distribution.

The high levels of ammonia slip were expected as a result of the engine geometry remaining unaltered during testing as shown in Figure 7.19. The engine was designed to operate with diesel fuel, usually under lean conditions. With these conditions it is expected that a degree of charge slip is observed, however when introducing a port fuelled gaseous fuel, the slip is exasperated. Alongside this, stoichiometric mixtures favour ammonia

combustion, so the lean conditions resulted in poor burning of ammonia adding further to the exhaust slip. Relatively low levels of NO_x emissions were observed, the emissions initially decreased as the ammonia substitution increase, reaching a minimum of 320 ppm at a rated engine load of 70%. The emissions then increased up as the SR approached the maximum, as shown in Figure 7.19. It is suspected that the initial decreasing is as a result of thermal NO_x production being curtailed by reduced combustion temperatures, the subsequent increases is as a result of fuel bound NO_x production increasing as a result of increased ammonia combustion.

In order to investigate lower load operation as well as the relationship between lambda and ammonia combustion, a 600 rpm load sweep was conducted with the engine throttled to 10%. By limiting the quantities of air reaching the chamber the fuel mixture became richer, approaching stoichiometric. The ammonia SR was able to be ranged from 35% to 55% at a significantly lower load, 32% to 50% rated engine load at 600 rpm. During this testing the relationship between ammonia combustion and lambda was similar to the unthrottled condition, at the highest SR, lambda was close to stoichiometric.

The reduced air flow decreases the combustion gas temperature at ignition as a result of the lower trapped mass in the cylinder, this reduction impacts the quality of combustion of both diesel and ammonia slowing the combustion significantly. The decrease in combustion quality resulted in high ammonia slip. In addition to this, the net heat release graph, shown in Figure 7.25, shows the absence of the pilot diesel fuel burn peak observed in previous testing, suggesting the conditions were too cold, inhibiting the initial burn. At the highest load condition, the heat release curve also revealed a highly delayed combustion which was indicative of a deterioration in diesel combustion quality, suggesting thermal limitations. Future

studies to look further into the relationship of ammonia substitution ratio and specific burn duration data would provide further insight into this. Despite the considerable slip, the ability to achieve high SRs at low loads suggests the need for an optimisation study to determine the “sweet spot” to favour ammonia combustion whilst maintaining initial diesel combustion. It also suggests the air-fuel ratio has a stronger relationship than the end-gas temperature for ammonia combustion.

The final investigation targeted maximum ammonia SR at 9 bar BMEP unthrottled for the speed points, 600, 800, and 1000 rpm. This testing enabled further assessment of the impact of lambda at varying speeds. 90% ammonia substitution ratio was achieved for the 600 and 800 rpm speed points, with a drop off at 1000 rpm suspected to be as a result of the fuelling system becoming flow limited, indicated by an increase in diesel mass flow rate and lambda at said point. Higher SRs were harder to attain at higher speeds under the fixed load condition, this is due to the narrower ammonia port fuel intake window due to increased piston speed. Optimised engine operation and injection timings have shown comparable levels of brake thermal efficiency to those under conventional diesel operation.

Under all conditions, dual-fuelled gaseous ammonia operation resulted in high ammonia slippage. Although some of this can be accounted for as a result of the engine geometries, the values superseded any potential use as a NO_x reductant in conjunction with a selective catalytic reduction system. As a result an additional ammonia oxidation step will be essential in the exhaust stream in addition to appropriate SCR operation to control tailpipe NO_x . A potential option to improve the NH_3 to NO_x ratio for effective SCR operation would be to introduce a degree of ammonia cracking to the fuelling system, cracking the ammonia into hydrogen would improve combustion velocity and reduce NH_3 slip.

Chapter 8

Conclusions &

Recommendations for Future

Work

In order to develop understanding of the use of alternative fuels such as ammonia and hydrogen within combustion engines, two experimental studies have been undertaken. A new capability has been developed which bridges the gap between foundational work within literature of optical combustion studies to real world applied engine combustion systems. Enabling future combustion studies which will provide routes to optimise advanced combustion systems such as turbulent jet ignition for use with alternative fuels.

Extending to the more practical implementation of ammonia as a fuel, a diesel engine retro-fit study has been undertaken. Within this study, a fueling system and testing rig has been adapted enabling flex-fuelling of multiple fuels including ammonia and hydrogen. This chapter provides a comprehensive summary of key findings and contributions to the field.

8.1 Novel optical constant volume combustion chamber

A novel, optically accessible, constant volume combustion chamber was designed to replicate heavy-duty engine conditions and geometries, with its modular design enabling the assessment of various ignition systems including spark ignition, turbulent jet ignition, and central electrode ignition with multiple fuels. The chamber was hydro-statically tested and verified to British Standards (BSEN 13445:2021 and PD5500) by an external provider. The chamber opens up a wide range of possible fundamental and applied combustion studies to further investigate alternative fuels such as ammonia and hydrogen as well as providing an experimental setup for computational model validation.

Studying the combustion characteristics of methane-air flames provided means of validating the chamber against literature results. Comparisons with literature values revealed a good correlation with literature with expected deviation as a result of the alternative spark initiation and geometries of the chamber. Testing with ammonia flames provided insight into the impact of buoyancy as a result of the slow flame speeds. Ammonia hydrogen testing was also completed in order to understand the influence of hydrogen as a combustion promoter with ammonia. Significant increases in flame speed were observed with increasing hydrogen substitution. Between 20-30% hydrogen substitution, the flames became cellular as a result of thermodynamic instabilities resulting in increased flame area and subsequent self acceleration of the flames.

Exploring the influence of the wall proximity to the spark initiation, a side view configuration was used to investigate methane-air flames. The results

indicated a clear influence causing slower flame speeds to be measured near the wall, expected to be as a result of heat transfer and limitations of flame stretch towards the wall. Removing the influence of the wall did not align the chamber with literature values, suggesting the impact of the wall proximity at the early kernel propagation impacts the entire flame progression. The results produced within these studies serve as a baseline for future work, particularly in comparing the use of advanced combustion systems in conjunction with alternative fuels.

8.2 Diesel engine retrofit for ammonia

An existing production Volvo diesel engine was modified to incorporate gaseous ammonia dual fuelling by ammonia port injection. The test bed was upgraded with a new fully integrated ECU enabling flexible fuelling of diesel, ammonia, and hydrogen with full control over engine parameters. The engine retained full diesel fall-back capability. The conversion was split into two stages with learning carried across from the first iteration to the next. The initial conversion consisted of an ammonia fumigation system in conjunction with in-house controllers and OEM engine control resulting in limited overall engine stability. The following conclusions were made in this initial development phase;

- The presence of liquid ammonia within the fuelling line necessitated the inclusion of a regulator to reduce pressure and prevent condensation. The sensitivity of the two phase ammonia storage tank to ambient temperatures can result in limitations on fuel flow rates. Further work on the rate of fuel extraction from large ammonia volumes is needed to understand the limitations on the flow demand

from the engine. High gaseous demand applications might require the use of a vaporiser to improve draw rate from tanks, otherwise rate is reliant on rate of evaporation which impacts temperature and reduces pressure.

- The injection rail design resulted in uneven fuelling of ammonia to the cylinders, to improve this the injection rail volume was increased to improve flow rates to the cylinders and reduce the impact of an injection on the total rail volume. The rail was upgraded to a dual feed system to improve the balancing further and digital rail pressure monitoring was introduced to track drops in pressure as a result of flow limitations.
- Stronger control of the engine parameters was necessary to optimise ammonia combustion and improve general engine stability.
- The air flow imbalance of the intake manifold impacts gaseous ammonia and hydrogen fuelling causing cylinder-to-cylinder variance.

The upgraded ECU provided a significantly improved level of control of the standard engine parameters as well as over the ammonia fuelling. This, alongside the ammonia fuel delivery system upgrade provided the capability to complete a new set of testing across a variety of speeds and loads. With the new upgraded system, the following was found;

- The new system achieved a substitution ratio of 90% ammonia to diesel fuelling at full engine load and 600 rpm (engine baseline speed). However due to ammonia flow limitations, high substitution ratios at higher speeds are only possible at lower loads.
- Achieving high substitution ratios relied on the air-fuel mixture to be close to stoichiometric ($\lambda = 1$) which favours ammonia com-

bustion over the standard lean operation used for diesel to improve emissions and efficiency.

- The quantity of diesel pilot injection had a strong impact on the combustion of ammonia. Greater amounts of pilot fuel significantly accelerate the total combustion process for an equivalent amount of ammonia.
- High ammonia slip was observed across all operating conditions at some points exceeding 10,000 ppm at 90% substitution ratio. These values were too high to be used in conjunction with current catalytic reduction technologies and would require specialist after-treatment to oxidise ammonia if not improved in combustion.

8.3 Overall implications and future work

This research contributes to the ongoing work around alternative fuels and enabling their application within real world combustion systems with a focus on heavy-duty engines. The novel constant volume combustion chamber serves as a bridge between the foundational work of laminar burning velocity measurements and the limitations within an engine to provide a tool to optimise future advanced combustion systems. The diesel engine retrofit work provides real world insights into the challenges and possibilities of developing these systems. Bringing together both projects, this research has provided two platforms for the study of alternative fuels, opening avenues for future work in optimising combustion, addressing emissions challenges and advancing the integration of alternative fuels into the real world.

Key challenges still exist for both ammonia and hydrogen related to their

carbon intensive production, challenges with handling, and limited investment into developing solutions. Further work in providing demonstrators will help to draw out opportunities and overcome difficulties in applying the fuels.

8.3.1 Novel optical combustion chamber

A key consideration taken when designing and developing the optical combustion chamber was its flexibility and modular-design to future-proof the equipment. The items listed provide a range of suggested avenues that can be investigated using the optical combustion chamber.

- To minimise uncertainty in the calculation of the equivalence ratio, a lambda sensor can be added into the chamber exhaust stream to provide a real measurement.
- The optical methodology is selected depending on the aims of the experimental work. When it comes to flame imaging, utilising a schlieren system will provide a more accurate understanding of the position of the flame front as well as further detail into the flame thickness and cellularity. Using an intensifier will provide detail into the reaction dynamics, providing insight into the concentration of specific chemical species such as OH radicals.
- To improve validation of computational modelling and to investigate the impact of the wall further, a study can be completed using an extended spark ignition device to emulate a central ignition in the current configuration.
- Utilising the modular design, the spark ignition head can be changed for the turbulent jet ignition head and an optimisation of the system

with ammonia and hydrogen mixtures can be carried out.

- In order to understand the thermal gradients that form as a result of the heating configuration a thermal camera could be utilised during a temperature test. This would provide information to inform heating duration to enable more accurate temperature testing.

The next stage of the research is to begin to investigate the use of passive turbulent jet ignition with ammonia and hydrogen. Previous engine studies have shown challenges with ignition of ammonia mixtures with this configuration. It is suspected that the challenges are as a result of both chemical and physical limitation of ammonia. The high quench distance of ammonia can result in failed spark initiation within the chamber. Key findings have suggested a reduction in emissions with the technology that can be further investigated with an optimisation study within the combustion chamber. Prior to these investigations, the chamber will be upgraded to use schlieren imaging and a lambda sensor will be fitted to the exhaust stream to improve accuracy of imaging and gas mixture control.

8.3.2 Ammonia-diesel engine retrofit

The iterative development of the dual fuel ammonia-hydrogen retrofit engine has resulted in a operational engine test rig with a high level of control that can be used in future studies. It is expected that this iteration will not be the last, however in its current state there is a wide range of investigations that can be completed to further inform future developments in the field. Initially completing a comprehensive engine map with a focus on maximum substitution ratio of ammonia under different speed-load conditions will provide a baseline for future optimisation work. The follow-

ing list provides an overview of key studies that will progress the engine development further:

- A comparative study of the performance and emissions characteristics obtained under ammonia dual fuel operation against standard diesel operation. With a focus on the production of soot as a result of running diesel close to stoichiometric.
- An investigation into the spacing and ignition timing of the diesel pilot and main injections with an aim to minimise ammonia slip and investigate the completeness of fuel mixing within the cylinder.
- An optimisation of the cylinder-to-cylinder ammonia injection quantities to account for the intake manifold air flow imbalance.
- A study of hydrogen enrichment to further improve ammonia combustion, with a focus on low substitution levels that are achievable with integrated ammonia cracking via exhaust heat.

References

- [1] Ephraim Bonah Agyekum et al. “A Critical Review of Renewable Hydrogen Production Methods: Factors Affecting Their Scale-Up and Its Role in Future Energy Generation”. In: *Membranes* 12.2 (2022). ISSN: 20770375. DOI: [10.3390/membranes12020173](https://doi.org/10.3390/membranes12020173).
- [2] ALICAT Scientific. *OPERATING MANUAL CODA-SERIES CORIOLIS MASS FLOW DEVICES*. Tech. rep. 2023.
- [3] G. E. Andrews and D. Bradley. “Determination of burning velocity by double ignition in a closed vessel”. In: *Combustion and Flame* 20.1 (1973), pp. 77–89. ISSN: 00102180. DOI: [10.1016/S0010-2180\(73\)81259-3](https://doi.org/10.1016/S0010-2180(73)81259-3). URL: [http://dx.doi.org/10.1016/S0010-2180\(73\)81259-3](http://dx.doi.org/10.1016/S0010-2180(73)81259-3).
- [4] Rik S.G. Baert et al. “Design and operation of a high pressure, high temperature cell for HD diesel spray diagnostics: Guidelines and results”. In: *SAE Technical Papers* (2009). ISSN: 26883627. DOI: [10.4271/2009-01-0649](https://doi.org/10.4271/2009-01-0649).
- [5] Saravanan Balusamy, Armelle Cessou, and Bertrand Lecordier. “Direct measurement of local instantaneous laminar burning velocity by a new PIV algorithm”. In: *Experiments in Fluids* 50.4 (2011), pp. 1109–1121. ISSN: 07234864. DOI: [10.1007/s00348-010-1027-5](https://doi.org/10.1007/s00348-010-1027-5).

- [6] Joachim Beeckmann et al. “Propagation speed and stability of spherically expanding hydrogen/air flames: Experimental study and asymptotics”. In: *Proceedings of the Combustion Institute* 36.1 (2017), pp. 1531–1538. ISSN: 15407489. DOI: [10.1016/j.proci.2016.06.194](https://doi.org/10.1016/j.proci.2016.06.194).
- [7] Sayan Biswas et al. “On ignition mechanisms of premixed CH₄/air and H₂/air using a hot turbulent jet generated by pre-chamber combustion”. In: *Applied Thermal Engineering* 106 (2016), pp. 925–937. ISSN: 13594311. DOI: [10.1016/j.applthermaleng.2016.06.070](https://doi.org/10.1016/j.applthermaleng.2016.06.070). URL: <http://dx.doi.org/10.1016/j.applthermaleng.2016.06.070>.
- [8] Matthias Bohnet. *Ullmann’s Encyclopedia of Industrial Chemistry*. Wiley, June 2000. DOI: [10.1002/14356007](https://doi.org/10.1002/14356007).
- [9] BOSCH. *Single Fire Coil P100-T - Technical Specification*. Tech. rep., pp. 3–5. URL: https://www.finjector.com/documents/4ec9f695740c8/0221604006_DataSheet_enUS_T6821266699.pdf.
- [10] D. Bradley, M. Lawes, and M. E. Morsy. “Flame speed and particle image velocimetry measurements of laminar burning velocities and Markstein numbers of some hydrocarbons”. In: *Fuel* 243.November 2018 (2019), pp. 423–432. ISSN: 00162361. DOI: [10.1016/j.fuel.2019.01.067](https://doi.org/10.1016/j.fuel.2019.01.067). URL: <https://doi.org/10.1016/j.fuel.2019.01.067>.
- [11] D. Bradley, M. Lawes, and C. G.W. Sheppard. “Combustion and the thermodynamic performance of spark ignition engines”. In: *Proceedings of the Institution of Mechanical Engineers, Part C: Journal of Mechanical Engineering* 214.1 (2000), pp. 257–268. ISSN: 09544062. DOI: [10.1243/0954406001522949](https://doi.org/10.1243/0954406001522949).

- [12] D. Bradley et al. “Laminar burning velocities of lean hydrogen-air mixtures at pressures up to 1.0 MPa”. In: *Combustion and Flame* 149.1-2 (2007), pp. 162–172. ISSN: 00102180. DOI: [10.1016/j.combustflame.2006.12.002](https://doi.org/10.1016/j.combustflame.2006.12.002).
- [13] Derek Bradley, P. H. Gaskell, and X. J. Gu. “Burning velocities, Markstein lengths, and flame quenching for spherical methane-air flames: A computational study”. In: *Combustion and Flame* 104.1-2 (1996), pp. 176–198. ISSN: 00102180. DOI: [10.1016/0010-2180\(95\)00115-8](https://doi.org/10.1016/0010-2180(95)00115-8).
- [14] British Standards Institution. *BS 4518:1982+A2:2014 Specification for metric dimensions of toroidal sealing rings ('O'-rings) and their housings*. Tech. rep. 1982.
- [15] British Standards Institution. *BS EN 10272-2016 Stainless steel bars for pressure purposes*. Tech. rep. 2016.
- [16] British Standards Institution. *BS EN 13445-1-2021 Unfired pressure vessels - General*. Tech. rep. 2021.
- [17] British Standards Institution. *BS EN 13445-3-2021 Unfired pressure vessels - Design*. Tech. rep. 2021.
- [18] British Standards Institution. *PD 5500:2021+A2:2022, Specification for unfired pressure vessels*. 2022. URL: <https://knowledge.bsigroup.com/products/pd-5500-2021-a2-2022-specification-for-unfired-pressure-vessels-1/standard>.
- [19] Michael P. Burke et al. “Effect of cylindrical confinement on the determination of laminar flame speeds using outwardly propagating flames”. In: *Combustion and Flame* 156.4 (2009), pp. 771–779. ISSN: 00102180. DOI: [10.1016/j.combustflame.2009.01.013](https://doi.org/10.1016/j.combustflame.2009.01.013). URL: <http://dx.doi.org/10.1016/j.combustflame.2009.01.013>.

- [20] Michael Campbell et al. “Study on the readiness and availability of low- and zero-carbon technology and marine fuels”. In: *DNV & Ricardo* 304.72 (2023).
- [21] Xu Chen et al. “Flame front evolution and laminar flame parameter evaluation of buoyancy-affected ammonia/air flames”. In: *International Journal of Hydrogen Energy* 46.77 (2021), pp. 38504–38518. ISSN: 03603199. DOI: [10.1016/j.ijhydene.2021.09.099](https://doi.org/10.1016/j.ijhydene.2021.09.099). URL: <https://doi.org/10.1016/j.ijhydene.2021.09.099>.
- [22] Zheng Chen. “On the accuracy of laminar flame speeds measured from outwardly propagating spherical flames: Methane/air at normal temperature and pressure”. In: *Combustion and Flame* 162.6 (2015), pp. 2442–2453. ISSN: 15562921. DOI: [10.1016/j.combustflame.2015.02.012](https://doi.org/10.1016/j.combustflame.2015.02.012). URL: <http://dx.doi.org/10.1016/j.combustflame.2015.02.012>.
- [23] Zheng Chen. “On the extraction of laminar flame speed and Markstein length from outwardly propagating spherical flames”. In: *Combustion and Flame* 158.2 (2011), pp. 291–300. ISSN: 00102180. DOI: [10.1016/j.combustflame.2010.09.001](https://doi.org/10.1016/j.combustflame.2010.09.001). URL: <http://dx.doi.org/10.1016/j.combustflame.2010.09.001>.
- [24] L Cohen. “Burning Velocities of Ammonia in Air and in Oxygen”. In: *Fuel* 34 (1955).
- [25] Corning. “Corning HPFS® 7979, 7980, 8655 Fused Silica Optical Materials Product Information Specialty Materials Division”. In: *Manual* (2014), pp. 1–8.
- [26] CRYSTRAN. “SAFETY DATA SHEET - QUARTZ (SiO₂) OPTICAL CRYSTAL”. In: *Material Safety Data Sheet* (2016). URL: http://energy.sandia.gov/wp/wp-content/gallery/uploads/SAND2012_7321.pdf.

- [27] Pavlos Dimitriou and Rahat Javaid. “A review of ammonia as a compression ignition engine fuel”. In: *International Journal of Hydrogen Energy* 45.11 (2020), pp. 7098–7118. ISSN: 03603199. DOI: [10.1016/j.ijhydene.2019.12.209](https://doi.org/10.1016/j.ijhydene.2019.12.209). URL: <https://doi.org/10.1016/j.ijhydene.2019.12.209>.
- [28] Petar Djinović and Ferdi Schüth. “Energy Carriers Made from Hydrogen”. In: *Electrochemical Energy Storage for Renewable Sources and Grid Balancing* (2015), pp. 183–199. DOI: [10.1016/B978-0-444-62616-5.00012-7](https://doi.org/10.1016/B978-0-444-62616-5.00012-7).
- [29] DNV. *BIOFUELS IN SHIPPING*. Tech. rep. 2023.
- [30] Suman Dutta. “A review on production, storage of hydrogen and its utilization as an energy resource”. In: *Journal of Industrial and Engineering Chemistry* 20.4 (2014), pp. 1148–1156. ISSN: 22345957. DOI: [10.1016/j.jiec.2013.07.037](https://doi.org/10.1016/j.jiec.2013.07.037). URL: <http://dx.doi.org/10.1016/j.jiec.2013.07.037>.
- [31] Catherine Duynslaegher. “Experimental and numerical study of ammonia combustion”. In: (2011). URL: <https://uclouvain.academia.edu/CatherineDuynslaegher>.
- [32] Jonas Egerer et al. “The economics of global green ammonia trade – “Shipping Australian wind and sunshine to Germany””. In: *Applied Energy* 334.December 2022 (2023), p. 120662. ISSN: 03062619. DOI: [10.1016/j.apenergy.2023.120662](https://doi.org/10.1016/j.apenergy.2023.120662). URL: <https://doi.org/10.1016/j.apenergy.2023.120662>.
- [33] F. N. Egolfopoulos et al. “Advances and challenges in laminar flame experiments and implications for combustion chemistry”. In: *Progress in Energy and Combustion Science* 43 (2014), pp. 36–67. ISSN: 03601285. DOI: [10.1016/j.pecs.2014.04.004](https://doi.org/10.1016/j.pecs.2014.04.004).

- [34] Oren Elishav et al. “Progress and Prospective of Nitrogen-Based Alternative Fuels”. In: *Chemical Reviews* (2020). ISSN: 15206890. DOI: [10.1021/acs.chemrev.9b00538](https://doi.org/10.1021/acs.chemrev.9b00538).
- [35] Public Health England. *Ammonia Incident Management*. Tech. rep. 2019. DOI: [10.1016/B978-1-4557-2367-6.00027-5](https://doi.org/10.1016/B978-1-4557-2367-6.00027-5).
- [36] EU. “European Commission-Press release European Green Deal: new law agreed to cut aviation emissions by promoting sustainable aviation fuels”. In: 2050.April (2023).
- [37] Daniel Floryan, Jerrod Hofferth, and William Saric. “Design , Assembly , and Calibration of a Focusing Schlieren System”. In: (2012), pp. 1–11.
- [38] Raymond Friedman and Edward Burke. “Measurement of temperature distribution in a low-pressure flat flame”. In: *The Journal of Chemical Physics* 22.5 (1954), pp. 824–830. ISSN: 00219606. DOI: [10.1063/1.1740197](https://doi.org/10.1063/1.1740197).
- [39] Stefano Frigo and Roberto Gentili. “Analysis of the behaviour of a 4-stroke Si engine fuelled with ammonia and hydrogen”. In: *International Journal of Hydrogen Energy* 38.3 (2013), pp. 1607–1615. ISSN: 03603199. DOI: [10.1016/j.ijhydene.2012.10.114](https://doi.org/10.1016/j.ijhydene.2012.10.114). URL: <http://dx.doi.org/10.1016/j.ijhydene.2012.10.114>.
- [40] Hajime Fujimoto et al. “Effects of Ambient Temperature and Oxygen Concentration on Soot Behavior in Diesel Flame”. In: *SAE Technical Papers 2005-Septe* (2005). ISSN: 01487191. DOI: [10.4271/2005-24-007](https://doi.org/10.4271/2005-24-007).
- [41] Bénédicte Galmiche, Fabien Halter, and Fabrice Foucher. “Effects of high pressure, high temperature and dilution on laminar burning velocities and Markstein lengths of iso-octane/air mixtures”. In: *Com-*

- Combustion and Flame* 159.11 (2012), pp. 3286–3299. ISSN: 00102180. DOI: [10.1016/j.combustflame.2012.06.008](https://doi.org/10.1016/j.combustflame.2012.06.008).
- [42] GeoPura. *Giants of industry, manufacturing and finance back UK green hydrogen pioneer GeoPura with £36m investment*. 2023. URL: <https://www.geopura.com/press-releases/giants-of-industry-manufacturing-and-finance-back-uk-green-hydrogen-pioneer-geopura-with-36m-investment/>.
- [43] S Giddey et al. “Ammonia as a Renewable Energy Transportation Media”. In: *ACS Sustainable Chem. Eng* 5 (2017), pp. 10231–10239. DOI: [10.1021/acssuschemeng.7b02219](https://doi.org/10.1021/acssuschemeng.7b02219). URL: <https://pubs.acs.org/sharingguidelines>.
- [44] L. Gillespie et al. “Aspects of laminar and turbulent burning velocity relevant to SI engines”. In: *SAE Technical Papers* 724 (2000). ISSN: 26883627. DOI: [10.4271/2000-01-0192](https://doi.org/10.4271/2000-01-0192).
- [45] Irvine Glassman. *Combustion*. 3rd. Elsevier, 2014. ISBN: 9780124079137. DOI: [10.1016/C2011-0-05402-9](https://doi.org/10.1016/C2011-0-05402-9). URL: <https://linkinghub.elsevier.com/retrieve/pii/C20110054029>.
- [46] Mayuri Goswami et al. “The effect of elevated pressures on the laminar burning velocity of methane+air mixtures”. In: *Combustion and Flame* 160.9 (2013), pp. 1627–1635. ISSN: 00102180. DOI: [10.1016/j.combustflame.2013.03.032](https://doi.org/10.1016/j.combustflame.2013.03.032). URL: <http://dx.doi.org/10.1016/j.combustflame.2013.03.032>.
- [47] Gabriel J. Gotama et al. “Measurement of the laminar burning velocity and kinetics study of the importance of the hydrogen recovery mechanism of ammonia/hydrogen/air premixed flames”. In: *Combustion and Flame* 236.x (2022), p. 111753. ISSN: 15562921. DOI: [10.1016/j.combustflame.2021.111753](https://doi.org/10.1016/j.combustflame.2021.111753). URL: <https://doi.org/10.1016/j.combustflame.2021.111753>.

- [48] Shawn M. Grannell et al. “The fuel mix limits and efficiency of a stoichiometric, ammonia, and gasoline dual fueled spark ignition engine”. In: *Journal of Engineering for Gas Turbines and Power* 130.4 (July 2008). ISSN: 07424795. DOI: [10.1115/1.2898837](https://doi.org/10.1115/1.2898837).
- [49] James T. Gray et al. “Ammonia fuel - Engine compatibility and combustion”. In: *SAE Technical Papers* 75.May (1966), pp. 785–807. ISSN: 26883627. DOI: [10.4271/660156](https://doi.org/10.4271/660156).
- [50] Christopher W. Gross and Song Charng Kong. “Performance characteristics of a compression-ignition engine using direct-injection ammonia-DME mixtures”. In: *Fuel* 103 (2013), pp. 1069–1079. ISSN: 00162361. DOI: [10.1016/j.fuel.2012.08.026](https://doi.org/10.1016/j.fuel.2012.08.026). URL: <http://dx.doi.org/10.1016/j.fuel.2012.08.026>.
- [51] X. J. Gu et al. “Laminar burning velocity and Markstein lengths of methane-air mixtures”. In: *Combustion and Flame* 121.1-2 (2000), pp. 41–58. ISSN: 00102180. DOI: [10.1016/S0010-2180\(99\)00142-X](https://doi.org/10.1016/S0010-2180(99)00142-X).
- [52] Fabien Halter et al. “Development of an optically accessible apparatus to characterize the evolution of spherically expanding flames under constant volume conditions”. In: *Combustion and Flame* 212 (2020), pp. 165–176. ISSN: 15562921. DOI: [10.1016/j.combustflame.2019.10.027](https://doi.org/10.1016/j.combustflame.2019.10.027).
- [53] Xinlu Han et al. “Experimental and kinetic modeling study of laminar burning velocities of NH₃/syngas/air premixed flames”. In: *Combustion and Flame* 213 (2020). ISSN: 15562921. DOI: [10.1016/j.combustflame.2019.11.032](https://doi.org/10.1016/j.combustflame.2019.11.032).
- [54] Xinlu Han et al. “The temperature dependence of the laminar burning velocity and superadiabatic flame temperature phenomenon for NH₃/air flames”. In: *Combustion and Flame* 217 (2020), pp. 314–

320. ISSN: 15562921. DOI: [10.1016/j.combustflame.2020.04.013](https://doi.org/10.1016/j.combustflame.2020.04.013).
URL: <https://doi.org/10.1016/j.combustflame.2020.04.013>.
- [55] M. I. Hassan, K. T. Aung, and G. M. Faeth. “Measured and predicted properties of laminar premixed methane/air flames at various pressures”. In: *Combustion and Flame* 115.4 (1998), pp. 539–550. ISSN: 00102180. DOI: [10.1016/S0010-2180\(98\)00025-X](https://doi.org/10.1016/S0010-2180(98)00025-X).
- [56] Akihiro Hayakawa et al. “Experimental investigation of stabilization and emission characteristics of ammonia/air premixed flames in a swirl combustor”. In: *International Journal of Hydrogen Energy* 42.19 (2017), pp. 14010–14018. ISSN: 03603199. DOI: [10.1016/j.ijhydene.2017.01.046](https://doi.org/10.1016/j.ijhydene.2017.01.046).
- [57] Akihiro Hayakawa et al. “Laminar burning velocity and Markstein length of ammonia/air premixed flames at various pressures”. In: *Fuel* 159 (2015), pp. 98–106. ISSN: 00162361. DOI: [10.1016/j.fuel.2015.06.070](https://doi.org/10.1016/j.fuel.2015.06.070). URL: <http://dx.doi.org/10.1016/j.fuel.2015.06.070>.
- [58] Akihiro Hayakawa et al. “NO formation/reduction mechanisms of ammonia/air premixed flames at various equivalence ratios and pressures”. In: *Mechanical Engineering Journal* 2.1 (2015), pp. 14–00402. DOI: [10.1299/mej.14-00402](https://doi.org/10.1299/mej.14-00402).
- [59] Health and Safety Executive. “List of Workplace Exposure Limits (WELS) (Fourth Edition 2020)”. In: *Hse 2002* (2020), pp. 1–61. ISSN: 978 0 7176 6733 8. URL: <https://www.hse.gov.uk/pubns/books/eh40.htm>.
- [60] John B. Heywood. *Internal combustion engine fundamentals*. Vol. 26. 02. 1988, pp. 26–0943. DOI: [10.5860/choice.26-0943](https://doi.org/10.5860/choice.26-0943).

- [61] Nathan Hinton, Richard Stone, and Roger Cracknell. “Laminar burning velocity measurements in constant volume vessels – Reconciliation of flame front imaging and pressure rise methods”. In: *Fuel* 211 (2018), pp. 446–457. ISSN: 00162361. DOI: [10.1016/j.fuel.2017.09.031](https://doi.org/10.1016/j.fuel.2017.09.031).
- [62] Nathan Ian David Hinton. “Measuring laminar burning velocities using constant volume combustion vessel technique”. In: C (2014).
- [63] Günter F. Hohenberg. “Advanced approaches for heat transfer calculations”. In: *SAE Technical Papers* (1979), pp. 2788–2806. ISSN: 26883627. DOI: [10.4271/790825](https://doi.org/10.4271/790825).
- [64] Bertram Hopkinson. *Explosions of coal-gas and air*. Vol. lxxvii. 1906.
- [65] Robert W. Howarth and Mark Z. Jacobson. “How green is blue hydrogen?” In: *Energy Science and Engineering* 9.10 (2021), pp. 1676–1687. ISSN: 20500505. DOI: [10.1002/ese3.956](https://doi.org/10.1002/ese3.956).
- [66] Jialong Huo et al. “Uncertainty reduction in laminar flame speed extrapolation for expanding spherical flames”. In: *Combustion and Flame* 189 (2018), pp. 155–162. ISSN: 15562921. DOI: [10.1016/j.combustflame.2017.10.032](https://doi.org/10.1016/j.combustflame.2017.10.032). URL: <https://doi.org/10.1016/j.combustflame.2017.10.032>.
- [67] Hydrogen Council. “Hydrogen scaling up : A sustainable pathway for the global energy transition. www.hydrogencouncil.com”. In: *Hydrogen scaling up: A sustainable pathway for the global energy transition* November (2017), p. 80. URL: www.hydrogencouncil.com.
- [68] Akinori Ichikawa et al. “Laminar burning velocity and Markstein length of ammonia/hydrogen/air premixed flames at elevated pressures”. In: *International Journal of Hydrogen Energy* 40.30 (2015),

- pp. 9570–9578. ISSN: 03603199. DOI: [10.1016/j.ijhydene.2015.04.024](https://doi.org/10.1016/j.ijhydene.2015.04.024). URL: <http://dx.doi.org/10.1016/j.ijhydene.2015.04.024>.
- [69] IEA. “Ammonia Technology Roadmap”. In: *Ammonia Technology Roadmap* (2021). DOI: [10.1787/f6daa4a0-en](https://doi.org/10.1787/f6daa4a0-en).
- [70] IEA. “The Future of Hydrogen for G20. Seizing today’s opportunities”. In: *Report prepared by the IEA for the G20, Japan* June (2019).
- [71] IEA. *The Potential and Challenges of ‘Drop-in’ Biofuels - The key role that co-processing will play in production*. Vol. 1. January. 2019, p. 156. ISBN: 9781910154618.
- [72] Balazs Ihracska. “Combustion of Alternative Fuels : Opto-Mechanical Design and Optical Investigation”. PhD thesis. 2016, p. 245.
- [73] IMO. “Resolution MEPC, 203(62) Amendments to the Annex of the protocol of 1997 to Amend the MARPOL”. In: *IMO publication* 203.July (2011), pp. 1–17. URL: <https://wwwcdn.imo.org/localresources/en/OurWork/Environment/Documents/Technical%20and%20operational%20Measures/Resolution%20MEPC.203%2862%29.pdf>.
- [74] IMO. “RESOLUTION MEPC.377(80) Adopted - 2023 IMO STRATEGY ON REDUCTION OF GHG EMISSIONS FROM SHIPS”. In: (2023). ISSN: 00027863.
- [75] IMO. “The Third IMO GHG Study 2014”. In: (2014). URL: <http://www.imo.org/en/OurWork/Environment/PollutionPrevention/AirPollution/Pages/Greenhouse-Gas-Studies-2014.aspx>.
- [76] British Standards Institution. *BS 3643-1-2007 ISO metric screw threads - Principles and basic data*. Tech. rep. 2007.

- [77] IPCC. “Climate Change 2023: Synthesis Report”. In: (2023). URL: <https://www.unep.org/resources/report/climate-change-2023-synthesis-report>.
- [78] IRENA. *A pathway to decarbonise the shipping sector by 2050*. Vol. 364. May. Abu Dhabi, 2021, p. 35. ISBN: 978-92-9260-330-4.
- [79] IRENA and AEA. *Innovation Outlook: Renewable Ammonia*. 2022, p. 144. ISBN: 978-92-9260-423-3.
- [80] Dehao Ju et al. “Comparison of open chamber and pre-chamber ignition of methane/air mixtures in a large bore constant volume chamber: Effect of excess air ratio and pre-mixed pressure”. In: *Applied Energy* 260. December 2019 (2020), p. 114319. ISSN: 03062619. DOI: [10.1016/j.apenergy.2019.114319](https://doi.org/10.1016/j.apenergy.2019.114319). URL: <https://doi.org/10.1016/j.apenergy.2019.114319>.
- [81] Ryuhei Kanoshima et al. “Effects of initial mixture temperature and pressure on laminar burning velocity and Markstein length of ammonia/air premixed laminar flames”. In: *Fuel* 310. PB (2022), p. 122149. ISSN: 00162361. DOI: [10.1016/j.fuel.2021.122149](https://doi.org/10.1016/j.fuel.2021.122149). URL: <https://doi.org/10.1016/j.fuel.2021.122149>.
- [82] Ltd Kawasaki Heavy Industries. *World’s First Liquefied Hydrogen Carrier SUIISO FRONTIER Launches Building an International Hydrogen Energy Supply Chain Aimed at Carbon-free Society*. 2019. URL: https://global.kawasaki.com/en/corp/newsroom/news/detail/?f=20191211_3487.
- [83] A. P. Kelley and C. K. Law. “Nonlinear effects in the extraction of laminar flame speeds from expanding spherical flames”. In: *Combustion and Flame* 156.9 (2009), pp. 1844–1851. ISSN: 00102180. DOI: [10.1016/j.combustflame.2009.04.004](https://doi.org/10.1016/j.combustflame.2009.04.004). URL: <http://dx.doi.org/10.1016/j.combustflame.2009.04.004>.

- [84] Wookyung Kim et al. “Experimental study on self-acceleration in expanding spherical hydrogen-air flames”. In: *International Journal of Hydrogen Energy* 43.27 (2018), pp. 12556–12564. ISSN: 03603199. DOI: [10.1016/j.ijhydene.2018.04.153](https://doi.org/10.1016/j.ijhydene.2018.04.153).
- [85] Gregory Kobrin. “Stainless Steels in Ammonia Production”. In: (1978), p. 22.
- [86] Emeric Kroch. “Ammonia - A fuel for motor buses”. In: *Journal of the Institute of Petroleum* (1945), pp. 213–223.
- [87] Panagiotis Kyrtatos et al. “Transferability of Insights from Fundamental Investigations into Practical Applications of Prechamber Combustion Systems”. In: *Ignition Systems for Gasoline Engines - 4th International Conference, December 6-7, 2018, Berlin, Germany* (2018), pp. 442–459.
- [88] David R Lancaster et al. “Effects of Turbulence on Spark-Ignition Engine Combustion”. In: Feb. 1976, pp. 689–710. DOI: [10.4271/760160](https://doi.org/10.4271/760160). URL: <https://www.sae.org/content/760160/>.
- [89] Marco Lubrano Lavadera, Xinlu Han, and Alexander A. Konnov. “Comparative effect of ammonia addition on the laminar burning velocities of methane, n-heptane, and iso-octane”. In: *Energy and Fuels* 35.9 (2021), pp. 7156–7168. ISSN: 15205029. DOI: [10.1021/acs.energyfuels.0c03424](https://doi.org/10.1021/acs.energyfuels.0c03424).
- [90] Chung K. Law. “Fuel options for next-generation chemical propulsion”. In: *AIAA Journal* 50.1 (2012), pp. 19–36. ISSN: 00011452. DOI: [10.2514/1.J051328](https://doi.org/10.2514/1.J051328).
- [91] Donggeun Lee and Han Ho Song. “Development of combustion strategy for the internal combustion engine fueled by ammonia and its operating characteristics”. In: *Journal of Mechanical Science and*

- Technology* 32.4 (2018), pp. 1905–1925. ISSN: 1738494X. DOI: [10.1007/s12206-018-0347-x](https://doi.org/10.1007/s12206-018-0347-x).
- [92] J. H. Lee, S. I. Lee, and O. C. Kwon. “Effects of ammonia substitution on hydrogen/air flame propagation and emissions”. In: *International Journal of Hydrogen Energy* 35.20 (2010), pp. 11332–11341. ISSN: 03603199. DOI: [10.1016/j.ijhydene.2010.07.104](https://doi.org/10.1016/j.ijhydene.2010.07.104). URL: <http://dx.doi.org/10.1016/j.ijhydene.2010.07.104>.
- [93] Bernard Lewis and Guenther von Elbe. *Combustion, Flames and Explosions of Gases*. 1987. DOI: <https://doi.org/10.1016/C2009-0-21751-X>.
- [94] Charles Lhuillier et al. “Combustion Characteristics of Ammonia in a Modern Spark-Ignition Engine”. In: *SAE Technical Papers* October (2019). ISSN: 01487191. DOI: [10.4271/2019-24-0237](https://doi.org/10.4271/2019-24-0237).
- [95] Charles Lhuillier et al. “Combustion Characteristics of Ammonia in a Modern Spark-Ignition Engine To cite this version : HAL Id : hal-02322493 Combustion Characteristics of Ammonia in a Modern Spark-Ignition Engine”. In: (2020).
- [96] Guoxiu Li et al. “Experimental study on the ignition and combustion mechanisms of a methane-air mixture in a divided constant-volume combustion chamber”. In: *Energy and Fuels*. Vol. 26. 8. 2012, pp. 4696–4702. DOI: [10.1021/ef300094u](https://doi.org/10.1021/ef300094u). URL: <https://pubs.acs.org/sharingguidelines>.
- [97] Jun Li et al. “Numerical study on laminar burning velocity and ignition delay time of ammonia flame with hydrogen addition”. In: *Energy* 126.x (2017), pp. 796–809. ISSN: 03605442. DOI: [10.1016/j.energy.2017.03.085](https://doi.org/10.1016/j.energy.2017.03.085). URL: <http://dx.doi.org/10.1016/j.energy.2017.03.085>.

- [98] Qingming Liu et al. “The characteristics of flame propagation in ammonia/oxygen mixtures”. In: *Journal of Hazardous Materials* 363 (2019), pp. 187–196. ISSN: 18733336. DOI: [10.1016/j.jhazmat.2018.09.073](https://doi.org/10.1016/j.jhazmat.2018.09.073).
- [99] Rui Liu, David S.K. Ting, and M. David Checkel. “Ammonia as a fuel for SI engine”. In: *SAE Technical Papers* 724 (2003). ISSN: 26883627. DOI: [10.4271/2003-01-3095](https://doi.org/10.4271/2003-01-3095).
- [100] M Barnwell Services. *Material Compatibility Chart1*. M Barnwell Services. *Material Compatibility Chart*. Tech. rep.
- [101] Douglas R. MacFarlane et al. “A Roadmap to the Ammonia Economy”. In: *Joule* 4.6 (2020), pp. 1186–1205. ISSN: 25424351. DOI: [10.1016/j.joule.2020.04.004](https://doi.org/10.1016/j.joule.2020.04.004). URL: <https://doi.org/10.1016/j.joule.2020.04.004>.
- [102] James J Mackenzie, District Columbia, and William H Avery. “Ammonia fuel: the key to hydrogen-based transportation”. In: (1996).
- [103] M Mägi. “Effect of Gasoline Fuel Additives on Combustion and Engine Performance”. In: (2015). URL: http://discovery.ucl.ac.uk/1462024/1/Thesis_Mart_Magi.pdf.
- [104] MAN Energy Solutions. “Methanol in shipping”. In: (2022), pp. 1–12. URL: <https://www.man-es.com/campaigns/download-Q3-2023/Download/methanol-in-shipping/d8358bd6-c66e-4dce-8656-4237259c5338/Methanol-Paper-SF>.
- [105] Carlos Marquez. “MARINE METHANOL: Future-Proof Shipping Fuel”. In: *Methanol Institute* (2023). URL: www.methanol.org.
- [106] Maria Chiara Massaro et al. “Potential and technical challenges of on-board hydrogen storage technologies coupled with fuel cell systems for aircraft electrification”. In: *Journal of Power Sources*

- 555.November 2022 (2023), p. 232397. ISSN: 03787753. DOI: [10 . 1016/j . jpowsour . 2022 . 232397](https://doi.org/10.1016/j.jpowsour.2022.232397). URL: [https://doi.org/10 . 1016/j . jpowsour . 2022 . 232397](https://doi.org/10.1016/j.jpowsour.2022.232397).
- [107] Michael James McGhee. “Factors influencing cycle-by-cycle combustion characteristics of a diesel engine under cold idling conditions”. PhD thesis. University of Nottingham, 2013.
- [108] Bowen Mei et al. “Experimental and kinetic modeling investigation on the laminar flame propagation of ammonia under oxygen enrichment and elevated pressure conditions”. In: *Combustion and Flame* 210 (2019), pp. 236–246. ISSN: 15562921. DOI: [10 . 1016/j . combustflame . 2019 . 08 . 033](https://doi.org/10.1016/j.combustflame.2019.08.033).
- [109] M. Metghalchi and J. C. Keck. “Laminar burning velocity of propane-air mixtures at high temperature and pressure”. In: *Combustion and Flame* 38.C (1980), pp. 143–154. ISSN: 00102180. DOI: [10 . 1016/ 0010-2180\(80\)90046-2](https://doi.org/10.1016/0010-2180(80)90046-2).
- [110] B. E. Milton and J. C. Keck. “Laminar burning velocities in stoichiometric hydrogen and hydrogenhydrocarbon gas mixtures”. In: *Combustion and Flame* 58.1 (1984), pp. 13–22. ISSN: 00102180. DOI: [10 . 1016/0010-2180\(84\)90074-9](https://doi.org/10.1016/0010-2180(84)90074-9).
- [111] C. S. Mørch et al. “Ammonia/hydrogen mixtures in an SI-engine: Engine performance and analysis of a proposed fuel system”. In: *Fuel* 90.2 (2011), pp. 854–864. ISSN: 00162361. DOI: [10 . 1016/j . fuel . 2010 . 09 . 042](https://doi.org/10.1016/j.fuel.2010.09.042).
- [112] Aliasghar Mozafari-Varnusfadrani. “Predictions and Measurements of Spark-Ignition Engine Characteristics using ammonia and other fuels”. PhD thesis. Queen Mary College, University of London, 1988.

- [113] NIST. *NIST Chemistry WebBook*. Tech. rep. 12. 2006, pp. 0293–43. DOI: <https://doi.org/10.18434/T4D303>.
- [114] Venkata Nori and Jerry Seitzman. “Evaluation of chemiluminescence as a combustion diagnostic under varying operating conditions”. In: *46th AIAA Aerospace Sciences Meeting and Exhibit* January (2008), pp. 1–14. DOI: [10.2514/6.2008-953](https://doi.org/10.2514/6.2008-953).
- [115] Sechul Oh et al. “Natural gas–ammonia dual-fuel combustion in spark-ignited engine with various air–fuel ratios and split ratios of ammonia under part load condition”. In: *Fuel* 290. December 2020 (2021), p. 120095. ISSN: 00162361. DOI: [10.1016/j.fuel.2020.120095](https://doi.org/10.1016/j.fuel.2020.120095). URL: <https://doi.org/10.1016/j.fuel.2020.120095>.
- [116] Ekenechukwu C. Okafor et al. “Experimental and numerical study of the laminar burning velocity of CH₄–NH₃–air premixed flames”. In: *Combustion and Flame* 187 (2018), pp. 185–198. ISSN: 15562921. DOI: [10.1016/j.combustflame.2017.09.002](https://doi.org/10.1016/j.combustflame.2017.09.002).
- [117] Ekenechukwu Chijioke Okafor et al. “Measurement and modelling of the laminar burning velocity of methane–ammonia–air flames at high pressures using a reduced reaction mechanism”. In: *Combustion and Flame* 204 (2019), pp. 162–175. ISSN: 15562921. DOI: [10.1016/j.combustflame.2019.03.008](https://doi.org/10.1016/j.combustflame.2019.03.008).
- [118] Farzan Parsinejad, James C. Keck, and Hameed Metghalchi. “On the location of flame edge in Shadowgraph pictures of spherical flames: A theoretical and experimental study”. In: *Experiments in Fluids* 43.6 (2007), pp. 887–894. ISSN: 07234864. DOI: [10.1007/s00348-007-0355-6](https://doi.org/10.1007/s00348-007-0355-6).
- [119] Thomas J. Pearsall and Charles G. Garabedian. “Combustion of anhydrous ammonia in diesel engines”. In: *SAE Technical Papers*

- 76.May (1967), pp. 3213–3221. ISSN: 26883627. DOI: [10 . 4271 / 670947](https://doi.org/10.4271/670947).
- [120] U. J. Pfahl et al. “Flammability limits, ignition energy, and flame speeds in H₂-CH₄-NH₃- N₂O-O₂-N₂ mixtures”. In: *Combustion and Flame* 123.1-2 (2000), pp. 140–158. ISSN: 00102180. DOI: [10.1016/S0010-2180\(00\)00152-8](https://doi.org/10.1016/S0010-2180(00)00152-8).
- [121] Peter H. Pfromm. “Towards sustainable agriculture: Fossil-free ammonia”. In: *Journal of Renewable and Sustainable Energy* 9.3 (2017). ISSN: 19417012. DOI: [10.1063/1.4985090](https://doi.org/10.1063/1.4985090). URL: <http://dx.doi.org/10.1063/1.4985090>.
- [122] PHOTRON. *Product Datasheet: FASTCAM NOVA S9*. Tech. rep.
- [123] Loreto Pizzuti et al. “Laminar Burning Velocity of Methane/Air Mixtures and Flame Propagation Speed Close to the Chamber Wall”. In: *Energy Procedia* 120 (2017), pp. 126–133. ISSN: 18766102. DOI: [10.1016/j.egypro.2017.07.145](https://doi.org/10.1016/j.egypro.2017.07.145). URL: <http://dx.doi.org/10.1016/j.egypro.2017.07.145>.
- [124] Maxime Pochet et al. “Ammonia-Hydrogen Blends in Homogeneous-Charge Compression-Ignition Engine”. In: (2020). DOI: [10.4271/2017-24-0087](https://doi.org/10.4271/2017-24-0087). Copyright.
- [125] C. J. Rallis and A. M. Garforth. “The determination of laminar burning velocity”. In: *Progress in Energy and Combustion Science* 6.4 (1980), pp. 303–329. ISSN: 03601285. DOI: [10 . 1016 / 0360 - 1285\(80\)90008-8](https://doi.org/10.1016/0360-1285(80)90008-8).
- [126] Aaron J. Reiter and Song Charng Kong. “Combustion and emissions characteristics of compression-ignition engine using dual ammonia-diesel fuel”. In: *Fuel* 90.1 (Jan. 2011), pp. 87–97. ISSN: 00162361. DOI: [10.1016/j.fuel.2010.07.055](https://doi.org/10.1016/j.fuel.2010.07.055).

- [127] Aaron J. Reiter and Song Charng Kong. “Demonstration of compression-ignition engine combustion using ammonia in reducing greenhouse gas emissions”. In: *Energy and Fuels* 22.5 (Sept. 2008), pp. 2963–2971. ISSN: 08870624. DOI: [10.1021/ef800140f](https://doi.org/10.1021/ef800140f). URL: <https://pubs-acsc-org.ezproxy.nottingham.ac.uk/doi/full/10.1021/ef800140f>.
- [128] Miriam Reyes et al. “Experimental characterization of burning velocities of premixed methane-air and hydrogen-air mixtures in a constant volume combustion bomb at moderate pressure and temperature”. In: *Applied Thermal Engineering* 130 (2018), pp. 684–697. ISSN: 13594311. DOI: [10.1016/j.applthermaleng.2017.10.165](https://doi.org/10.1016/j.applthermaleng.2017.10.165). URL: <https://doi.org/10.1016/j.applthermaleng.2017.10.165>.
- [129] Matteo C. Romano et al. “Comment on “How green is blue hydrogen?”” In: *Energy Science and Engineering* 10.7 (2022), pp. 1944–1954. ISSN: 20500505. DOI: [10.1002/ese3.1126](https://doi.org/10.1002/ese3.1126).
- [130] Paul D. Ronney. “Effect of Chemistry and Transport Properties on Near-Limit Flames at Microgravity”. In: *Combustion Science and Technology* 59.1-3 (1988), pp. 123–141. ISSN: 1563521X. DOI: [10.1080/00102208808947092](https://doi.org/10.1080/00102208808947092).
- [131] Paul D. Ronney and Harold Y. Wachman. “Effect of gravity on laminar premixed gas combustion I: Flammability limits and burning velocities”. In: *Combustion and Flame* 62.2 (1985), pp. 107–119. ISSN: 00102180. DOI: [10.1016/0010-2180\(85\)90139-7](https://doi.org/10.1016/0010-2180(85)90139-7).
- [132] G. Rozenchan et al. “Outward propagation, burning velocities, and chemical effects of methane flames up to 60 ATM”. In: *Proceedings of the Combustion Institute* 29.2 (2002), pp. 1461–1470. ISSN: 15407489. DOI: [10.1016/s1540-7489\(02\)80179-1](https://doi.org/10.1016/s1540-7489(02)80179-1).

- [133] Kyunghyun Ryu, George E. Zacharakis-Jutz, and Song Charng Kong. “Effects of gaseous ammonia direct injection on performance characteristics of a spark-ignition engine”. In: *Applied Energy* 116 (2014), pp. 206–215. ISSN: 03062619. DOI: [10.1016/j.apenergy.2013.11.067](https://doi.org/10.1016/j.apenergy.2013.11.067). URL: <http://dx.doi.org/10.1016/j.apenergy.2013.11.067>.
- [134] Khizer Saeed and C. R. Stone. “The modelling of premixed laminar combustion in a closed vessel”. In: *Combustion Theory and Modelling* 8.4 (2004), pp. 721–743. ISSN: 13647830. DOI: [10.1088/1364-7830/8/4/004](https://doi.org/10.1088/1364-7830/8/4/004).
- [135] C. San Marchi and B. P. Somerday. “Technical Reference on Hydrogen Compatibility of Materials Austenitic Stainless Steel: type 316 (code 2103)”. In: 316.code 2103 ().
- [136] R. W. Schefer. “Flame sheet imaging using CH chemiluminescence”. In: *Combustion Science and Technology* 126.1-6 (1997), pp. 255–279. ISSN: 00102202. DOI: [10.1080/00102209708935676](https://doi.org/10.1080/00102209708935676).
- [137] Phillip Schweitzer. *Corrosion Engineering Handbook*. 2007.
- [138] Shell. *Quest CO2 Capture Ratio Performance*. Tech. rep. 2021, p. 7.
- [139] Krishna Prasad Shrestha et al. “An experimental and modeling study of ammonia with enriched oxygen content and ammonia/hydrogen laminar flame speed at elevated pressure and temperature”. In: *Proceedings of the Combustion Institute* 38.2 (2021), pp. 2163–2174. ISSN: 15407489. DOI: [10.1016/j.proci.2020.06.197](https://doi.org/10.1016/j.proci.2020.06.197). URL: <https://doi.org/10.1016/j.proci.2020.06.197>.
- [140] Tao Shu et al. “An experimental study of laminar ammonia/methane/air premixed flames using expanding spherical flames”. In: *Fuel* 290. September 2020 (2021), p. 120003. ISSN: 00162361. DOI: [10.1016/j.fuel](https://doi.org/10.1016/j.fuel).

- 2020.120003. URL: <https://doi.org/10.1016/j.fuel.2020.120003>.
- [141] Harpreet Singh et al. “A critical review of technologies, costs, and projects for production of carbon-neutral liquid e-fuels from hydrogen and captured CO₂”. In: *Energy Advances* 9 (2022), pp. 580–605. ISSN: 27531457. DOI: [10.1039/d2ya00173j](https://doi.org/10.1039/d2ya00173j).
- [142] V. Smil. “Detonator of the population explosion”. In: *Nature* 400.6743 (1999), p. 415. ISSN: 00280836. DOI: [10.1038/22672](https://doi.org/10.1038/22672).
- [143] Collin Smith, Alfred K. Hill, and Laura Torrente-Murciano. “Current and future role of Haber-Bosch ammonia in a carbon-free energy landscape”. In: *Energy and Environmental Science* 13.2 (2020), pp. 331–344. ISSN: 17545706. DOI: [10.1039/c9ee02873k](https://doi.org/10.1039/c9ee02873k).
- [144] Owen Irby Smith. “LEAN LIMIT COMBUSTION IN AN EXPANDING CHAMBER”. In: (1977).
- [145] E. S. Starkman, G. E. James, and H. K. Newhall. “Ammonia as a diesel engine fuel: Theory and application”. In: *SAE Technical Papers* 75.May (1967), pp. 765–784. ISSN: 26883627. DOI: [10.4271/670946](https://doi.org/10.4271/670946).
- [146] Toni Tahtouh, Fabien Halter, and Christine Mounaïm-Rousselle. “Measurement of laminar burning speeds and Markstein lengths using a novel methodology”. In: *Combustion and Flame* 156.9 (2009), pp. 1735–1743. ISSN: 00102180. DOI: [10.1016/j.combustflame.2009.03.013](https://doi.org/10.1016/j.combustflame.2009.03.013). URL: <http://dx.doi.org/10.1016/j.combustflame.2009.03.013>.
- [147] Kenji Takizawa et al. “Burning velocity measurements of nitrogen-containing compounds”. In: *Journal of Hazardous Materials* 155.1-2

- (2008), pp. 144–152. ISSN: 03043894. DOI: [10.1016/j.jhazmat.2007.11.089](https://doi.org/10.1016/j.jhazmat.2007.11.089).
- [148] TC Ltd. *Mineral Insulated Thermocouples - Type 12*. Tech. rep., pp. 0–5.
- [149] The Royal Society. *Ammonia: zero-carbon fertiliser, fuel and energy store. Policy Briefing*. Tech. rep. 2020. URL: <https://royalsociety.org/topics-policy/projects/low-carbon-energy-programme/green-ammonia/>.
- [150] The Royal Society. *Sustainable synthetic carbon based fuels for transport POLICY BRIEFING Sustainable synthetic carbon based fuels for transport: Policy briefing*. 2019. ISBN: 978-1-78252-422-9. URL: <https://royalsociety.org/topics-policy/projects/low-carbon-energy-programme/sustainable-synthetic-carbon-based-fuels-for-transport/>.
- [151] Zhenyu Tian et al. “An experimental and kinetic modeling study of premixed NH₃/CH₄/O₂/Ar flames at low pressure”. In: *Combustion and Flame* 156.7 (2009), pp. 1413–1426. ISSN: 00102180. DOI: [10.1016/j.combustflame.2009.03.005](https://doi.org/10.1016/j.combustflame.2009.03.005). URL: <http://dx.doi.org/10.1016/j.combustflame.2009.03.005>.
- [152] Stephen Turns. *An Introduction To Combustion*. 2000.
- [153] UNCTAD. *Review of Maritime Transport 2022*. Tech. rep. 2022. URL: <https://unctadstat.unctad.org/EN/Classifications.html..>
- [154] UNFCCC. *The Paris Agreement*. 2015. URL: <https://unfccc.int/process-and-meetings/the-paris-agreement/the-paris-agreement>.

- [155] Federico Ustolin, Alessandro Campari, and Rodolfo Taccani. “An Extensive Review of Liquid Hydrogen in Transportation with Focus on the Maritime Sector”. In: *Journal of Marine Science and Engineering* 10.9 (2022). ISSN: 20771312. DOI: [10.3390/jmse10091222](https://doi.org/10.3390/jmse10091222).
- [156] A. Valera-Medina et al. “Review on ammonia as a potential fuel: From synthesis to economics”. In: *Energy and Fuels* 35.9 (2021), pp. 6964–7029. ISSN: 15205029. DOI: [10.1021/acs.energyfuels.0c03685](https://doi.org/10.1021/acs.energyfuels.0c03685).
- [157] Emilien Varea et al. “Measurement of laminar burning velocity and Markstein length relative to fresh gases using a new postprocessing procedure: Application to laminar spherical flames for methane, ethanol and isooctane/air mixtures”. In: *Combustion and Flame* 159.2 (2012), pp. 577–590. ISSN: 00102180. DOI: [10.1016/j.combustflame.2011.09.002](https://doi.org/10.1016/j.combustflame.2011.09.002). URL: <http://dx.doi.org/10.1016/j.combustflame.2011.09.002>.
- [158] Robin John Varghese et al. “Measurement of laminar burning velocities of methane-air mixtures simultaneously at elevated pressures and elevated temperatures”. In: *Fuel* 257.June (2019), p. 116120. ISSN: 00162361. DOI: [10.1016/j.fuel.2019.116120](https://doi.org/10.1016/j.fuel.2019.116120). URL: <https://doi.org/10.1016/j.fuel.2019.116120>.
- [159] Sebastian Verhelst et al. “Methanol as a fuel for internal combustion engines”. In: *Progress in Energy and Combustion Science* 70 (2019), pp. 43–88. ISSN: 03601285. DOI: [10.1016/j.pecs.2018.10.001](https://doi.org/10.1016/j.pecs.2018.10.001).
- [160] Niels de Vries. “REPORT (THESIS) Safe and effective application of ammonia as a marine fuel”. In: (2019). URL: <https://repository.tudelft.nl/>.
- [161] Du Wang et al. “Numerical study of the premixed ammonia-hydrogen combustion under engine-relevant conditions”. In: *International Jour-*

- nal of Hydrogen Energy* 46.2 (2021), pp. 2667–2683. ISSN: 03603199. DOI: [10.1016/j.ijhydene.2020.10.045](https://doi.org/10.1016/j.ijhydene.2020.10.045). URL: <https://doi.org/10.1016/j.ijhydene.2020.10.045>.
- [162] Ning Wang et al. “Laminar burning characteristics of ammonia/hydrogen/air mixtures with laser ignition”. In: *International Journal of Hydrogen Energy* 46.62 (2021), pp. 31879–31893. ISSN: 03603199. DOI: [10.1016/j.ijhydene.2021.07.063](https://doi.org/10.1016/j.ijhydene.2021.07.063). URL: <https://doi.org/10.1016/j.ijhydene.2021.07.063>.
- [163] Yifan Wang and Laurence A. Wright. “A Comparative Review of Alternative Fuels for the Maritime Sector: Economic, Technology, and Policy Challenges for Clean Energy Implementation”. In: *World* 2.4 (2021), pp. 456–481. DOI: [10.3390/world2040029](https://doi.org/10.3390/world2040029).
- [164] Fredrik R. Westlye, Anders Ivarsson, and Jesper Schramm. “Experimental investigation of nitrogen based emissions from an ammonia fueled SI-engine”. In: *Fuel* 111.2 (2013), pp. 239–247. ISSN: 00162361. DOI: [10.1016/j.fuel.2013.03.055](https://doi.org/10.1016/j.fuel.2013.03.055). URL: <http://dx.doi.org/10.1016/j.fuel.2013.03.055>.
- [165] C. K. Wu and C. K. Law. “On the determination of laminar flame speeds from stretched flames”. In: *Symposium (International) on Combustion* 20.1 (1985), pp. 1941–1949. ISSN: 00820784. DOI: [10.1016/S0082-0784\(85\)80693-7](https://doi.org/10.1016/S0082-0784(85)80693-7).
- [166] Fujia Wu et al. “Uncertainty in stretch extrapolation of laminar flame speed from expanding spherical flames”. In: *Proceedings of the Combustion Institute* 35.1 (2015), pp. 663–670. ISSN: 15407489. DOI: [10.1016/j.proci.2014.05.065](https://doi.org/10.1016/j.proci.2014.05.065). URL: <http://dx.doi.org/10.1016/j.proci.2014.05.065>.
- [167] Yu Xie et al. “Intrinsic cellular instabilities of hydrogen laminar outwardly propagating spherical flames”. In: *Fuel* 327. June (2022),

- p. 125149. ISSN: 00162361. DOI: [10.1016/j.fuel.2022.125149](https://doi.org/10.1016/j.fuel.2022.125149). URL: <https://doi.org/10.1016/j.fuel.2022.125149>.
- [168] Arda Yapicioglu and Ibrahim Dincer. “Performance assesment of hydrogen and ammonia combustion with various fuels for power generators”. In: *International Journal of Hydrogen Energy* 43.45 (2018), pp. 21037–21048. ISSN: 03603199. DOI: [10.1016/j.ijhydene.2018.08.198](https://doi.org/10.1016/j.ijhydene.2018.08.198). URL: <https://doi.org/10.1016/j.ijhydene.2018.08.198>.
- [169] Ahmed Yasiry et al. “Experimental Study on the Effect of Hydrogen Addition on the Laminar Burning Velocity of Methane/Ammonia–Air Flames”. In: *Applied Sciences (Switzerland)* 13.10 (2023). ISSN: 20763417. DOI: [10.3390/app13105853](https://doi.org/10.3390/app13105853).
- [170] George Elias Zacharakis-Jutz. “Performance characteristics of ammonia engines using direct injection strategies”. In: *MSc Thesis* 13032 (2013), pp. 1–91.
- [171] V. F. Zakaznov, L. A. Kursheva, and Z. I. Fedina. “Determination of normal flame velocity and critical diameter of flame extinction in ammonia-air mixture”. In: *Combustion, Explosion, and Shock Waves* 14.6 (1978), pp. 710–713. ISSN: 00105082. DOI: [10.1007/BF00786097](https://doi.org/10.1007/BF00786097).
- [172] C. Zamfirescu and I. Dincer. “Using ammonia as a sustainable fuel”. In: *Journal of Power Sources* 185.1 (2008), pp. 459–465. ISSN: 03787753. DOI: [10.1016/j.jpowsour.2008.02.097](https://doi.org/10.1016/j.jpowsour.2008.02.097).
- [173] Hong Guang Zhang et al. “Fuel combustion test in constant volume combustion chamber with built-in adaptor”. In: *Science China Technological Sciences* 53.4 (2010), pp. 1000–1007. ISSN: 16747321. DOI: [10.1007/s11431-009-0407-7](https://doi.org/10.1007/s11431-009-0407-7). URL: www.springerlink.com.

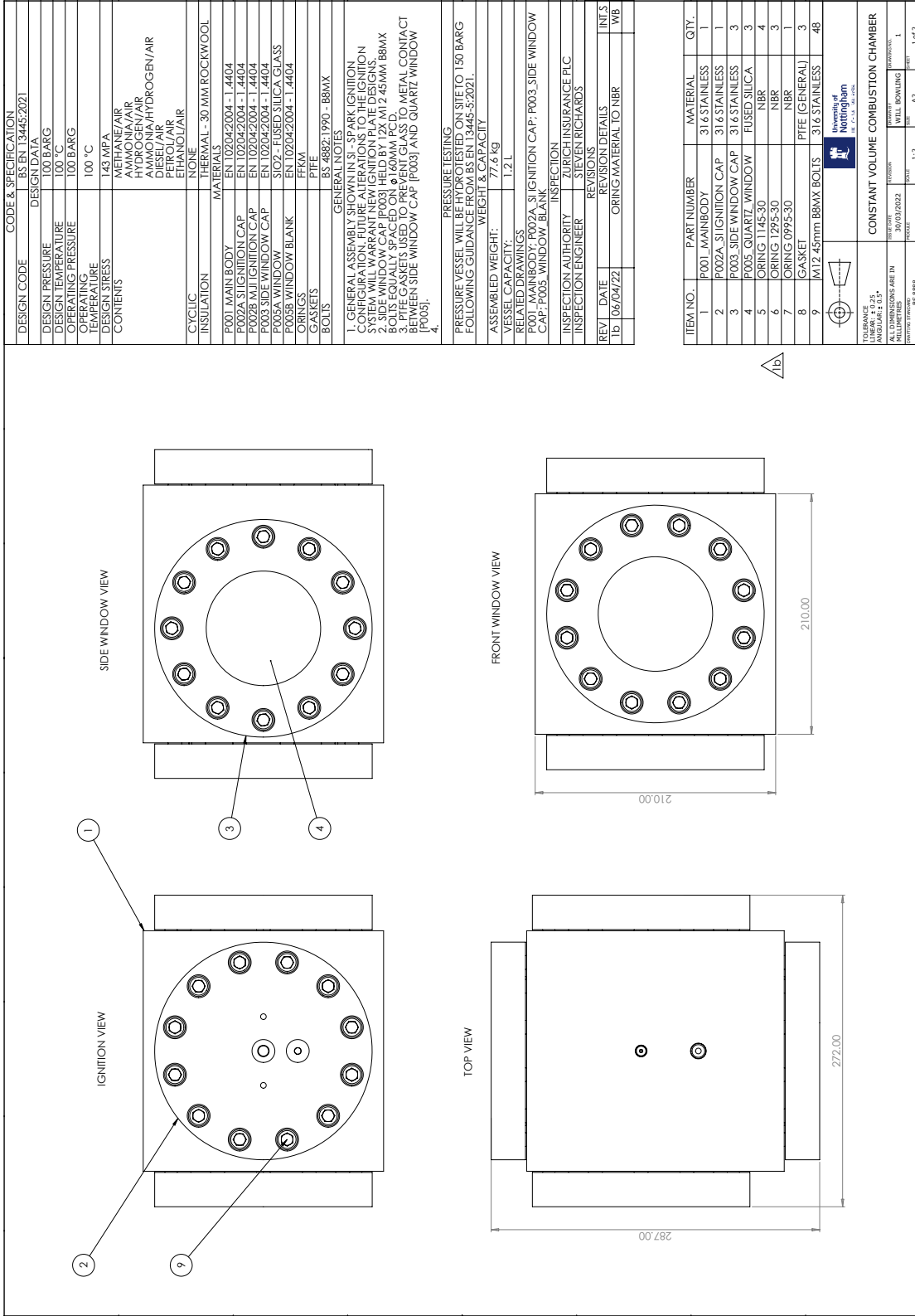
- [174] Xiaolei Zhang et al. “Visualization study on the effects of pre-chamber jet ignition and methane addition on the combustion characteristics of ammonia/air mixtures”. In: *Fuel* 338.December 2022 (2023), p. 127204. ISSN: 00162361. DOI: [10.1016/j.fuel.2022.127204](https://doi.org/10.1016/j.fuel.2022.127204). URL: <https://doi.org/10.1016/j.fuel.2022.127204>.
- [175] H. Zhao and N. Ladommatos. “Optical diagnostics for in-cylinder mixture formation measurements in IC engines”. In: *Progress in Energy and Combustion Science* 24.4 (1998), pp. 297–336. ISSN: 03601285. DOI: [10.1016/S0360-1285\(98\)80026-9](https://doi.org/10.1016/S0360-1285(98)80026-9).
- [176] S. Zitouni, P. Brequigny, and C. Mounaim-Rousselle. “Influence of hydrogen and methane addition in laminar ammonia premixed flame on burning velocity, Lewis number and Markstein length”. In: *Combustion and Flame* 253.x (2023). ISSN: 15562921. DOI: [10.1016/j.combustflame.2023.112786](https://doi.org/10.1016/j.combustflame.2023.112786).

Appendices

Appendix A

Combustion Chamber

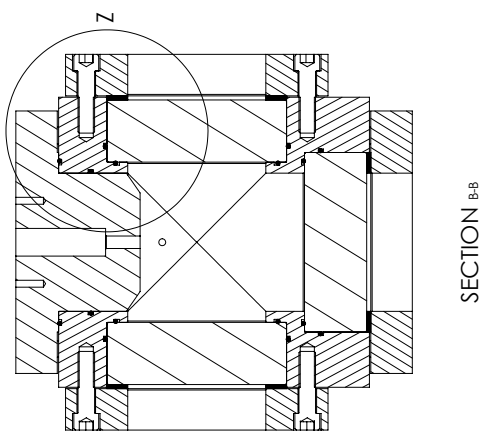
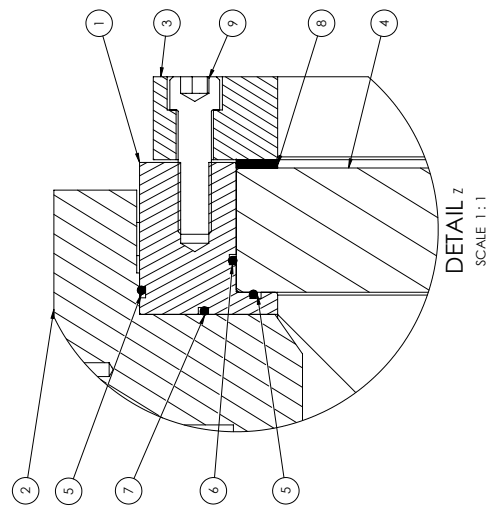
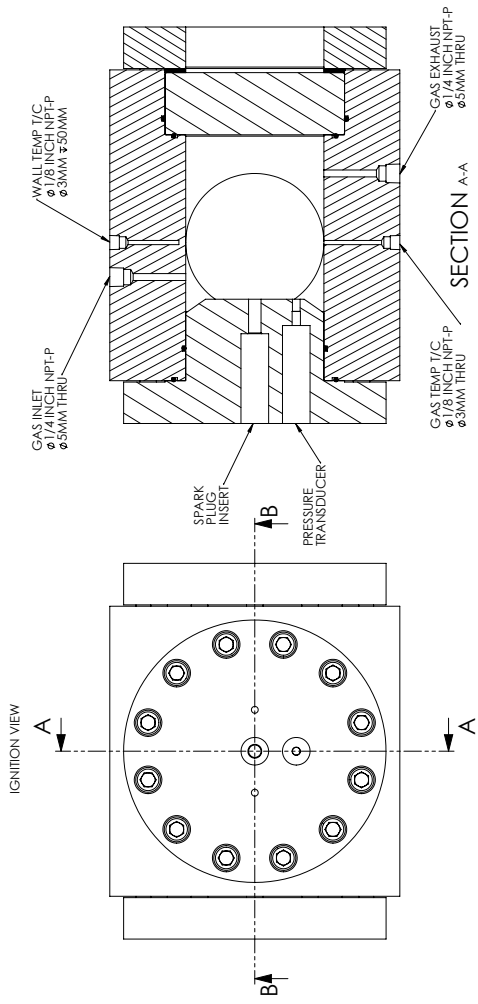
Technical Drawings



CODE & SPECIFICATION				
DESIGN CODE	BS EN 13445:2021			
DESIGN DATA				
DESIGN PRESSURE	100 BARG			
DESIGN TEMPERATURE	100 °C			
OPERATING PRESSURE	100 BARG			
OPERATING TEMPERATURE	100 °C			
DESIGN STRESS	143 MPa			
CONTENTS	METHANE/AIR AMMONIA/AIR ACETYLENE/AIR AMMONIA/HYDROGEN/AIR DIESEL/AIR PETROL/AIR ETHANOL/AIR			
CYCLIC MATERIAL	30 MM ROCKWOOL			
INSULATION MATERIALS				
P001 MAIN BODY	EN 10204:2004 - 1.4404			
P002A SI IGNITION CAP	EN 10204:2004 - 1.4404			
P002B MJ1 IGNITION CAP	EN 10204:2004 - 1.4404			
P003 SIDE WINDOW CAP	EN 10204:2004 - 1.4404			
P005A WINDOW	SI02 - FUSED SILICA GLASS			
P005B WINDOW BLANK	EN 10204:2004 - 1.4404			
ORINGS	FFKM			
GASKETS	PTFE			
BOLTS	BS 4882:1990 - 88MX			
GENERAL NOTES				
1. GENERAL ASSEMBLY SHOWN IN 3D FORK IGNITION CAP IS A REFERENCE ONLY. THE FINAL DESIGN SYSTEM WILL WARRANT NEW IGNITION PLATE DESIGNS.				
2. SIDE WINDOW CAP (P003) HELD BY 12X M12 45MM 88MX BOLTS EQUALLY SPACED ON Ø 160MM P.C.D.				
3. THE SIDE WINDOW CAP (P003) MUST BE IN CONTACT BETWEEN SIDE WINDOW CAP (P003) AND QUARTZ WINDOW (P005).				
4.				
PRESSURE TESTING				
PRESSURE VESSEL WILL BE HYDROTESTED ON SITE TO 150 BARG FOLLOWING GUIDANCE FROM BS EN 13445-3:2021.				
ASSEMBLED WEIGHT:	7.50 kg			
VESSEL CAPACITY:	1.2 L			
WEIGHT DRAWINGS				
P001 MAIN BODY; P002A SI IGNITION CAP; P003 SIDE WINDOW CAP; P005 WINDOW BLANK				
INSPECTION AUTHORITY	ZURICH INSURANCE PLC			
INSPECTION ENGINEER	SIEVEN RICHARDS			
REVISIONS				
REV	DATE	REVISION DETAILS	INT'S	WB
Tb	06/04/22	ORING MATERIAL TO NBR		

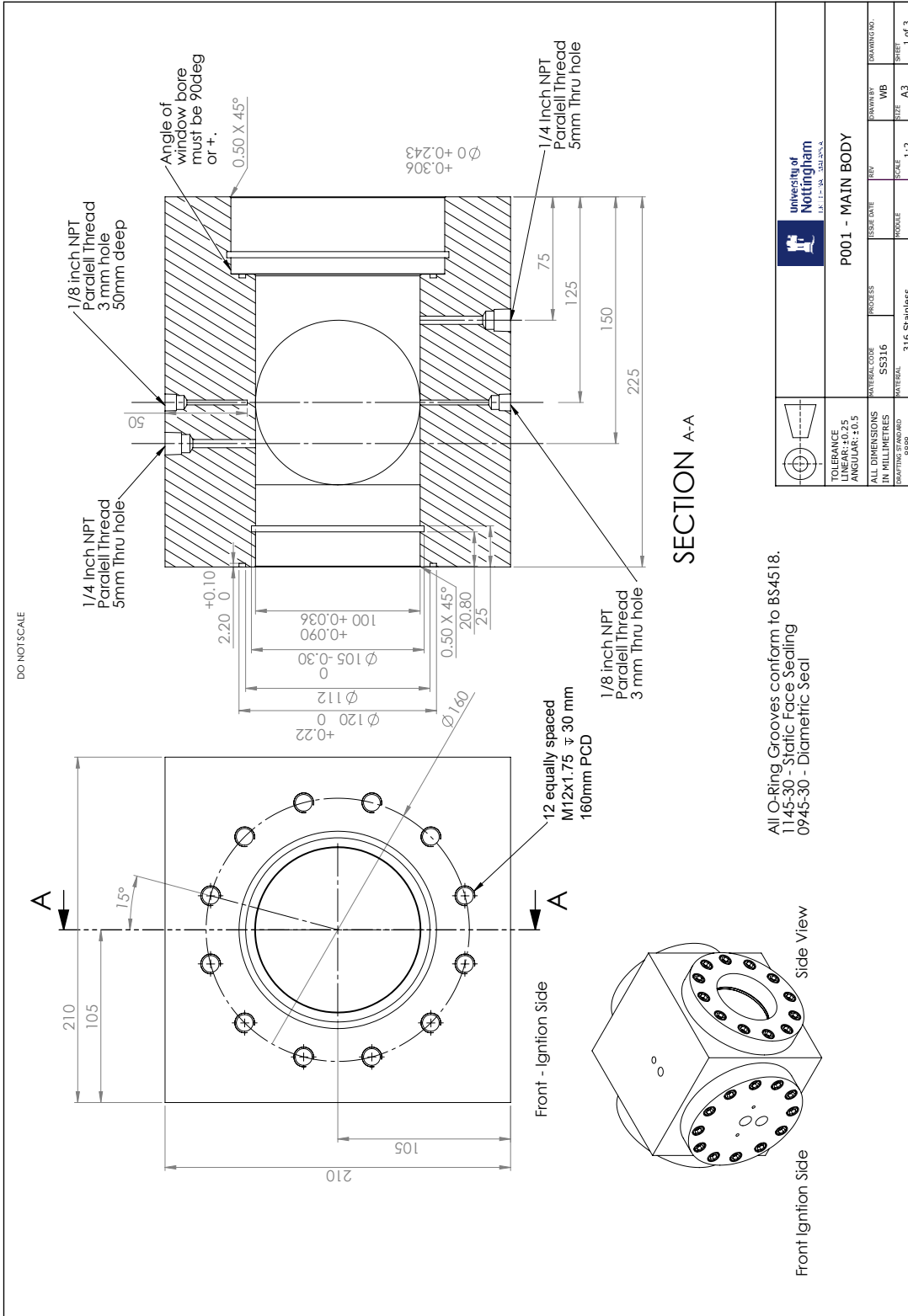
ITEM NO.	PART NUMBER	MATERIAL	QTY.
1	P001 MAIN BODY	316 STAINLESS	1
2	P002A SI IGNITION CAP	316 STAINLESS	1
3	P003 SIDE WINDOW CAP	316 STAINLESS	3
4	P005 QUARTZ WINDOW	FUSED SILICA	3
5	ORING T145-30	NBR	4
6	ORING T295-30	NBR	3
7	ORING 0995-30	NBR	1
8	GASKET	PTFE (GENERAL)	3
9	M12 45mm 88MX BOLTS	316 STAINLESS	48

CONSTANT VOLUME COMBUSTION CHAMBER	
DATE	30/03/2022
REVISION	
WILL BOWLING	1
SCALE	1:2
HEET	A2
OF 2	1 OF 2

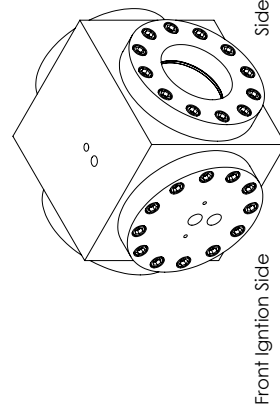
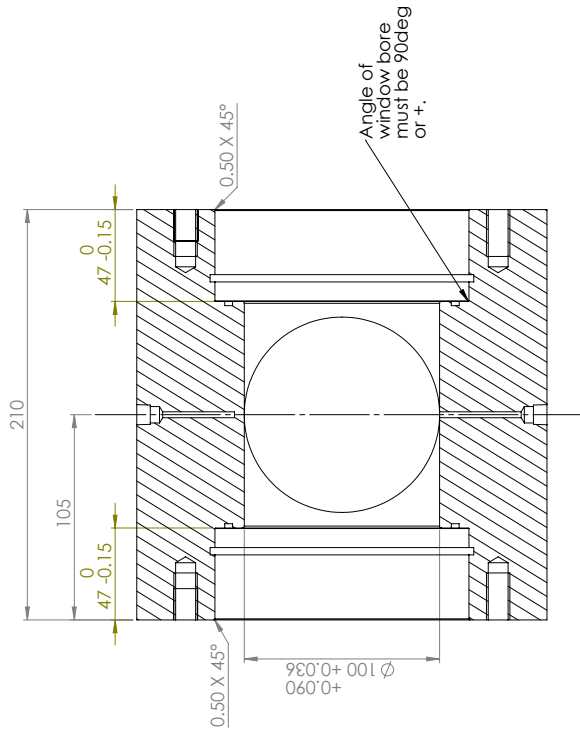
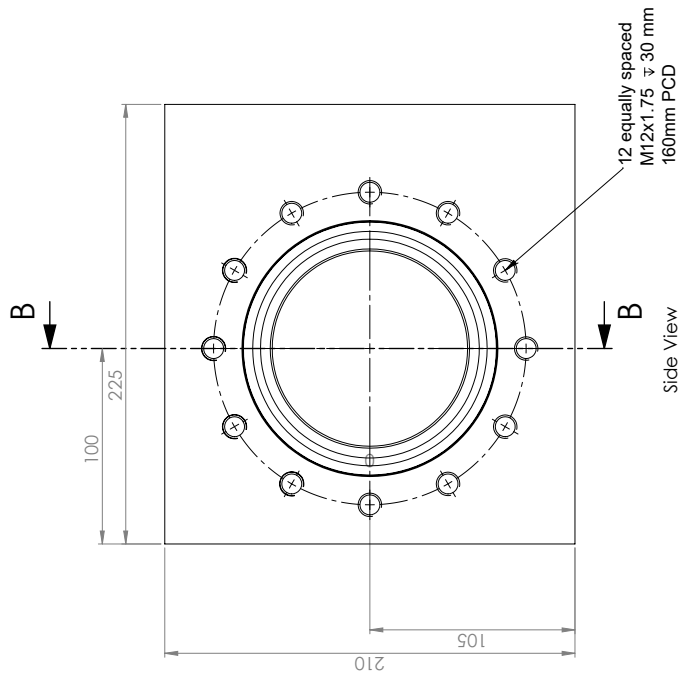


ITEM NO.	PART NUMBER	MATERIAL	QTY.
1	PO01_MAINBODY	316 STAINLESS	1
2	PO02A_STIIGNITION CAP	316 STAINLESS	1
3	PO03_SIDE WINDOW CAP	316 STAINLESS	3
4	PO05_QUARTZ WINDOW	FUSED SILICA	3
5	ORING 1145-30	NBR	4
6	ORING 1295-30	NBR	3
7	ORING 0995-30	NBR	1
8	GASKET	PIPE (GENERAL)	3
9	M12 45mm B8WX BOLTS	316 STAINLESS	48

 University of Nottingham NG7 2RD, LEICESTERSHIRE, ENGLAND	
PROJECT: CONSTANT VOLUME COMBUSTION CHAMBER	
DRAWN BY: J. S.	CHECKED BY:
DATE: 30/03/2022	SCALE: 1:1
SHEET NO: 1	SHEET: 2 of 2



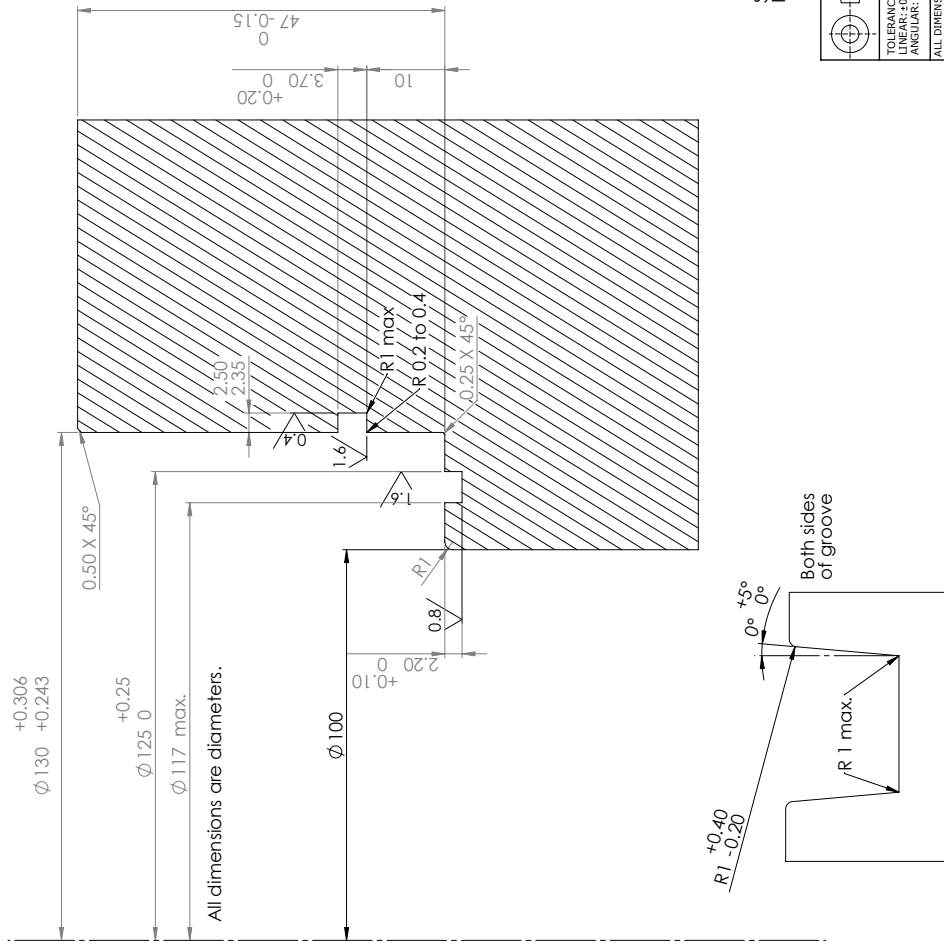
DO NOT SCALE



		University of Nottingham <small>U.S. 1-800-343-2000</small>	
		P001 - MAIN BODY	
TOLERANCE LINEAR: ±0.25 ANGULAR: ±0.5		PROCESS SS316	
ALL DIMENSIONS IN MILLIMETRES		MATERIAL CODE 316 Stainless	
DRAWING STANDARD 8888		MATERIAL 316 Stainless	
ISSUE DATE REV		SCALE 1:2	
DRAWN BY WB		SIZE A3	
DRAWING NO.		SHEET 2 of 3	

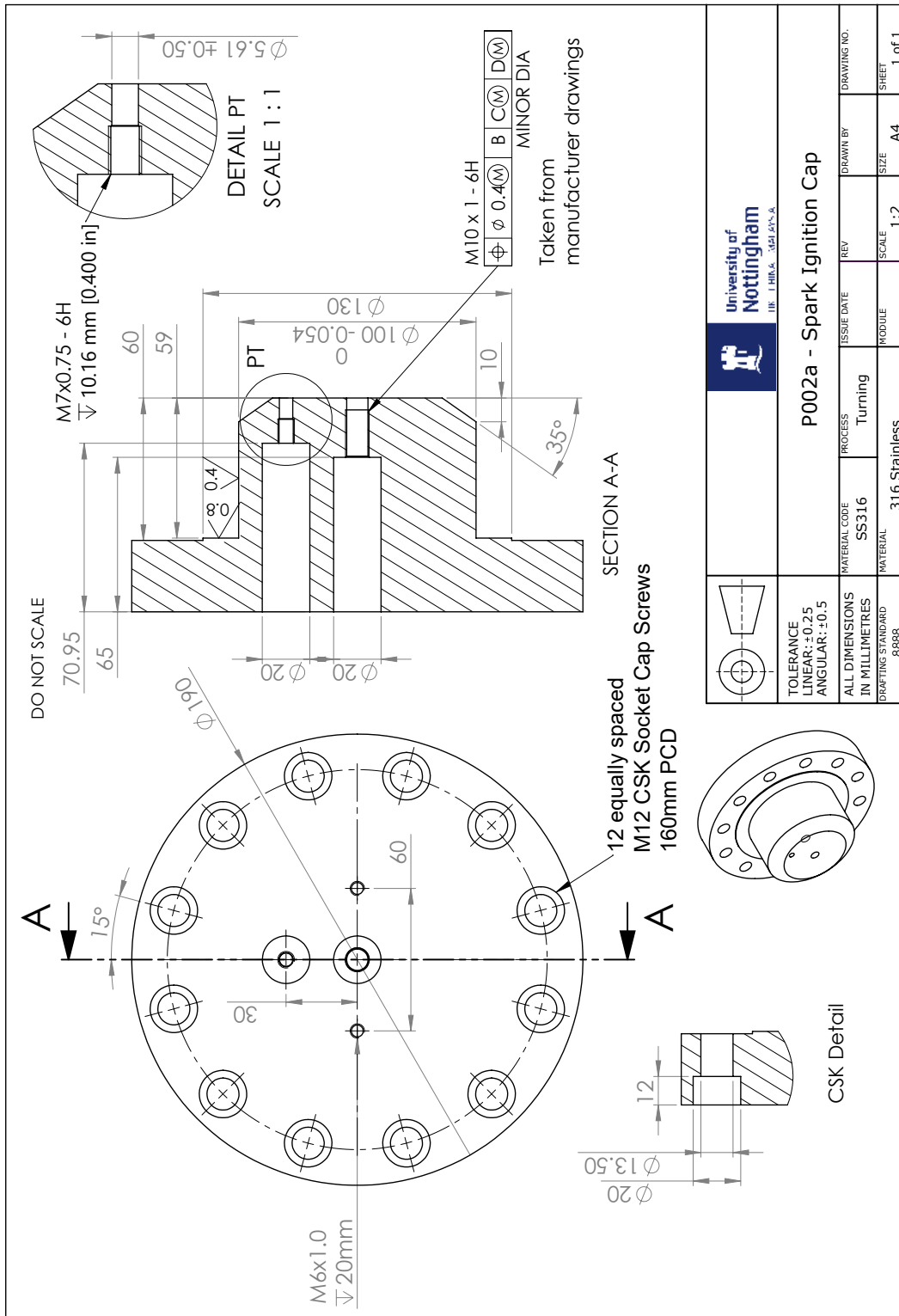
DO NOT SCALE

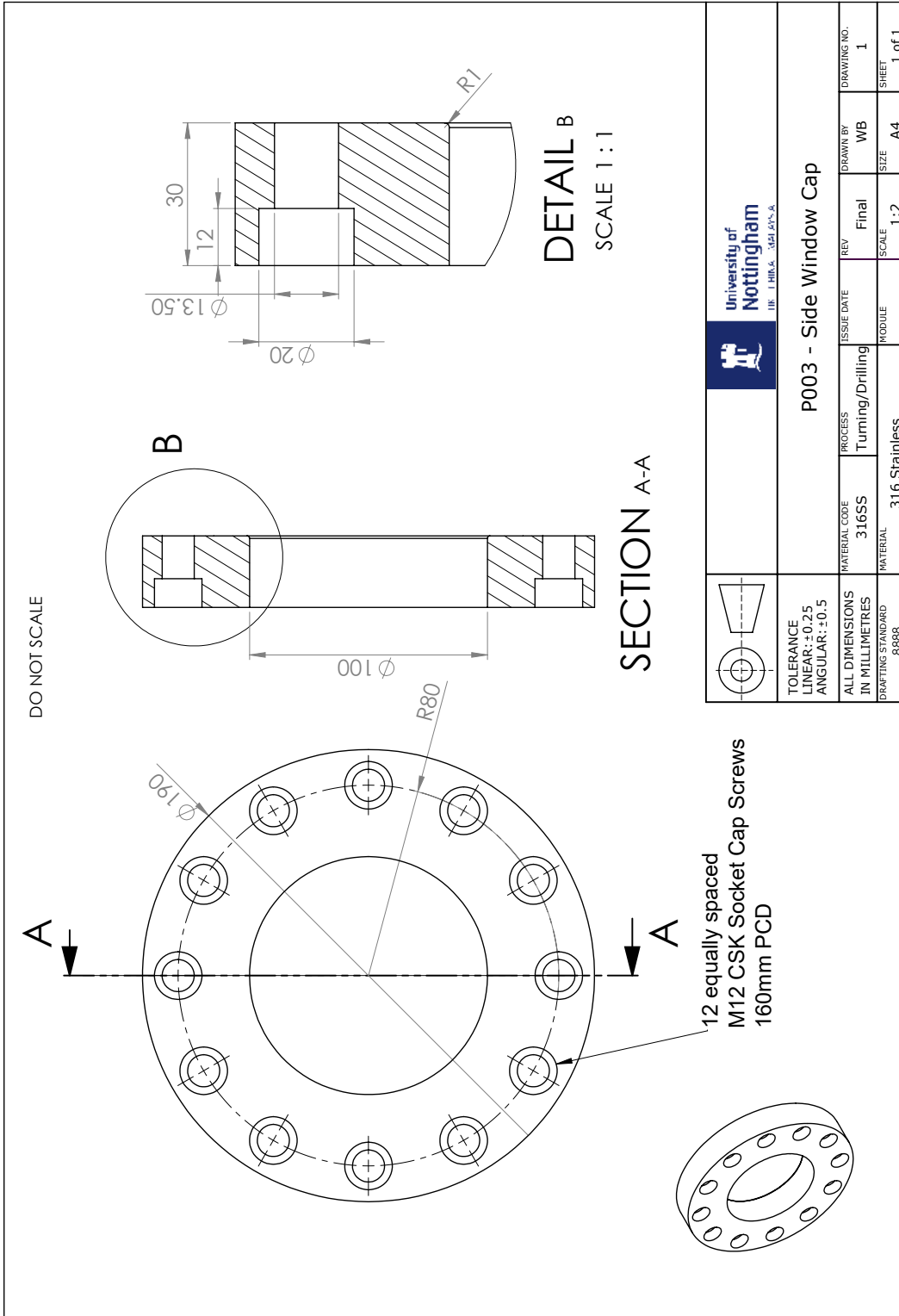
Common design for all window O-Ring Grooves



Surface Finish Notes
Fits and Tolerances Notes

		University of Nottingham U.S. 1-2-34-567890-1	
TOLERANCE LINEAR: ±0.25 ANGULAR: ±0.5		P001 - MAIN BODY	
ALL DIMENSIONS IN MILLIMETRES		ISSUE DATE	
DRAWING STANDARD 8888		MATERIAL CODE SS316	
PROCESS 316 Stainless		SCALE 1:1	
MATERIAL 316 Stainless		DRAWN BY WB	
		SIZE A3	
		SHEET 3 of 3	


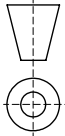


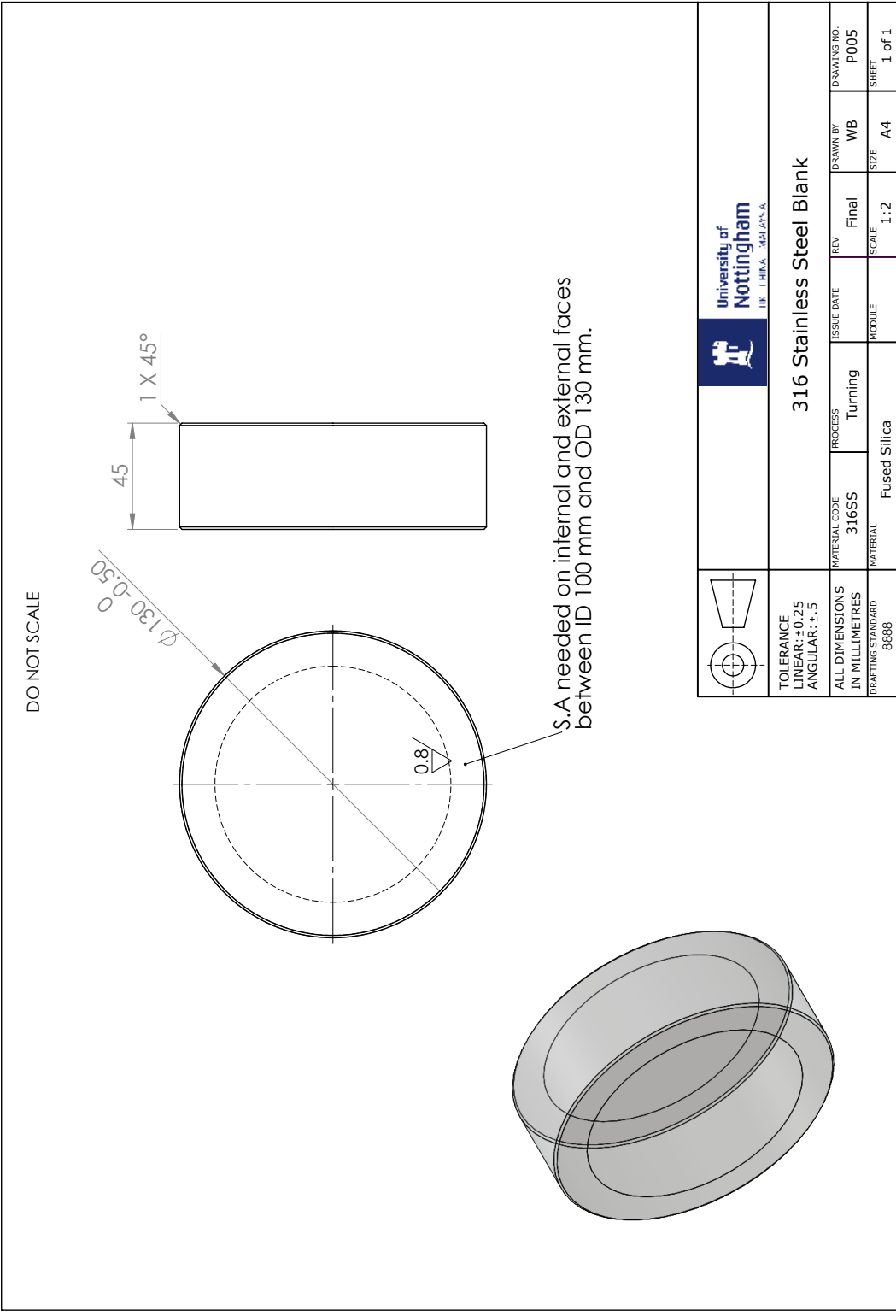



DETAIL B
SCALE 1 : 1

SECTION A-A

12 equally spaced
M12 CSK Socket Cap Screws
160mm PCD

 University of Nottingham IB, I, H, K, A, S, A, P, S, A		P003 - Side Window Cap		DRAWING NO. 1
 TOLERANCE LINEAR: ±0.25 ANGULAR: ±0.5	MATERIAL CODE 316SS	ISSUE DATE Final	DRAWN BY WB	SHEET 1 of 1
ALL DIMENSIONS IN MILLIMETRES	PROCESS Turning/Drilling	MODULE 1:2	SCALE A4	
DRAFTING STANDARD 8888	MATERIAL 316 Stainless			



 University of Nottingham <small>U N I H I R A A P H I L A S A</small>	
316 Stainless Steel Blank	
TOLERANCE LINEAR: ±0.25 ANGULAR: ±5	ISSUE DATE REV Final
MATERIAL CODE 316SS	PROCESS Turning
MATERIAL Fused Silica	SCALE 1:2
DRAFTING STANDARD 8888	DRAWING NO. P005 SHEET 1 of 1

Appendix B

Finite Element Analysis Report



DESIGN DOCUMENT

PROJECT DETAILS

Project Name: Constant Volume Combustion Chamber

Document Date: 04/08/2022

Design Engineer: William Bowling (PhD Student)
william.bowling@nottingham.ac.uk

Supervisor: Professor Alasdair Cairns

Location: Lab D09, RAD Building, Jubilee Campus

DESIGN INFORMATION

Maximum Allowable Pressure: 100 bar

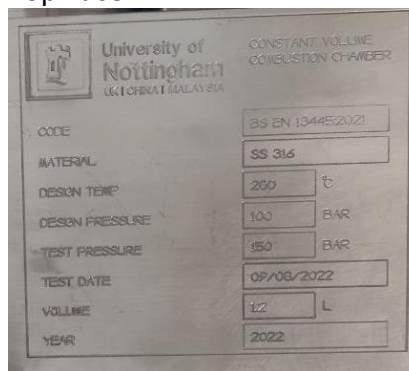
Design Pressure: 100 bar

Design Temperature: 100°C

Capacity: 1.2 L

Containing Fluids: Anhydrous Ammonia
Methane
Hydrogen
Diesel
Methanol

Markings: Top Face



TESTING DETAILS

Test Date: 09/08/2022

Pressure	Time Duration	Status
150 [bar]	30 [mins]	Passed

Hydrostatic Testing is conducted according to standards BSEN 13445:2021

CONTENTS

This report contains the following information as per BSEN13445:2021;

- **Design Information**
- **Design Functionality**
- **Material Selection and Compatibility**
- **Design Calculations**
- **Finite Element Analysis**
- **Design Drawings**

ADDITIONAL NOTES

DESIGN FUNCTIONALITY

This chamber is a bespoke design able to provide the environmental conditions needed to compare spark ignition, turbulent jet ignition and dual-fuel operation inside a generic engine cylinder via optical access. The specific design characteristics were selected to ensure a reasonable representation of heavy-duty engine conditions. These experiments intend to compare the apparent laminar flame speeds associated with various ignition techniques; spark ignition and turbulent jet ignition, with a combination of various fuels and fuel mixtures (diesel, methane, ethanol, methanol, ammonia, and hydrogen).

MATERIAL SELECTION AND COMPATIBILITY

The intention of the device is to be used to investigate the fundamental combustion characteristics of various fuels, as a result the chamber must be compatible with a wide range of fuels. The fuels identified in the table below, are chosen due to planned experiments with the device, these are considered in the initial design. Any additional fuels used must be assessed for material compatibility issues with the device assembly.

Table 1 - Fuel Material Compatibility Considerations

Fuel Used	Potential Material Compatibility Issues
Methane/Natural Gas	Carbon Steel, EPDM, Natural Rubber, Polyurethane, Silicone.
Ammonia	Viton, ABS Plastic, Brass, Copper, FKM, Natural Rubber.
Hydrogen	Risk of permeation, stress related cracking (hydrogen embrittlement)
Diesel/Bio-Diesel	EPDM, Natural Rubber, Silicone.

The materials used in the assembly are listed below.

Table 2 - Constant Volume Combustion Chamber parts list

Part Number	Name	Material
P001	Main Body	316 Stainless Steel – 1.4401
P002a/b	Ignition Cap [variation; SI/MJI]	316 Stainless Steel – 1.4401
P003	Window Cap	316 Stainless Steel – 1.4401
P005a	Optical Window	Fused Silica
P005b	Optical Window - Blank	316 Stainless Steel – 1.4401
006	O-ring	NBR
010	Gasket	PTFE

The materials used in the main body of the CVCC will have areas that will be exposed to the fuels being used, as a result material compatibility is very important. Type 316 stainless steel was selected as the material making up the main body and caps of the combustion rig. This alloy has a high nickel and molybdenum content that improves its corrosion resistance and high-temperature strength as well as promotes a superior hydrogen compatibility¹.

Table 3 - Material Compatibility Assessment

Material Compatibility Assessment				
Fuel Used/Material	316 Steel	Stainless	Fused Silica	NBR
Methane/Natural Gas	A		A	A
Ammonia	A		A	A
Hydrogen	A		A	A
Diesel/Bio-Diesel	A		A	A

<https://www.cambridgereactordesign.com/ammonite/pdf/Chemical-Compatibility.pdf>

DESIGN CALCULATIONS

Nominal Design Stress

EN 13445-3:2014 provides the necessary means to design by formula (DBF) to ensure the main body is above the minimum required wall thicknesses for the desired pressure the calculations were then verified using Solidworks FEA modelling.

The designated operation of the device falls under Load Case 0, which includes considerations for the internal calculation pressure as defined in 5.3.10 as well as the maximum dead loads from 5.3.2.4.2.1.

Load Case	Types of Load	Load Combination	Allowable tensile stress for shells	Allowable compressive stress for shells	Allowable tensile stress for anchor bolts	Explanation
LCO	Pi, Gmax	Pi & Gmax	fd	σc,all	fB,op	Operation with internal pressure

For an internal pressure, the maximum allowable pressure shall not be less than the differential pressure which will exist at the specified location in the chamber when the pressure relieving device starts to relieve. (7.5 MPa). The absolute value of the design pressure shall not be smaller than the absolute value of the maximum allowable pressure.

316 Stainless Steel (1.4401) is an austenitic steel with a minimum rupture elongation of 40%. As a result the nominal design stress for normal operating load cases can be calculated from section 6.5 of BS EN 13445-3:2021. This states the nominal design stress shall not exceed the greater of the two values;

- a) Derived in section 6.4.1 - The nominal design stress for normal operating load cases f shall not exceed f_d , the minimum 1 % proof strength at calculation temperature, as given in the technical specification for the material, divided by the safety factor 1,5.

From the tables below, the minimum 1 % proof strength at calculation temperature is 175 MPa and therefore the nominal design stress from this method is;

$$f_a = \frac{175}{1.5} = 116.6 \text{ MPa}$$

- b) if a value of R_m/T is available, the smaller of two values:
 - the minimum tensile strength at calculation temperature, as given in the technical specification for the material, divided by the safety factor 3,0; and
 - the minimum 1 % proof strength at calculation temperature, as given in the technical specification for the material divided by the safety factor 1,2.

From the tables below, the nominal design strength from this method is the smaller of the two following;

The minimum tensile strength at calculation temperature is 430 MPa and therefore the nominal design stress is;

$$f_a = \frac{390}{3} = 130 \text{ MPa}$$

Or the minimum 1 % proof strength at calculation temperature is 210 MPa therefore the nominal design stress is;

$$f_a = \frac{210}{1.2} = 175 \text{ MPa}$$

Using BS EN 10272:2016 Stainless steel bars for pressure purposes for mechanical properties, the following information is provided.

Table 4 - Minimum values for the 0,2 % and 1,0 % -proof strength of austenitic steels at elevated temperatures in the solution annealed condition (100 – 300°C for 1.4401) from BS EN 10272:2016

Steel Number	0,2 % proof strength Rp0,2 [MPa] min. at a temperature (in °C) of					1,0 % proof strength Rp1,0 [MPa] min. at a temperature (in °C) of					Limit temperature °C
	100	150	200	250	300	100	150	200	250	300	
1.4401	175	158	145	135	127	210	190	175	165	155	300

Table 5 - Minimum values for the tensile strength of austenitic steels at elevated temperatures in the solution annealed condition

Steel Grade		Tensile Strength Rm [MPa] min. at a temperature (in °C) of					
Steel Name	Steel No.	100	150	200	250	300	350
X5CrNiMo17-12-2	1.4401	430	410	390	385	380	380

Following the method from BS EN 13445-3:2021, the nominal design strength at the operating temperature of 200°C is given as $fd = 130$ MPa.

Cylindrical Shell Required Thickness Calculations

Due to the nature of the design, the pressure vessel is not considered to be a thin cylindrical shell and therefore does not conform to methods from BS EN 13445-3. To verify the design of the vessel the hoop stress will be calculated from a simplified design.

The design has a 210 mm square cross-section with a 100mm bore cut out, therefore, to confirm the yield stress safety factor the hoop stress can be overestimated by assuming a thickness of 55mm. The maximum stress will be found at the inner wall when $r = 50$ mm.

$$\text{Hoop Stress, } \sigma_{\theta} = p \left[\frac{r_o^2 + r_i^2}{r_o^2 - r_i^2} \right]$$

Where r_i is the internal radius, r_o is the outer radius and p is the internal pressure. **Therefore, the maximum internal pressure of 10 MPa (100 bar) results in a maximum hoop stress of 15.86 MPa. Providing a safety factor of 9 when compared to the nominal design strength.**

This does not consider the axial forces as a result of the bolted end caps, or the additional counterbored hole. These will be considered during the FEA simulations.

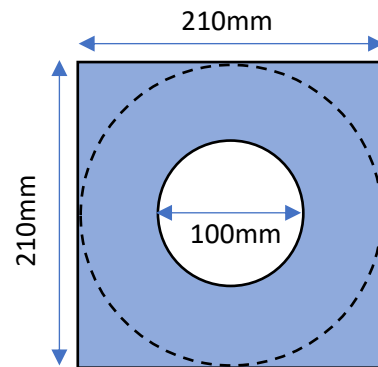


Figure 1 - Representative cross-section used for stress calculations

Optical Window Thickness Calculations

The optical elements in this design will be in a “port-hole” style commonly used in optical combustion chambers. The window is a supported plane-parallel circular element so as a result the thickness can be derived from the calculated stresses and the desired safety factor. The maximum stress on a uniformly loaded window is given by

$$S_{Max} = \frac{K D^2 P}{4T^2}$$

Where S_{Max} is the maximum stress, K is the empirical constant (0.75 for this context), D is the unsupported diameter for a circular window, and T is the thickness of the window. These variables are shown in the diagram in figure 8. Since

$$S_{Max} = \frac{F_a}{SF}$$

Where F_a is the apparent elastic limit of the material and SF is the safety factor. Rearranging these equations, the thickness of the window is given by

$$T = D \sqrt{\frac{SF * K}{4}} * \sqrt{\frac{P}{F_a}}$$

Considering the working pressure of 100 bar (10 MPa), the unsupported diameter of 100mm, K value of 0.75, and the allowable stress of 55MPa with a safety factor of 4,

$$T = D \sqrt{\frac{SF * K}{4}} * \sqrt{\frac{P}{F_a - \sigma_T}}$$

$$T = 100 * \sqrt{\frac{4 * 0.75}{4}} * \sqrt{\frac{10}{(41)}} = 42.77 \text{ mm}$$

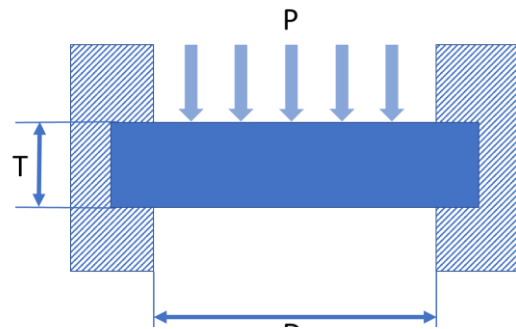


Figure 2 – Representative diagram of a clamped pressure vessel window.

The final thickness of the optical windows was chosen to be 45 mm, this provided a SF of over 4 at a pressure of 100 bar.

Table 1: Physical parameters of fused silica

Temperature (°C)	Thermal conductivity (W / (m · K))	Heat Capacity (J / (kg · K))	Density (kg / m ³)	Expansion coefficient /10 ⁻⁷ (1 / K)	Young modulus (10 ⁹ Pa)	Poisson ratio
20	1.30	740	2200	2.76	71.44	0.158
250	1.56	987	2200	7.95	70.76	0.153
500	1.84	1121	2200	5.75	70.30	0.150
750	2.13	1178	2200	4.68	70.43	0.148
1000	2.40	1121	2200	4.17	71.05	0.150
1500	2.26	1246	2200	5.10	73.79	0.160
1700	2.28	1273	2200	6.00	75.45	0.166
2000	\	\	2200	11.45	85.28	0.21
2500	2.38	1273	2200	11.45	\	\

Bolt Loading Calculations

Each cap fixed to the main body will be subject to a pressure of 100 bar distributed across a 100mm circular face. To account for the case in which an o-ring fails, the distribution used will be the full face of the window – 130 mm.

$$\begin{aligned} \text{Force} &= \text{Pressure} * \text{Area} \\ &= 10.0 * 10^6 * \pi * (65 * 10^{-3})^2 \\ &= 132.2 \text{ kN} \end{aligned}$$

This force is held by 12 equally spaced bolts, resulting in a force of;

$$\frac{132.2 \text{ kN}}{12} = 11.1 \text{ kN per bolt}$$

Following the recommended design stress values from PD 5500, alongside the metric bolt root areas in accordance with BS 3643-1:2007, M12x1.75 Bolts were selected. The bolt design stress is,

$$\frac{11.1 \text{ kN}}{76.25 \text{ mm}^2} = 145.1 \text{ MPa}$$

Which is within the recommended design stress values from Table 3.8-1 in PD 5500 for BS4882 grades B8MX at 200°C, 148 MPa therefore the safety factor is 1.

Hydrostatic Test Pressure Calculations

The test pressure shall be determined by the greater of:

$$P_t = 1,25. P_d \frac{f_a}{f_{T_d}} \quad \text{or} \quad P_t = 1,43. P_s$$

Where, P_t is the test pressure, P_d and T_d are the coincident design pressure and temperature values for the maximum load case, P_s is the maximum allowable pressure, f_a is the nominal design stress at test temperature, f_{T_d} is the nominal design stress at the maximum design temperature.

$$P_t = 1,25 \cdot 10,0 \frac{175}{145} = 15.08 \text{ MPa} \quad \text{or} \quad P_t = 1,43 \cdot 10,0 = 14.3 \text{ MPa}$$

The bolt loading in this scenario is as follows

$$\begin{aligned} \text{Force} &= \text{Pressure} * \text{Area} \\ &= 15.0 * 10^6 * \pi * (65 * 10^{-3})^2 \\ &= 199.1 \text{ kN} \end{aligned}$$

This force is held by 12 equally spaced bolts, resulting in a force of;

$$\frac{199.1 \text{ kN}}{12} = 16.6 \text{ kN per bolt}$$

The bolt design stress is,

$$\frac{16.6 \text{ kN}}{76.25 \text{ mm}^2} = 217,6 \text{ MPa}$$

In accordance to pd5500, Allowable stress = $207 * 1.25 =$

FINITE ELEMENT ANALYSIS – 12 bolt simulations

The following section details the finite element analysis work performed using Solidworks. It details the input data, mesh data, stress and deflection results.

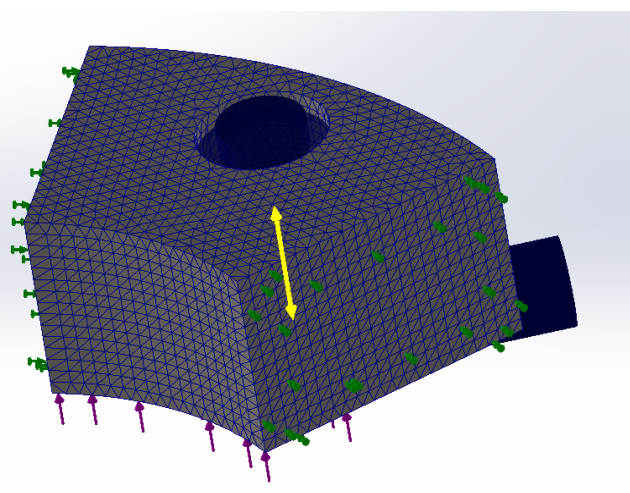
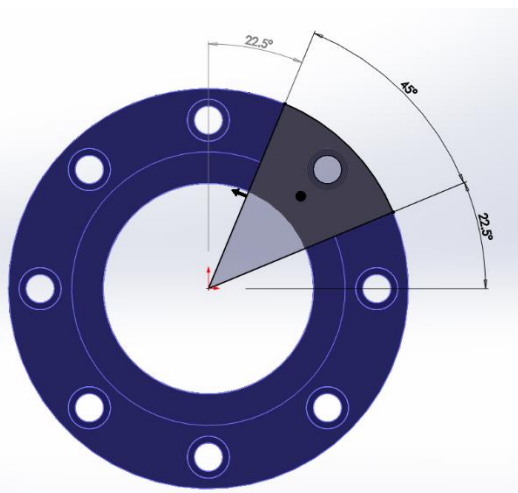
Window Cap

Geometry, Loading and Meshing

The force caused by the internal pressure of the device is transferred from the fused silica window onto the gasket and then equally distributed about the window cap via the contact with the gasket. The total force transferred is,

$$\begin{aligned} \text{Force} &= \text{Pressure} * \text{Area} \\ &= 10.0 \text{ MPa} * \pi * (50e - 3)^2 \\ &= 78540 \text{ N} \end{aligned}$$

Utilising the cyclic symmetry of the geometry, the model is simplified to a single fixture and then constrained using a Foundation Bolt as shown in the figures below. Meshing details are also included below.



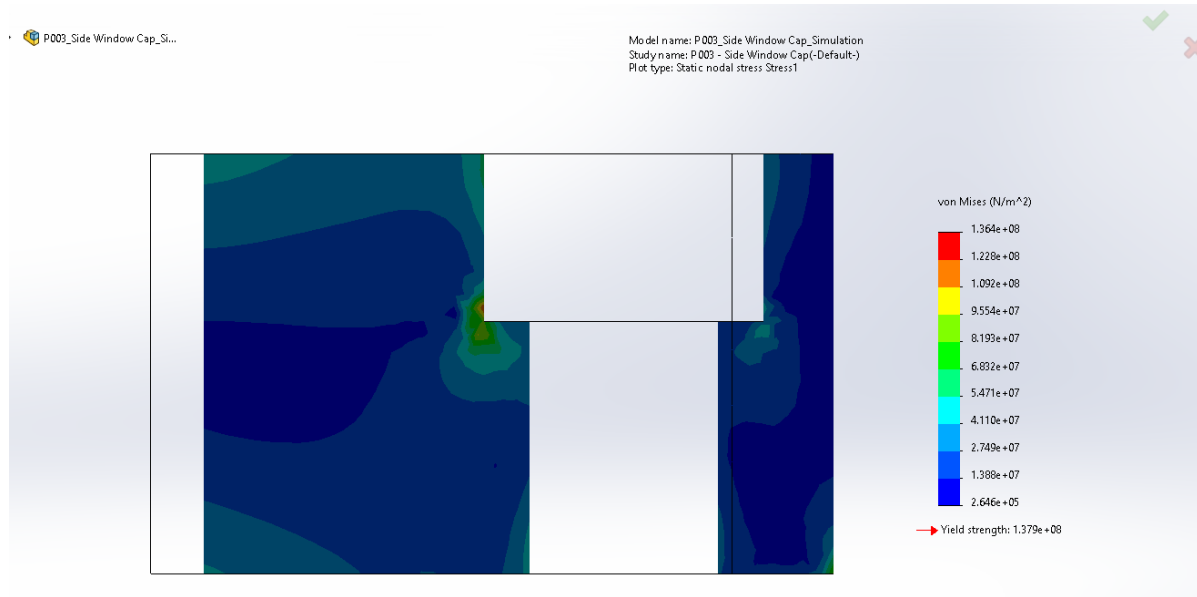
Study name

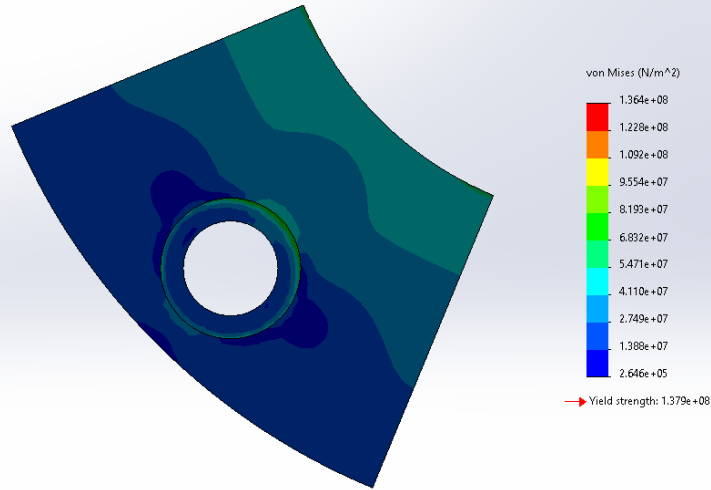
P003 - Window Caps

Mesh type	Solid Mesh
Mesher Used	Standard mesh
Jacobian points for High quality mesh	16 points
Element size	2.06643 mm
Tolerance	0.103322 mm
Mesh quality	High
Total nodes	74546
Total elements	51425
Maximum Aspect Ratio	3.6878
Percentage of elements with Aspect Ratio < 3	99.9
Percentage of elements with Aspect Ratio > 10	0
Percentage of distorted elements	0
Number of distorted elements	0

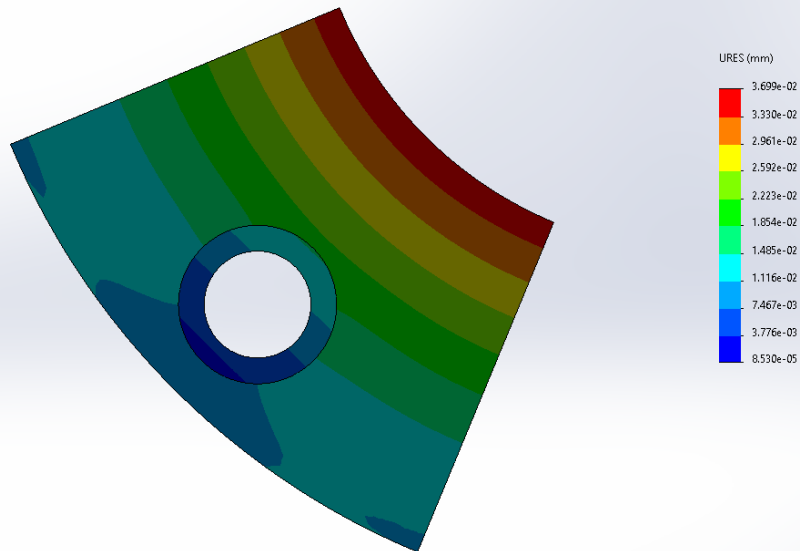
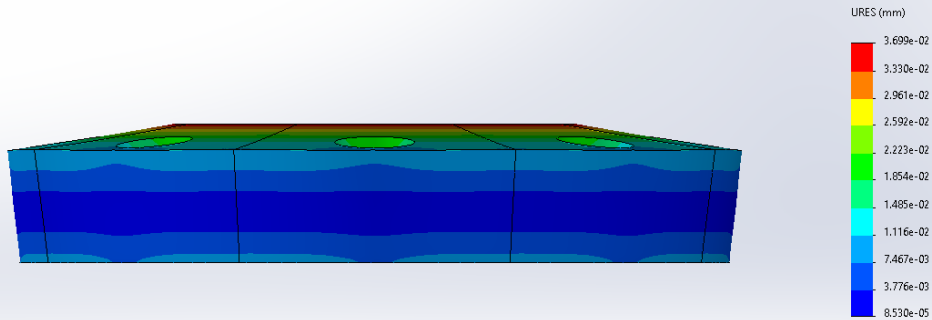
Results

Stress concentration analysis was performed and the results are shown below. A section was taken through the centre of the bolt to show the areas of high stress. The highest stress observed by the model was 136.4 MPa. This is below the nominal design stress as calculated from BS EN 13445.



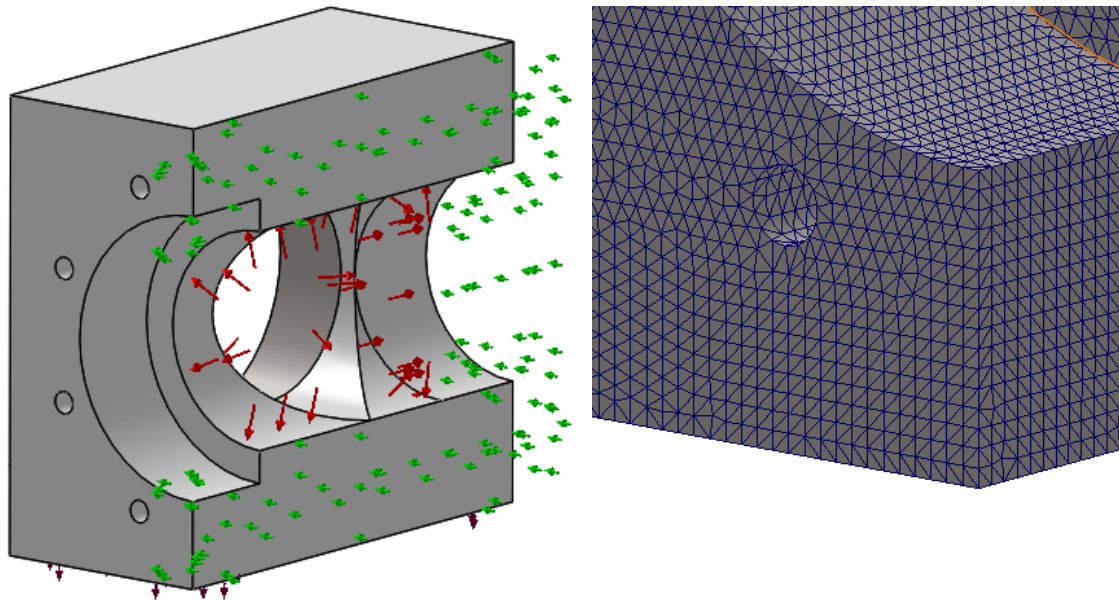


Additional deformation results are shown below, scaled up 196 times to demonstrate the deflection. The maximum, as expected is around the inner rim of the design, demonstrating a displacement of 0.037 mm.



Main Body Simulation
Geometry, Loading and Meshing

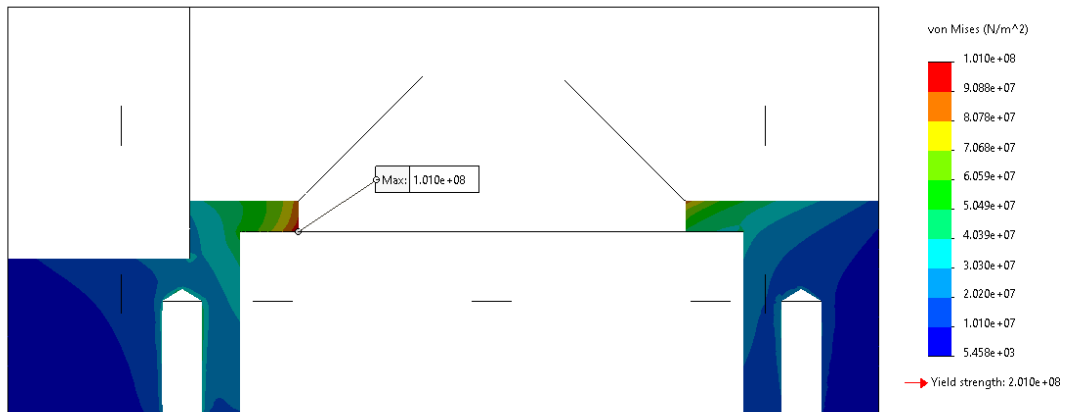
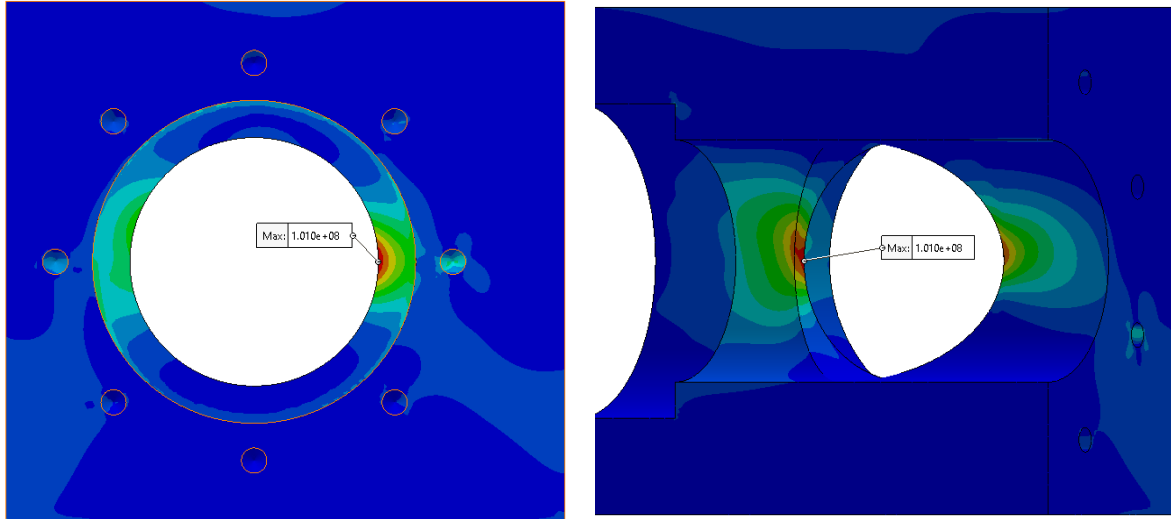
To efficiently simulate the main body, smaller features such as the thermocouple holes, gas inlets and o-ring grooves were removed from the geometry and the model symmetry was taken advantage of. The figure below details the loading and constraints that were assigned to the model, the red arrows indicate a 10.0 MPa pressure distributed on the inner face of the model. The green arrows indicate the symmetric constraint and the purple arrows on the lower section highlights the bottom face which is under a fixed constraint.



Study name	Design Pressure 100 bar Study (-Default-)
Mesh type	Solid Mesh
Mesher Used	Standard mesh
Jacobian points for High quality mesh	16 points
Element size	2.5 mm
Tolerance	0.125 mm
Mesh quality	High
Total nodes	1373213
Total elements	980248
Maximum Aspect Ratio	43.858
Percentage of elements with Aspect Ratio < 3	99.9
Percentage of elements with Aspect Ratio > 10	0
Percentage of distorted elements	0
Number of distorted elements	0

Results

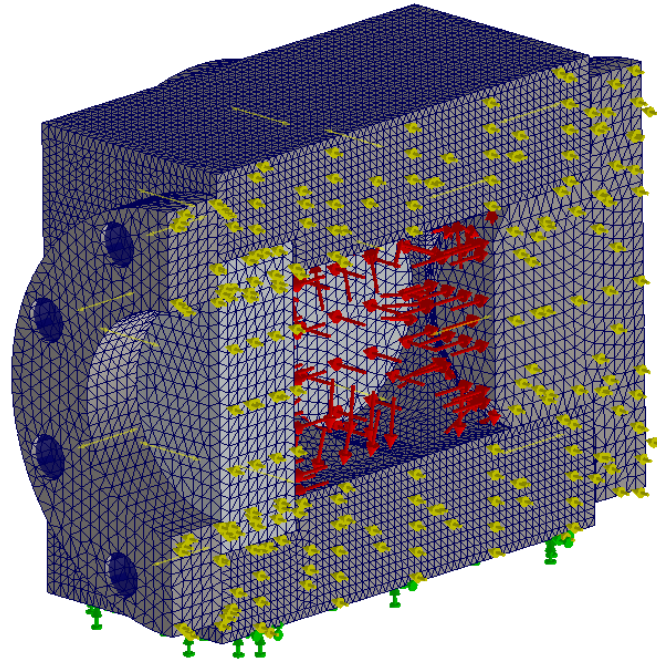
Stress concentration analysis was performed and the results are shown below. A section was taken perpendicular to the symmetry plane to highlight the distribution of stress through the thinnest portion of the design, when fully assembled this section would be fully supported by the fused silica face. The highest stress observed by the model was 101 MPa.



Full Assembly Simulation

Geometry, Loading and Meshing

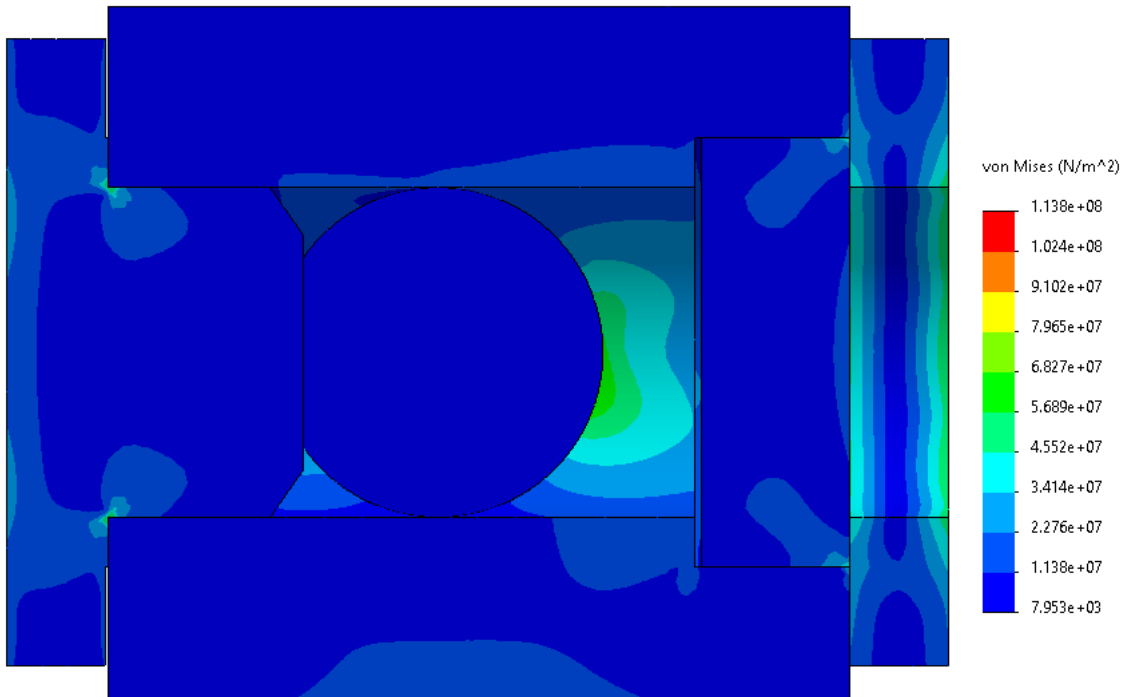
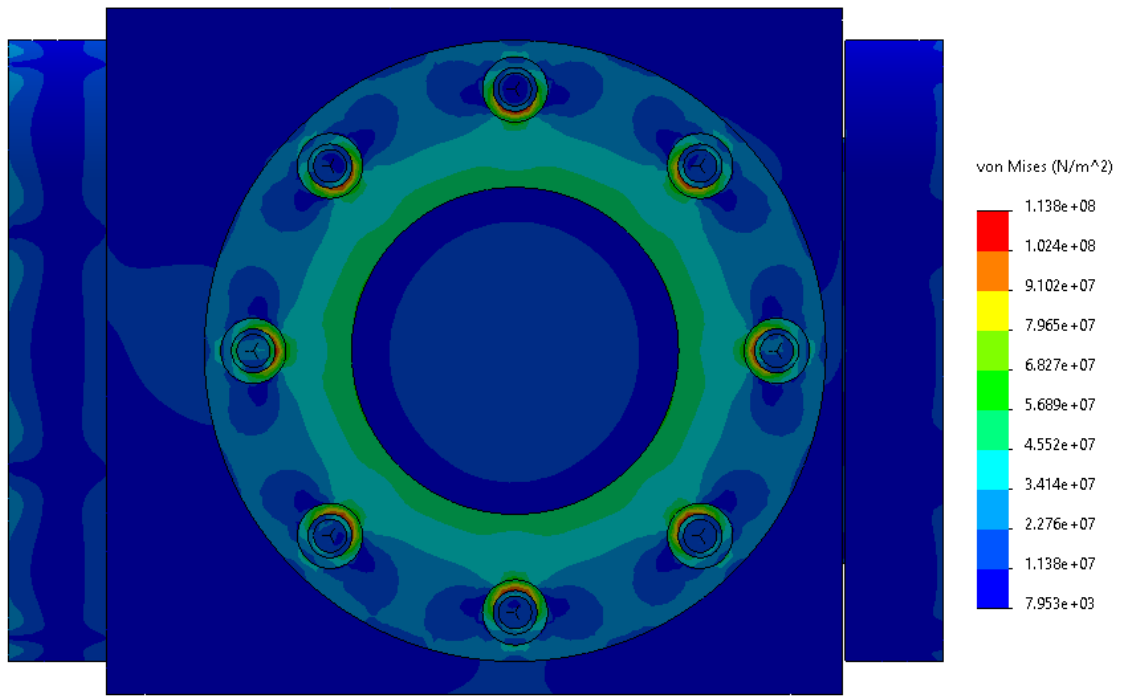
Similar to the main body simulation, the line of symmetry is utilised to reduce computational time. Additionally smaller features such as o-ring grooves and thermocouple holes were removed. The red arrows represent the internal pressure loading of the chamber, the yellow arrows highlight the symmetrical constraint in the model and the green arrows highlight the fixed constraint on the bottom of the model. The meshing was prioritised on the main body with a 4 mm maximum element size.

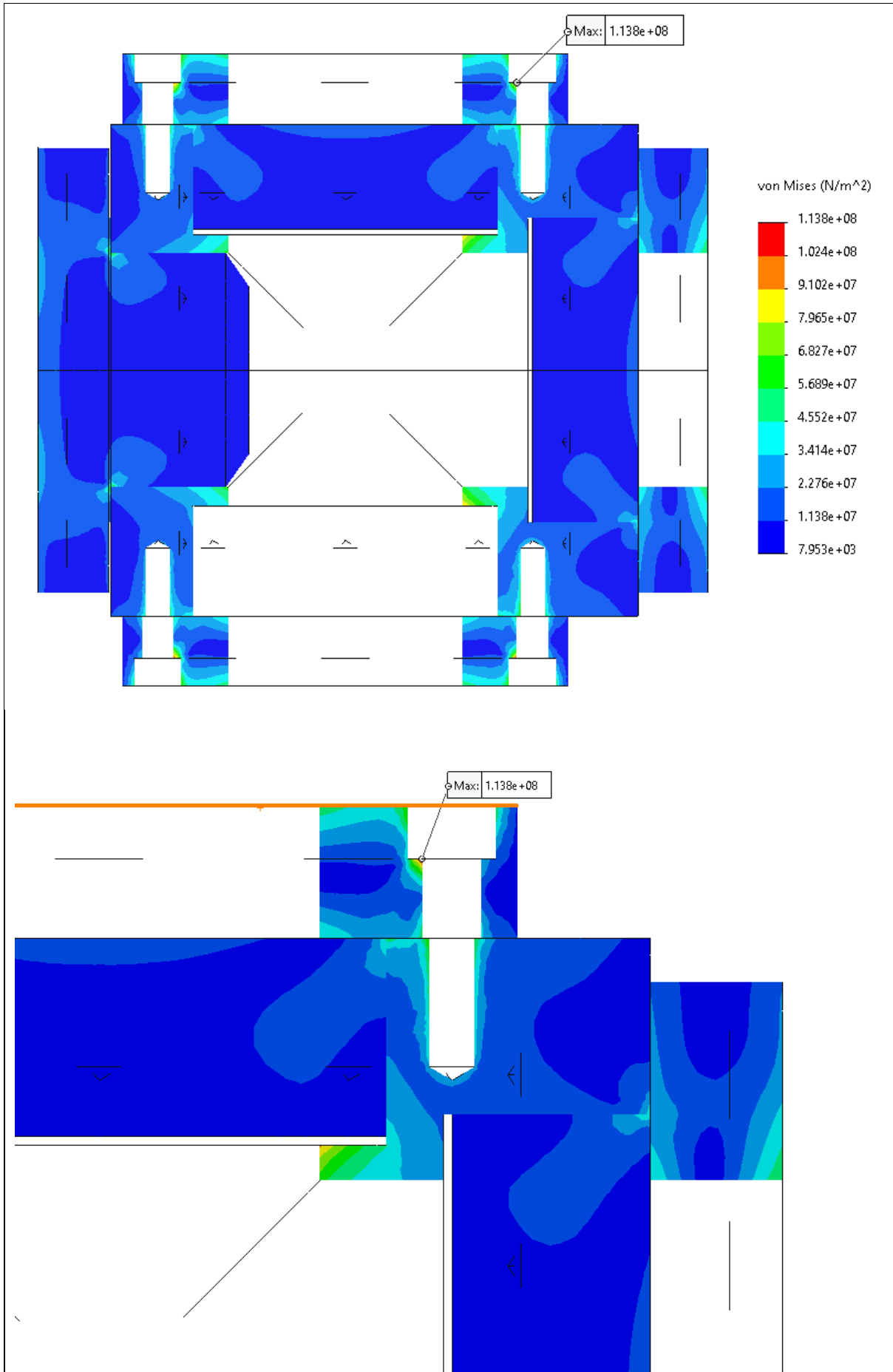


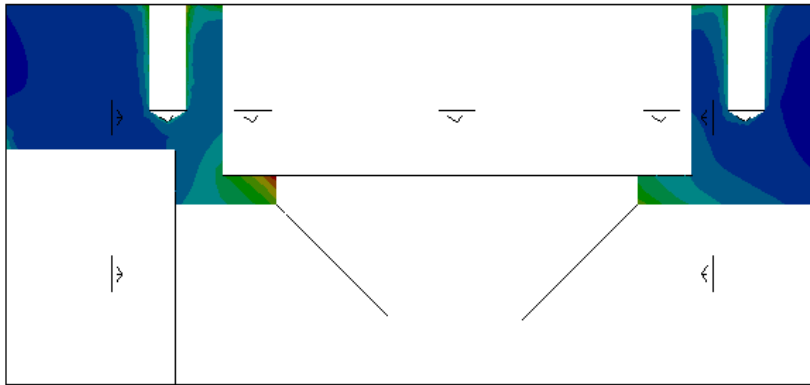
Study name	100 Bar Asy Study_Hi Res (-Default-)
Mesh type	Solid Mesh
Mesher Used	Standard mesh
Jacobian points for High quality mesh	16 points
Element size	4 mm
Tolerance	0.2 mm
Mesh quality	High
Total nodes	788951
Total elements	547294
Maximum Aspect Ratio	27.342
Percentage of elements with Aspect Ratio < 3	99.9
Percentage of elements with Aspect Ratio > 10	0.00164
Percentage of distorted elements	0
Number of distorted elements	0

Results

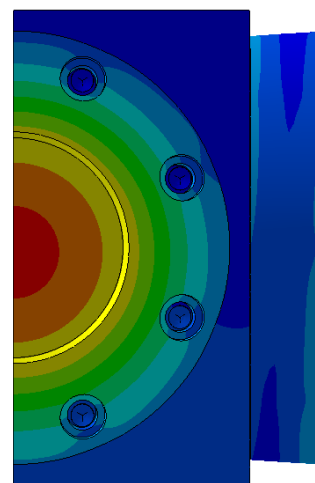
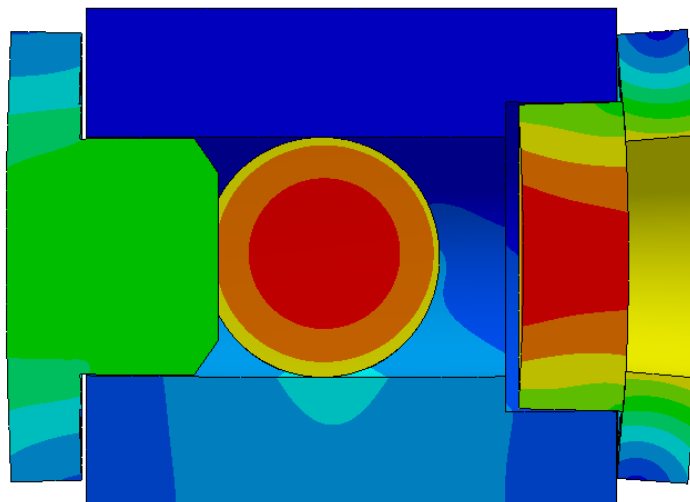
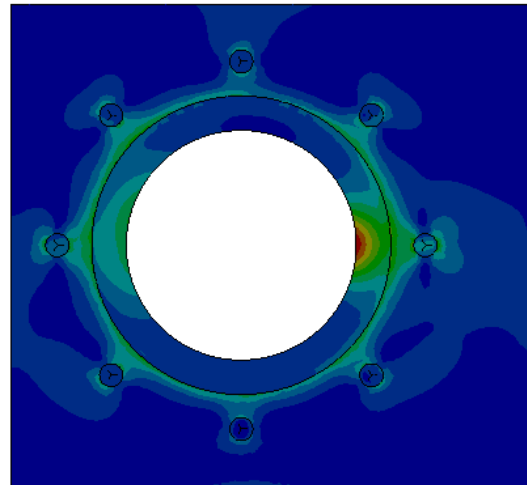
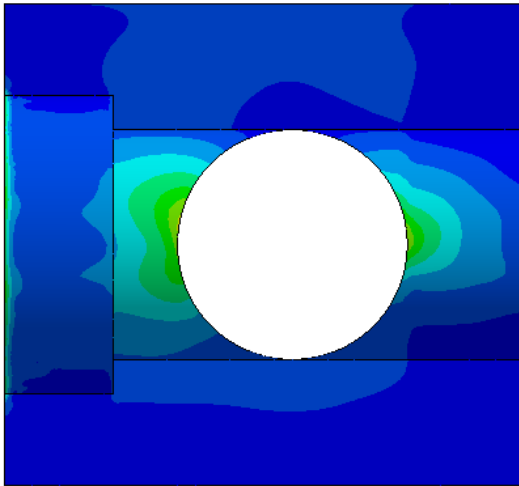
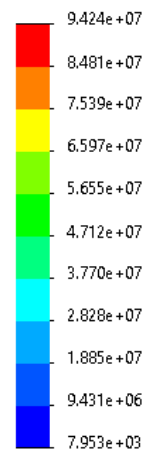
Results of the stress concentration analysis is shown below, the maximum stress observed by the assembly under 100 bar of pressure is 113.8 MPa, this is below the allowable design stress calculated previously of 143MPa. It is important to note that the high values of stress are seen at the bolting positions, these are expected due to the modelling of bolt loads in the software and are expected to be over-approximated by the simulation.



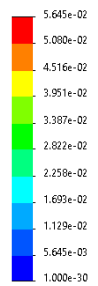




von Mises (N/m²)



URES (mm)



DESIGN REVIEW SUMMARY

Project Number	PS22-0395	Document Revision 1	
Client Name	Nottingham University	Pressure Equipment	Constant Volume Test Chamber

Initial Assessment

Engineer:	Steven Richards	Status:	Approved	Date:	01-03-22
-----------	-----------------	---------	----------	-------	----------

Pipework Criteria			
Design Pressure PS	100Barg	Design Temperature TS	100°C
Design Code	PD5500 Intent	Description	Third Party Inspection Only
DN / Volume	1.2 Litre	Fluid State	Gas
PESR Assessment	N/A	Fluid Group	1
PESR Assess Table	N/A	PESR Category/Module	N/A






PESR Module adopted by Manufacturer	N/A
-------------------------------------	-----

Review	
Calculations to design code	Yes
Test pressure	> PESR2016, PD5500 = 143Barg
Supporting PESR documentation	N/A
WPQR's / WPAR's	N/A
Nameplate details	TBC
Hazard analysis	N/A

Comments/Notes
All comments addressed, approval subject to satisfactory hydrotest.

Drawing / Documentation reviewed		
Title	Drawing/Document no.	Revision / Revision Date
General arrangement drawing	1 – Page 1 to 2	1b (10-5-22)
P001 – Main Body	P001 – Main Body page 1 to 3	- (10-5-22)
P002a – Spark Ignition Cap	P002a – Spark Ignition Cap	- (10-5-22)
P003 – Side Window Cap	P003 – Side Window Cap	- (10-5-22)
P005 – Steel Window Blank	P005 – Steel Window Blank	P005 (10-05-22)

Revision details -

 GA_Constant Volume Combustion Cham...	10/05/2022 11:25
 P001_MainBody	10/05/2022 11:25
 P002a_SI Ignition Cap	10/05/2022 11:25
 P003_Side Window Cap	10/05/2022 11:25
 P005_Window_Blank	10/05/2022 11:25

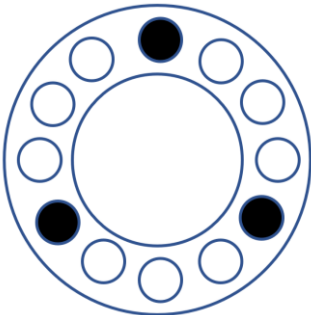
Appendix C

Combustion Chamber

Assembly Manual

Combustion Chamber Assembly Manual

Written by: Will Bowling

Chamber Disassembly	
1	Initial Checks Make sure chamber is at ambient. Have a place ready to put the glass, preferably back into box under desk. Exhaust line open
2	Silver Bolts Undo silver bolts completely and then put in 2 turns. Open the air line and slowly increase pressure, no more than 2 bar. Pulse it if needs be, so switch on then off. Glass/Ignition plate will slowly eject from chamber.
3	Black Bolts In the drawer take the longer black bolts and replace three of the silver bolts. Assemble opposite from one another.  Remove the remaining silver bolts. Repeat air pressure increase to push window as far as possible. Make sure plastic gasket is still between glass and metal.
4	Ejecting the glass Make sure pressure is at ambient or close to. Remove black bolts and retaining metal ring. Wearing gloves carefully remove glass and place in box.
5	If you are removing multiple windows, do each window up to silver bolts first to help with removal.

Chamber Reassembly	
1	<p>Initial Checks</p> <p>Make sure the chamber vent line is open Check o-rings for any damage</p>
2	<p>Setting the windows</p> <p>Use vacuum grease, on the orings to keep them in place. Use vacuum grease around the edge of the window to help with assembly. Carefully push window into place. Will probably not go all the way in. Fit the metal retaining ring with the plastic gasket using the black screws and screw all the way in. ½ turn of resistance for each screw to prevent imbalance.</p>
3	<p>Silver Screws</p> <p>Make sure the plastic gasket is in place. Add silver screws around retaining ring. Switch on vacuum pump, and bring chamber pressure down very slightly. 0.7 bar. ½ turn of resistance on each of the silver screws. Doing opposing screws each time. Vacuum more if struggling but do so very carefully. Too high vacuum will “pop” window into place and potentially damage it. Remove black screws and replace with silver.</p>
4	<p>Tightening</p> <p>Once screws are fully in and the glass is tight – there should be able 0.5 mm space between retaining ring and main body. Vacuum down chamber fully and retighten screws. Just nip them up, do not over tighten. Make sure you are screwing in screws that are opposite one another.</p>
5	<p>Checks</p> <p>Pressurise chamber with compressed air Vacuum chamber down and nip up screws again.</p>
6	<p>Pressure drop test</p> <p>Using helium, pressurise chamber (making sure fuel line is closed). 9 bar is enough. Write down pressure and wait 30 mins. Pressure drop should be less than 0.1 bar.</p>

Appendix D

Combustion Chamber Mixture Properties

The burned and unburned densities were evaluated from gas equilibrium calculations with thermo-transport data of Tian et al [151].

Table D.1: Properties of methane-air mixtures employed in this study.

P_i	Equivalence Ratio ϕ	Unburned Density ρ_u	Burned Density ρ_b	ρ_b / ρ_u
0.1	0.8	1.1243	0.1678	0.1492
0.1	0.9	1.1198	0.1561	0.1394
0.1	1	1.1153	0.1483	0.1330
0.1	1.1	1.1109	0.1469	0.1322
0.1	1.2	1.1065	0.1488	0.1345
0.1	1.3	1.1023	0.1513	0.1373
0.3	0.8	1.1243	0.1678	0.1492
0.3	0.9	1.1198	0.1561	0.1394
0.3	1	1.1153	0.1483	0.1330
0.3	1.1	1.1109	0.1469	0.1322
0.3	1.2	1.1065	0.1488	0.1345
0.3	1.3	1.1023	0.1513	0.1373
0.5	0.8	1.1243	0.1678	0.1492
0.5	0.9	1.1198	0.1561	0.1394
0.5	1	1.1153	0.1483	0.1330
0.5	1.1	1.1109	0.1469	0.1322
0.5	1.2	1.1065	0.1488	0.1345
0.5	1.3	1.1023	0.1513	0.1373

Table D.2: Properties of ammonia-air mixtures employed in this study.

P_i	Equivalence Ratio ϕ	Unburned Density ρ_u	Burned Density ρ_b	ρ_b / ρ_u
0.3	0.9	3.248	0.465	0.1432
	1	3.222	0.437	0.1356
	1.1	3.198	0.438	0.1370
0.5	0.9	5.413	0.775	0.1432
	1	5.37	0.727	0.1354
	1.1	5.33	0.729	0.1368

Table D.3: Properties of ammonia-hydrogen-air mixtures employed in this study.

P_i	Equivalence Ratio ϕ	Unburned Density ρ_u	Burned Density ρ_b	ρ_b / ρ_u
0.1	0	1.074	0.146	0.1359
0.1	0.1	1.057	0.144	0.1362
0.1	0.2	1.040	0.143	0.1375
0.1	0.3	1.016	0.140	0.1379
0.1	0.5	0.973	0.136	0.1396
0.3	0	3.222	0.437	0.1356
0.3	0.1	3.172	0.431	0.1359
0.3	0.2	3.120	0.426	0.1365
0.3	0.3	3.047	0.418	0.1373
0.3	0.5	2.918	0.405	0.1388
0.5	0	5.370	0.727	0.1354
0.5	0.1	5.287	0.718	0.1358
0.5	0.2	5.200	0.708	0.1362
0.5	0.3	5.079	0.726	0.1430
0.5	0.5	4.863	0.724	0.1488